

Synthesis and structure-property relationship of mullite-type oxides

Dissertation

zur Erlangung des Doktorgrades der Naturwissenschaften

-Dr. rer. nat.-

Vorgelegt dem Promotionsausschuss
des Fachbereichs 02 (Biologie/Chemie)
der Universität Bremen



University
of Bremen

von

Kowsik Ghosh

Chemische Kristallographie fester Stoffe

Universität Bremen, Germany

Bremen, im Dezember 2021

Diese Arbeit wurde in der Arbeitsgruppe „Chemische Kristallographie fester Stoffe“ von Herrn Prof. Dr. Thorsten M. Gesing an der Universität Bremen im Zeitraum von Oktober 2018 bis September 2021 angefertigt.

Begutachtung des schriftlichen Teils:

1. Gutachter: Prof. Dr. Reinhard X. Fischer, University of Bremen

2. Gutachter: Prof. Dr. Claus Rücher, Leibniz Universität Hannover

3. Gutachter: Prof. Dr. Jürgen Schreuer, Ruhr-Universität Bochum

Begutachtung des schriftlichen Teils: Abgabe 20.12.2021

Datum der Verteidigung: 10.02.2021 (10th February, 2022)

Mitglieder des Prüfungsausschusses:

1. Prof. Dr. Jens Beckmann, Fachbereich 02 Biologie/Chemie, Institut für Anorganische Chemie und Kristallographie, Metallorganische Chemie der Hauptgruppenelemente, Universität Bremen

2. Prof. Dr. Reinhard X. Fischer, Kristallographie, GEO, University of Bremen

3. Prof. Thorsten M. Gesing, Fachbereich 02 Biologie/Chemie, Institut für Anorganische Chemie und Kristallographie, Chemische Kristallographie fester Stoffe, Universität Bremen

4. Prof. Dr. Ella Schmidt, Fachbereich 05 Geowissenschaften, Kristallographie, Universität Bremen

5. PD Dr. M. Mangir Murshed, Fachbereich 02 Biologie/Chemie, Institut für Anorganische Chemie und Kristallographie, Chemische Kristallographie fester Stoffe, Universität Bremen.

6. Carla Uribe, Fachbereich 02 Biologie/Chemie, Institut für Anorganische Chemie und Kristallographie, Student im Masterstudiengang Chemie, Universität Bremen

Synthesis and structure-property relationship of mullite-type oxides

Dissertation

to obtain the doctoral degree in natural sciences

-Dr. rer. nat.-

Submitted to the doctoral committee

of Faculty 02 (Biology / Chemistry)

at the University of Bremen



University
of Bremen

from

Kowsik Ghosh

Institute of Inorganic Chemistry and Crystallography

University of Bremen, Germany

Bremen, December 2021

This work was carried out in the working group "Institute of Inorganic Chemistry and Crystallography" by Prof. Dr. Thorsten M. Gesing at the University of Bremen from October 2018 to September 2021.

Assessment of the written part:

1st reviewer: Prof. Dr. Reinhard X. Fischer, University of Bremen

2nd reviewer: Prof. Dr. Claus Rüscher, Leibniz Universität Hannover

3rd reviewer: Prof. Dr. Jürgen Schreuer, Ruhr-Universität Bochum

Date of submission: 20th December, 2021.

Date of defense: 10.02.2021 (10th February, 2022)

Examination committee:

1. Prof. Dr. Jens Beckmann, Fachbereich 02 Biologie/Chemie, Institut für Anorganische Chemie und Kristallographie, Metallorganische Chemie der Hauptgruppenelemente, Universität Bremen
2. Prof. Dr. Reinhard X. Fischer, Kristallographie, GEO, University of Bremen
3. Prof. Thorsten M. Gesing, Fachbereich 02 Biologie/Chemie, Institut für Anorganische Chemie und Kristallographie, Chemische Kristallographie fester Stoffe, Universität Bremen
4. Prof. Dr. Ella Schmidt, Fachbereich 05 Geowissenschaften, Kristallographie, Universität Bremen
5. PD Dr. M. Mangir Murshed, Fachbereich 02 Biologie/Chemie, Institut für Anorganische Chemie und Kristallographie, Chemische Kristallographie fester Stoffe, Universität Bremen.
6. Carla Uribe, Fachbereich 02 Biologie/Chemie, Institut für Anorganische Chemie und Kristallographie, Student im Masterstudiengang Chemie, Universität Bremen

Acknowledgments

First of all, I would like to thank Prof. Dr. Thorsten M. Gesing for allowing me to work in his group, for his continuous support and valuable suggestions. Many thanks to my advisor, PD. Dr. M. Mangir Murshed for his guidance and the inspiring discussions, suggestions to improve my manuscripts and research. I am also grateful to Dr. Lars Robben and Mrs. Gabriele Ebert for their kind help during my stay.

I am honored that Prof. Dr. Reinhard X. Fischer from the University of Bremen, Prof. Dr. Claus Rüscher from Leibniz Universität Hannover and Prof. Dr. Jürgen Schreuer from Ruhr-Universität Bochum are willing to serve as the reviewer of my dissertation. I appreciate their time and suggestions for improving my dissertation.

For the all collaboration works I thank Dr. Michael Fischer (GEO, University of Bremen), Dr. Thomas Frederichs (GEO, University of Bremen), Dr. Qiang Zhang (POWGEN, SNS Oak Ridge, USA) and Dr. Naveen K. C. Muniraju (Institute of Physics, Croatia).

I am indebted to my lovely colleagues, past and present in the AG Gesing group for being good friends to me. Special thanks Mathias Gogolin, Niels Lefeld and Pengyun Chen for helpful scientific discussion and having lots of fun together.

I am thankful to Dr. Michael Wendschuh, Dr. Iris Spiess and Dr. Johannes Birkenstock in the AG Fischer group at the University of Bremen for the management and training of the X-ray diffractometers.

For financial support I thank to University of Bremen for carrying out my research and DAAD for project funding and supporting to present my research at IUCr 2021 Congress conference.

Last but not the least I am grateful to my family for encouraging and being always with me, in particular, my brother Souvik Ghosh who always boost my mental health. I am indebted to my small cricket group in Bremen who always made me fresh and healthy for research after playing cricket at the weekend.

Ort, Datum: Bremen, 15.12.2021

Erklärungen zur elektronischen Version und zur Überprüfung einer Dissertation

Hiermit betätige ich gemäß §7, Abs. 7, Punkt 4, dass die zu Prüfungszwecken beigelegte elektronische Version meiner Dissertation identisch ist mit der abgegebenen gedruckten Version.

Ich bin mit der Überprüfung meiner Dissertation gemäß §6 Abs. 2, Punkt 5 mit qualifizierter Software im Rahmen der Untersuchung von Plagiatsvorwürfen einverstanden.

Unterschrift

Declaration

I hereby declare that this submission is my own work and that, to the best of my knowledge and belief, it contains no material previously published or written by another person nor material which to a substantial extent has been accepted for the award of any other degree or diploma of the university or other institute of higher learning, except where due acknowledgment has been made in the text.

Signature: _____ Date: 15.12.2021

Declaration

Versicherung an Eides Statt

Hiermit versichere ich, Kowsik Ghosh,

Lilienthaler Heerstr. 6, 28359, Bremen, Deutschland

an Eides statt durch meine Unterschrift, dass ich die vorstehende Arbeit mit dem Titel

„*Synthesis and structure-property relationship of mullite-type oxides*“ selbständig und ohne fremde Hilfe angefertigt und alle Stellen, die ich wörtlich dem Sinne nach aus Veröffentlichungen entnommen habe, als solche kenntlich gemacht habe, mich auch keiner anderen als der angegebenen Literatur oder sonstiger Hilfsmittel bedient habe.

Ich versichere an Eides statt, dass ich die vorgenannten Angaben nach bestem Wissen und Gewissen gemacht habe und dass die Angaben der Wahrheit entsprechen und ich nichts verschwiegen habe.

Die Strafbarkeit einer falschen eidesstattlichen Versicherung ist mir bekannt, namentlich die Strafandrohung gemäß § 156 StGB bis zu drei Jahren Freiheitsstrafe oder Geldstrafe bei vorsätzlicher Begehung der Tat bzw. gemäß § 161 Abs. 1 StGB bis zu einem Jahr Freiheitsstrafe oder Geldstrafe bei fahrlässiger Begehung.

Kowsik Ghosh

Bremen, 15.12.2021

**Declaration on the contribution of the candidate to a multi-author article/manuscript
which is included as a chapter in the submitted doctoral thesis**

Chapter 3:

Contribution of the candidate in % of the total workload (up to 100 % for each of the following categories):

Experimental concept and design:	ca. 80 %
Experimental work and/or acquisition of (experimental) data:	ca. 100 %
Data analysis and interpretation:	ca. 80 %
Preparation of Figures and Tables:	ca. 100 %
Drafting of the manuscript:	ca. 70 %

Chapter 4:

Contribution of the candidate in % of the total workload (up to 100 % for each of the following categories):

Experimental concept and design:	ca. 80 %
Experimental work and/or acquisition of (experimental) data:	ca. 90 %
Data analysis and interpretation:	ca. 70 %
Preparation of Figures and Tables:	ca. 95 %
Drafting of the manuscript:	ca. 70 %

Chapter 5:

Contribution of the candidate in % of the total workload (up to 100 % for each of the following categories):

Experimental concept and design:	ca. 80 %
Experimental work and/or acquisition of (experimental) data:	ca. 80 %
Data analysis and interpretation:	ca. 70 %
Preparation of Figures and Tables:	ca. 90 %
Drafting of the manuscript:	ca. 70 %

Date: 15.12.2021

Signatures:

Table of Contents

Acknowledgments	5
Declaration	7
Publications	11
List of Abbreviations	12
Zusammenfassung	13
Summary	15
Thesis structure	17
Chapter 1	18
Introduction.....	18
Chapter 2	36
Experimental methods	36
Details of declaration on own contributions to the publications	42
Chapter 3	45
Synthesis and characterization of $(\text{Bi}_{1-x}\text{R}_x)_2\text{Mn}_4\text{O}_{10}$	45
Chapter 4	73
Aluminum to germanium inversion in mullite-type RAlGeO_5	73
Chapter 5	121
Structural, vibrational, thermal and magnetic properties of mullite-type NdMnTiO_5 ceramic	121
Chapter 6	146
Synthesis of relevant O10-phases and characterizations	146
Outlook.....	150
Appendix	152
Curriculum Vitae	154

Publications

K. Ghosh, M.M. Murshed*, T.M. Gesing; Synthesis and characterization of $(\text{Bi}_{1-x}\text{R}_x)_2\text{Mn}_4\text{O}_{10}$: structural, spectroscopic and thermogravimetric analyses for R = Nd, Sm and Eu; *Journal of Materials Science* 54 (21) (2019) 13651-13659. Doi:10.1007/s10853-019-03852-7

K. Ghosh, M.M. Murshed*, M. Fischer, T.M. Gesing; Aluminum to germanium inversion in mullite-type RAlGeO_5 : characterization of a rare phenomenon for R = Y, Sm – Lu; *Journal of the American Ceramic Society* 105 (2022) 728-741. Doi:10.1111/jace.18085

K. Ghosh, M.M. Murshed*, T. Frederichs, T.M. Gesing; Structural; vibrational, thermal and magnetic properties of NdMnTiO_5 ceramic, *Journal of the American Ceramic Society* (Accepted 2021). DOI: 10.1111/jace.18261

List of Abbreviations

ADP	Atomic displacement parameter
DASF	Derivative absorption spectrum fitting
DSC	Differential scanning calorimetry
DTA	Differential thermal analysis
FC	Field cooling
FTIR	Fourier transform infrared
LEP	Lone electron pair
LDV	Liebau density vector
NPD	Neutron powder diffraction
ORNL	Oak Ridge National Laboratory
PXRD	Powder X-ray diffraction
SNS	Spallation Neutron Source
TGA	Thermogravimetric analysis
T_N	Néel transition temperature
XRD	X-ray diffraction
XRPD	X-ray powder diffraction
WLE	Wang-Liebau eccentricity
ZFC	Zero-field cooling

Zusammenfassung

Oxide des Mullit-Typs ziehen aufgrund ihrer Kristallstruktur, magnetischen und multiferroischen Eigenschaften die Aufmerksamkeit der Forschung auf sich. Substitution der chemischen Zusammensetzung in Mullit-Oxiden bietet die Möglichkeit einer Vielzahl neuer Phasen, wodurch deren strukturellen und chemisch-physikalischen Eigenschaften beeinflussen werden.. Im Rahmen dieser kumulativen Dissertation wurden mullitartige Oxide vom Typ der O10-Phasen synthetisiert und untersucht.

Um zu verstehen, welche Rolle die LEP-Kationen für die strukturelle Stabilität in O10-Phasen spielen, berichteten wir über eine systematische Substitution von Bi^{3+} durch Seltenerd-Kationen, d. h. Nd^{3+} , Sm^{3+} und Eu^{3+} in $\text{Bi}_2\text{Mn}_4\text{O}_{10}$ -Verbindungen [1]. Alle polykristallinen Proben kristallisieren in der orthorhombischen Raumgruppe *Pbam*, was durch Rietveld Verfeinerung der Pulverröntgendaten nachgewiesen werden konnte. Die eckenverknüpften MnO_6 Oktaeder formen hierbei eine unendlich lange Kette entlang der c-Achse und sind durch verzerrt tetragonal eckenverknüpfte MnO_5 -Pyramiden verbunden. Im Käfig zwischen den Polyederketten sitzen die R^{3+} Kationen ($R = \text{Bi}, \text{Nd}, \text{Sm}$ und Eu), welche einen RO_8 Polyeder formen. Um die Stärke der stereochemischen Aktivität des LEP-Kations zu bestimmen wurde der Wang-Liebau-Exzentrizitätsparameter (WLE) aus den Strukturdaten berechnet, der eine lineare Abnahme des WLE-Werts in $(\text{Bi}_{1-x}\text{R}_x)_2\text{Mn}_4\text{O}_{10}$ ($R = \text{Nd}, \text{Sm}$ und Eu) zeigt. Während die Substitution von Übergangsmetallkationen in verschiedenen Polyederzentren durch Nicht-Übergangsmetallkationen viele Phasen dieser O10-Mullit-Typ-Familie ermöglicht, fehlte bis jetzt eine komplette Reihe dieser Mullit-Typ-Verbindungen mit R -Kationen und $\text{Al}^{3+}/\text{Ge}^{4+}$, obwohl die Ionenradien und die Al/Ge-O-Bindungsabstände ziemlich ähnlich sind. Daher berichteten wir über die Synthese und Charakterisierung von RAlGeO_5 ($R = \text{Y}, \text{Sm-Lu}$)-Phasen [2]. Für diese sogenannten O10-Phasen vom Mullit-Typ wurde eine seltene Inversion von Al/Ge zwischen oktaedrischer und pyramidalen Koordination beobachtet, mit Inversionsparametern zwischen 0.22(1) und 0.30(1) für

verschiedene *R*-Kationen. Selektive Raman-Banden im Bereich höherer Wellenzahlen unterstützen die beobachtete Inversion von Al/Ge zwischen zwei Koordinationspolyedern. Aufgrund der zentrosymmetrischen Struktur der mullitartigen $\text{Bi}_2\text{Mn}_4\text{O}_{10}$ -Verbindung wurde der mikroskopische Ursprung der Multiferroizität durch ein komplexes Zusammenspiel zwischen Spinordnung, hochpolarisierbarem Bi^{3+} mit stereochemisch aktivem einsamen Elektronenpaar, $\text{Mn}^{3+}/\text{Mn}^{4+}$ -Ladungsordnung und geometrischen Verzerrungen der MnO_y -Koordinationspolyeder erklärt. Auf der Suche nach neuen Multiferroika berichten wir über die Synthese und Charakterisierung der isostrukturellen NdMnTiO_5 -Verbindung vom O10-Mullit-Typ [3]. Die Kationen Mn^{3+} und Ti^{4+} sind oktaedrisch bzw. pyramidal lokalisiert. Die höhere Zersetzungstemperatur von NdMnTiO_5 im Vergleich zu anderen RMn_2O_5 -Phasen wird durch eine höhere Bindungsstärke von Ti-O-Bindungen gegenüber den Mn-O-Bindungen erklärt. Die temperaturabhängige magnetische DC-Suszeptibilität deutet auf einen Phasenübergang (T_N) von paramagnetisch zu antiferromagnetisch bei 43(1) K hin. Die inverse Suszeptibilität im paramagnetischen Bereich über 120 K folgt dem Curie-Weiss-Gesetz, was zu einem magnetischen Moment von 6.33(1) μB pro Formeleinheit führt. Neutronenbeugungsdaten, die bei 7.5 K gesammelt wurden, zeigen, dass die magnetischen Momente von Nd^{3+} und Mn^{3+} in NdMnTiO_5 mit einem Ausbreitungsvektor $\mathbf{k} = (0, 0.238, 0.117)$ inkommensurabel geordnet sind.

References

- [1] K. Ghosh, M.M. Murshed, T.M. Gesing; Synthesis and characterization of $(\text{Bi}_{1-x}\text{R}_x)_2\text{Mn}_4\text{O}_{10}$: structural, spectroscopic and thermogravimetric analyses for $\text{R} = \text{Nd}, \text{Sm}$ and Eu ; *Journal of Materials Science* 54(21) (2019) 13651-13659. Doi:10.1007/s10853-019-03852-7
- [2] K. Ghosh, M.M. Murshed, M. Fischer, T.M. Gesing; Aluminum to germanium inversion in mullite-type RAlGeO_5 : characterization of a rare phenomenon for $\text{R} = \text{Y}, \text{Sm} - \text{Lu}$; *Journal of the American Ceramic Society* 105 (2022) 728-741. Doi:10.1111/jace.18085
- [3] K. Ghosh, M.M. Murshed, T. Frederichs, T.M. Gesing, structural; vibrational, thermal and magnetic properties of NdMnTiO_5 , *Journal of the American Ceramic Society* (Accepted 2021). DOI: 10.1111/jace.18261

Summary

Mullite-type oxides draw intensive research attention because of their crystal structures, magnetic and multiferroic properties. Diverse chemical compositions in mullite-type oxides can offer plenty of new phases with novel crystal-chemico-physical properties. The main objective of this work is to study the structure-property relationships of mullite-type oxides as function of chemical composition. Within the scope of this cumulative dissertation, the O10-mullite-phases were synthesized and studied.

To understand whether the lone electron pair (LEP) containing cation play a role for structural stability in O10-phases, a systematic substitution of Bi^{3+} by rare-earth cations Nd^{3+} , Sm^{3+} and Eu^{3+} in the $\text{Bi}_2\text{Mn}_4\text{O}_{10}$ compound [1] was carried out (Chapter 3). Rietveld refinement of powder X-ray diffraction data indicated that all polycrystalline samples crystalize in orthorhombic space group *Pbam*, where the edge-sharing MnO_6 octahedra form an infinite chain along the c-axis and interconnected by edge-sharing MnO_5 distorted tetragonal pyramids. The R^{3+} cation ($R = \text{Bi}, \text{Nd}, \text{Sm}$ and Eu) sits in the channels between the polyhedral chains, forming distorted RO_8 polyhedra. To measure the strength of stereochemical activity of LEP-cation, Wang-Liebau eccentricity (WLE) parameter was calculated from the structural data, showing a linear decrease of WLE value in $(\text{Bi}_{1-x}\text{R}_x)_2\text{Mn}_4\text{O}_{10}$ ($R = \text{Nd}, \text{Sm}$ and Eu). Whereas substitution of transition metal cations in different polyhedral sites by non-transition metal cations can offer a plenty of phases of this O10-mullite-type family, mullite-type compounds with R -cations and $\text{Al}^{3+}/\text{Ge}^{4+}$ were still missing though the ionic radii and Al/Ge-O bond distances in a given coordination are quite similar. As such, synthesis and characterization of RAlGeO_5 ($R = \text{Y}, \text{Sm-Lu}$) phases [2] were studied (Chapter 4). A rare inversion of Al/Ge between octahedral and pyramidal sites have been observed for these O10-phases, and the inversion parameter found to be between 0.22(1) and 0.30(1) for different R -cations. Selective vibrational features at higher wavenumber regions further complement the inversion of Al/Ge between two coordination sites. Due to centrosymmetric structure of the

mullite-type $\text{Bi}_2\text{Mn}_4\text{O}_{10}$ compound the microscopic origin of the multiferroicity requires convincing explanation in terms of complex interplay between spin-ordering, highly polarizable Bi^{3+} with stereo-chemically active LEP, $\text{Mn}^{3+}/\text{Mn}^{4+}$ charge-ordering and geometric distortions of the MnO_y coordination polyhedra. As such, mullite-type NdMnTiO_5 [3] was synthesized followed by multi-tool characterizations (chapter 5). The Mn^{3+} and Ti^{4+} cations were observed to be located in the octahedral and pyramidal site, respectively. The higher decomposition temperature of NdMnTiO_5 , compared to other RMn_2O_5 phases, was explained in terms of higher bond strength of Ti-O than those of Mn-O. Temperature-dependent DC magnetic susceptibility suggested paramagnetic to antiferromagnetic phase transition (T_N) at 43(1) K. Inverse susceptibility in the paramagnetic region above 120 K followed the Curie-Weiss law, resulting in a magnetic moment of 6.33(1) μ_B per formula unit. Neutron diffraction data collected at 7.5 K revealed that the magnetic moments of Nd^{3+} and Mn^{3+} in NdMnTiO_5 are incommensurately ordered with a propagation vector $\mathbf{k} = (0, 0.238, 0.117)$.

References

- [1] K. Ghosh, M.M. Murshed, T.M. Gesing; Synthesis and characterization of $(\text{Bi}_{1-x}\text{R}_x)_2\text{Mn}_4\text{O}_{10}$: structural, spectroscopic and thermogravimetric analyses for R = Nd, Sm and Eu; *Journal of Materials Science* 54(21) (2019) 13651-13659. Doi:10.1007/s10853-019-03852-7
- [2] K. Ghosh, M.M. Murshed, M. Fischer, T.M. Gesing; Aluminum to germanium inversion in mullite-type RAIGeO_5 : characterization of a rare phenomenon for R = Y, Sm – Lu; *Journal of the American Ceramic Society* 105 (2022) 728-741. Doi:10.1111/jace.18085
- [3] K. Ghosh, M.M. Murshed, T. Frederichs, T.M. Gesing, structural; vibrational, thermal and magnetic properties of NdMnTiO_5 , *Journal of the American Ceramic Society* (Accepted 2021). DOI: 10.1111/jace.18261

Key words: Mullite, structure property relationship, vibrational property, optical property, thermal stability, magnetic property, WLE, LEP.

Thesis structure

This dissertation is submitted as cumulative research work. That is, the main frame of the thesis is based on three manuscripts (DOI: <https://doi.org/10.1007/s10853-019-03852-7>, <https://doi.org/10.1111/jace.18085> and <https://doi.org/10.1111/jace.18261>) published in peer-reviewed journals and some relevant follow up works. In **chapter 1**, different types of mullite-type oxides are reviewed in particular on their crystal structures, properties and applications. **Chapter 2** describes the common experimental methods used for synthesis, characterization, and the associated instrumental setups. **Chapter 3, 4 and 5** are representation (mimic) these three manuscripts. **Chapter 3** introduces synthesis and characterization of $(\text{Bi}_{1-x}\text{R}_x)_2\text{Mn}_4\text{O}_{10}$: structural, spectroscopic and thermogravimetric analyses for $R = \text{Nd}, \text{Sm}$ and Eu . In the **chapter 4**, aluminum to germanium inversion in mullite-type RAlGeO_5 : characterization of a rare phenomenon for $R = \text{Y}, \text{Sm} - \text{Lu}$ is discussed. **Chapter 5** describes the structural, vibrational, thermal, and magnetic properties of NdMnTiO_5 ceramic. **Chapter 6** represents some follow up works on the isostructural compounds to those in **chapter 3 - 5**. Respective cited references were presented at the end of each chapter.

Chapter 1

Introduction

The rapid growth of science and technology demands not only the fundamental research but also diverse applications on the fields, leading to mostly shape the modern societal lives. The synthesis of new materials with unique properties is always key features for different applications. Mullite and mullite-type materials are demanding research field (**Figure 1.1**) for various technological applications with interesting structural features. Mullite materials showed a wide range technical applications due to their fascinating properties such as low density, high thermal stability, low thermal expansion and conductivity and excellent thermal shock behavior [1-4]. The traditional applications of mullite materials are more frequents due to their availability in large amounts at relatively low costs [2, 4]. For instance, typical applications of monolithic mullite materials are as thermocouple tubes, crucibles, heat exchangers, advanced refractories, catalyst supported devices, substrates for silicon solar cells, optical materials electronic packaging materials and dental ceramic components [3, 5-10]. To stop oxidation induced degradation of most of the metals and non-oxide materials, deposition thin mullite layers on these susceptible materials using physical or chemical or chemical deposition techniques applied to achieve the stability on oxidizing atmosphere [2, 4]. Mullite coatings because of its admirable characteristics of excellent creep behavior, good corrosion resistance ability and suitable strength and toughness [11, 12], are also applied on the substrates for hot gas and oily water cleaning [13-15]. Due to their high-temperature insulating characteristics, mullite fibers are used for electrical insulation of electrodes in smelting furnaces, rotary or tube kiln seals. Mullite fiber fabrics are also successfully used for diesel emission filters [16-18].

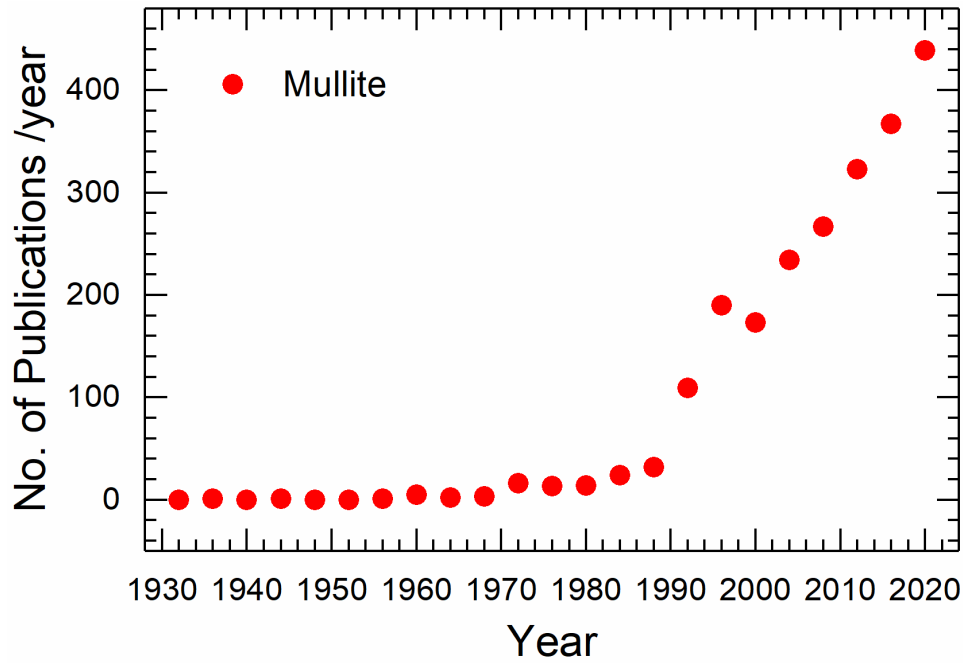


Figure 1.1: Publications per year using the keywords ‘mullite’ (source: web of science).

A demonstration of mullite compounds with different chemical composition is desired to better understand the relationship between crystal structure and properties of mullite compounds. Mullite belongs to the mullite-type crystal structure which are characterized and in principle classified by Fischer and Schneider [19] and Fischer et al. [20]. The key backbone feature of mullite-type crystal structure is the single chain of edge-sharing octahedra in highest tetragonal aristotype, that is, $P4/mbm$ symmetry. The mullite-type crystals must be formed in the subgroup of this highest symmetry in such a way that the aspect ratio of **a**- and **b**-dimension lies close to 1 [19]. The octahedral chains could be cross-linked by tetrahedra (e.g. AlO_4 and SiO_4 in sillimanite and mullite) [21, 22], trigonal pyramid (e.g. AlO_5 in Andalusite) [23, 24], square pyramid (e.g., Mn_2O_8 in $Bi_2Mn_4O_{10}$), trigonal planar (e.g., BO_3 in B-doped mullite and $PbMBO_4$) [25, 26] and double tetrahedra (e.g., Fe_2O_7 in $Bi_2Fe_4O_9$) [27] groups rising of different mullite-type compounds. Depending on the cross-linking groups, these mullite-type compounds are further sub-divided into, so called, O10- (e.g., $R_2Mn_4O_{10}$; $R = Bi, Y, \text{rare-earth}$) [28-36], O9- (e.g., $Bi_2M_4O_9$ [37-49] and $A_4B_2O_9$ [50-55]) and O8-phases

(e.g., PbMBO_4 [56-61] and schafarzikites [62-69]). Each phase is different by crystal structure as well as their chemico-physical properties point of view. The O10-phases crystallize as $\text{Dy}_2\text{Mn}_4\text{O}_{10}$ structure type [70]. And their crystal structure can be described in the orthorhombic space group $Pbam$, where edge-sharing MnO_6 octahedra form infinite chains running parallel to the c -axes (**Figure 1.2**). These chains are interconnected by Mn_2O_8 edge-sharing square-pyramid units. Octahedral chain connecting to its adjacent layer by double pyramids form a 5-ring channel where DyO_8 polyhedral sites are located (**Figure 1.2**). It is well established that the Mn^{4+} cations are located in the MnO_6 octahedral sites and Mn^{3+} in the MnO_5 pyramidal site [35, 36, 71]. The structure of $\text{Bi}_2\text{Mn}_4\text{O}_{10}$ (O10-phases) are closely related to the $\text{Bi}_2\text{M}_4\text{O}_9$ (O9-phases) [37-49] and differs by only one oxygen atom in the connecting link of octahedral sites. That is, the octahedral chains are interconnected by double-tetrahedral (M_2O_7) units in O9-phases (**Figure 1.3**).

The slight but significant stereochemical activity of the $6s^2$ lone electron pair (LEP) of the Bi^{3+} cations seem also to be responsible for the LEP-driven polarizability [72]. To measure the magnitude of the stereochemical activity of the LEP-cations in a given crystal structure, Wang-Liebau eccentricity (WLE) [73-77] and Liebau density vector (LDV) have been recently introduced [72]. While WLE provides only a scalar magnitude, LDV bears vector characteristic [72]. Since calculation of LDV requires accurate electron density (density functional theory (DFT) is an appropriate tool) [72], WLE could be readily obtained from the crystal data. Within the seminal works of Wang and Liebau the concept of WLE was mostly limited showing a correlation between WLE and the structural bond valence sum (BVS) of the LEP-cation [74]. The higher WLE values of Bi^{3+} cations in $\text{Bi}_2\text{Mn}_4\text{O}_9$ compound than that of in $\text{Bi}_2\text{Mn}_4\text{O}_{10}$ compound [72] signposts not only the higher stereochemical activity of Bi^{3+} cations [72] but also this stereochemical activity of LEP-cation might or might not play a role for the structural stability of O10-phases.

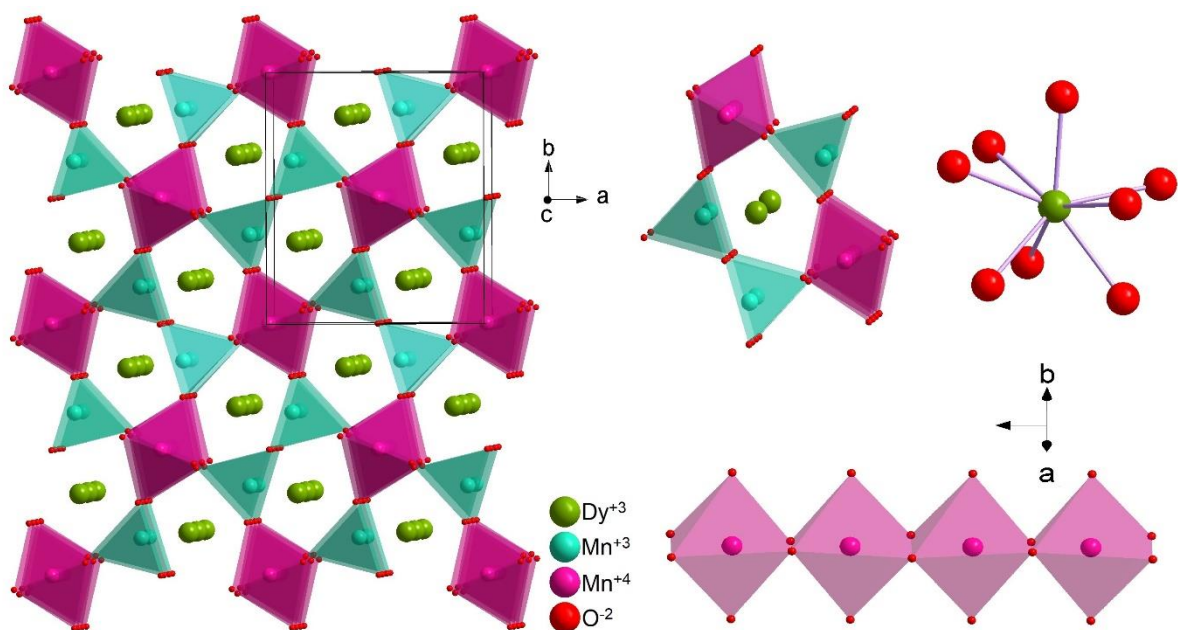


Figure 1.2: Representative crystal structure of $\text{Dy}_2\text{Mn}_4\text{O}_{10}$ mullite-type compound (O10-phase) showing octahedral chain in the c -direction, 5-ring channel and DyO_8 polyhedra.

As such, whereas no replacement of Bi^{3+} cation by other non-LEP-cations in O9-phases are seen so far, there are plenty of compounds have been reported with non-LEP rare-earth cations in O10-structure type, giving of $R_2\text{Mn}_4\text{O}_{10}$ compounds ($R =$ rare earth) [28, 78]. However, Alanso et al. showed that a high oxygen pressure required for the synthesis of $R_2\text{Mn}_4\text{O}_{10}$ compounds ($R = \text{La, Pr, Sm, Nd, Eu}$) [78]. On this regard, we found a miscibility works to describe whether LEP-cations play a role in structural stability of O10-compounds or not. In this thesis, we reported a systematic work of solid solutions of $(\text{Bi}_{1-x}\text{R}_x)\text{Mn}_4\text{O}_{10}$ ($R = \text{Nd, Eu and Sm}$) compounds. A detail structural, spectroscopic, and thermal properties of all the compounds were described in **chapter 3**.

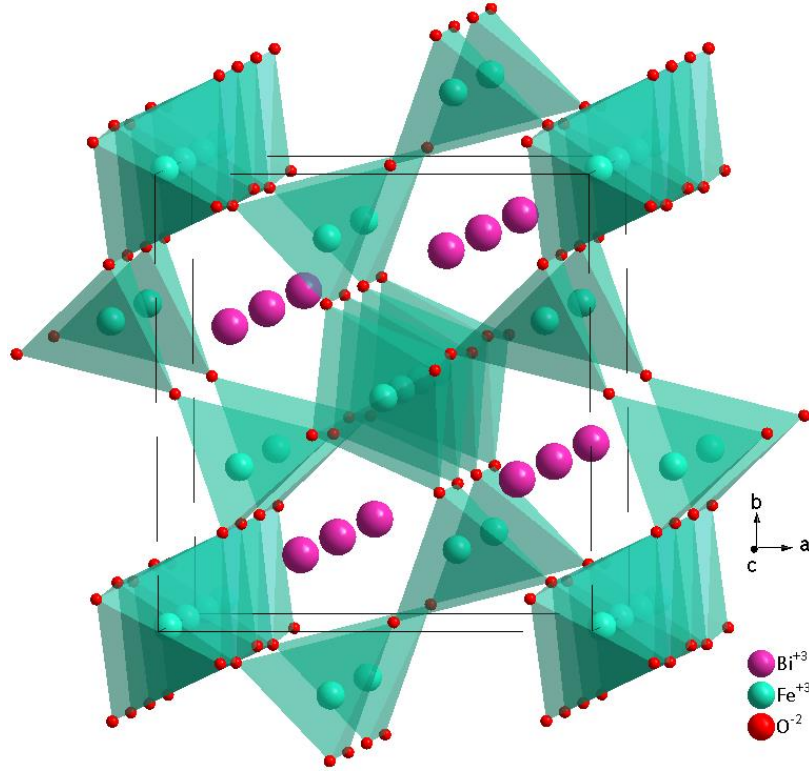


Figure 1.3: Representative crystal structure of $\text{Bi}_2\text{Fe}_4\text{O}_9$ (O9-phase) mullite-type compound.

Two different dipoles from Mn^{4+}O_6 (along **c**-axis) and Mn^{3+}O_5 (along **b**-axis) polyhedra in different directions [30] in O10-phases leading to poor electrical polarization [35, 79] could be associated to the small ferroelectric displacement which are difficult to be detected within the experimental uncertainty. The charge-ordering between Mn^{3+} and Mn^{4+} is one of the factors for generation of ferroelectricity in the $R_2\text{Mn}_4\text{O}_{10}$ compounds [80]. Not only the *R*-sites but also the substitution of manganese with other transitional cations such as Fe^{3+} and Cr^{3+} gives $R_2\text{Mn}_2\text{Fe}_2\text{O}_{10}$ ($R = \text{Y, Ho, Er}$) [32-34] and $R_2\text{Mn}_2\text{Cr}_2\text{O}_{10}$ ($R = \text{Y, Sm-Tb, Ho and Er}$) [29, 81] phases where tertiary cations are located on pyramidal sites. Therefore, general formula can be explicated as $R_2M'_2M''_2\text{O}_{10}$. Replacement of transition cations either in octahedral or pyramidal site is not only limited by transition element but also with non-transition element. The Ge^{4+} substitution along with transition cation Cr^{3+} forms $R_2\text{Cr}_2\text{Ge}_2\text{O}_{10}$ ($R = \text{Nd-Er, Y}$) phases [82] where a disorder of Cr/Ge between octahedral and pyramidal sites were reported [82]. Due to its structural changes with disorder phenomenon these phases also

differ of their chemico-physical properties from other O10-phases. Further substitution of non-transition cations e.g. Al^{3+} , Ge^{4+} and non-magnetic cation such as Ti^{4+} on the octahedral or pyramidal sites give rise of $R_2M_2\text{Ti}_2\text{O}_{10}$ ($R = \text{Pr, Nd, Sm, Eu, Gd}$ and $M = \text{Cr, Fe}$) [83] and $R_2\text{Al}_2\text{Ge}_2\text{O}_{10}$ ($R = \text{Y, Sm, Eu}$) [84] and ErAlGeO_5 [85] extend the mullite-type O10 family members. Substitution of transition cations on different polyhedral sites make the change in crystal structure as well as their chemico-physical properties. Nguyen et al. [71] showed distribution of Mn^{3+} and Mn^{4+} cations over octahedral and pyramidal sites in $\text{Bi}_2\text{Mn}_4\text{O}_{10}$. They also found the disorder of $\text{Fe}^{3+}/\text{Mn}^{4+}$ between different sites when on the substitution of Fe^{3+} cations to form $\text{Bi}_2\text{Mn}_{4-x}\text{Fe}_x\text{O}_{10}$ ($0 \leq x \leq 1$) [71]. Moreover, substitution of Ti^{4+} and Al^{3+} in $\text{Bi}_2\text{Mn}_4\text{O}_{10}$ [71] suggested that Ti^{4+} and Al^{3+} occupied the octahedral and square pyramidal sites, respectively. Whereas the closeness of Al^{3+} and Ge^{4+} cations such as ionic radii [86] and similar Al/Ge-O bond distances makes the alumogermanates as common minerals [87-90] in nature, it is strange that there are few alumogermanate mullite-type O10-phases. Their similar behaviors influence the physical properties by leading disorders [91-93] which are more common spinals [94-96]. Single crystal study of mullite-type ErAlGeO_5 [85] indicated disorder of $\text{Al}^{3+}/\text{Ge}^{4+}$ between octahedral and pyramidal sites. However, the study on a full series of powder phases with different rare-earth cations and their physical properties are absent in this O10 mullite-type structure. On this regard, we synthesized a series of $R\text{AlGeO}_5$ ($R = \text{Y, Sm-Lu}$) phases (O10-phases as $R_2\text{Al}_2\text{Ge}_2\text{O}_{10}$) and the samples were characterized by XRPD, vibrational and UV/Vis spectroscopy, thermogravimetric analysis. The detailed investigations are mentioned in **chapter 4**.

Magnetic properties and ferroelectric behaviors [97] of O10-phases are the key features of these compounds. As such, one of the fascinating properties of $R_2\text{Mn}_4\text{O}_{10}$ phases is the magnetoelectric effect [98-100] implying a correlation between magnetic ordering and ferroelectricity, that is, the application of external magnetic field leads to the electric polarization [101, 102]. The details of magnetic transition temperature and type of magnetic

transition of various O10-phases are shown in **table 1.1**. All the $R_2Mn_4O_{10}$ phases showed the antiferromagnetic magnetic with the transition temperature T_N of about or below 40 K [28, 30, 31, 99, 103-117]. The second transitions (**Table 1.1**) were explained to be related to the ferroelectric transitions for $R_2Mn_4O_{10}$ phases. In this regard to get higher transition temperature, Mn^{3+} cations in $R_2Mn_4O_{10}$ were replaced by Fe^{3+} and Cr^{3+} in the pyramidal position resulted $R_2Fe_2Mn_2O_{10}$ ($R = Y, Ho, Er$) [32-34] and $R_2Cr_2Mn_2O_{10}$ ($R = Y, Sm-Tb, Ho$ and Er) [29, 81]. While ferrimagnetic ordering was reported with transition temperature of about 153-165 K for $R_2Fe_2Mn_2O_{10}$ ($R = Y, Ho, Er$) [32-34] and 85 K for $Y_2Cr_2Mn_2O_{10}$ [29], paramagnetic behavior noticed for $R_2Cr_2Mn_2O_{10}$ ($R = Sm-Tb, Ho$ and Er) [81]. However, substitution of non-magnetic and non-transition cation such as Ge^{4+} in place of transition cation, the antiferromagnetic ordering displayed at very low temperature (T_N) of about 2.5 K for $Nd_2Cr_2Ge_2O_{10}$ [82] and no such transition has been detected for $Eu_2Cr_2Ge_2O_{10}$ and $Sm_2Cr_2Ge_2O_{10}$ [82]. Furthermore, $Nd_2Fe_2Ti_2O_{10}$ [118, 119] and $Nd_2Cr_2Ti_2O_{10}$ [120] also showed relatively lower T_N value of 18.5 and 20.5 K, respectively. The magnetic ordering of $R_2Mn_4O_{10}$ family are dependent on the size of the R^{3+} cations. For instance, whereas $Bi_2Mn_4O_{10}$ [30] and $La_2Mn_4O_{10}$ [31] showed commensurate magnetic ordering, R^{3+} cations with relatively lower ionic radii in $R_2Mn_4O_{10}$ showed incommensurate ordering [99, 103-117]. To understand the type of magnetic ordering and epicenter of multiferroic behavior of this system with centrosymmetric space group (here $Pbam$), **figure 1.4** depicted different magnetic contributions of $Nd_2Mn_4O_{10}$ [103], an analog of O10-phases. In the loop of 5-ring channel formed by three pyramidal and two octahedral site (**figure 1.4**), there are three types of magnetic interactions, named J_3 , J_4 and J_5 referring the antiferromagnetic spin coupling between $Mn^{3+} \leftrightarrow Mn^{4+}$, $Mn^{4+} \leftrightarrow Mn^{3+}$ and $Mn^{3+} \leftrightarrow Mn^{3+}$ magnetic sublattices [103].

Table 1.1: Type of magnetic ordering and transition temperature /K for some O10-phases.

O10 phase	Transition Temperature /K	Type of magnetic ordering	References
Bi ₂ Mn ₄ O ₁₀	39	*AFM, Commensurate	[30, 107]
La ₂ Mn ₄ O ₁₀	31	AFM, Commensurate	[31]
Pr ₂ Mn ₄ O ₁₀	25 and 18	AFM, Commensurate	[121, 122]
Nd ₂ Mn ₄ O ₁₀	30, 20 and 5	AFM, Incommensurate	[103]
Sm ₂ Mn ₄ O ₁₀	34 and 28	AFM, Incommensurate	[104]
Eu ₂ Mn ₄ O ₁₀	40	AFM, Incommensurate	[105]
Gd ₂ Mn ₄ O ₁₀	40	AFM, Incommensurate	[106]
Tb ₂ Mn ₄ O ₁₀	43	AFM, Commensurate	[107-109]
Dy ₂ Mn ₄ O ₁₀	44, 18 and 8	AFM, Incommensurate	[110, 111]
Y ₂ Mn ₄ O ₁₀	45	AFM, Incommensurate	[99, 112, 113]
Ho ₂ Mn ₄ O ₁₀	39	AFM, Incommensurate	[110]
Er ₂ Mn ₄ O ₁₀	25	AFM, Incommensurate	[109]
Tm ₂ Mn ₄ O ₁₀	44, 36 and 25	AFM, Commensurate	[114]
Yb ₂ Mn ₄ O ₁₀	32 and 6	AFM, Incommensurate	[115]
Y ₂ Fe ₂ Mn ₂ O ₁₀	165	Ferrimagnetic	[32]
Ho ₂ Fe ₂ Mn ₂ O ₁₀	153	Ferrimagnetic	[34]
Er ₂ Fe ₂ Mn ₂ O ₁₀	165	Ferrimagnetic	[33]
Y ₂ Cr ₂ Mn ₂ O ₁₀	85	Ferrimagnetic	[29]
Nd ₂ Cr ₂ Ge ₂ O ₁₀	2.6	AFM	[82]
Nd ₂ Fe ₂ Ti ₂ O ₁₀	18.5	AFM, commensurate	[83, 118, 119]
Nd ₂ Cr ₂ Ti ₂ O ₁₀	20.5	AFM, commensurate	[120, 123]

*AFM = Antiferromagnetic

With lowering the temperature, the AFM nature of Cairo-pentagonal (J_3 , J_4 and J_5 couplings) system induce magnetic frustration which leads to the displacement of Mn³⁺ cations from its centrosymmetric system to release the magnetic frustration. This is known as *exchange striction* mechanism where the inversion symmetry is broken to induce the ferroelectricity along the **b**-direction [108, 124, 125]. Two types of magnetic coupling in the Mn⁴⁺O₆

octahedral chain are known for J_1 and J_2 coupling. Where J_1 refers to the Mn^{4+} - Mn^{4+} interactions through R^{3+} layers, J_2 belongs through the Mn^{3+} layers (**figure 1.4**).

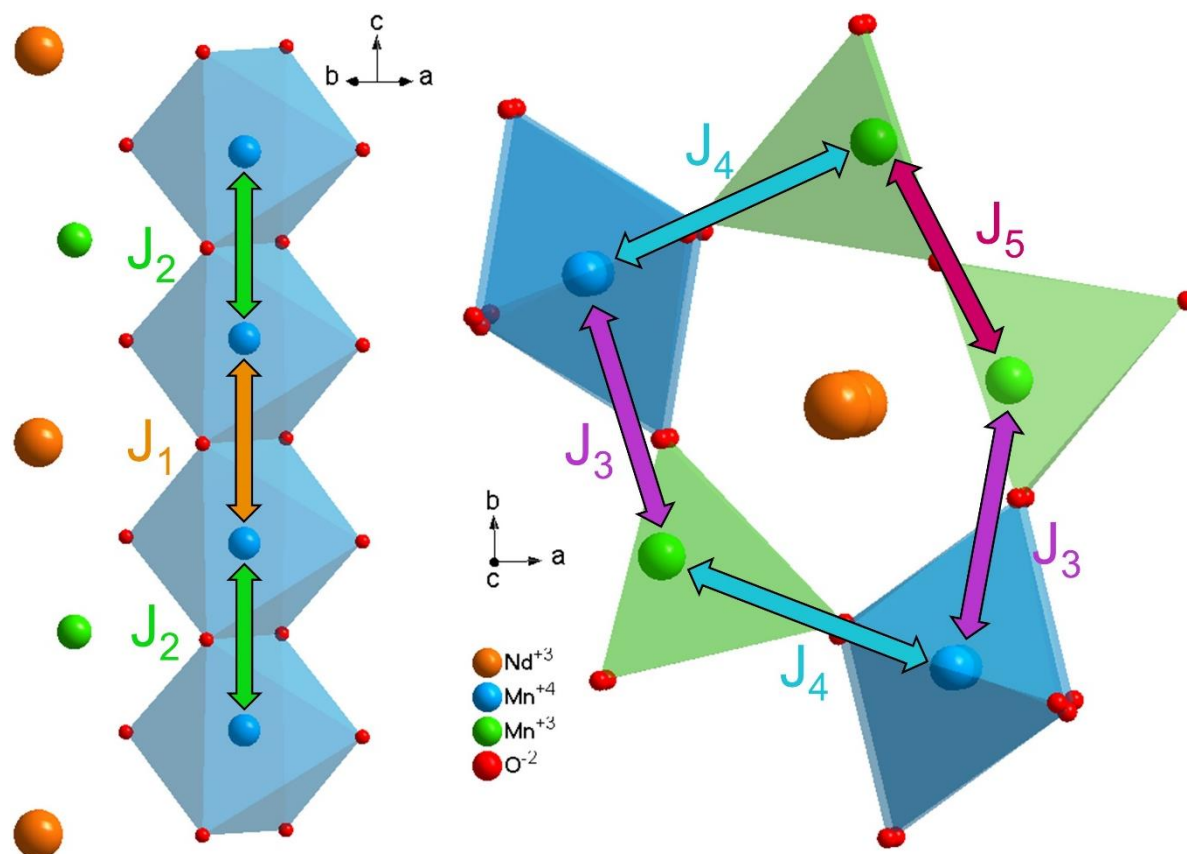


Figure 1.4: A representative different magnetic lattices of Mn^{4+} and Mn^{3+} cations in $\text{Nd}_2\text{Mn}_4\text{O}_{10}$.

A direct Mn^{4+} - O - Mn^{4+} ferromagnetic J_1 interaction and indirect Mn^{4+} - O - Mn^{3+} - O - Mn^{4+} antiferromagnetic coupling made the commensurately alignment in $\text{Bi}_2\text{Mn}_4\text{O}_{10}$ phase [30]. Here the ionic radii of R^{3+} cation plays a role for the magnetic alignment of Mn^{4+} cations in MnO_6 octahedra. As the ionic radii decreases from left to right in lanthanide series due to lanthanide contraction, the $\langle \text{Mn}^{4+}\text{-O} \rangle$ bond lengths shorten accordingly [126]. As a consequence, the enhanced J_2 coupling resulted the incommensurability of the magnetic structures along the c -direction for $R_2\text{Mn}_4\text{O}_{10}$ phases with relatively lower ionic radii [105, 108, 109, 111, 116, 117]. Since Ge^{4+} or Ti^{4+} cations are occupied the pyramidal site, it is

therefore understood that the relatively lower transition temperature (T_N) for $R_2Cr_2Ge_2O_{10}$ ($R = Nd-Er, Y$) [82], $Nd_2Fe_2Ge_2O_{10}$ [118, 119] and $Nd_2Cr_2Ge_2O_{10}$ [120] might be due to the absent of J_3 , J_4 and J_5 couplings. Intrinsically, magnetic interactions between Mn^{3+} and Ti^{4+} (non-magnetic but transition cation) would be interesting in this O10-mullite-type structure. Herein this thesis, we described the nuclear and magnetic structure of $Nd_2Mn_2Ti_2O_{10}$ along with its vibrational and thermal properties. The details are described in **chapter 5**.

Reference

- [1] I.A. Aksay, D.M. Dabbs, M. Sarikaya, Mullite for structural, electronic and optical applications, *Journal of the American Ceramic Society* 74(10) (1991) 2343-2358. Doi:10.1111/j.1151-2916.1991.tb06768.x
- [2] H. Schneider, R.X. Fischer, J. Schreuer, D.J. Green, Mullite: Crystal structure and related properties, *Journal of the American Ceramic Society* 98(10) (2015) 2948-2967. Doi:10.1111/jace.13817
- [3] H. Schneider, S. Komarneni, Mullite, WILEY-VCH Verlag GmbH & Co. KGaA, Weinheim (2005) 1-487.
- [4] H. Schneider, J. Schreuer, B. Hildmann, Structure and properties of mullite — A review, *Journal of the European Ceramic Society* 28(2) (2008) 329-344. Doi:10.1016/j.jeurceramsoc.2007.03.017
- [5] A. Focsa, I. Gordon, J.M. Auger, A. Slaoui, G. Beaucarne, J. Poortmans, C. Maurice, Thin film polycrystalline silicon solar cells on mullite ceramics, *Renewable Energy* 33(2) (2008) 267-272. Doi:10.1016/j.renene.2007.05.038
- [6] A. Gahler, J.G. Heinrich, J. Günster, Direct laser sintering of Al_2O_3 - SiO_2 dental ceramic components by layer-wise slurry deposition, *Journal of the American Ceramic Society* 89(10) (2006) 3076-3080. Doi:10.1111/j.1551-2916.2006.01217.x
- [7] S. Schaafhausen, E. Yazhenskikh, A. Walch, S. Heidenreich, M. Müller, Corrosion of alumina and mullite hot gas filter candles in gasification environment, *Journal of the European Ceramic Society* 33(15-16) (2013) 3301-3312. Doi:10.1016/j.jeurceramsoc.2013.05.024
- [8] A. Slaoui, S. Bourdais, G. Beaucarne, J. Poortmans, S. Reber, Polycrystalline silicon solar cells on mullite substrates, *Solar Energy Materials & Solar Cells* 71 (2002) 245-252. Doi:10.1016/S0927-0248(01)00063-0
- [9] P. Viravathana, N. Sukwises, S. Boonpa, S. Larpkiattaworn, Na_2WO_4 -Mn/mullite catalysts for oxidative coupling of methane, *Advanced Materials Research* 287-290 (2011) 3015-3019. Doi:10.4028/www.scientific.net/AMR.287-290.3015
- [10] X. Zhao, Y. Cong, F. Lv, L. Li, X. Wang, T. Zhang, Mullite-supported Rh catalyst: a promising catalyst for the decomposition of N_2O propellant, *ChemComm* 46(17) (2010) 3028-30. Doi:10.1039/b925085a
- [11] S. Basu, V.K. Sarin, Mullite coatings, in *Mullite*, edited by H. Schneider and S. Komarneni. WILEY-VCH, Weinheim (2005) 349-376.
- [12] S.N. Basu, T. Kulkarni, H.Z. Wang, V.K. Sarin, Functionally graded chemical vapor deposited mullite environmental barrier coatings for Si-based ceramics, *Journal of the European Ceramic Society* 28(2) (2008) 437-445. Doi:10.1016/j.jeurceramsoc.2007.03.007

- [13] M. Abbasi, M. Mirfendereski, M. Nikbakht, M. Golshenas, T. Mohammadi, Performance study of mullite and mullite–alumina ceramic MF membranes for oily waste waters treatment, *Desalination* 259(1-3) (2010) 169-178. Doi:10.1016/j.desal.2010.04.013
- [14] O. Bakhtiari, M. Samei, H. Taghikarimi, T. Mohammadi, Preparation and characterization of mullite tubular membranes, *Desalination and Water Treatment* 36(1-3) (2012) 210-218. Doi:10.5004/dwt.2011.2431
- [15] H. Shokrkar, A. Salahi, N. Kasiri, T. Mohammadi, Mullite ceramic membranes for industrial oily wastewater treatment: experimental and neural network modeling, *Water Sci Technol* 64(3) (2011) 670-676. Doi:10.2166/wst.2011.655
- [16] C.H.H. Hsiung, A.J. Pyzik, F. De Carlo, X. Xiao, S.R. Stock, K.T. Faber, Microstructure and mechanical properties of acicular mullite, *Journal of the European Ceramic Society* 33(3) (2013) 503-513. Doi:10.1016/j.jeurceramsoc.2012.09.017
- [17] A.J. Pyzik, C.G. Li, New design of a ceramic filter for diesel emission control applications, *Applied Ceramic Technology* 2(6) (2005) 440-451. Doi:10.1111/j.1744-7402.2005.02045.x
- [18] A.J. Pyzik, C.S. Todd, C. Han, Formation mechanism and microstructure development in acicular mullite ceramics fabricated by controlled decomposition of fluorotopaz, *Journal of the European Ceramic Society* 28(2) (2008) 383-391. Doi:10.1016/j.jeurceramsoc.2007.03.021
- [19] R.X. Fischer, *The mullite-type family of crystal structure*, Wiley-VCH, Weinheim (2005) 1-46.
- [20] R.X. Fischer, A. Gaede-Köhlera, J. Birkenstocka, H. Schneider, Mullite and mullite-type crystal structures, *International Journal of Materials Research* 103 (2012) 402-407. Doi:10.3139/146.110713
- [21] R.J. Angel, C.T. Prewitt, Crystal structure of mullite: A re-examination of the average structure, *American Mineralogist* 71(11-12) (1986) 1476-1482.
- [22] C.W. Burnham, Refinement of the crystal structure of sillimanite, *Zeitschrift für Kristallographie* 118 (1963) 127-148. Doi:10.1524/zkri.1963.118.1-2.127
- [23] C.W. Burnham, M.J. Buerger, Refinement of the crystal structure of andalusite, *Zeitschrift für Kristallographie* 115 (1961) 269-290. Doi:10.1524/zkri.1961.115.3-4.269
- [24] T. Pilati, F. Demartin, C.M. Gramaccioli, Transferability of empirical force fields in silicates: Lattice-dynamical evaluation of atomic displacement parameters and thermodynamic properties for the Al_2OSiO_4 polymorphs *Acta Cryst. B* 53 (1997) 82-94. Doi:10.1107/S0108768196011482
- [25] H. Lühns, A. Senyshyn, S.P. King, J.V. Hanna, H. Schneider, R.X. Fischer, Neutron diffraction and ^{11}B solid state NMR studies of the crystal structure of B-doped mullite, *Zeitschrift für Kristallographie* 228 (2013) 457-466. Doi:10.1524/zkri.2013.1595
- [26] H. Park, R. Lam, J.E. Greedan, J. Barbier, Synthesis, crystal Structure, crystal Chemistry, and magnetic properties of PbMBO_4 (M = Cr, Mn, Fe): A new structure type exhibiting one-dimensional magnetism, *Chem. Mater.* 15 (2003) 1703-1712. Doi:10.1021/cm0217452
- [27] H. Koizumi, N. Niizeki, T. Ikeda, An X-ray study on Bi_2O_3 - Fe_2O_3 system, *Jpn J Appl Phys* 3 (1964) 495-496. Doi:10.1143/jjap.3.495
- [28] J.A. Alonso, M.T. Casais, M.J. Martínez-Lope, J.L. Martínez, M.T. Fernández-Díaz, A structural study from neutron diffraction data and magnetic properties of RMn_2O_5 (R = La, rare earth), *Journal of Physics: Condensed Matter* 9(40) (1997) 8515-8526. Doi:10.1088/0953-8984/9/40/017
- [29] J.A. Alonso, M.J. Martínez-Lope, M.T. Casais, J.L. Martínez, V. Pomjakushin, Synthesis, structural, and magnetic characterization of YCrMnO_5 , *European Journal of Inorganic Chemistry* (13) (2005) 2600-2606. Doi:10.1002/ejic.200401057

- [30] A. Muñoz, J.A. Alonso, M.T. Casais, M.J. Martínez-Lope, J.L. Martínez, M.T. Fernández-Díaz, Magnetic structure and properties of BiMn_2O_5 oxide: A neutron diffraction study, *Physical Review B* 65(14) (2002) 144423. Doi:10.1103/PhysRevB.65.144423
- [31] A. Muñoz, J.A. Alonso, M.T. Casais, M.J. Martínez-Lope, J.L. Martínez, M.T. Fernández-Díaz, A study of the magnetic structure of LaMn_2O_5 from neutron powder diffraction data, *European Journal of Inorganic Chemistry* 2005(4) (2005) 685-691. Doi:10.1002/ejic.200400548
- [32] A. Muñoz, J.A. Alonso, M.J. Martínez-Lope, J.L. Martínez, Synthesis, structural, and magnetic characterization of a new ferrimagnetic oxide: YFeMnO_5 , *Chemistry of Materials* 16(21) (2004) 4087-4094. Doi:10.1021/cm049239v
- [33] A. Muñoz, J.A. Alonso, M.J. Martínez-Lope, J.L. Martínez, Synthesis and study of the crystallographic and magnetic structure of the ferrimagnetic oxide ErFeMnO_5 , *Physical Review B* 72(18) (2005) 184402. Doi:10.1103/PhysRevB.72.184402
- [34] A. Muñoz, J.A. Alonso, M.J. Martínez-Lope, J.L. Martínez, Synthesis and study of the crystallographic and magnetic structure of HoFeMnO_5 , *European Journal of Inorganic Chemistry* 2007(14) (2007) 1972-1979. Doi:10.1002/ejic.200601144
- [35] F. Ziegler, L. Köhler, H. Gibhardt, T.M. Gesing, M.M. Murshed, O. Sobolev, A. Piovano, G. Eckold, Characterization of Multiferroic $\text{Bi}_2\text{Mn}_4\text{O}_{10}$ by Dielectric and Neutron Spectroscopy, *Physica Status Solidi B-Basic Solid State Physics* 256(7) (2019) 7. Doi:10.1002/pssb.201800668
- [36] F. Ziegler, M.M. Murshed, H. Gibhardt, O. Sobolev, T.M. Gesing, G. Eckold, Mechanical properties of multiferroic $\text{Bi}_2\text{Mn}_4\text{O}_{10}$: Full set of elastic constants determined by inelastic neutron scattering, *Physica Status Solidi B-Basic Solid State Physics* 253(5) (2016) 976-982. Doi:10.1002/pssb.201552670
- [37] M. Burianek, M. Mühlberg, M. Woll, M. Schmucker, T.M. Gesing, H. Schneider, Single-crystal growth and characterization of mullite-type orthorhombic $\text{Bi}_2\text{M}_4\text{O}_9$ ($\text{M} = \text{Al}^{3+}, \text{Ga}^{3+}, \text{Fe}^{3+}$), *Crystal Research and Technology* 44(10) (2009) 1156-1162. Doi:10.1002/crat.200900465
- [38] M. Curti, A. Kirsch, L.I. Granone, F. Tarasi, G. López-Robledo, D.W. Bahnemann, M.M. Murshed, T.M. Gesing, C.B. Mendive, Visible-light photocatalysis with mullite-type $\text{Bi}_2(\text{Al}_{1-x}\text{Fe}_x)_4\text{O}_9$: Striking the balance between bandgap narrowing and conduction band lowering, *ACS Catalysis* 8(9) (2018) 8844-8855. Doi:10.1021/acscatal.8b01210
- [39] R.X. Fischer, H. Schneider, T.M. Gesing, Temperature-dependent X-ray diffraction studies of mullite-type $(\text{Bi}_{1-x}\text{Sr}_x)_2\text{M}_4\text{O}_9$ phases, *Acta Crystallographica a-Foundation and Advances* 65 (2009) 232. Doi:10.1107/S010876730909521x
- [40] T.M. Gesing, R.X. Fischer, M. Burianek, M. Mühlberg, T. Debnath, C.H. Ruscher, J. Ottinger, J.C. Buhl, H. Schneider, Synthesis and properties of mullite-type $(\text{Bi}_{1-x}\text{Sr}_x)_2(\text{M}^{1-y}\text{M}^2_y)_4\text{O}_{9-x}$ ($\text{M} = \text{Al}, \text{Ga}, \text{Fe}$), *Journal of the European Ceramic Society* 31(16) (2011) 3055-3062. Doi:10.1016/j.jeurceramsoc.2011.04.004
- [41] T.M. Gesing, M. Schowalter, C. Weidenthaler, M.M. Murshed, G. Nenert, C.B. Mendive, M. Curti, A. Rosenauer, J.C. Buhl, H. Schneider, R.X. Fischer, Strontium doping in mullite-type bismuth aluminate: a vacancy investigation using neutrons, photons and electrons, *Journal of Materials Chemistry* 22(36) (2012) 18814-18823. Doi:10.1039/c2jm33208f
- [42] T.F. Krenzel, J. Schreuer, T.M. Gesing, M. Burianek, M. Mühlberg, H. Schneider, Thermal expansion and elastic properties of mullite-type $\text{Bi}_2\text{Ga}_4\text{O}_9$ and $\text{Bi}_2\text{Fe}_4\text{O}_9$ single crystals, *International Journal of Materials Research* 103(4) (2012) 438-448. Doi:10.3139/146.110718
- [43] M.M. Murshed, T.M. Gesing, Anisotropic thermal expansion and anharmonic phonon behavior of mullite-type $\text{Bi}_2\text{Ga}_4\text{O}_9$, *Materials Research Bulletin* 48(9) (2013) 3284-3291. Doi:10.1016/j.materresbull.2013.05.007

- [44] M.M. Murshed, C.B. Mendive, M. Curti, M. Sehovic, A. Friedrich, M. Fischer, T.M. Gesing, Thermal expansion of mullite-type $\text{Bi}_2\text{Al}_4\text{O}_9$: A study by X-ray diffraction, vibrational spectroscopy and density functional theory, *Journal of Solid State Chemistry* 229 (2015) 87-96. Doi:10.1016/j.jssc.2015.05.010
- [45] M.M. Murshed, G. Nenert, M. Burianek, L. Robben, M. Muhlberg, H. Schneider, R.X. Fischer, T.M. Gesing, Temperature-dependent structural studies of mullite-type $\text{Bi}_2\text{Fe}_4\text{O}_9$, *Journal of Solid State Chemistry* 197 (2013) 370-378. Doi:10.1016/j.jssc.2012.08.062
- [46] S. Ohmann, P. Fielitz, L. Dorrer, G. Borchardt, T.M. Gesing, R.X. Fischer, C.H. Ruscher, J.C. Buhl, K.D. Becker, H. Schneider, Electrical conductivity of mullite-type $\text{Bi}_2\text{Al}_4\text{O}_9$ ceramics in air, *Solid State Ionics* 211 (2012) 46-50. Doi:10.1016/j.ssi.2012.01.030
- [47] H. Schneider, R.X. Fischer, T.M. Gesing, J. Schreuer, M. Muhlberg, Crystal chemistry and properties of mullite-type $\text{Bi}_2\text{M}_4\text{O}_9$: An overview, *International Journal of Materials Research* 103(4) (2012) 422-429. Doi:10.3139/146.110716
- [48] S.U. Weber, T. Gesing, J. Röder, F.J. Litterst, R.X. Fischer, K.D. Becker, Temperature-dependent Fe-57 Mossbauer spectroscopy and local structure of mullite-type $\text{Bi}_2(\text{Fe}_x\text{Al}_{1-x})_4\text{O}_9$ ($0.1 \leq x \leq 1$) solid solutions, *International Journal of Materials Research* 103(4) (2012) 430-437. Doi:10.3139/146.110701
- [49] S.U. Weber, T.M. Gesing, G. Eckold, R.X. Fischer, F.J. Litterst, K.D. Becker, Temperature-dependent Fe-57 Mossbauer spectroscopy and local structure of the mullite-type $\text{Bi}_2(\text{Fe}_x\text{Ga}_{1-x})_4\text{O}_9$ ($0.1 \leq x \leq 1$) solid solution, *Journal of Physics and Chemistry of Solids* 75(3) (2014) 416-426. Doi:10.1016/j.jpics.2013.11.013
- [50] R.X. Fischer, V. Kahlenberg, D. Voll, K.J.D. MacKenzie, M.E. Smith, B. Schnetger, H.J. Brumsack, H. Schneider, Crystal structure of synthetic $\text{Al}_4\text{B}_2\text{O}_9$: A member of the mullite family closely related to boralsilite, *American Mineralogist* 93(5-6) (2008) 918-927. Doi:10.2138/am.2008.2744
- [51] K. Hoffmann, T.J.N. Hooper, M.M. Murshed, O. Dolotko, Z. Revay, A. Senyshyn, H. Schneider, J.V. Hanna, T.M. Gesing, R.X. Fischer, Formation, stability and crystal structure of mullite-type $\text{Al}_{6-x}\text{B}_x\text{O}_9$, *Journal of Solid State Chemistry* 243 (2016) 124-135. Doi:10.1016/j.jssc.2016.08.018
- [52] K. Hoffmann, T.J.N. Hooper, H. Zhao, U. Kolb, M.M. Murshed, M. Fischer, H. Luhrs, G. Nenert, P. Kudejova, A. Senyshyn, H. Schneider, J.V. Hanna, T.M. Gesing, R.X. Fischer, Crystal chemical characterization of mullite-type aluminum borate compounds, *Journal of Solid State Chemistry* 247 (2017) 173-187. Doi:10.1016/j.jssc.2016.12.027
- [53] K. Hoffmann, M.M. Murshed, R.X. Fischer, H. Schneider, T.M. Gesing, Synthesis and characterization of mullite-type $(\text{Al}_{1-x}\text{Ga}_x)_4\text{B}_2\text{O}_9$, *Zeitschrift Fur Kristallographie-Crystalline Materials* 229(10) (2014) 699-708. Doi:10.1515/zkri-2014-1785
- [54] H.S. Zhao, K. Hoffmann, Y. Krysiak, B. Barton, H. Schneider, T.M. Gesing, R.X. Fischer, U. Kolb, Structural investigation of mullite-type $\text{Al}_4\text{B}_2\text{O}_9$ by electron diffraction, *Acta Crystallographica a-Foundation and Advances* 72 (2016) S430-S430. Doi:10.1107/S2053273316093682
- [55] H.S. Zhao, Y. Krysiak, K. Hoffmann, B. Barton, L. Molina-Luna, R.B. Neder, H.J. Kleebe, T.M. Gesing, H. Schneider, R.X. Fischer, U. Kolb, Elucidating structural order and disorder phenomena in mullite-type $\text{Al}_4\text{B}_2\text{O}_9$ by automated electron diffraction tomography, *Journal of Solid State Chemistry* 249 (2017) 114-123. Doi:10.1016/j.jssc.2017.02.023
- [56] T.M. Gesing, C.B. Mendive, M. Curti, D. Hansmann, G. Nenert, P.E. Kalita, K.E. Lipinska, A. Huq, A.L. Cornelius, M.M. Murshed, Structural properties of mullite-type $\text{Pb}(\text{Al}_{1-x}\text{Mn}_x)\text{BO}_4$, *Zeitschrift Fur Kristallographie-Crystalline Materials* 228(10) (2013) 532-543. Doi:10.1524/zkri.2013.1640
- [57] M. Gogolin, M.M. Murshed, M. Ende, R. Miletich, T.M. Gesing, Uniaxial negative thermal expansion in the mullite- and borax-type PbAlBO_4 polymorphs, *Journal of Materials Science* 55(1) (2020) 177-190. Doi:10.1007/s10853-019-04013-6

- [58] M.M. Murshed, T.M. Gesing, Lattice thermal expansion of mullite-type PbMBO_4 for $M = \text{Al, Ga, Fe}$ and Mn , *Acta Crystallographica a-Foundation and Advances* A68 (2012) s195.
- [59] M.M. Murshed, G. Nenert, T.M. Gesing, Crystal structure of mullite-type $\text{PbMn}_{0.5}\text{Al}_{0.5}\text{BO}_4$ determined by combined X-ray and neutron diffraction data, *Zeitschrift Fur Kristallographie-New Crystal Structures* 227(3) (2012) 285-286. Doi:10.1524/ncrs.2012.0181
- [60] H. Park, J. Barbier, R.P. Hammond, Crystal structure and polymorphism of PbAlBO_4 , *Solid State Sciences* 5 (2003) 565-571. Doi:10.1016/S1293-2558(03)00056-6
- [61] H. Park, R. Lam, J.E. Greedam, J. Barbier, Synthesis, crystal structure, crystal chemistry, and magnetic properties of PbMBO_4 ($M = \text{Cr, Mn, Fe}$): A new structure type exhibiting one-dimensional magnetism, *Chemistry of Materials* 15 (2003) 1703-1712. Doi:10.1021/cm0217452
- [62] A. Byström, A. Westgren, Crystal Structure of Pb_3O_4 and SnPb_2O_4 , *Arkiv for Kemi Mineralogi Och Geologi* B16 (1943) 1-7.
- [63] R. Fischer, F. Pertlik, Verfeinerung der Kristallstruktur des Schafarzikits, FeSb_2O_4 , *Tschermaks Mineralogische Und Petrographische Mitteilungen* 22 (1975) 206. Doi:10.1007/Bf01087842
- [64] J.A. Gonzalo, D.E. Cox, G. Shirane, The Magnetic Structure of FeSb_2O_4 , *Physical Review* 147(2) (1966) 415-418. Doi:10.1103/PhysRev.147.415
- [65] S.T. Gross, The Crystal Structure of Pb_3O_4 , *Journal of American Chemical Society* 65 (1943) 1107. Doi:10.1021/ja01246a029
- [66] F. Pertlik, Zur Synthese von Kristallen von CuAs_2O_4 (Trippkeit) und $\text{Cu}_2\text{As}_3\text{O}_6\text{CH}_3\text{COO}$, *Z. anorg. allg. Chem.* 436 (1977) 201-206. Doi:10.1002/zaac.19774360124
- [67] L. Tokody, Beiträge zur kenntnis der kristallographischen und physikalischen eigenschaften des Schafarzikits, *Zeitschrift Fur Kristallographie* 62 (1925) 123. Doi:10.1524_zkri.1925.62.1.123
- [68] H.T. Witteveen, Magnetic suceptibility of NiAs_2O_4 and NiSb_2O_4 , *Solid State Communications* 9 (1971) 1313-1315. Doi:10.1016/0038-1098(71)90086-X
- [69] J. Zemann, Formel und Kristallstruktur des Schafarzikits, *Tschermaks mineralogische und petrographische Mitteilungen* 2 (1951) 166-175. Doi:10.1007/BF01127892
- [70] S.C. Abrahams, J.L. Bernstein, Crystal structure of paramagnetic DyMn_2O_5 at 298 K, *J Chem Phys* 46(10) (1967) 3776. Doi:10.1063/1.1840450
- [71] M.L. Ninh Nguyen, Annie Ducouret, Bernard Raveau, Distribution of Mn^{3+} and Mn^{4+} species between octahedral and square pyramidal sites in $\text{Bi}_2\text{Mn}_4\text{O}_{10}$ -type structure, *Journal of Materials Chemistry* 9 (1999) 731-734. Doi:10.1039/A808094A
- [72] M. Curti, T.M. Gesing, M.M. Murshed, T. Bredow, C.B. Mendive, Liebau density vector: a new approach to characterize lone electron pairs in mullite-type materials, *Zeitschrift Fur Kristallographie-Crystalline Materials* 228(12) (2013) 629-634. Doi:10.1524/zkri.2013.1686
- [73] X. Wang, F. Liebau, Influence of lone-pair electrons of cations on bond-valence parameters, *Zeitschrift für Kristallographie* 211 437-439. Doi:10.1524/zkri.1996.211.7.437
- [74] X. Wang, F. Liebau, Studies on bond and atomic valences. I. correlation between bond valence and bond angles in Sb^{III} chalcogen compounds: the influence of lone-electron pairs, *Acta crystallogr. B* 52(1) (1996) 7-15. Doi:10.1107/s0108768195004472
- [75] X. Wang, F. Liebau, Influence of polyhedron distortions on calculated bond-valence sums for cations with one lone electron pair, *Acta Crystallogr. B* 63(Pt 2) (2007) 216-228. Doi:10.1107/S0108768106055911
- [76] X. Wang, F. Liebau, On the optimization of bond-valence parameters: artifacts conceal chemical effects, *Acta Crystallogr. B* 65(Pt 1) (2009) 96-98. Doi:10.1107/S010876810804086X
- [77] X. Wang, F. Liebau, The contribution to bond valences by lone electron pairs, *MRS Proceedings* 848 (2011). Doi:10.1557/proc-848-ff7.4

- [78] J.A. Alonso, M.T. Casais, M.J. Martínez-Lope, I. Rasines, High oxygen pressure preparation, structural refinement, and thermal behavior of RMn_2O_5 (R = La, Pr, Nd, Sm, Eu), *Journal of Solid State Chemistry* 129 (1997) 105-112. Doi:10.1006/jssc.1996.7237
- [79] K.J.D. MacKenzie, T. Dougherty, J. Barrel, The electronic properties of complex oxides of bismuth with the mullite structure, *Journal of the European Ceramic Society* 28(2) (2008) 499-504. Doi:10.1016/j.jeurceramsoc.2007.03.012
- [80] J. Brink van den, D.I. Khomskii, Multiferroicity due to charge ordering, *Journal of Physics: Condensed Matter* 20(43) (2008) 434217. Doi:10.1088/0953-8984/20/43/434217
- [81] F. Pomiro, J. Lohr, E.V.P. Miner, V. Nassif, R.D. Sánchez, R.E. Carbonio, Crystal structure, magnetic and electrical properties of compounds in the RCrMnO_5 family (R = Sm, Eu, Gd, Tb, Ho and Er) synthesized under high oxygen pressure, *European Journal of Inorganic Chemistry* 2015(28) (2015) 4737-4749. Doi:10.1002/ejic.201500662
- [82] R.V. Shpanchenko, A.A. Tsirlin, E.S. Kondakova, E.V. Antipov, C. Bougerol, J. Hadermann, G. van Tendeloo, H. Sakurai, E. Takayama-Muromachi, New germanates RCrGeO_5 (R = Nd–Er, Y): Synthesis, structure, and properties, *Journal of Solid State Chemistry* 181(9) (2008) 2433-2441. Doi:10.1016/j.jssc.2008.05.043
- [83] G. Buisson, Etude par rayons X et neutrons de la serie isomorphe ATiO_5 (A = Cr, Mn, Fe, T = Terres rares), *J. Phys. Chem. Solids* 31 (1970) 1171-1183. Doi:10.1016/0022-3697(70)90326-4
- [84] O. Jarchow, K.H. Klaska, M. Werk, Erste Seltene Erden-Aluminium-Germanate vom Typ REAlGeO_5 , *Naturwissenschaften* 68(2) (1981) 92. Doi:10.1007/bf01047230
- [85] A. Durand, O. Mentre, F. Abraham, T. Fukuda, B. Elouadi, Crystal structure of ErAlGeO_5 and evidence of a peculiar double coordination sphere of Al(III) and Ge(IV) cations, *Solid State Sciences* 8(2) (2006) 155-161. Doi:10.1016/j.solidstatesciences.2005.08.016
- [86] R.D. Shannon, Revised effective ionic radii and systematic studies of interatomic distances in halides and chalcogenides, *Acta Crystallogr A* A32(5) (1976) 751-767. Doi:10.1107/s0567739476001551
- [87] J. Barbier, M.E. Fleet, Investigation of phase-relations in the $(\text{Na,K})\text{AlGeO}_4$ system, *Physics and Chemistry of Minerals* 16(3) (1988) 276-285. Doi:10.1007/BF00220695
- [88] S. Kume, T. Matsumoto, Dense form of germanate orthoclase (KAlGe_3O_8), *Journal of Geophysical Research* 71(20) (1966) 4999-5000. Doi:10.1029/JZ071i020p04999
- [89] T. Malcherek, M.A. Charoenter, H. Kroll, E.K.H. Salje, Cation ordering in $\text{BaAl}_2\text{Ge}_2\text{O}_8$ -feldspar : implications for the II-C1 phase transition in anorthite, *Physics and Chemistry of Minerals* 26(4) (1999) 354-366. Doi:10.1007/s002690050195
- [90] M. Wolfgang Friedrich, Y. Vojdan-Shemshadi, H. Pentinghaus, Transmission electron microscopic study of antiphase domains in $\text{CaAl}_2\text{Ge}_2\text{O}_8$ -feldspar, *Physics and Chemistry of Minerals* 14(3) (1987) 235-237. Doi:10.1007/bf00307987
- [91] M.C. Gordillo, C.P. Herrero, Al, Ge ordering in aluminogermanate sodalites - a Monte-Carlo study, *Journal of Physics and Chemistry of Solids* 55(11) (1994). Doi:10.1016/0022-3697(94)90199-6
- [92] T. Malcherek, H. Kroll, E.K.H. Salje, Al,Ge cation ordering in $\text{BaAl}_2\text{Ge}_2\text{O}_8$ -feldspar: monodomain ordering kinetics, *Physics and Chemistry of Minerals* 27(3) (2000) 203-212. Doi:10.1007/s002690050008
- [93] M. Weiss, D.A. Weber, A. Senyshyn, J. Janek, W.G. Zeier, Correlating transport and structural properties in $\text{Li}_{1-x}\text{Al}_x\text{Ge}_{2-x}(\text{PO}_4)_3$ (LAGP) prepared from aqueous solution, *ACS Appl Mater Interfaces* 10(13) (2018) 10935-10944. Doi:10.1021/acsami.8b00842
- [94] L.I. Granone, A.C. Ulpe, L. Robben, S. Klimke, M. Jahns, F. Renz, T.M. Gesing, T. Bredow, R. Dillert, D.W. Bahnemann, Effect of the degree of inversion on optical properties of spinel ZnFe_2O_4 , *Physical Chemistry Chemical Physics* 20(44) (2018) 28267-28278. Doi:10.1039/c8cp05061a

- [95] E.C. O'Quinn, J. Shamblin, B. Perlov, R.C. Ewing, J. Neufeind, M. Feygenson, I. Gushev, M. Lang, Inversion in $Mg_{1-x}Ni_xAl_2O_4$ spinel: New insight into local structure, *Journal of American Chemical Society* 139(30) (2017) 10395-10402. Doi:10.1021/jacs.7b04370
- [96] U. Schmocker, F. Waldner, The inversion parameter with respect to the space group of $MgAl_2O_4$ spinels, *J. Phys. C: Solid State Phys.* 9 (1976) L235. Doi:10.1088/0022-3719/9/9/003
- [97] I. Kagomiya, K. Kohn, T. Uchiyama, Structure and Ferroelectricity of RMn_2O_5 , *Ferroelectrics* 280 (2011) 131-143. Doi:10.1080/00150190214799
- [98] A. Inomata, K. Kohn, Pyroelectric effect and possible ferroelectric transition of helimagnetic $GdMn_2O_5$, YMn_2O_5 and YMn_2O_5 , *Journal of Physics: Condensed Matter* 8 (1996) 2673-2678. Doi:10.1088/0953-8984/8/15/016
- [99] A.M. Kadomtseva, Y.F. Popov, G.P. Vorob'ev, K.I. Kamilov, P.N. Makhov, M.M. Tehranchi, A. Phirouznia, Induced by magnetic field spin reorientation in YMn_2O_5 , *Physica B* 329 (2003) 856-857. Doi:10.1016/S0921-4526(02)02570-X
- [100] Y.F. Popov, A.M. Kadomtseva, S.S. Krotov, G.P. Vorob'ev, M.M. Lukina, Magnetolectric Effect in YMn_2O_5 in strong pulsed magnetic fields, *Ferroelectrics* 279(1) (2002) 147-156. Doi:10.1080/00150190214788
- [101] Y. Noda, H. Kimura, M. Fukunaga, S. Kobayashi, I. Kagomiya, K. Kohn, Magnetic and ferroelectric properties of multiferroic RMn_2O_5 , *Journal of Physics: Condensed Matter* 20(43) (2008). Doi:10.1088/0953-8984/20/43/434206
- [102] Y.F. Popov, A.M. Kadomtseva, S.S. Krotov, G.P. Vorob'ev, K.I. Kamilov, M.M. Lukina, M.M. Tegranchi, Magnetic and structural phase transitions in YMn_2O_5 ferromagnetoelectric crystals induced by a strong magnetic field, *Journal of Experimental and Theoretical Physics* 96 (2003) 961-965. Doi:10.1134/1.1581951
- [103] S. Chattopadhyay, V. Balédent, F. Damay, A. Gukasov, E. Moshopoulou, P. Auban-Senzier, C. Pasquier, G. André, F. Porcher, E. Elkaim, C. Doubrovsky, M. Greenblatt, P. Foury-Leylekian, Evidence of multiferroicity in $NdMn_2O_5$, *Physical Review B* 93(10) (2016) 104406. Doi:10.1103/PhysRevB.93.104406
- [104] Y. Ishii, S. Horio, M. Mitarashi, T. Sakakura, M. Fukunaga, Y. Noda, T. Honda, H. Nakao, Y. Murakami, H. Kimura, Observation of magnetic order in multiferroic $SmMn_2O_5$ studied by resonant x-ray magnetic scattering, *Physical Review B* 93(6) (2016). Doi:10.1103/PhysRevB.93.064415
- [105] V. Polyakov, V. Plakhty, M. Bonnet, P. Burllet, L.P. Regnault, S. Gavrilov, I. Zobkalo, O. Smirnov, Coupled magnetic and structural transitions in $EuMn_2O_5$ as studied by neutron diffraction and three-dimensional polarization analysis, *Physica B Condensed Matter* 297(1-4) (2001) 208-212. Doi:10.1016/S0921-4526(00)00851-6
- [106] C. Vecchini, A. Bombardi, L.C. Chapon, N. Lee, P.G. Radaelli, S.-W. Cheong, Magnetic phase diagram and ordered ground state of $GdMn_2O_5$ multiferroic studied by x-ray magnetic scattering, *Journal of Physics: Conference Series* 519 (2014) 012004. Doi:10.1088/1742-6596/519/1/012004
- [107] L.M. Volkova, D.V. Marinin, Crystal chemistry aspects of the magnetically induced ferroelectricity in $TbMn_2O_5$ and $BiMn_2O_5$, *Journal of Physics: Condensed Matter* 21(1) (2009) 015903. Doi:10.1088/0953-8984/21/1/015903
- [108] L.C. Chapon, G.R. Blake, M.J. Gutmann, S. Park, N. Hur, P.G. Radaelli, S.W. Cheong, Structural anomalies and multiferroic behavior in magnetically frustrated $TbMn_2O_5$, *Physical Review Letters* 93(17) (2004) 177402. Doi:10.1103/PhysRevLett.93.177402
- [109] P.P. Gardner, C. Wilkinson, J.B. Forsyth, B.M. Wanklyn, The magnetic structures of the rare-earth manganates $ErMn_2O_5$ and $TbMn_2O_5$, *Journal of Physics C: Solid State Physics* 21 (1988) 5653-61. Doi:10.1088/0022-3719/21/33/009

- [110] G.R. Blake, L.C. Chapon, P.G. Radaelli, S. Park, N. Hur, S.W. Cheong, J. Rodríguez-Carvajal, Spin structure and magnetic frustration in multiferroic RMn_2O_5 ($\text{R} = \text{Tb}, \text{Ho}, \text{Dy}$), *Physical Review B* 71(21) (2005). Doi:10.1103/PhysRevB.71.214402
- [111] C. Wilkinson, F. Sinclair, P. Gardner, J.B. Forsyth, B.M.R. Wanklyn, The antiferromagnetic structure of DyMn_2O_5 at 4.2 K, *Journal of Physics C: Solid State Physics* 14 (1981) 1671-1683. Doi:10.1088/0022-3719/14/11/027
- [112] I. Kagomiya, K.-i. Kakimoto, H. Ohsato, Precursor phenomenon on ferroelectric transition in multiferroic YMn_2O_5 , *Journal of the European Ceramic Society* 30(2) (2010) 255-258. Doi:10.1016/j.jeurceramsoc.2009.05.035
- [113] P.G. Radaelli, C. Vecchini, L.C. Chapon, P.J. Brown, S. Park, S.W. Cheong, Incommensurate magnetic structure of YMn_2O_5 : A stringent test of the multiferroic mechanism, *Physical Review B* 79(2) (2009). Doi:10.1103/PhysRevB.79.020404
- [114] S. Kobayashi, H. Kimura, Y. Noda, K. Kohn, Neutron diffraction study of magnetic ordering associated with ferroelectricity in TmMn_2O_5 , *Journal of the Physical Society of Japan* 74 (2005) 468-472. Doi:10.1143/JPSJ.74.468
- [115] Y. Koyata, H. Nakamura, N. Iwata, A. Inomata, K. Kohn, Electric and magnetic low-temperature phase transitions of YbMn_2O_5 , *Journal of the Physical Society of Japan* 65 (1996). Doi:10.1143/JPSJ.65.1383
- [116] G. Buisson, Structures magnetiques sinusoidales et helicoidales de la terre rare dans TMn_2O_5 , *Physica status solidi A* 17 (1973) 191. Doi:10.1002/pssa.2210170121
- [117] G. Buisson, Ordre helimagnetique du manganese dans la serie TMn_2O_5 , *Physica status solidi A* 16 (1973) 533. Doi:10.1002/pssa.2210160223
- [118] I. Yaeger, Magnetic susceptibility studies of NdFeTiO_5 single crystals, *Journal of Applied Physics* 49(3) (1978) 1513-1515. Doi:10.1063/1.324940
- [119] I. Yaeger, Crystal growth and magnetic properties of NdFeTiO_5 , *Materials Research Bulletin* 13(8) (1978) 819-825. Doi:10.1016/0025-5408(78)90045-4
- [120] M. Greenblatt, R.M. Hornreich, B. Sharon, Magnetolectric compounds with two sets of magnetic sublattices: UCrO_4 and NdCrTiO_5 , *Journal of Solid State Chemistry* 10(4) (1974) 371-376. Doi:10.1016/0022-4596(74)90046-2
- [121] A. Munoz, J.A. Alonso, M.J. Martinez-Lope, V. Pomjakushin, G. Andre, On the magnetic structure of PrMn_2O_5 : a neutron diffraction study, *J Phys Condens Matter* 24(7) (2012) 076003. Doi:10.1088/0953-8984/24/7/076003
- [122] C. Doubrovsky, G. André, A. Gukasov, P. Auban-Senzier, C.R. Pasquier, E. Elkaim, M. Li, M. Greenblatt, F. Damay, P. Foury-Leylejian, Magnetic phase transitions in PrMn_2O_5 : Importance of ion-size threshold size effects in RMn_2O_5 compounds ($\text{R} = \text{rare earth}$), *Physical Review B* 86(17) (2012). Doi:10.1103/PhysRevB.86.174417
- [123] K. Gautam, A. Ahad, K. Dey, S.S. Majid, S. Francoual, V.G. Sathe, I. da Silva, D.K. Shukla, Symmetry breaking and spin lattice coupling in NdCrTiO_5 , *Physical Review B* 100(10) (2019) 104106. Doi:10.1103/PhysRevB.100.104106
- [124] S.W. Cheong, M. Mostovoy, Multiferroics: a magnetic twist for ferroelectricity, *Nature Materials* 6 (2007) 13-20. Doi:10.1038/nmat1804
- [125] P.G. Radaelli, L.C. Chapon, A neutron diffraction study of RMn_2O_5 multiferroics, *Journal of Physics: Condensed Matter* 20(43) (2008). Doi:10.1088/0953-8984/20/43/434213
- [126] K. Ghosh, M.M. Murshed, T.M. Gesing, Synthesis and characterization of $(\text{Bi}_{1-x}\text{R}_x)_2\text{Mn}_4\text{O}_{10}$: structural, spectroscopic and thermogravimetric analyses for $\text{R} = \text{Nd}, \text{Sm}$ and Eu , *Journal of Materials Science* 54(21) (2019) 13651-13659. Doi:10.1007/s10853-019-03852-7

Chapter 2

Experimental methods

2.1. Synthesis

The O10-phases were synthesized using conventional solid-state sol-gel process. Stoichiometric amount of either oxides or nitrates were mixed with 10-20 wt.% glycerin (1,2,3-propantriol) into a glass beaker and heated at 353 K under magnetic stirring for about half an hour. In this step, the nitrates were decomposed and release nitrous, NO_x gas to form a gel solution. This gel was further dried at 473 K for about 2 h for complete decomposition of nitrates. A foam-like solid was formed in this step which afterward was homogenously crushed into powder and put into a corundum or platinum crucible followed by heating at high temperature for 48-72 h to get polycrystalline powder samples. In some cases, the samples were re-ground and re-heated for several hours or days. This intermediate grinding and re-heating for a longer period helped avoid formation of respective perovskite phases [1]. Synthesis process of each O10-compounds were described in detail in chapter 3 to 5.

2.2. Powder X-ray diffraction

X-ray powder-diffraction experiments were carried out using a Panalytical X'Pert Pro powder diffractometer in Bragg-Brentano geometry with $\text{CuK}_{\alpha 1,2}$ ($\lambda_{\text{K}\alpha 1} = 154.05929(5)$ pm, $\lambda_{\text{K}\alpha 2} = 154.4414(2)$ pm) radiation. This instrument is equipped with a divergence slit (0.25°), an anti-scatter slit (0.5°), a soller slit (0.04 rad) and a mask (10 mm) in the primary beam. A soller slit (0.04 rad), a Ni-filter, and a X'Celerator detector system are used in the secondary beam. The Rietveld refinement of all recorded PXRD data was performed using "DiffracPlus Topas 6 software" (Bruker AXS GmbH, Karlsruhe, Germany) [2]. The instrument profiles were determined by the fundamental parameter approach, where the fundamental parameters were fitted against a LaB_6 standard reference sample.

2.3. Neutron powder diffraction (NPD)

Temperature-dependent Time-of-flight (TOF) NPD data were collected at the Spallation Neutron Source (SNS) at Oak Ridge National Laboratory on the high-resolution neutron powder diffractometer POWGEN. The sample loaded in 8 mm diameter vanadium can. Longer measured datasets (1 h) collected between 7.5 K and 300 K covered a d -spacing from 30 pm to 620 pm. The Rietveld refinements were performed using GSAS-II [3]. The magnetic structure refinements were carried out using *FullProf* [4]. It is worth noting that POWGEN uses a TOF profile function that varies from the standard lineshape originally derived for GSAS [5]. The variation in peak shape and peak position with the POWGEN diffractometer is calculated using a function related to thermal and epithermal components of the neutron spectrum and implemented in GSAS-II to accurately determine the metric parameters.

2.4. Bond Valence Sum (BVS)

Bond Valence Sum [6] is an approach based on Pauling second rule with summarizing a large number of crystal structures and considering the basic laws of structural chemistry. According to the Bond Valence theory, the valence of an atom is distributed on each bond it participates in, that is, each chemical bond has a bond valence S_i , which is determined by the bond length with the following equation:

$$S_i = \exp \left[\frac{(R_0 - R_i)}{B} \right]$$

where R_i is the observed bond length, R_0 is an empirical parameter expressing the ideal bond length when the element has exactly valence, and B is an empirical constant, typically 37.0 pm. R_0 and B usually can be referred in the relevant literature [6]. Thereby, if the coordination environment of an atom is known, its Bond Valence Sum (BVS) can be calculated:

$$BVS = \sum_i S_i$$

The *Bondstr* software within the FullProf suite was utilized to perform the BVS calculation throughout this dissertation.

2.5. UV/Vis reflectance spectroscopy

Optical diffuse reflectance spectra were recorded at room temperature on a Shimadzu UV-2600 (Shimadzu, Kyoto, Japan) spectrophotometer equipped with an ISR-2600 plus two-detector integrating sphere (Pike Technologies, USA). Data were collected in the range of 200 nm to 850 nm with a step of 1 nm. A standard BaSO₄ sample was used as reference for the baseline correction.

The diffuse reflectance spectra of samples were converted to $F(R)$ spectra according to the Kubelka-Munk function [7]:

$$F(R) = \frac{(1 - R)^2}{2R}$$

where R is reflectance. The Tauc's method [8, 9] followed by the Kubelka-Munk function are commonly used to estimate the bandgap energy by finding the intercept of the abscissa from the following relations:

$$F(R) = B(h\nu - E_g)^n$$

Where h is the Planck's constant, ν is the frequency of light, E_g is the bandgap in eV and n is the type of optical transition. That is, $n = 1/2, 2/3, 2$ or 3 denoted as direct allowed, direct forbidden, indirect allowed and indirect forbidden transition, respectively. Recently, the derivation of absorption spectrum fitting (DASF) method [10] was proposed for thin films to calculate the bandgap energies without any presumption of the nature of the transition. Based on this, the DASF can also be expressed as follows proposed by Kirsch et al. [1, 11] for powder samples:

$$\frac{\ln(F(R))}{d(h\nu)} = \frac{n}{(h\nu - E_g)}$$

Combining the results of the absolute bandgap width determination using the DASF method with the values for a direct or indirect transition obtained by the Tauc method, determine the type and width of the bandgap of powder samples.

2.6. Fourier transform infrared (FTIR) spectroscopy

Fourier transform infrared (FTIR) spectra were recorded on a Bruker IFS66v/S spectrometer (Bruker Optik GmbH, Ettlingen, Germany) using the standard KBr method. Approx. 2 mg sample was mixed with 200 mg dried KBr and pressed at 100 kN, forming disks of 12 mm in diameter. The reference pellet consists of 200 mg dried KBr only. Measurements were carried out between 370 cm^{-1} and 4000 cm^{-1} with a total acquisition of 128 spectra, leading to a spectral resolution of 2 cm^{-1} .

2.7. Raman Spectroscopy

Raman spectra were recorded on a LabRam ARAMIS (Horiba Jobin Yvon) Micro-Raman spectrometer equipped with different laser working at 532 nm, 633 nm and 785 nm. The use of different long working distance objectives (Olympus) with respective numerical aperture provide a focus spot of about 1-2 μm diameter when closing the confocal hole to 200 μm . Raman spectra were collected in the different range with a spectral resolution of approximately 1.2 cm^{-1} using a grating of 1800 grooves/mm and a thermoelectrically cooled CCD detector (Synapse, 1024 x 256 pixels). The spectral positions were calibrated against the Raman mode of Si before and after the sample measurements. The position of the Si peak was repeatedly measured against the Rayleigh line (0.0 cm^{-1}) yielding a value of $520.7 \pm 0.1\text{ cm}^{-1}$. The linearity of the spectrometer was calibrated against the emission lines of a neon lamp. For the spectrum at the ambient condition, the baseline was corrected and fitted with Pseudo-Voigt line shape.

2.8. Thermogravimetric analysis

Simultaneous thermogravimetric analysis and differential scanning calorimetry (TGA/DSC) measurements were performed on a simultaneous TGA/DSC 3+ STAR e system (Mettler Toledo, Schwerzenbach, Switzerland). Approx. 20 mg of each polycrystalline samples were measured with a heating rate of 10 K/min and a continuous N₂ flow of 20 mL/min from room temperature to the destination temperature. Afterward, the data were normalized to the respective mass. Evaluation of DTA curves were done by “Mettler Toledo STARe Evaluation Software” to get the decomposition temperature, where intercept of two fitting lines of before and after the decomposition treated as the decomposition temperature. An empty corundum crucible was used as a reference. A drift correction was applied based on the empty crucible data.

2.9. Magnetic susceptibility

Temperature-dependent DC magnetic susceptibility measurements were carried out with a Magnetic Property Measurement System MPMS-XL7 (Quantum Design, San Diego, USA) using the field-cooling process in the range from 2 K to 300 K with an incremental cooling rate of 2 K/min at a magnetic field of 0.01 T. The magnetic signal was well above the standard deviations, where the order of the instrumental noise was estimated to be $\sim 10^{-11} \text{Am}^2$. Polycrystalline samples were sealed in a gel capsule and attached to a nonmagnetic sample holder.

Reference

[1] A. Kirsch, M.M. Murshed, F.J. Litterst, T.M. Gasing, Structural, Spectroscopic, and Thermoanalytic Studies on Bi₂Fe₄O₉: Tunable Properties Driven by Nano- and Polycrystalline States, *Journal of Physical Chemistry C* 123(5) (2019) 3161-3171. Doi:10.1021/acs.jpcc.8b09698

- [2] A.A. Coelho, TOPAS and TOPAS-Academic: an optimization program integrating computer algebra and crystallographic objects written in C++, *Journal of Applied Crystallography* 51(1) (2018) 210-218. Doi:10.1107/s1600576718000183
- [3] B.H. Toby, EXPGUI, a graphical user interface for GSAS, *Journal of Applied Crystallography* 34 (2001) 201-213. Doi:10.1107/S0021889801002242
- [4] J. Rodríguez-Carvajal, Recent advances in magnetic structure determination by neutron powder diffraction, *Physica B: Condensed Matter* 192 (1993) 55-69. Doi:10.1016/0921-4526(93)90108-I
- [5] R.B.V. Dreele, J.D. Jorgensen, C.G. Windsor, Rietveld refinement with spallation neutron powder diffraction data, *Journal of Applied Crystallography* 15 (1982) 581-589. Doi:10.1107/S0021889882012722
- [6] I.D. Brown, D.A. Termatt, Bond-valence parameters obtained from a systematic analysis of the inorganic crystal structure database, *Acta Crystallographica B* 41 (1985) 244-247. Doi:10.1107/S0108768185002063
- [7] P. Kubelka, New contributions to the optics of intensely light-scattering materials. Part I, *Journal of the Optical Society of America* 38(5) (1948) 448-457. Doi:10.1364/josa.38.000448
- [8] J. Tauc, R. Grigorovici, A. Vancu, Optical properties and electronic structure of amorphous germanium, *Physica status solidi B* 15(2) (1966) 627-637. Doi:10.1002/pssb.19660150224
- [9] J. Tauc, A. Menth, States in the gap, *Journal of Non-Crystalline Solids* 8-10(C) (1972) 569-585. Doi:10.1016/0022-3093(72)90194-9
- [10] D. Souri, Z.E. Tahan, A new method for the determination of optical band gap and the nature of optical transitions in semiconductors, *Applied Physics B* 119(2) (2015) 273-279. Doi:10.1007/s00340-015-6053-9
- [11] A. Kirsch, M.M. Murshed, M. Schowalter, A. Rosenauer, T.M. Gesing, Nanoparticle precursor into polycrystalline $\text{Bi}_2\text{Fe}_4\text{O}_9$: An evolutionary investigation of structural, morphological, optical, and vibrational properties, *Journal of Physical Chemistry C* 120(33) (2016) 18831-18840. Doi:10.1021/acs.jpcc.6b04773

Details of declaration on own contributions to the publications

The results presented in this cumulative dissertation were obtained in collaborations with several other groups. In this section, I specifically announce my own contributions to the individual publications.

The work presented in **chapter 3** is based on a previously published as: Kowsik Ghosh, M. Mangir Murshed, Thorsten. M. Gesing; Synthesis and characterization of $(\text{Bi}_{1-x}\text{R}_x)_2\text{Mn}_4\text{O}_{10}$: structural, spectroscopic and thermogravimetric analyses for $\text{R} = \text{Nd}$, Sm and Eu ; *Journal of Materials Science* 54(21) (2019) 13651-13659. Doi:10.1007/s10853-019-03852-7.

I conducted the following tasks:

- Writing of the main manuscript (co-operation with Prof. Dr. Thorsten M. Gesing and PD Dr. Mangir Murshed).
- Generation of the figures.
- Solid state synthesis of the samples.
- Perform the measurements of PXRD, Raman and FTIR spectroscopy as well as their evaluation and interpretation, structure determination, and Rietveld refinements.
- Evaluation of TGA data and their interpretation

I did not conduct the following tasks:

TGA measurements (carried out by Julia Butzlaff).

The work presented in **chapter 4** is based on a previously published as: Kowsik Ghosh, M. Mangir Murshed, Michael Fischer, Thorsten. M. Gesing; Aluminum to germanium inversion in mullite-type RAlGeO_5 : characterization of a rare phenomenon for $\text{R} = \text{Y}$, $\text{Sm} - \text{Lu}$; *Journal of the American Ceramic Society* 105 (2022) 728-741. Doi:10.1111/jace.18085.

I conducted the following tasks:

- Writing of the main manuscript (co-operation with Prof. Dr. Thorsten M. Gesing and PD Dr. Mangir Murshed).
- Generation of the figures (except fig. 1, done by Prof. Dr. Thorsten M. Gesing).
- Solid state synthesis of the samples.
- Perform the measurements of PXRD, Raman, FTIR and UV/Vis spectroscopy as well as their evaluation and interpretation, structure determination, and Rietveld refinements.
- Evaluation of DFT calculated results and their interpretation.
- Evaluation of TGA/DSC data and their interpretation.

I did not conduct the following tasks:

- DFT calculation of the vibrational properties and electronic bandgap (carried out by Dr. Michael Fischer)
- TGA/DSC measurements (carried out by Julia Butzlaff).

The work presented in **chapter 5** is based on a previously published as: Kowsik Ghosh, M. Mangir Murshed, Thomas Frederichs, Naveen K. C. Muniraju, Thorsten. M. Gesing; Structural, vibrational, thermal and magnetic properties of NdMnTiO₅ ceramic; *Journal of the American Ceramic Society* (Accepted 2021). DOI: 10.1111/jace.18261

I conducted the following tasks:

- Writing of the main manuscript (co-operation with Prof. Dr. Thorsten M. Gesing, PD Dr. Mangir Murshed and Dr. Naveen K. C. Muniraju).
- Generation of the figures (except fig. 7 and 9).
- Solid state synthesis of the sample.

- Perform the measurements of PXRD, Raman and FTIR spectroscopy as well as their evaluation and interpretation, structure determination, and Rietveld refinements.
- Evaluation of neutron powder diffraction data at ambient temperature and their interpretation.
- Evaluation of magnetic susceptibility data and their interpretation.
- Evaluation of TGA/DSC data and their interpretation.

I did not conduct the following tasks:

- Magnetic susceptibility measurements (done by Dr. Thomas Frederichs).
- Neutron powder diffraction measurements (done out by Dr. Qiang Zhang).
- Evaluation of magnetic structure refinement, interpretation and generation of respective figures (Fig. 7 and 9) (carried out by Dr. Naveen K. C. Muniraju)
- TGA/DSC measurements (carried out by Julia Butzlaff).

Chapter 3

Synthesis and characterization of $(\text{Bi}_{1-x}\text{R}_x)_2\text{Mn}_4\text{O}_{10}$: structural, spectroscopic and thermogravimetric analyses for R = Nd, Sm and Eu

A published paper “Reproduced with permission from Springer Nature”.
<https://rd.springer.com/article/10.1007%2Fs10853-019-03852-7>. Copy right permission site:
<https://www.nature.com/nature-portfolio/reprints-and-permissions/permissions-requests#Author%20reuse> and/or <https://www.springer.com/gp/rights-permissions/obtaining-permissions/882>

Kowsik Ghosh¹, M. Mangir Murshed^{1,2*}, Thorsten M. Gesing^{1,2}

¹University of Bremen, Institute of Inorganic Chemistry and Crystallography, Leobener Straße 7, D-28359 Bremen, Germany

²University of Bremen, MAPEX Center for Materials and Processes, Bibliothekstraße 1, D-28359 Bremen, Germany

*Corresponding author: e-mail address: murshed@uni-bremen.de, phone: +49 (0)421 218 63144, fax: +49 421 218 63145.

Abstract

Mullite-type $\text{Bi}_2\text{Mn}_4\text{O}_{10}$ and $\text{R}_2\text{Mn}_4\text{O}_{10}$ (R = rare-earth element) compounds are isostructural and are of ongoing research attentions because of their interesting crystal structures and the associated multiferroic properties. We report three series of mullite-type $(\text{Bi}_{1-x}\text{R}_x)_2\text{Mn}_4\text{O}_{10}$ compounds for $\text{R} = \text{Nd}, \text{Sm}$ and Eu prepared by solid state synthesis methods. Each phase of the solid solutions is characterized by X-ray powder diffraction followed by Rietveld refinement. Evolutions of the metric parameters, interatomic bond distances, averaged crystallite size and microstrain are carried out with respect to the compositional x -value. This study also emphasizes on how the crystal-chemistry changes upon successive change of the stereochemical activity of the lone electron pair of the Bi^{3+} cation using the Wang-Liebau eccentricity parameter. Selective vibrational features have been discussed based on the Raman and Fourier transform infrared spectra. The thermal stability of the endmembers is analyzed from the thermogravimetric data, demonstrating that the endmember $\text{Bi}_2\text{Mn}_4\text{O}_{10}$ differently decomposes than that of the other $\text{R}_2\text{Mn}_4\text{O}_{10}$ compounds.

1. Introduction

The mullite-type $\text{Bi}_2\text{Mn}_4\text{O}_{10}$ and $\text{R}_2\text{Mn}_4\text{O}_{10}$ (R = rare-earth element) compounds (O10 compounds) are isostructural and well-studied systems for their crystal chemistry [1-3], magnetic [3, 4], ferroelectric [5, 6] and multiferroic[7] properties. The crystal structure of $\text{Bi}_2\text{Mn}_4\text{O}_{10}$ is described using orthorhombic space group $Pbam$ [1], where the edge-sharing MnO_6 octahedra forms an infinite chain along the c -axis and interconnected by edge-sharing MnO_5 distorted tetragonal pyramids [8], as shown in **Figure 1**. The structure is closely related to the mullite-type $\text{Bi}_2\text{Mn}_4\text{O}_9$ (O9) compounds [9-12] which differ only by having double-tetrahedra units instead of double-square bipyramids interconnecting the octahedral chains. It is well established that Mn^{4+} in $\text{Bi}_2(\text{Mn}^{3+})_2(\text{Mn}^{4+})_2\text{O}_{10}$ is located in the MnO_6 octahedra and Mn^{3+} in the MnO_5 square-pyramid [13]. The Bi^{3+} cation sits in the channels between the polyhedral chains, forming distorted BiO_8 polyhedra.

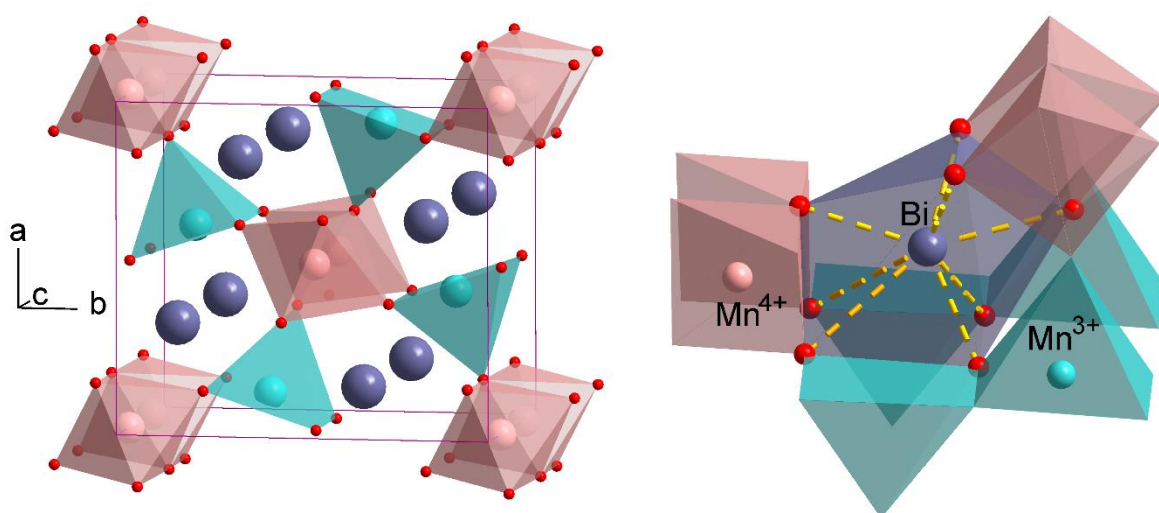


Figure 1: Representative crystal structure of $\text{Bi}_2\text{Mn}_4\text{O}_{10}$, showing MnO_6 octahedra and MnO_5 and BiO_8 coordination.

The slight but significant stereochemical activity of the $6s^2$ lone electron pair (LEP) of the Bi^{3+} cations seems also to be responsible for the LEP-driven polarizability, however, not the essential steric factor for the phase stability [14]. As a measure of magnitude of the stereochemical activity, the Liebau density vector (LDV) and the Wang-Liebau eccentricity

(WLE) parameter of the BiO_8 polyhedra are much higher in $\text{Bi}_2\text{Fe}_4\text{O}_9$ than those in $\text{Bi}_2\text{Mn}_4\text{O}_{10}$ [14]. The microscopic origin of ferroelectricity can be understood in terms of ordering of the LEPs (with certain admixture of p -orbitals) in the polarization direction [15]. However, the dipoles of the constituent Mn^{4+}O_6 (along c -axis) and Mn^{3+}O_5 (along b -axis) polyhedra are oriented in different directions [2], leading to poor electrical polarization [5, 16] and the associated ferroelectric displacement is too small to be detected within the experimental uncertainty. The common factor that leads to ferroelectricity in the $\text{R}_2\text{Mn}_4\text{O}_{10}$ compounds is the charge-ordering between Mn^{3+} and Mn^{4+} [7]. Therefore, either the polarizability of the Bi^{3+} LEP or charge ordering, or polyhedral tilting can be regarded as possible sources of the ferroelectric behavior in these phases. Substitution of LEP-containing Bi^{3+} with R^{3+} leads to a rich crystal chemistry with varying physical properties. For instance, whereas each member of $\text{R}_2\text{Mn}_4\text{O}_{10}$ possesses incommensurate magnetic character [17], $\text{Bi}_2\text{Mn}_4\text{O}_{10}$ shows a commensurate [18] magnetic structure although their Néel temperatures lie close to 40 (± 1) K. With increasing Bi-cation in the $(\text{La}_{1-x}\text{Bi}_x)_2\text{Mn}_4\text{O}_{10}$ system develops successive distortion of the $(\text{La,Bi})\text{O}_8$ unit, leading to different magnetic properties [19]. Moreover, the crystal-physical properties of $\text{R}_2\text{Mn}_4\text{O}_{10}$ greatly depend on the type of R-cation. A bond-valence sum (BVS) study [20] revealed that the tensile and compressive stresses are gradually released as the size of the R^{3+} cation decreases [3]. $(\text{Bi}_{0.9}\text{Eu}_{0.1})_2\text{Mn}_4\text{O}_{10}$ exhibits a ferromagnetic ordering with a Curie temperature of 46 K -slightly above the T_N of either $\text{Eu}_2\text{Mn}_4\text{O}_{10}$ or $\text{Bi}_2\text{Mn}_4\text{O}_{10}$ [6]. Whereas $\text{Bi}_2\text{Mn}_4\text{O}_{10}$ showed weak ferroelectric [5], the permittivity of $(\text{Bi}_{0.9}\text{Eu}_{0.1})_2\text{Mn}_4\text{O}_{10}$ was found much higher than that of $\text{Bi}_2\text{Mn}_4\text{O}_{10}$ [6]. In this regard, a complete solid solution is not so far available. The present study addresses whether a full miscibility between Bi^{3+} and R^{3+} cations (Nd, Sm, Eu) occur at the similar Wyckoff position in the $(\text{Bi}_{1-x}\text{R}_x)_2\text{Mn}_4\text{O}_{10}$ crystal structure. Each phase of the solid solutions is characterized by X-ray powder diffraction, Raman and Fourier transform infrared (FTIR) spectroscopies, and thermogravimetric analyses. The solid solution particularly emphasizes on

how the crystal-chemistry changes upon successive change of the stereochemical activity of the Bi^{3+} -cation in these mullite-type series.

2. Experimental

2.1. Synthesis

Stoichiometric amount of R_2O_3 (Nd_2O_3 , Sm_2O_3 and Eu_2O_3), $\text{Bi}(\text{NO}_3)_3 \cdot 5\text{H}_2\text{O}$ and $\text{Mn}(\text{NO}_3)_2 \cdot 4\text{H}_2\text{O}$ were mixed with 10 wt.% glycerine (1,2,3-propantriol) into a glass beaker and heated at 353 K under magnetic stirring for about half an hour. The sample was further heated at 473 K for about 2 h. Afterward, the foam-like solid was homogenously crushed into powder and put into a corundum crucible followed by heating at 973 K. After a reaction period of 72h, the samples were cooled down to room temperature with a cooling rate of 8 K /min. The samples were then re-ground and re-heated for another seven days. This intermediate mixing and re-heating for a longer period helped avoid formation of RMnO_3 perovskite phases [21]. The applied glycerin method is useful when there is no issue of subtle changes of oxidation states due to redox potentials of the starting cations. For the chemical composition of $(\text{Bi}_{1-x}\text{R}_x)_2\text{Mn}_4\text{O}_{10}$, 11 samples were produced for each series ($x = 0 - 1.0$).

2.2. X-ray diffraction

X-ray powder diffraction data were collected on an X'Pert MPD PRO diffractometer (PANalytical GmbH, Almelo, The Netherlands) equipped with an X'Celerator multi-strip (128) detector system. The X-ray patterns were collected using Ni-filtered $\text{CuK}_{\alpha 1,2}$ radiation ($\lambda_{\text{K}\alpha 1} = 154.05929(5)$ pm, $\lambda_{\text{K}\alpha 2} = 154.4414(2)$ pm) in Bragg-Brentano geometry. Data were collected at ambient condition from 5 to $135^\circ 2\theta$ with a step width of $0.0167^\circ 2\theta$ and a measurement time of 75s per step. The obtained data were refined using the Rietveld method (TOPAS V4.2, Bruker AXS) and the fundamental parameter approach was used for profile fitting, where the fundamental parameters were fitted against a standard material (LaB_6). The

starting atomic coordinates were taken from the single crystal data [22]. During Rietveld refinements the background, sample displacement, metric parameters, profile parameters and atomic coordinates were optimized. In some cases, the isotropic displacement parameters were constrained between atoms (Bi/R) located at the similar Wyckoff sites. Since the occupancy factor between Bi^{3+} and the R^{3+} in the $(\text{Bi}_{1-x}\text{R}_x)_2\text{Mn}_4\text{O}_{10}$ system does not show significant deviation, the corresponding occupancy factor has been fixed to the nominal compositional x -value. The average crystallite size (ACS) was calculated from all the observed X-ray reflections, which is described as $L_{Vol}(IB)$ by the TOPAS suite. $L_{Vol}(IB)$ refers to the volume-weighted mean of the coherently diffracted domain size using the integral breadth for the description of the reflection profile. Since the reflection profile is intrinsically associated with the size, shape, distribution and defects (strain) of the domains [23, 24], the $L_{Vol}(IB)$ values throughout this study should be considered as ‘apparent’ ACS for spherical crystallites with a unimodal distribution. Within the TOPAS facilities, the pseudo-Voigt profile function was deconvoluted into Gaussian and Lorentzian components, describing the ACS and the micro-strain (ϵ_0), respectively.

2.3. Spectroscopy

The Fourier transform infrared (FTIR) spectra were collected on a Bruker IFS66v/S spectrometer using the standard KBr method between 370 cm^{-1} and 4000 cm^{-1} . The Raman spectra were recorded on a LabRam ARAMIS (Horiba Jobin Yvon) Micro_Raman spectrometer equipped with laser working at 633 nm and less than 20mW . A $50\times$ objective (Olympus) with a numerical aperture of 0.75 provides a focus spot of about $2\text{ }\mu\text{m}$ diameter when closing the confocal hole to $200\text{ }\mu\text{m}$. Each spectrum ranges between 90 cm^{-1} and 750 cm^{-1} with a spectral resolution of approximately 1.2 cm^{-1} using a grating of 1800 grooves/mm and a thermoelectrically cooled CCD detector (Synapse, 1024×256 pixels).

2.4. Thermal analysis

TGA/DSC measurements were performed on TGA/DSC 3⁺ STAR^e System of Mettler Toledo. The samples were measured with a heating rate of 20 K/min and a continuous N₂ flow of 20 mL/min from 300 K to 1473 K. Afterward, the spectra were normalized to their individual mass. Approximately 10 mg of each sample was measured relative to an empty corundum crucible as the reference. A drift correction was applied based on the crucible data.

3. Results and discussion

The X-ray powder diffraction patterns of (Bi_{1-x}R_x)₂Mn₄O₁₀ are shown in **Figure S1** (Supplementary Information), and representative Rietveld refinement plots of the endmembers are shown in **Figure 2**. The refined metric parameters and selective interatomic distances are given in **Table S1**, **Table S2** and **Table S3** (Supplementary Information), respectively. The metric parameters of the end-members Bi₂Mn₄O₁₀, Nd₂Mn₄O₁₀, Sm₂Mn₄O₁₀ and Eu₂Mn₄O₁₀ are in good agreement with those of the reported values by Burianek et al. [22], Popov et al. [25], Kagomiya et al. [26] and Popov et al. [27], respectively. The substitution of Bi³⁺ with the Nd⁺³, Sm⁺³ and Eu⁺³ cations leads to contraction of the *a*-, and *c*-, and elongation of the *b*-cell parameter, as shown in **Figure 3**. The overall contraction of the cell volume can be explained due to successive decrease of the ionic radius in the order Bi³⁺ (131 pm) > Nd⁺³ (124.9 pm) > Sm⁺³ (121.9 pm) > Eu⁺³ (120.6 pm) [28] for eight coordinated (Bi/R)O₈ polyhedra. For comparison, metric parameters of the (Bi_{1-x}La_x)₂Mn₄O₁₀ solid solution are also plotted (**Fig. 3**). Clearly, the common trend does not hold for (Bi_{1-x}La_x)₂Mn₄O₁₀ series [19]. For a difference of 10.4 pm of the ionic radii between Bi³⁺ and Eu³⁺ cations, the cell volume contracts about 3% for the Eu₂Mn₄O₁₀ end-member.

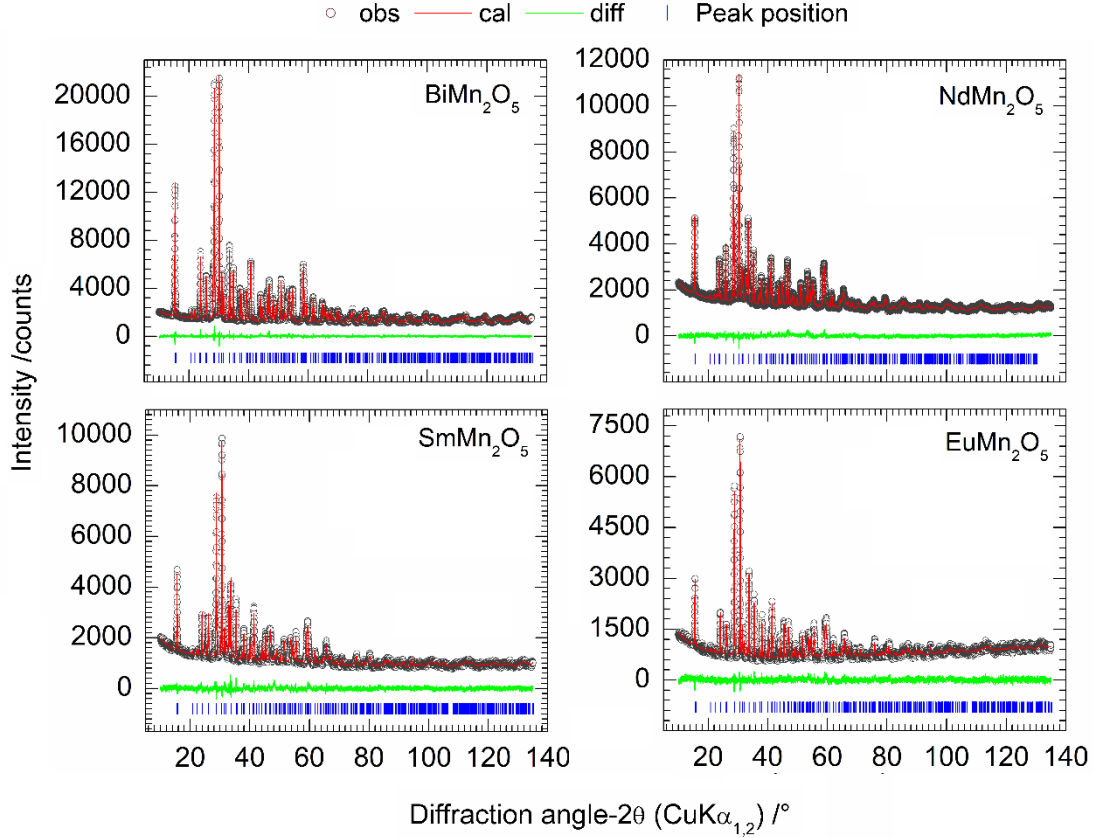


Figure 2: X-ray powder data Rietveld plots of the endmembers of the $(\text{Bi}_{1-x}\text{R}_x)_2\text{Mn}_4\text{O}_{10}$ series.

Whereas the ionic radius of La^{3+} cation (130 pm) is slightly smaller than that of the Bi^{3+} cation (131 pm) [27], the cell volume of $\text{La}_2\text{Mn}_4\text{O}_{10}$ [19] is about 3% greater than that of $\text{Bi}_2\text{Mn}_4\text{O}_{10}$. This discrepancy can be explained in terms of higher polyhedral volume of LaO_8 with strong compressive and tensile stresses [3]. The global instability index of about 0.2 v.u. [3] also infers to the preparation of the $\text{La}_2\text{Mn}_4\text{O}_{10}$ sample with high oxygen pressure [29]. In this regard, debates are still ongoing whether the samples contains interstitial oxygen due to associated preparation at oxygen pressure [29]. It is interesting to note that the departure from the Vegard's line is more pronounced for the smaller ionic sizes. For instance, the non-linearity is successively more pronounced from La- to Eu-compounds with respect to compositional x-value (**Fig. 3**). This trend is also consistent with the averaged $(\text{Bi/R})\text{-O}$ bond distances $\langle \text{Bi/R-O} \rangle$, as shown in **Figure 4**.

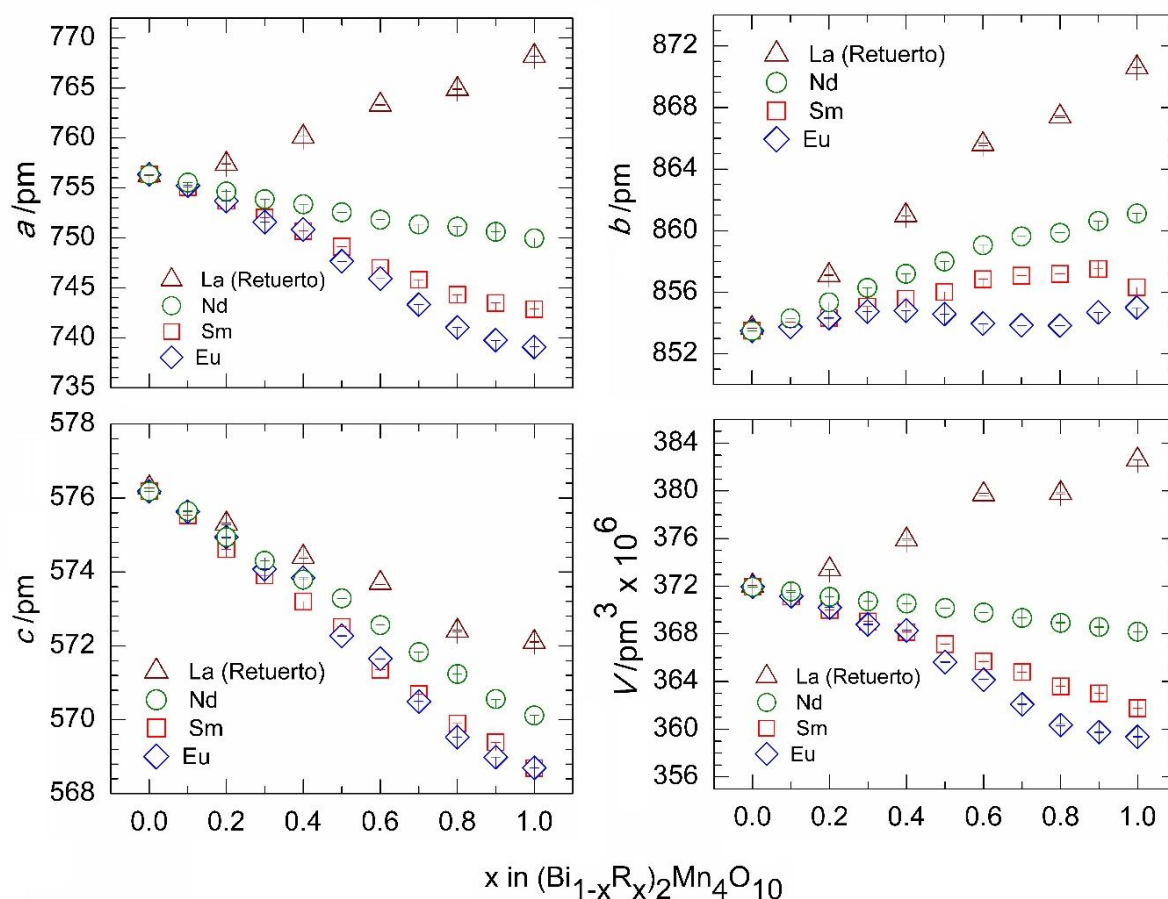


Figure 3: Evolution of the metric parameters while changing the compositional x in $(\text{Bi}_{1-x}\text{R}_x)_2\text{Mn}_4\text{O}_{10}$. For comparison, data of corresponding La compounds [19] are also plotted.

That is, the $\langle \text{Bi/R-O} \rangle$ rapidly decreases for the Eu- and Sm-containing compounds than that of the Nd-series. In contrast, the La-series follows a linear trend with positive slope. The trend seems to be consistent with the respective ionic sizes. The $\langle \text{Mn}(1)\text{-O} \rangle$ in the MnO_6 octahedra fluctuates within the mean value of 192 pm (**Tab. S3**). However, in the mid-range of x -value, both the Sm- and Eu-series exhibit higher deviation from the mean value, which can be associated with the respective elongation/contraction and the associated geometric distortions of the MnO_6 octahedra. The $\langle \text{Mn}(2)\text{-O} \rangle$ in the MnO_5 pyramids decreases, however, with high uncertainties for each series (**Tab. S3**).

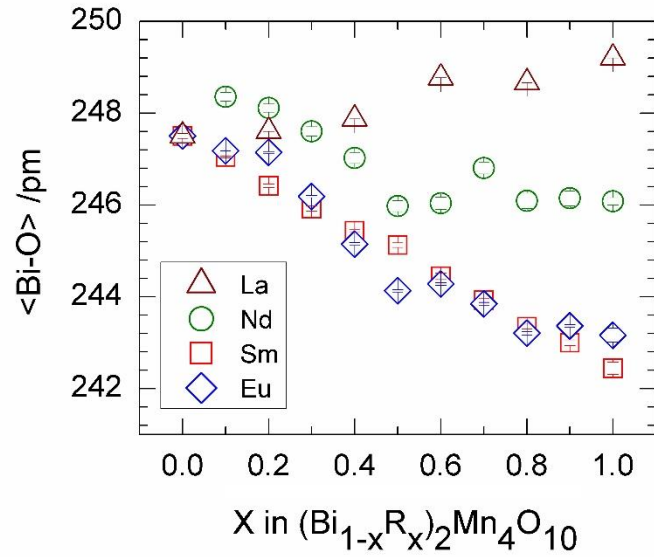


Figure 4: Evolution of the averaged (Bi/R)-O bond distances ($\langle\text{Bi/R-O}\rangle$) while changing the compositional x in $(\text{Bi}_{1-x}\text{R}_x)_2\text{Mn}_4\text{O}_{10}$. For comparison, data of La-compounds [19] are also plotted.

As a measure of the polyhedral distortion due to stereochemical activity of the LEPs of Bi^{3+} cation, the WLE parameter linearly decreases with increasing dilution of the Bi^{3+} in the $(\text{Bi}_{1-x}\text{La}_x)_2\text{Mn}_4\text{O}_{10}$ system, as shown in **Figure 5**. For comparison, the lowest WLE-value for $x = 0$ must be considered due to purely geometric distortion of the RO_8 coordination without any contribution from the LEP. A slight positive hump (above the linear trend) can be seen for the $(\text{Bi}_{1-x}\text{Sm}_x)_2\text{Mn}_4\text{O}_{10}$ and $(\text{Bi}_{1-x}\text{Eu}_x)_2\text{Mn}_4\text{O}_{10}$ compounds for $x = 0.4 - 0.6$, which can be explained in terms of the additional geometric distortion in the mid-range of the solid solutions. In this regard, the WLE parameter cannot distinguish between purely geometric distortion and the stereochemical activity-led distortion of the Bi^{3+} cation [30]. $\text{Bi}_2\text{Mn}_4\text{O}_{10}$ crystallizes with an ACS of approximately 513(14) nm, which gradually decreases to 126(3) nm for $x = 0.3$ in the $(\text{Bi}_{1-x}\text{Nd}_x)_2\text{Mn}_4\text{O}_{10}$ series and stays almost constant till $x = 1.0$, as shown in **Figure 6**.

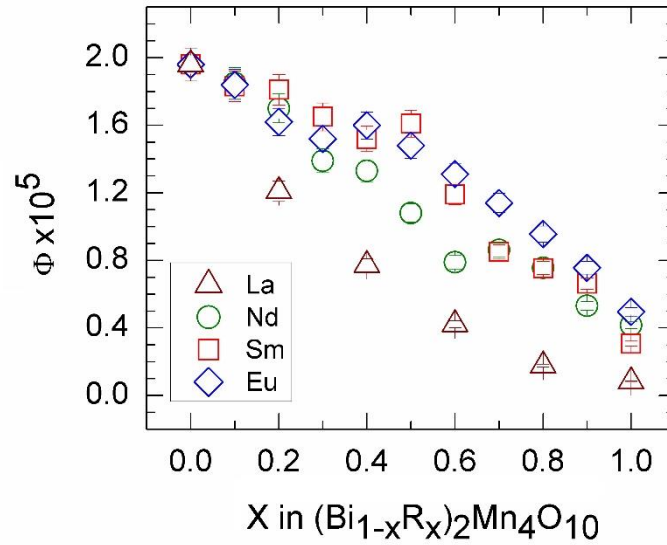


Figure 5: Changes of the absolute value of the Wang-Liebau eccentricity parameter (Φ) with respect to compositional x in $(\text{Bi}_{1-x}\text{R}_x)_2\text{Mn}_4\text{O}_{10}$. For comparison, data of La-compounds [19] are also plotted.

Of particular contrasts, the ACS for the Sm- and Eu-containing compounds show a rapid drop for $x = 0.1$. Afterward, the ACS only fluctuates around an averaged value of 100(20) nm up to $x = 1$. The microstrain (**Fig. 6**) in the mid-range of each series show higher values (**Fig. 6**). The mid-range hump is more pronounced for the for $(\text{Bi}_{1-x}\text{Eu}_x)_2\text{Mn}_4\text{O}_{10}$ compounds due to higher deviation of ionic radius between Bi^{3+} and R^{3+} cation.

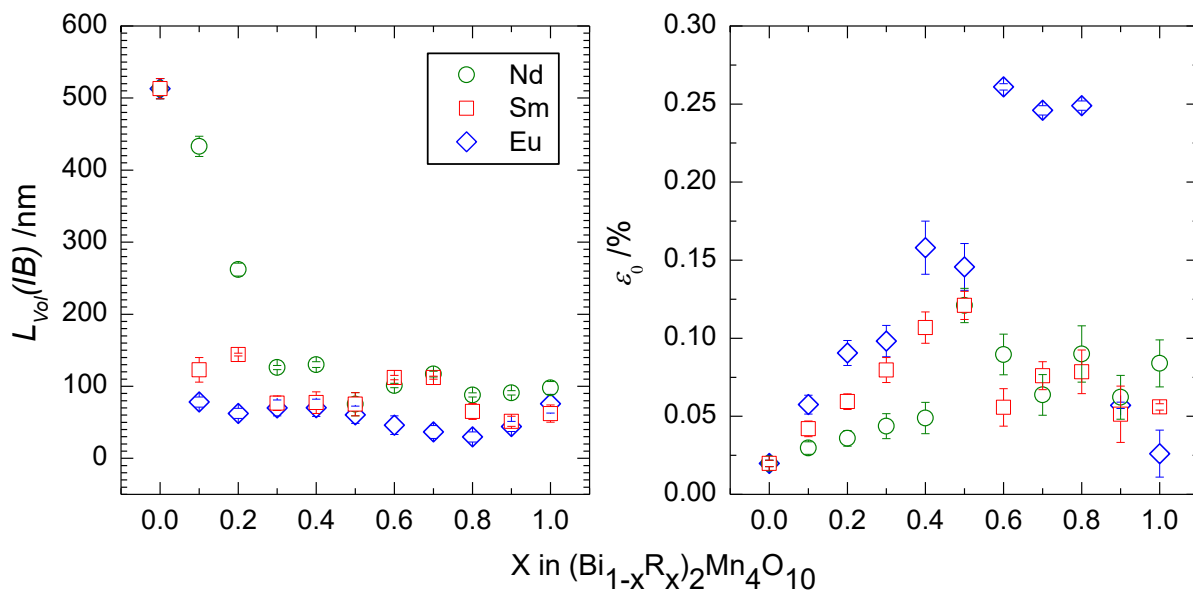


Figure 6: Changes of the average crystallite size ($L_V(IB)$) and microstrain (ϵ_0) with respect to compositional x in $(Bi_{1-x}R_x)_2Mn_4O_{10}$.

3.2. Spectroscopy

Factor group analysis predicts 96 modes ($13A_{1g} + 13B_{1g} + 11B_{2g} + 11B_{3g} + 9A_{1u} + 9B_{1u} + 15B_{2u} + 15B_{3u}$), where 48 modes are Raman active ($13A_{1g} + 13B_{1g} + 11B_{2g} + 11B_{3g}$), 45 are infrared active ($9A_{1u} + 8B_{1u} + 14B_{2u} + 14B_{3u}$). $B_{1u} + B_{2u} + B_{3u}$ represent the acoustic modes and all nine A_{1u} modes are optically silent. **Figure S2** (Supplementary Information) shows stack plots of the Raman spectra for three series of compounds. **Figure 7** shows the Raman shift at the better-resolved (high intensity) high- ($500 - 700 \text{ cm}^{-1}$) and at low-frequency ($150 - 250 \text{ cm}^{-1}$) regions. Lattice dynamics calculations suggests the bands at 655 cm^{-1} and 609 cm^{-1} belong to the Mn-O stretching (A_g and B_{1g}) of the MnO_6 octahedra [31]. Assuming a red-shift of approximately $5(2) \text{ cm}^{-1}$ at ambient condition due to quasi-harmonic (volume-dependent) and intrinsic anharmonicity (temperature-dependent), the observed band maxima at $650(1) \text{ cm}^{-1}$ ($FWHM$ of $17(2) \text{ cm}^{-1}$) and $606(1) \text{ cm}^{-1}$ ($FWHM$ of $17(2) \text{ cm}^{-1}$) can be associated with these A_g and B_{1g} modes. The $\langle Mn-O \rangle$ bond length is slightly (2 pm) shorter in MnO_6 octahedron than in MnO_5 pyramidal one (Tab. S3). However, such marginal difference can

hardly show distinctive spectral contribution within the spectral resolution. Therefore, it is conceivable that the high frequency region between 500 cm^{-1} and 650 cm^{-1} observed for the $\text{Bi}_2\text{Mn}_4\text{O}_{10}$ system is contributed by the stretching modes of Mn-O bonds of both MnO_5 and MnO_6 polyhedra (**Fig. S2**).

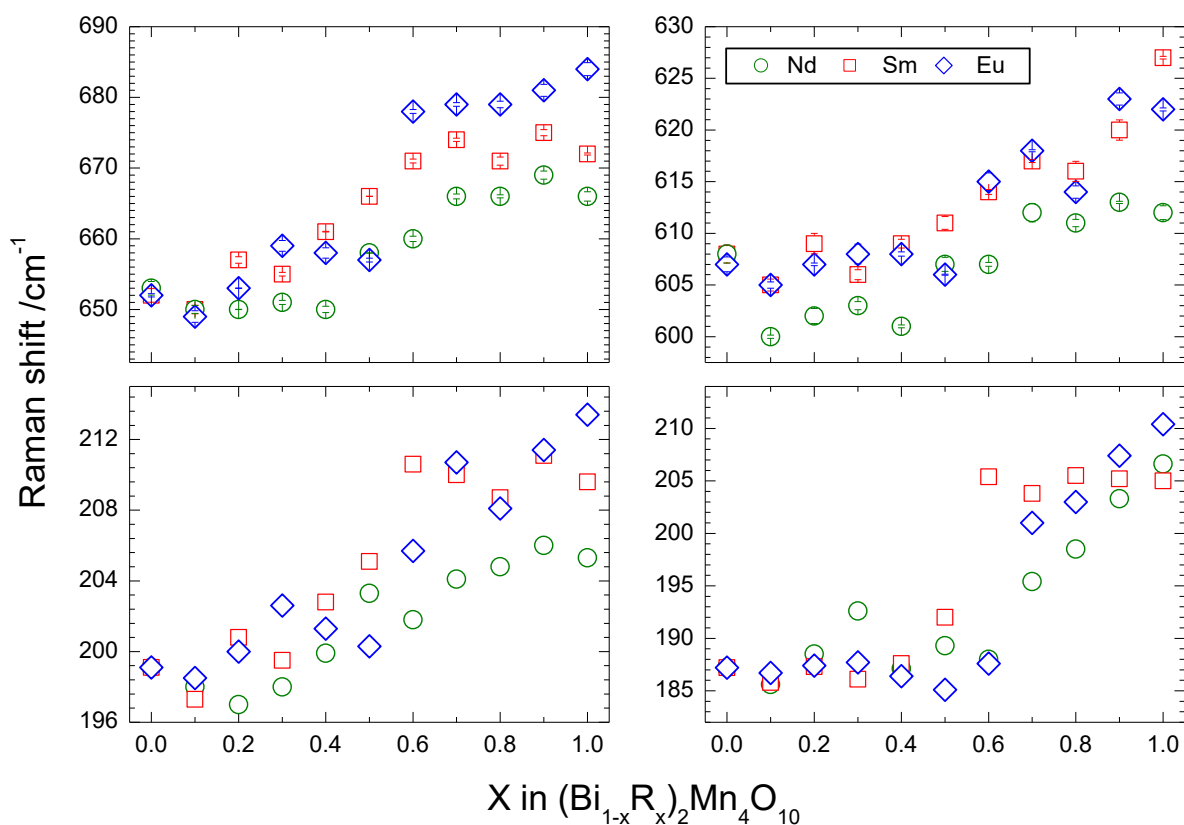


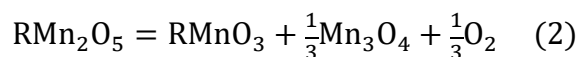
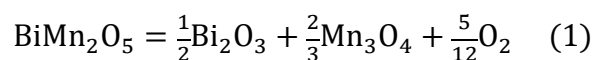
Figure 7: Changes of Raman mode frequencies with respect to compositional x in $(\text{Bi}_{1-x}\text{R}_x)_2\text{Mn}_4\text{O}_{10}$.

With increasing x -value both band maxima showed a sigmoid behavior, which can be assigned to the change of the $\langle\text{Mn}(2)\text{-O}\rangle$ bond lengths (Tab. S3). The low-frequency region is mainly contributed by the BiO_8 polyhedra (**Fig. 7**). The sigmoidal change of the band maximum is associated with the slightly sigmoidal behaviors of the $\langle\text{Bi-O}\rangle$ bond distances. Since the $\langle\text{Bi-O}\rangle$ increases for the La-containing systems [19], it is expected that the La-series would show the opposite behaviors than those of the Nd-, Sm- and Eu-samples. As a centrosymmetric system, where the Raman active modes are IR inactive and *vice versa*, we

also follow the infrared spectra at ambient condition. **Figure S3** represents the comparative views between the spectra of the solid solutions along with a representative fit. The compound model requires 19 bands. The change of frequency of some better-resolved bands are comparable with the previous report [31] as well as the observed Raman bands.

3.3. Thermal analysis

Thermogravimetric analysis, as shown in **Figure 8**, agrees with the observation of Li et al. [32] that the by $R_2Mn_4O_{10}$ compounds are more stable than $Bi_2Mn_4O_{10}$. The weight loss of 3.31(1)%, 3.42(2)%, 3.40(1)% and 3.41(3)% were observed for $Bi_2Mn_4O_{10}$, $Nd_2Mn_4O_{10}$, $Sm_2Mn_4O_{10}$, $Eu_2Mn_4O_{10}$, respectively. The amount of weight loss confirms that $Bi_2Mn_4O_{10}$ decomposes into Mn_3O_4 and Bi_2O_3 , and $R_2Mn_4O_{10}$ decomposes into $RMnO_3$ perovskite and Mn_3O_4 according to the following reactions:



During heating the first point of inflection (onset temperature) was identified as the decomposition temperature at 1145 K, 1323 K, 1322 K and 1340 K, respectively for $Bi_2Mn_4O_{10}$, $Nd_2Mn_4O_{10}$, $Sm_2Mn_4O_{10}$, $Eu_2Mn_4O_{10}$, which gradually decreases with increasing the ionic radii (**Fig. 8**). The stability of the compounds can also be correlated to their respective bond strength of 337.2 ± 12.6 , 479 ± 10 , 565 ± 13 , 703 ± 13 kJ/mol for Bi-O, Eu-O, Sm-O and Nd-O, respectively [33]. The presence of excess oxygen reported in some members of the series [29] was not so far observed the investigated systems.

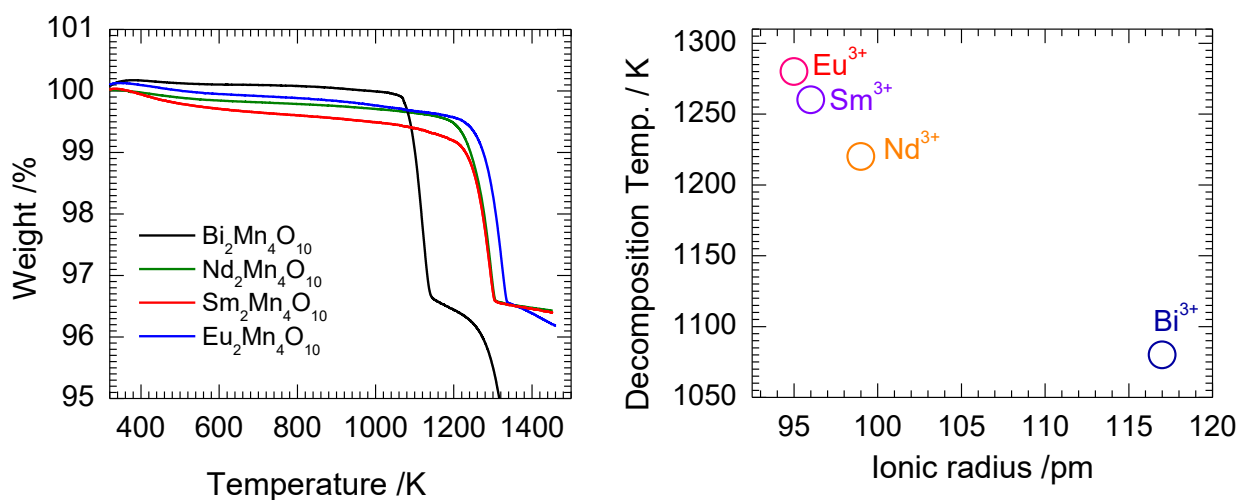


Figure 8: Weight loss during the gravimetric thermal analyses of $\text{Bi}_2\text{Mn}_4\text{O}_{10}$ and $\text{R}_2\text{Mn}_4\text{O}_{10}$ (left) and stability comparison between them with respect to their ionic radii (right).

4. Summary

Whereas the endmembers are well studied systems, a chemical miscibility has been tested in the mullite-type $(\text{Bi}_{1-x}\text{R}_x)_2\text{Mn}_4\text{O}_{10}$ series for ($\text{R} = \text{Nd}, \text{Sm}, \text{Eu}$ and $x = 0 - 1.0$). A detailed structural, spectroscopic and thermogravimetric analysis were performed for each compound. The trend of the structural features such as metric parameters, average crystallite size, microstrain, Wang-Liebau eccentricity parameter (measures of the polyhedral distortion due to stereochemical activity of the lone electron pairs of a given cation) have been followed with respect to the compositional x . Following selective vibrational bands showed a non-linear trend in the mid-range values of x , which was explained in terms of the changes of the associated bond distances. The thermogravimetric analysis of the end-members confirmed that $\text{Bi}_2\text{Mn}_4\text{O}_{10}$ differently decomposes than that of the $\text{R}_2\text{Mn}_4\text{O}_{10}$ compounds.

Reference

- [1] R.X. Fischer, Mullite, in: H. Schneider, S. Komarneni (Eds.), Wiley-VCH, Weinheim, 2005: pp. 1–46.

- [2] A. Muñoz, M.T. Fernández-Díaz, Magnetic structure and properties of BiMn_2O_5 oxide: A neutron diffraction study, *Phys. Rev. B.* 65 (2002) 144423. doi:10.1103/PhysRevB.65.144423.
- [3] J.A. Alonso, M.T. Casais, M.J. Martínez-Lope, J.L. Martínez, M.T. Fernández-Díaz, A structural study from neutron diffraction data and magnetic properties of RMn_2O_5 (R = La, rare earth), *J. Phys. Condens. Matter.* 9 (1997) 8515–8526. doi:10.1088/0953-8984/9/40/017.
- [4] L.M. Volkova, D. V Marinin, Crystal chemistry aspects of the magnetically induced ferroelectricity in TbMn_2O_5 and BiMn_2O_5 , *J. Phys. Condens. Matter.* 21 (2009) 015903. doi:10.1088/0953-8984/21/1/015903.
- [5] F. Ziegler, L. Köhler, H. Gibhardt, T.M. Gesing, M.M. Murshed, O. Sobolev, A. Piovano, G. Eckold, Characterization of Multiferroic $\text{Bi}_2\text{Mn}_4\text{O}_{10}$ by Dielectric and Neutron Spectroscopy, 1800668 (2019) 1–7. doi:10.1002/pssb.201800668.
- [6] Z.H. Sun, B.L. Cheng, S. Dai, K.J. Jin, Y.L. Zhou, H.B. Lu, Z.H. Chen, G.Z. Yang, Effect of Ce substitution on magnetic and dielectric properties of BiMn_2O_5 , *J. Appl. Phys.* 99 (2006) 084105. doi:10.1063/1.2190716.
- [7] J. Van Den Brink, D.I. Khomskii, Multiferroicity due to charge ordering, *J. Phys. Condens. Matter.* (2008) 22. doi:10.1088/0953-8984/20/43/434217.
- [8] Z.R. Kann, J.T. Auletta, E.W. Hearn, S.-U. Weber, K.D. Becker, H. Schneider, M.W. Lufaso, Mixed crystal formation and structural studies in the mullite-type system $\text{Bi}_2\text{Fe}_4\text{O}_9$ – $\text{Bi}_2\text{Mn}_4\text{O}_{10}$, *J. Solid State Chem.* 185 (2012) 62–71. doi:10.1016/j.jssc.2011.10.046.
- [9] N. Niizeki, M. Wachi, The crystal structures of $\text{Bi}_2\text{Mn}_4\text{O}_{10}$, $\text{Bi}_2\text{Al}_4\text{O}_9$ and $\text{Bi}_2\text{Fe}_4\text{O}_9$, *Z. Krist.* 127 (1968) 173–187. doi:10.1524/zkri.1968.127.1-4.173.
- [10] M.M. Murshed, T.M. Gesing, Anisotropic thermal expansion and anharmonic phonon behavior of mullite-type $\text{Bi}_2\text{Ga}_4\text{O}_9$, *Mater. Res. Bull.* 48 (2013) 3284–3291. doi:10.1016/j.materresbull.2013.05.007.
- [11] M. Mangir Murshed, C.B. Mendive, M. Curti, M. Šehović, A. Friedrich, M. Fischer, T.M. Gesing, Thermal expansion of mullite-type $\text{Bi}_2\text{Al}_4\text{O}_9$: A study by X-ray diffraction, vibrational spectroscopy and density functional theory, *J. Solid State Chem.* 229 (2015) 87–96. doi:10.1016/j.jssc.2015.05.010.
- [12] M.M. Murshed, G. Nénert, M. Burianek, L. Robben, M. Mühlberg, H. Schneider, R.X. Fischer, T.M. Gesing, Temperature-dependent structural studies of mullite-type $\text{Bi}_2\text{Fe}_4\text{O}_9$, *J. Solid State Chem.* 197 (2013). doi:10.1016/j.jssc.2012.08.062.
- [13] N. Nguyen, M. Legrain, A. Ducouret, B. Raveau, Distribution of Mn^{3+} and Mn^{4+} species between octahedral and square pyramidal sites in $\text{Bi}_2\text{Mn}_4\text{O}_{10}$ -type structure, *J. Mater. Chem.* 9 (1999) 731–734. doi:10.1039/a808094a.
- [14] M. Curti, T.M. Gesing, M.M. Murshed, T. Bredow, C.B. Mendive, Liebau density vector: A new approach to characterize lone electron pairs in mullite-type materials, *Z. Krist.* 288 (2013) 629–634. doi:10.1524/zkri.2013.1686.
- [15] D. Khomskii, Classifying multiferroics: Mechanisms and effects, *Physics (College Park, Md.)* 2 (2009) 20. doi:10.1103/Physics.2.20.
- [16] K.J.D. MacKenzie, T. Dougherty, J. Barrel, The electronic properties of complex oxides of bismuth with the mullite structure, *J. Eur. Ceram. Soc.* 28 (2008) 499–504. doi:10.1016/j.jeurceramsoc.2007.03.012.

- [17] S. Petit, V. Balédent, C. Doubrovsky, M.B. Lepeit, M. Greenblatt, B. Wanklyn, P. Foury-Leylekian, Investigation of the electromagnon excitations in the multiferroic TbMn_2O_5 , *Phys. Rev. B.* 87 (2013) 140301. doi:10.1103/PhysRevB.87.140301.
- [18] C. Vecchini, L. Chapon, P. Brown, T. Chatterji, S. Park, S.-W. Cheong, P. Radaelli, Commensurate magnetic structures of RMn_2O_5 (R=Y, Ho, Bi) determined by single-crystal neutron diffraction, *Phys. Rev. B.* 77 (2008) 134434–11. doi:10.1103/PhysRevB.77.134434.
- [19] M. Retuerto, A. Muñoz, M.J. Martínez-Lope, M. Garcia-Hernandez, G. André, K. Krezhov, J.A. Alonso, Influence of the Bi^{3+} electron lone pair in the evolution of the crystal and magnetic structure of $\text{La}_{1-x}\text{Bi}_x\text{Mn}_2\text{O}_5$ oxides., *J. Phys. Condens. Matter.* 25 (2013) 216002. doi:10.1088/0953-8984/25/21/216002.
- [20] I.D. Brown, *The Chemical Bond in Inorganic Chemistry, The Bond Valence Model*, Oxford University Press, 2002.
- [21] A. Kirsch, M.M. Murshed, F.J. Litterst, T.M. Gesing, Structural , Spectroscopic , and Thermoanalytic Studies on $\text{Bi}_2\text{Fe}_4\text{O}_9$: Tunable Properties Driven by Nano- and Polycrystalline States, *J. Phys. Chem. C.* 123 (2019) 3161–3171. doi:10.1021/acs.jpcc.8b09698.
- [22] M. Burianek, T.F. Krenzel, M. Schmittner, J. Schreuer, R.X. Fischer, M. Mühlberg, G. Nénert, H. Schneider, T.M. Gesing, Single crystal growth and characterization of mullite-type $\text{Bi}_2\text{Mn}_4\text{O}_{10}$, 103 (2012) 449–455.
- [23] D. Balzar, Voigt-function model in diffraction line-broadening analysis, *Microstruct. Anal. from Diffr.* (1999) 44. doi:10.1.1.30.7311.
- [24] D. Balzar, N. Audebrand, M. Daymond, A. Fitch, A. Hewat, J.I. Langford, A. Bail, D. Louer, O. Masson, C. McCowan, N. Popa, P. Stephens, B. Toby, Size – strain line-broadening analysis of the ceria round-robin sample, *Appl. Crystallogr.* 37 (2004) 911–924. doi:10.1107/S0021889804022551.
- [25] G. Popov, M. Greenblatta, W.H. McCarroll, Synthesis of LnMn_2O_5 (Ln = Nd, Pr) crystals using fused salt electrolysis, *Mater. Res. Bull.* 35 (2000) 1661–1667. doi:10.1016/S0025-5408(00)00372-X.
- [26] I. Kagomiya, S. Matsumoto, K. Kohn, Y. Fukuda, T. Shoubu, H. Kimura, Y. Noda, N. Ikeda, Lattice Distortion at Ferroelectric Transition of YMn_2O_5 , *Ferroelectrics.* 286 (2003) 167–174. doi:10.1080/00150190390206347.
- [27] Y.F. Popov, A.M. Kadomtseva, G.P. Vorob'ev, V.A. Sanina, A.K. Zvezdin, M.M. Tehranchi, Low-temperature phase transition in EuMn_2O_5 induced by a strong magnetic field, *Phys. B.* 284 (2000) 1402–1403. doi:Doi 10.1016/S0921-4526(99)02565-X.
- [28] R.D. Shannon, Revised effective ionic radii and systematic studies of interatomic distances in halides and chalcogenides, *Acta Crystallogr. Sect. A.* 32 (1976) 751–767. doi:10.1107/S0567739476001551.
- [29] J.A. Alonso, M.T. Casais, M.J. Martínez-Lope, I. Rasines, High Oxygen Pressure Preparation, Structural Refinement, and Thermal Behavior of RMn_2O_5 (R = La, Pr, Nd, Sm, Eu), *J. Solid State Chem.* 129 (1997) 105–112. doi:10.1006/jssc.1996.7237.
- [30] X. Wang, F. Liebau, Influence of polyhedron distortions on calculated bond-valence sums for cations with one lone electron pair, *Acta Crystallogr. B.* 63 (2007) 216–228. doi:10.1107/S0108768106055911.

- [31] F.M. Silva Júnior, C.W.A. Paschoal, R.M. Almeida, R.L. Moreira, W. Paraguassu, M.C. Castro Junior, A.P. Ayala, Z.R. Kann, M.W. Lufaso, Room-temperature vibrational properties of the BiMn_2O_5 mullite, *Vib. Spectrosc.* 66 (2013) 43–49. doi:10.1016/j.vibspec.2013.01.010.
- [32] C. Li, S. Thampy, Y. Zheng, J.M. Kweun, Y. Ren, J.Y. Chan, H. Kim, M. Cho, Y.Y. Kim, J.W.P. Hsu, K. Cho, Thermal stability of mullite RMn_2O_5 (R = Bi , Y , Pr , Sm or Gd): combined density functional theory and experimental study, *J. Phys. Condens. Matter.* 28 (2016) 125602. doi:10.1088/0953-8984/28/12/125602.
- [33] J. Kerr, *CRC Handbook of Chemistry and Physics*, 64th ed., CRC Press, Boca Raton, FL, 1984.

Acknowledgement

Kowsik Ghosh gratefully thanks the University of Bremen for the financial supports. He also acknowledges DAAD (Funding ID: 57340829) and BISIP (Bremen International Students Internship Program) for their supports in partly finance this project.

Supplementary Information

Synthesis and characterization of $(\text{Bi}_{1-x}\text{R}_x)_2\text{Mn}_4\text{O}_{10}$: structural, spectroscopic and thermogravimetric analyses for $\text{R} = \text{Nd}, \text{Sm}$ and Eu

Kowsik Ghosh¹, M. Mangir Murshed^{1,2*}, Thorsten M. Gesing^{1,2}

¹University of Bremen, Institute of Inorganic Chemistry and Crystallography, Leobener Straße 7, D-28359 Bremen, Germany

²University of Bremen, MAPEX Center for Materials and Processes, Bibliothekstraße 1, D-28359 Bremen, Germany

*Corresponding author: e-mail address: murshed@uni-bremen.de, phone: +49 (0)421 218 63144, fax: +49 421 218 63145.

Table S1: Metric parameters of $(\text{Bi}_{1-x}\text{R}_x)_2\text{Mn}_4\text{O}_{10}$ obtained from X-ray powder data Rietveld refinements.

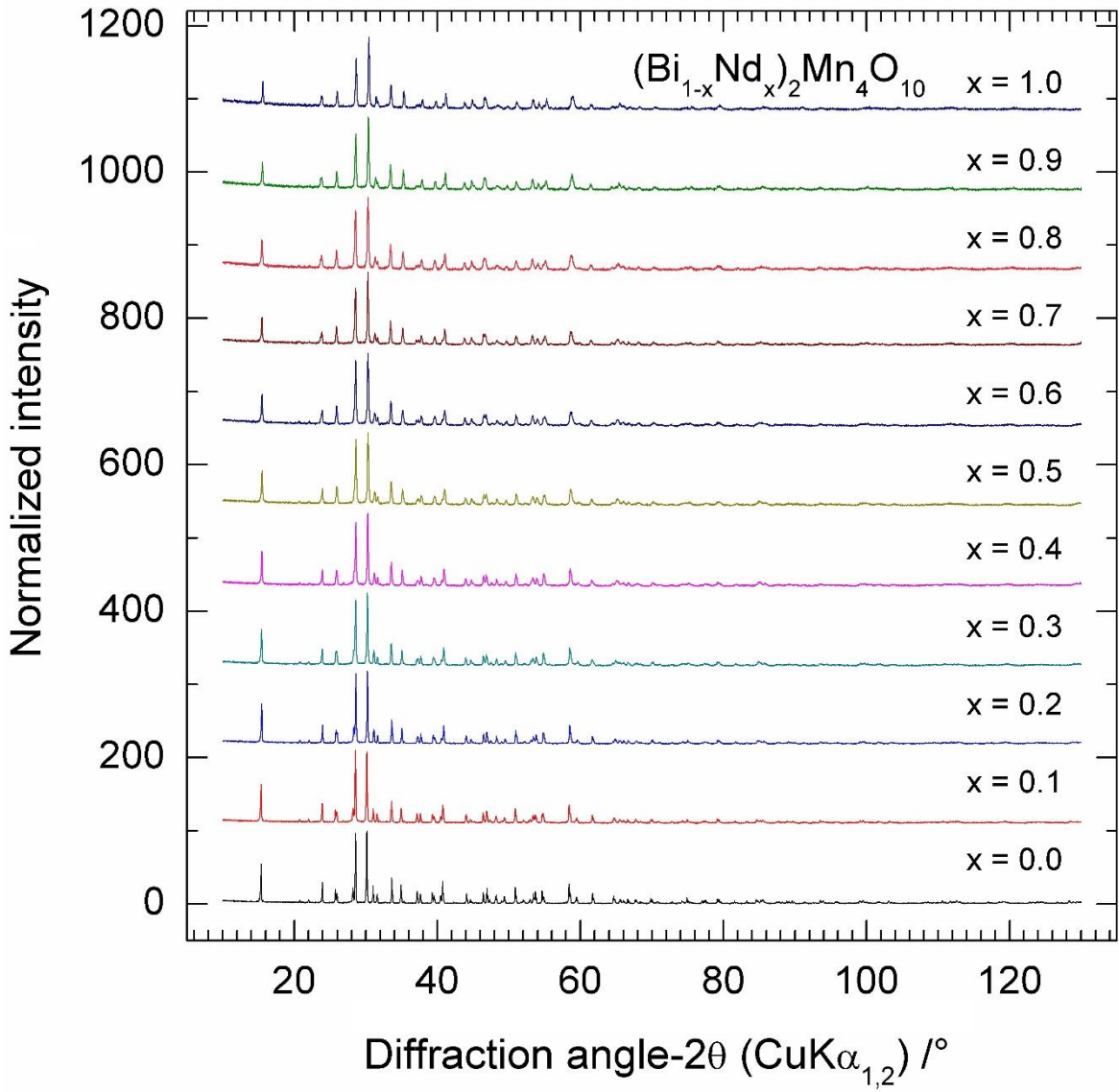
x	a /pm	b /pm	c /pm	V /pm³ x10⁶
(Bi_{1-x}Nd_x)₂Mn₄O₁₀				
0.0	756.09(1)	853.57(8)	576.16(5)	371.84(6)
0.1	755.54(1)	854.31(4)	575.64(5)	371.56(1)
0.2	754.63(7)	855.34(3)	574.94(3)	371.10(9)
0.3	753.89(1)	856.28(1)	574.29(6)	370.73(2)
0.4	753.38(6)	857.21(2)	573.79(4)	370.56(1)
0.5	752.57(1)	858.00(1)	573.27(7)	370.17(1)
0.6	751.81(1)	859.06(1)	572.53(1)	369.77(1)
0.7	751.36(1)	859.61(1)	571.82(6)	369.33(1)
0.8	751.12(1)	859.83(1)	571.21(1)	368.91(1)
0.9	750.62(1)	860.62(1)	570.55(1)	368.58(1)
1.0	750.30(1)	860.30(1)	569.94(1)	367.89(1)
(Bi_{1-x}Sm_x)₂Mn₄O₁₀				
0.0	756.32(1)	853.49(3)	576.18(5)	371.93(6)
0.1	755.09(1)	854.06(5)	575.52(9)	371.15(7)
0.2	753.72(5)	854.35(7)	574.62(6)	370.02(9)
0.3	752.09(1)	855.07(2)	573.89(7)	369.06(9)
0.4	750.71(1)	855.59(1)	573.19(4)	368.15(9)
0.5	749.14(1)	856.05(1)	572.51(1)	367.14(7)
0.6	746.99(5)	856.83(6)	571.36(8)	365.70(7)
0.7	745.80(6)	857.09(1)	570.70(3)	364.80(6)
0.8	744.29(1)	857.17(1)	569.89(6)	363.59(1)
0.9	743.50(1)	857.54(1)	569.42(1)	363.05(1)
1.0	742.46(1)	857.39(1)	568.92(1)	362.16(1)
(Bi_{1-x}Eu_x)₂Mn₄O₁₀				
0.0	756.27(4)	853.65(4)	576.28(2)	372.04(4)
0.1	755.28(4)	853.77(5)	575.65(5)	371.20(6)
0.2	753.75(2)	854.36(9)	574.98(8)	370.28(2)
0.3	751.60(6)	854.78(6)	574.10(2)	368.83(9)
0.4	750.90(3)	854.96(1)	573.95(3)	368.47(2)
0.5	748.69(4)	854.90(5)	572.97(5)	366.73(9)
0.6	745.94(6)	854.23(3)	571.70(2)	364.29(2)
0.7	743.25(2)	854.13(6)	570.55(5)	362.20(9)
0.8	740.77(7)	853.86(3)	569.28(6)	360.08(6)
0.9	739.60(4)	853.68(7)	568.91(5)	359.24(9)
1.0	739.01(5)	854.68(7)	568.82(4)	359.28(2)

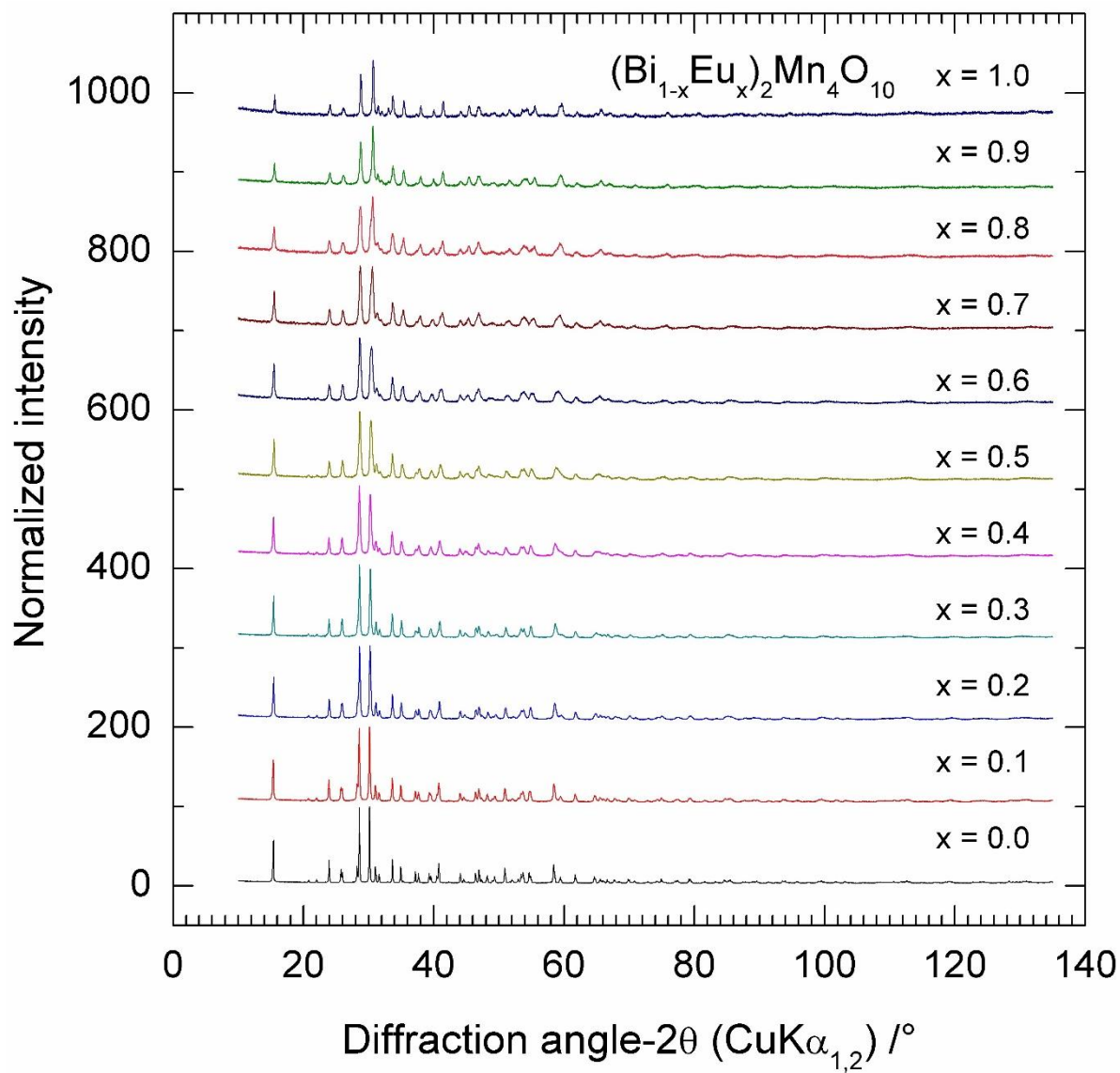
Table S2: Selective interatomic bond distances [pm] in the (Bi/R)₈ polyhedra of the (Bi_{1-x}R_x)₂Mn₄O₁₀ compounds obtained from X-ray powder data Rietveld refinements.

(Bi_{1-x}Nd_x)₂Mn₄O₁₀						
x	Bi-O(11)	Bi-O(11)	Bi-O(2)	Bi-O(2)	Bi-O(3)	Mean
0.0	233.8(8)	239.0(7)	279.4(5)	225.0(5)	249.3(5)	247.5(6)
0.1	232.9(9)	241.4(9)	279.2(9)	226.7(8)	250.5(8)	248.4(9)
0.2	232.5(9)	243.6(9)	274.7(8)	228.9(8)	250.8(8)	248.1(9)
0.3	234.2(9)	241.9(9)	271.7(8)	231.7(8)	249.0(8)	247.6(9)
0.4	236.6(9)	243.3(9)	269.8(9)	231.2(9)	247.2(9)	247.0(9)
0.5	237.7(9)	244.4(9)	265.0(9)	233.4(9)	244.4(9)	246.0(9)
0.6	242.1(9)	244.5(9)	263.0(9)	235.8(9)	245.0(9)	246.0(9)
0.7	235.5(9)	245.0(9)	261.7(9)	239.2(9)	246.1(9)	246.8(9)
0.8	236.9(9)	243.5(9)	258.7(9)	239.2(9)	246.3(9)	246.1(9)
0.9	236.2(9)	244.3(9)	254.7(9)	244.4(9)	245.3(9)	246.2(9)
1.0	242.1(1)	243.0(9)	254.1(7)	241.8(7)	246.0(8)	246.1(8)
(Bi_{1-x}Sm_x)₂Mn₄O₁₀						
0.0	233.8(8)	239.0(7)	279.4(5)	225.0(5)	249.3(5)	247.5(6)
0.1	234.8(1)	239.3(1)	277.4(3)	225.8(1)	248.00(8)	247.1(2)
0.2	235.5(8)	239.6(8)	275.5(5)	225.6(5)	247.0(6)	246.4(4)
0.3	236.2(1)	240.9(1)	273.1(8)	226.9(7)	245.1(8)	245.9(5)
0.4	236.5(1)	241.5(1)	270.6(4)	228.0(1)	244.3(9)	245.4(2)
0.5	237.2(1)	242.1(1)	270.9(8)	226.8(7)	243.1(9)	245.1(5)
0.6	239.1(2)	242.4(2)	264.9(9)	230.7(9)	241.5(1)	244.5(7)
0.7	239.4(1)	242.6(1)	259.1(6)	234.6(6)	241.0(9)	243.9(4)
0.8	239.4(2)	243.6(2)	256.7(8)	235.5(7)	239.7(1)	243.4(5)
0.9	241.2(2)	244.0(2)	255.1(9)	236.1(8)	238.3(1)	243.0(6)
1.0	242.1(9)	243.8(9)	246.9(9)	242.8(9)	237.1(9)	242.4(9)
(Bi_{1-x}Eu_x)₂Mn₄O₁₀						
0.0	233.8(8)	238.97(7)	279.4(5)	225.0(5)	249.3(5)	247.5(6)
0.1	234.6(1)	238.35(1)	276.9(8)	226.0(7)	249.3(7)	247.2(8)
0.2	234.7(8)	239.29(8)	275.0(2)	228.4(3)	248.3(6)	247.2(2)
0.3	235.2(1)	239.62(1)	270.9(3)	229.1(3)	247.3(7)	246.2(2)
0.4	234.6(1)	240.09(2)	267.9(4)	228.1(4)	247.2(1)	245.2(3)
0.5	235.1(1)	240.16(1)	263.8(3)	229.0(4)	246.1(1)	244.1(3)
0.6	234.3(2)	240.97(2)	262.9(4)	231.3(4)	245.3(1)	244.3(3)
0.7	234.8(1)	241.07(2)	260.0(4)	233.0(4)	244.5(1)	243.9(3)
0.8	235.2(2)	241.51(3)	256.5(5)	234.8(5)	243.2(2)	243.2(4)
0.9	237.2(2)	240.16(2)	254.0(3)	236.8(3)	244.0(1)	243.4(3)
1.0	238.6(9)	240.24(9)	250.0(9)	239.6(9)	243.6(9)	243.2(9)

Table S3: Selective interatomic bond distances [pm] in the Mn1O₆ and Mn2O₅ polyhedra of the (Bi_{1-x}R_x)₂Mn₄O₁₀ compounds obtained from X-ray powder data Rietveld refinements.

(Bi_{1-x}Nd_x)₂Mn₄O₁₀								
x	Mn(1)O₆				Mn(2)O₅			
	Mn-O(11) 2x	Mn-O(12) 2x	Mn-O(2) 2x	Mean	Mn-O(12) 1x	Mn-O(3) 2x	Mn-O(2) 2x	Mean
0.0	196.5(6)	188.9(6)	191.4(5)	192.3(5)	205.5(8)	190.2(5)	193.5(5)	194.6(6)
0.1	195.9(1)	187.6(9)	192.2(8)	191.9(8)	206.3(4)	188.4(8)	191.9(8)	193.4(9)
0.2	195.4(4)	184.7(9)	191.9(9)	190.7(8)	210.6(7)	187.8(8)	191.4(8)	193.8(9)
0.3	196.6(1)	189.5(9)	193.1(9)	193.1(9)	202.5(5)	189.2(8)	189.3(8)	191.9(9)
0.4	193.8(1)	185.8(9)	194.4(6)	191.4(9)	207.0(5)	189.8(7)	190.5(9)	193.5(9)
0.5	191.0(1)	186.7(9)	191.3(3)	189.7(9)	207.8(5)	192.3(9)	192.4(9)	195.5(9)
0.6	188.9(8)	189.5(8)	190.8(7)	189.7(9)	202.6(2)	188.9(7)	189.9(7)	192.1(8)
0.7	195.3(1)	185.1(8)	191.0(2)	190.5(7)	208.3(2)	189.7(8)	189.4(6)	193.3(4)
0.8	195.3(1)	186.0(5)	194.0(3)	191.8(7)	207.1(5)	188.7(9)	188.7(9)	192.4(7)
0.9	196.5(1)	187.2(5)	191.9(2)	191.8(7)	207.0(4)	189.8(9)	187.1(9)	192.2(7)
1.0	192.2(1)	186.2(9)	192.6(8)	190.3(9)	206.7(8)	188.9(8)	189.2(7)	192.6(8)
(Bi_{1-x}Sm_x)₂Mn₄O₁₀								
0.0	196.5(6)	188.9(6)	191.4(5)	192.3(5)	205.5(8)	190.2(5)	193.5(5)	194.6(6)
0.1	203.5(2)	190.5(9)	191.7(7)	195.2(7)	191.7(6)	192.3(3)	192.5(6)	192.3(7)
0.2	196.1(2)	189.8(7)	193.2(6)	193.1(5)	201.1(9)	191.5(2)	192.3(4)	193.7(5)
0.3	198.8(3)	194.7(8)	193.4(8)	195.6(8)	188.4(5)	193.6(3)	191.0(6)	191.5(8)
0.4	194.9(3)	194.7(6)	193.4(8)	194.4(8)	191.7(5)	192.9(3)	191.5(6)	192.1(8)
0.5	193.3(3)	196.7(6)	192.0(8)	194.0(8)	189.3(5)	192.7(3)	194.1(6)	192.6(8)
0.6	196.9(4)	194.8(5)	192.4(9)	194.7(6)	186.0(2)	195.1(4)	190.9(8)	191.6(9)
0.7	192.1(3)	189.1(9)	191.8(7)	191.1(9)	199.1(5)	192.5(2)	191.8(5)	193.6(7)
0.8	191.5(3)	186.2(9)	193.2(9)	190.3(8)	203.2(5)	193.1(3)	190.5(6)	194.1(8)
0.9	194.3(3)	191.4(9)	193.8(9)	193.2(9)	192.6(2)	195.6(3)	188.8(7)	192.3(8)
1.0	191.3(9)	191.1(7)	193.6(9)	192.0(6)	194.4(9)	194.2(9)	188.1(9)	191.8(7)
(Bi_{1-x}Eu_x)₂Mn₄O₁₀								
0.0	196.5(6)	188.9(5)	191.4(5)	192.3(5)	205.5(8)	190.2(5)	193.5(5)	194.6(6)
0.1	191.5(3)	190.0(7)	191.4(0)	191.0(4)	212.6(9)	188.2(2)	194.1(2)	195.5(5)
0.2	198.3(2)	191.5(7)	191.6(2)	193.8(4)	197.7(9)	191.4(2)	190.4(3)	192.3(5)
0.3	198.1(3)	194.5(9)	191.7(3)	194.8(5)	192.5(7)	191.3(3)	191.0(4)	191.4(6)
0.4	198.9(4)	195.6(6)	191.8(5)	195.4(9)	190.9(7)	192.2(4)	191.6(6)	191.7(7)
0.5	197.5(3)	192.7(6)	191.8(4)	194.0(6)	195.4(2)	190.8(3)	192.3(5)	192.3(7)
0.6	197.4(4)	190.4(5)	191.6(5)	193.1(9)	198.7(7)	191.1(4)	189.7(6)	192.1(7)
0.7	196.4(4)	188.0(9)	191.5(4)	192.0(9)	202.0(7)	190.0(4)	189.3(6)	192.1(6)
0.8	195.9(5)	192.2(7)	191.4(5)	193.2(9)	195.2(2)	189.2(4)	189.3(7)	190.4(9)
0.9	194.4(3)	191.0(9)	191.6(2)	192.3(6)	199.0(6)	187.8(3)	188.9(5)	190.5(7)
1.0	195.4(9)	187.0(5)	191.8(9)	191.4(6)	202.9(3)	188.8(6)	187.6(9)	191.2(8)





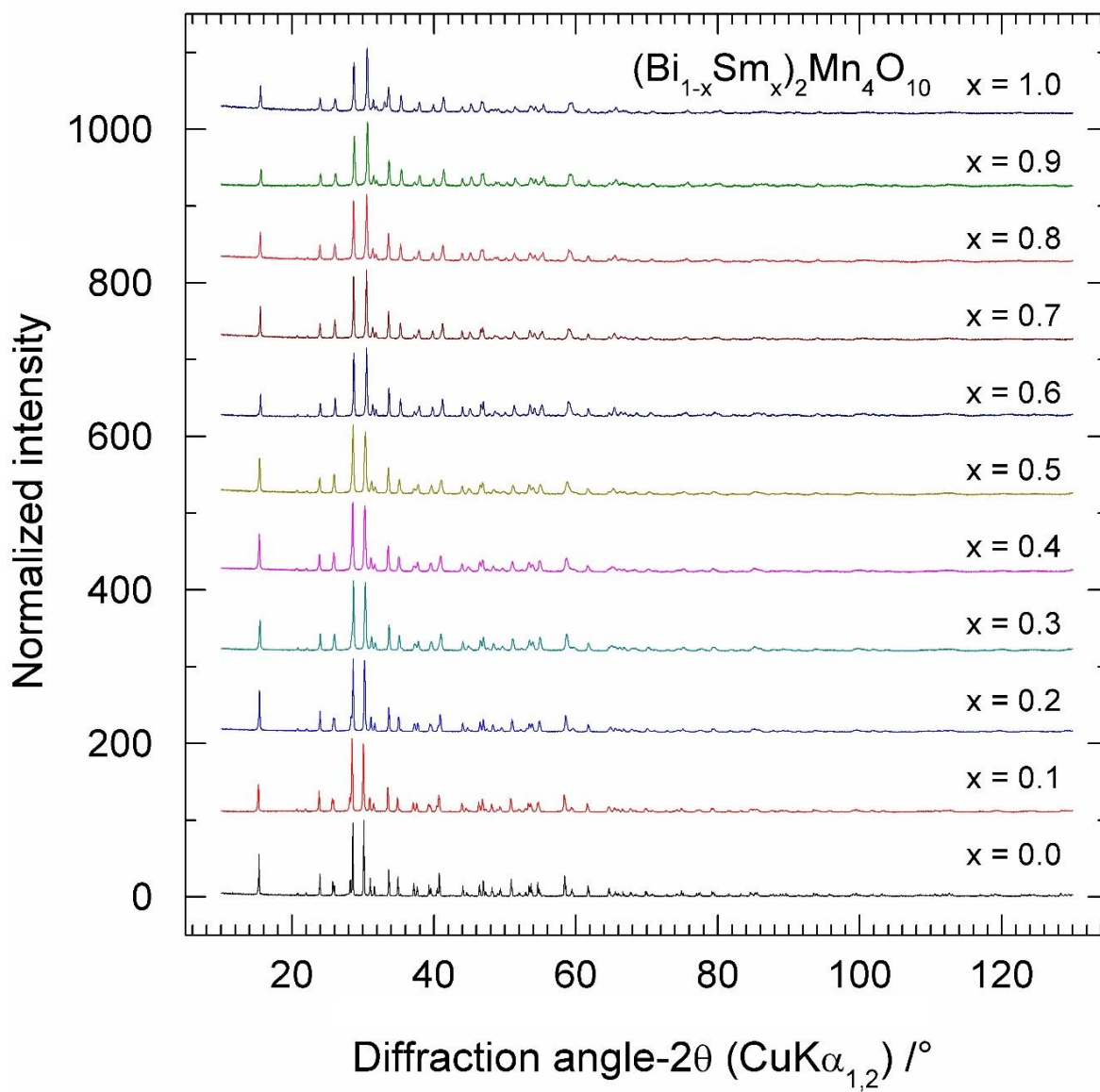


Figure S1: X-ray powder diffraction patterns of $(\text{Bi}_{1-x}\text{R}_x)_2\text{Mn}_4\text{O}_{10}$.

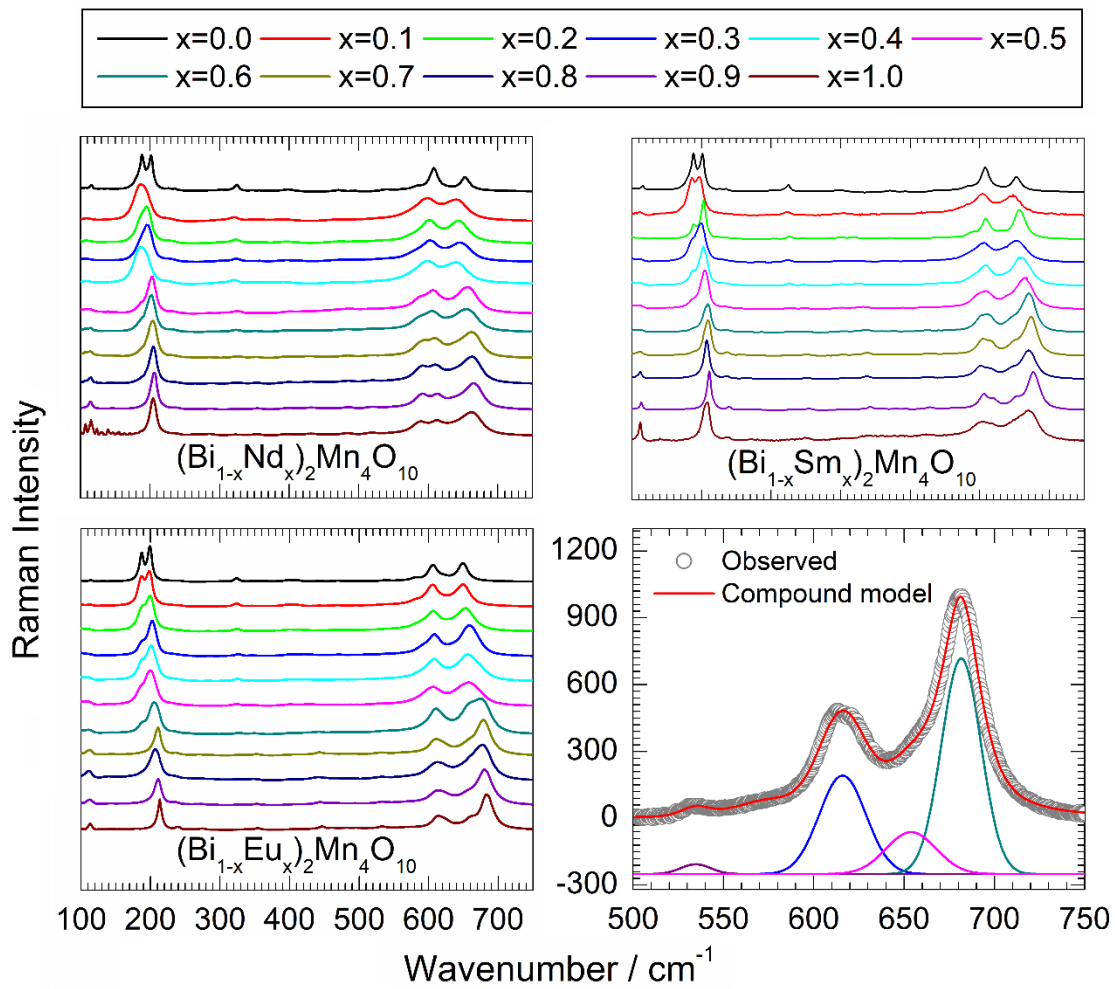


Figure S2: Raman spectra of $(\text{Bi}_{1-x}\text{R}_x)_2\text{Mn}_4\text{O}_{10}$ at ambient condition. A representative fitting of the bands at high frequency region (**right-bottom**).

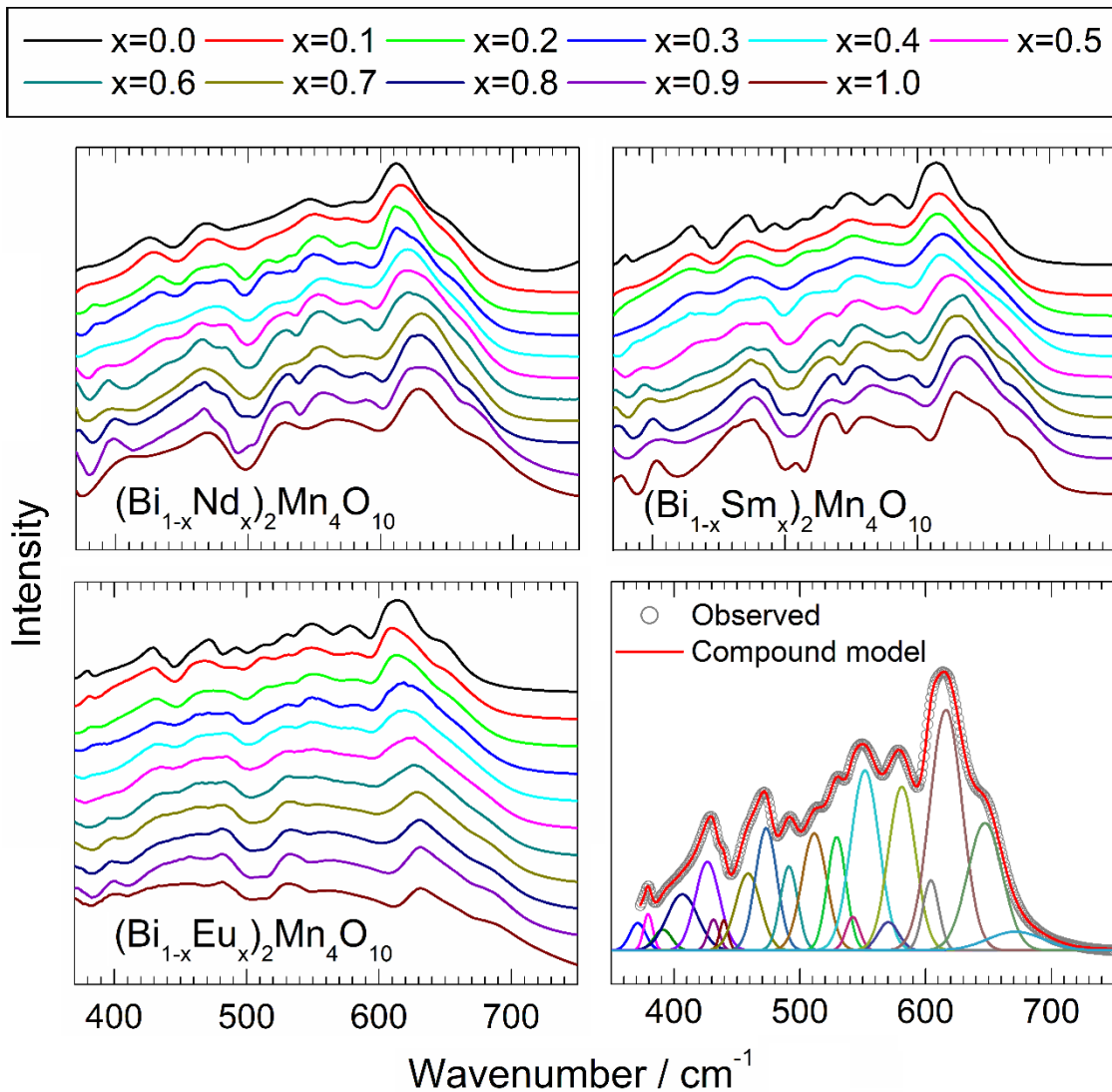


Figure S3: FTIR spectra of $(\text{Bi}_{1-x}\text{R}_x)_2\text{Mn}_4\text{O}_{10}$ at ambient condition. A representative fitting of the bands in the mid-infrared region (**right-bottom**).

Chapter 4

Aluminum to germanium inversion in mullite-type $RAlGeO_5$: characterization of a rare phenomenon for $R = Y, Sm - Lu$

A published paper “Reproduced with permission from The American Ceramic Society”.
<https://ceramics.onlinelibrary.wiley.com/doi/10.1111/jace.18085>. Copy right permission site:
<https://www.wiley.com/network/researchers/latest-content/how-to-clear-permissions-for-a-thesis-or-dissertation>

Kowsik Ghosh^{1#}, M. Mangir Murshed^{1,2*#}, Michael Fischer^{2,3#}, Thorsten M. Gesing^{1,2#}

¹Institute of Inorganic Chemistry and Crystallography, University of Bremen, Faculty of Biology and Chemistry, Leobener Straße 7, D-28359 Bremen, Germany

²MAPEX Center for Materials and Processes, University of Bremen, Bibliothekstraße 1, D-28359 Bremen, Germany

³Crystallography, Faculty of Geosciences, University of Bremen, Klagenfurter Straße 2-4, D-28359 Bremen, Germany

*Corresponding author: e-mail address: murshed@uni-bremen.de, phone: +49 (0)421 218 63144, fax: +49 421 218 63145.

#ORCID:

KG: 0000-0003-2622-7046

MMM: 0000-0002-9063-372X

MF: 0000-0001-5133-1537

TMG: 0000-0002-4119-2219

Abstract

Mullite-type RMn_2O_5 ($R = Y$, rare-earth element) ceramics are of ongoing research attentions because of their interesting crystal-chemical, physical, and thermal properties. We report a detailed structural, spectroscopic and thermal analysis of the series of mullite-type $RAI\text{GeO}_5$ ($R = Y, \text{Sm-Lu}$) phases. Polycrystalline samples are prepared by solid-state synthesis methods. Each sample is characterized by X-ray powder diffraction followed by Rietveld refinements, showing that they are isotypic and crystallize in the space group $Pbam$. The change of the metric parameters is explained in term of the lanthanide contraction effect. A rare inversion of Al/Ge between octahedral and pyramidal sites have been observed for these mullite-type so called O10 compounds, and the inversion parameter found to be between 0.22(1) and 0.30(1) for different R -cations. The $\langle \text{Al/Ge-O} \rangle$ bond distances and their bond valence sums (BVSs) support the respective inversions. Density functional theory (DFT) calculated phonon density of states (PDOS) and electronic band structures are compared for the vibrational and electronic band gap features, respectively. Analysis of UV/Vis absorption spectra using both derivation of absorption spectra fitting (DASF) and Tauc's methods demonstrates that each of the $RAI\text{GeO}_5$ O10 compounds is high bandgap semiconductor, possessing direct transition between 4.1(1) and 5.4(1) eV. Both Raman and Fourier transform infrared spectra show clear red shift (quasi-harmonic) of the vibrational wavenumbers with respect to the ionic radii of the R -cations. Selective Raman bands at higher wavenumber region further complement the inversion of Al/Ge between two coordination sites. The higher decomposition temperature of the $RAI\text{GeO}_5$ compounds, compared to those of RMn_2O_5 phases, is explained in terms of higher bond strength of Al/Ge-O than those of Mn-O. Irrespective to the inversion between Al- and Ge-sites, the decomposition temperature also depends on the type of R -cation in $RAI\text{GeO}_5$.

Introduction

Mullite-type RMn_2O_5 ceramics with $R = \text{Bi}, \text{Y}$ and rare-earth elements crystallize in the DyMn_2O_5 structure type ¹ and, they are well-studied phases for their crystal chemistry^{2, 3, 4}, magnetic ^{2, 4} and ferroelectric ^{5, 6} properties. One of the interesting features of these phases is the existence of two different valence states of manganese and the multiferroic behaviors ^{7, 8}. The crystal structure of DyMn_2O_5 , as shown in **figure 1**, can be described in the orthorhombic space group $Pbam$ ⁷, where the edge-sharing MnO_6 octahedra form infinite chains running parallel to the crystallographic c -axis. These chains are interconnected by double-pyramidal $[\text{Mn}_2\text{O}_2\text{O}_{6/2}]$ building units formed by two edge-sharing MnO_5 tetragonal pyramids (**Fig. 1**). It is well established that the Mn^{4+} cations in $\text{Dy}(\text{Mn}^{3+})(\text{Mn}^{4+})\text{O}_5$ are located in the MnO_6 octahedra and Mn^{3+} in the MnO_5 pyramid ^{6, 9, 10}. Interconnecting three pyramids and two octahedra leads to the formation of manganese 5-ring channels (**Fig. 1**) where the Dy^{3+} cation is located. These Dy^{3+} are coordinated by eight oxygen atoms forming distorted DyO_8 polyhedra linked to each other, building a 4-ring channel (**Fig. 1**). The infinite octahedral chains are the dominant (but not only ³) criterion for mullite-type phases which could be subdivided into so-called O8-phase ^{11, 12, 13, 14} (e.g., PbMBO_4 ^{11, 12, 13, 15, 16, 17} and schafarikites LM_2O_4 ^{18, 19, 20, 21, 22, 23, 24, 25}), O9-phase (e.g., BiMO ^{26, 27, 28, 29, 30, 31, 32, 33, 34, 35, 36, 37, 38} and ABO ^{39, 40, 41, 42, 43, 44}) and O10-phase (e.g., BiMO ^{6, 10, 45, 46}). The DyMn_2O_5 structure type belongs to the O10 phase which differs from the O9 BiMO phases with only an additional oxygen atom. That is, the addition of one oxygen in the double-tetrahedral (M_2O_7) building unit in O9 phase is transformed into a double-pyramidal (M_2O_8) ⁴⁷ unit in the O10 phases.

Substitution of manganese by other transition metal cations allows to unveil some quaternary systems such as $R\text{FeMnO}_5$ ($R = \text{Y}, \text{Ho}, \text{Er}$), where Fe^{3+} locates at the centroid of the MO_5 pyramid and Mn^{4+} at the MO_6 octahedra ^{48, 49, 50}. Moreover, placing suitable candidates in either of the MO_5 , MO_6 and RO_8 polyhedral sites can give rise to a plethora of $RM'M''\text{O}_5$ compounds where the M-cations are not limited only to transition elements. That is,

compounds such as $R\text{CrGeO}_5$ ($R = \text{Nd-Er, Y}$)⁵¹, $R\text{AlGeO}_5$ ($R = \text{Y, Sm, Eu}$)⁵² and ErAlGeO_5 ⁵³ extend the mullite-type O10 family members, replacing the transition metal cation in the octahedra and, in both pyramid and octahedra, respectively.

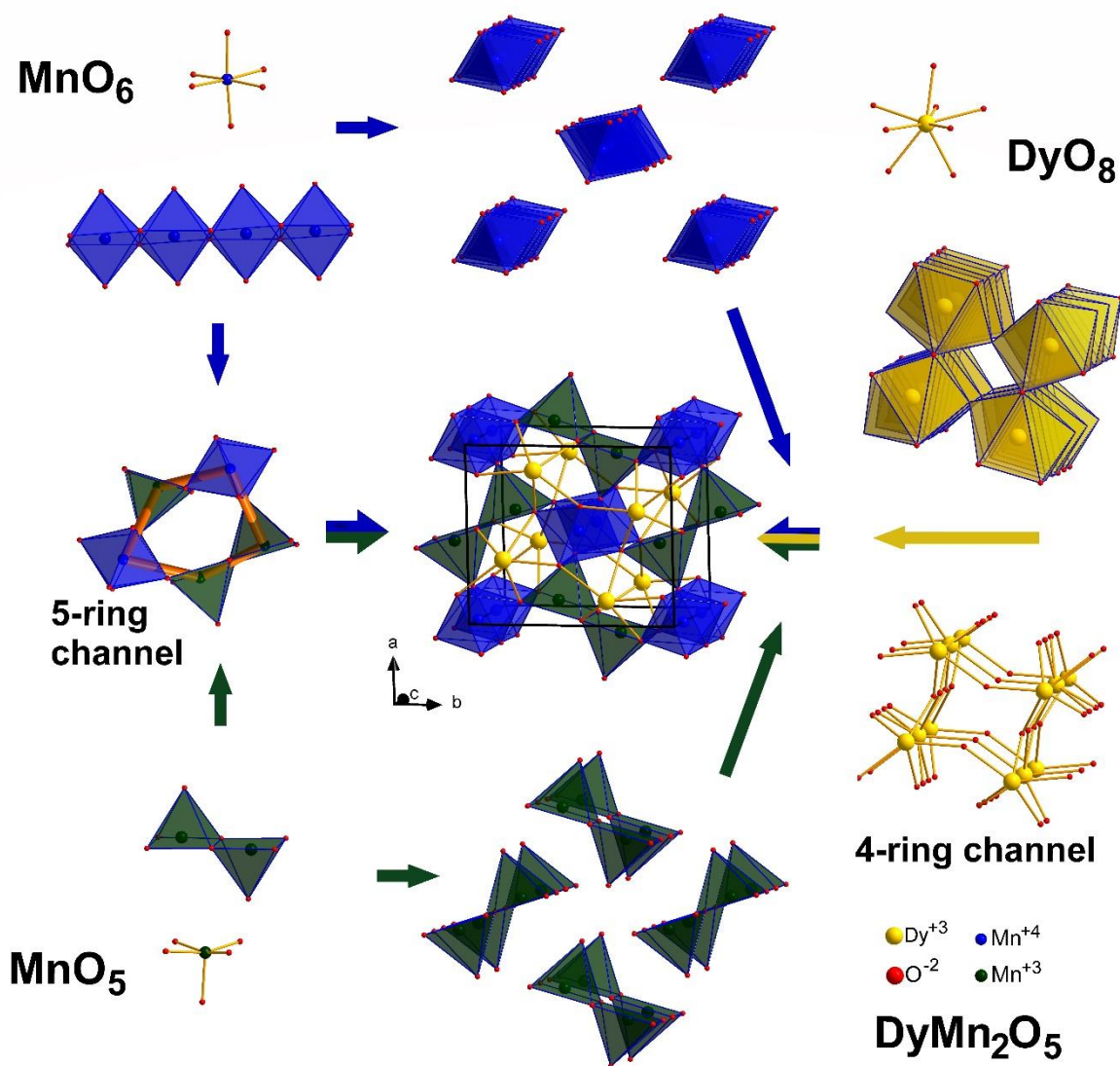


Figure 1: Building units and crystal structure of DyMn_2O_5 , showing the Mn^{4+}O_6 and Mn^{3+}O_5 and DyO_8 coordination and their connectivity.

Due to close ionic radii of Al^{3+} and Ge^{4+} ⁵⁴ and almost similar Al/Ge-O bond distances, the alumogermanates are known to occur as communal minerals^{55, 56, 57, 58} in nature. Moreover, this closeness can lead to positional disorder between them^{59, 60, 61}, leading to influence the physical properties, for instance, of inversion spinels^{62, 63, 64}. As such, Ge/Al disordering

between the MO_5 and MO_6 sites was reported in ErAlGeO_5 ⁵³ where an inversion parameter $x = 0.27(1)$ was found, defined as $\text{Er}^{\text{O}}[\text{Al}_{1-x}\text{Ge}_x]_{\text{P}}[\text{Ge}_{1-x}\text{Al}_x]\text{O}_5$. On the other hand, the difference of one formal valence charge between Al^{3+} and Ge^{4+} combined with their preference to similar coordination can lead to unequal distributions away from the known inversion. This may lead to the possibility of variable charges of the associated R -cations. Therefore, RAlGeO_5 would be an excellent playground to tune the structural charge of the R -cation via Al/Ge distribution in the given polyhedra. Beside a few crystal structures^{52, 53}, details of the physico-chemical properties of these mullite-type compounds remain unexplored. Herein, we represent the synthesis of RAlGeO_5 ($R = \text{Y, Sm- Lu}$) followed by their characterizations using X-ray powder diffraction, Raman, Fourier transform infrared (FTIR) and UV/Vis spectroscopes, and thermogravimetric analysis. YAlGeO_5 is chosen as the lightest (d -block) element for density functional theory (DFT) calculations to better understand the electronic and vibrational properties. Moreover, the theoretical results are compared with those of the experimental observations of the lanthanide (f -block element) containing phases.

2. Experimental

2.1. Synthesis

All RAlGeO_5 ($R = \text{Y, Sm - Lu}$) samples were prepared from the stoichiometric mixtures of respective R_2O_3 (99.99%, Alfa Aesar), $\text{Al}(\text{NO}_3)_3 \cdot 9\text{H}_2\text{O}$ (99.2%, VWR Chemicals) and GeO_2 (99.99%, Alfa Aesar) using the glycerin method. By adding 20 wt.% of glycerin to the stoichiometric quantities of the educts, the mixture was put into a glass beaker and heated at 353 K in an oil bath under magnetic stirring, followed by heating at 473 K in a furnace for about two hours. During the heating process, a dry foam was formed which was crushed into a fine powder, placed in a platinum crucible, and heated at 1473 K for 48 hours in air to obtain the final micro-crystalline products.

2.2. X-ray diffraction

X-ray powder diffraction (XRPD) data were collected on an X'Pert MPD PRO diffractometer (PANalytical GmbH, Almelo, The Netherlands) equipped with an X'Celerator multi-strip detector. The X-ray patterns were collected using Ni-filtered $\text{CuK}_{\alpha 1,2}$ radiation ($\lambda_{\text{K}\alpha 1} = 154.05929(5)$ pm, $\lambda_{\text{K}\alpha 2} = 154.4414(2)$ pm) in Bragg-Brentano geometry. Data were collected at ambient condition from 5 to $85^\circ 2\theta$ with a step width of $0.0167^\circ 2\theta$ and a measurement time of 75 s per step. The obtained data were refined using the Rietveld method (TOPAS V4.2, Bruker AXS) and the fundamental parameter approach was used for profile fitting, where the fundamental parameters were fitted against a standard material (LaB_6). The starting atomic coordinates were taken from the results of the structure refinement published by Bertaut et al.⁶⁵ for BiMn_2O_5 . Parameters like background, sample displacement, metric, profile and atomic positions and displacements were optimized during the Rietveld refinements. In some cases, the isotropic displacement parameters were constrained between co-shared atoms at $4e$ and $4h$ Wyckoff positions. The average crystallite size (ACS) was calculated from all observed X-ray reflections, which is described as $L_{\text{Vol}}(\text{IB})$ by the TOPAS suite. $L_{\text{Vol}}(\text{IB})$ refers to the volume-weighted mean of the coherently diffracted domain size using the integral breadth for the description of the reflection profile. Since the reflection profile is intrinsically associated with the size, shape, distribution and defects (strain) of the domains^{66, 67}, the $L_{\text{Vol}}(\text{IB})$ values throughout this study should be considered as 'apparent' ACS for spherical crystallites with a unimodal distribution. Within the TOPAS facilities, the pseudo-Voigt profile function was deconvoluted into Gaussian and Lorentzian components, describing the ACS ($L_{\text{Vol}}(\text{IB})$) and the micro-strain (ε_0), respectively. $R\text{AlGeO}_5$ samples for $R = \text{Sm}, \text{Tb} - \text{Lu}$ contain a considerable amount of impurities (5 - 10 wt.%) like $R_2\text{Ge}_2\text{O}_7$ and $R_3\text{Al}_5\text{O}_{12}$ ^{68, 69} and were therefore not taken for further spectroscopic and thermogravimetric investigations.

2.3. UV/Vis spectroscopy

Diffuse UV/Vis reflectance spectra were collected on a Shimadzu 2700 UV/Vis spectrophotometer equipped with a UV/Vis DiffuseIR cell (Pike Technologies). Barium sulfate was used for baseline correction. Data were collected in a slow scanning mode from 250 to 850 nm wavelength using 0.5 nm steps. An averaged spectrum was calculated from eight scans for each sample.

2.4. Vibrational spectroscopy

Fourier transform infrared (FTIR) spectra were collected in the mid-infrared range from 370 to 4000 cm^{-1} on a Bruker IFS66v/S spectrometer. The MIR spectrum was collected using the standard KBr method (2 mg of each sample mixed with 200 mg KBr), obtained from 128 scans with a spectral resolution of 2 cm^{-1} . The Raman spectra were recorded on a LabRam ARAMIS (Horiba Jobin Yvon) Micro-Raman spectrometer equipped with three lasers working at 532, 633, and 785 nm and power less than 20mW. A 50 \times objective (Olympus) with a numerical aperture of 0.75 provides a focus spot of less than 2 μm diameter when closing the confocal hole to 200 μm . Each spectrum ranges between 100 and 1000 cm^{-1} with a spectral resolution of approximately 1.2 - 3.2 cm^{-1} using a grating of 1800 grooves/mm and a thermoelectrically cooled CCD detector (Synapse, 1024 \times 256 pixels).

2.5. Thermogravimetry

TGA/DSC measurements were taken on TGA/DSC 3⁺ STARe System of Mettler Toledo. The samples were measured with a heating rate of 10 K/min and a continuous N₂ flow of 20 mL/min from 300 to 1823 K. An amount of 19.8(1) mg of YAlGeO₅, 23.4(1) mg of EuAlGeO₅, and 22.4(1) mg of GdAlGeO₅ powder samples was measured relative to an empty corundum crucible reference. Evaluation of DTA curves were done by “Mettler Toledo STARe Evaluation Software” to get the decomposition temperature, where intercept of two fitting lines of before and after the decomposition treated as the decomposition temperature. A

drift correction to the data was applied using an empty corundum sample crucible measurement.

2.6. Density functional theory (DFT)

To avoid the strongly correlated behaviors of the *f*-elements, DFT calculations were performed on the YAlGeO₅ compound for the electronic and vibrational properties. The CASTEP code⁷⁰ was used for a completely Al/Ge ordered YAlGeO₅ structure, where Al- and Ge-atom are located in the AlO₆ and GeO₅ polyhedra, respectively. To evaluate the effect of the inversion, additional calculations were carried out for which the main-group elements in the polyhedra were exchanged, leading to GeO₆ and AlO₅ polyhedra. These calculations employed the PBEsol exchange-correlation functional⁷¹, on-the-fly generated norm-conserving pseudopotentials, and a cutoff energy of 1200 eV. Both the metric parameters and atomic coordinates were optimized using a 3×3×4 Monkhorst-Pack grid of *k*-points to sample the first Brillouin zone. The optimized metric parameters ($a = 723.0$ pm, $b = 832.0$ pm, $c = 562.0$ pm) are in good agreement with those of the experimental values ($a = 723.1(2)$ pm, $b = 834.2(2)$ pm, $c = 560.2(2)$ pm, see later), giving confidence in the suitability of the approach. Subsequently, the electronic band structure, phonon density of states (PDOS), IR and Raman spectra were computed for the DFT-optimized structures. The linear response method^{72, 73, 74},⁷⁵ was used for the calculations of the phonon properties employing a 3×2×4 grid of *q*-points in the dynamical matrix calculation. The PDOS and partial contributions of the non-equivalent atoms were visualized using a Gaussian broadening of 3.34 cm⁻¹ and normalized in a way that the integral of the total PDOS is equal to unity. For a computational feasibility, rather a smaller *k*-point grid (2×2×3) was used for the calculations of IR and Raman intensity with a broadening of 10 cm⁻¹.

3. Results and discussion

Crystal structure

Using the glycerin method $RAlGeO_5$ ($R = Y, Sm - Lu$) compounds could be successfully synthesized. However, X-ray powder data Rietveld refinements confirmed only $YAlGeO_5$, $EuAlGeO_5$ and $GdAlGeO_5$ were obtained as phase pure.

Table 1: X-ray powder data Rietveld refined structural parameter of $RAlGeO_5$ compounds with the space group of $Pbam$.

GdAlGeO ₅ , $R_{wp} = 2.49$, $R_p = 1.96$, $GOF = 1.19$						
Atom	Site	Occupancy	x	y	z	$U_{iso} / 10^{-4} \text{pm}^2$
Gd	4g	1	0.1403(1)	0.3279(1)	0	0.26(1)
Al/Ge(1)	4e	0.73(1)/0.27(1)	0	0	0.2545(1)	0.29(1)
Ge/Al(2)	4h	0.27(1)/0.73(1)	0.3837(1)	0.1431(1)	½	0.25(1)
O11	4g	1	0.1570(1)	0.0511(1)	0	0.30(1)
O12	4h	1	0.1597(1)	0.0663(1)	½	0.25(1)
O2	8i	1	0.1075(1)	0.7868(1)	0.2621(1)	0.48(1)
O3	4f	1	0	½	0.2914(1)	1.37(1)
YAlGeO ₅ , $R_{wp} = 4.43$, $R_p = 3.41$, $GOF = 1.77$						
Y	4g	1	0.1408(1)	0.3278(1)	0	0.44(1)
Al/Ge(1)	4e	0.72(1)/0.28(1)	0	0	0.2522(1)	0.31(1)
Ge/Al(2)	4h	0.28(1)/0.72(1)	0.3839(1)	0.1432(1)	½	0.42(1)
O11	4g	1	0.1607(1)	0.0537(1)	0	0.39(1)
O12	4h	1	0.1519(1)	0.0672(1)	½	0.250(1)
O2	8i	1	0.1067(1)	0.7884(1)	0.2573(1)	0.61(1)
O3	4f	1	0	½	0.2842(1)	0.73(1)
EuAlGeO ₅ , $R_{wp} = 3.04$, $R_p = 2.38$, $GOF = 1.29$						
Eu	4g	1	0.1406(1)	0.3274(1)	0	0.25(1)
Al/Ge(1)	4e	0.75(1)/0.25(1)	0	0	0.2492(1)	0.27(1)
Ge/Al(2)	4h	0.25(1)/0.75(1)	0.3833(1)	0.1432(1)	½	0.56(1)
O11	4g	1	0.1576(1)	0.0526(1)	0	0.26(1)
O12	4h	1	0.1586(1)	0.0645(2)	½	0.26(1)
O2	8i	1	0.1050(1)	0.7867(1)	0.2605(1)	0.31(1)
O3	4f	1	0	½	0.2955(1)	0.95(1)

For the other samples $R_2Ge_2O_7$ and $R_3Al_5O_{12}$ ^{68, 69} were additionally obtained as much as 10 wt-%. The representative Rietveld refinement plot of $GdAlGeO_5$ is shown in **figure 2** and those of other samples in **figure S1-10** (Supplementary Information). The crystal structural parameters for the pure phases are given in **table 1**, and those of the samples containing additional phases - in **table S1**. The interatomic distances for all phases are shown in **table**

S2. Alike other RMn_2O_5 compounds^{2, 76}, the XRPD data Rietveld refinements confirmed each phase crystallizes in the orthorhombic $DyMn_2O_5$ structure type¹. When the refinements were carried out with fixed and full occupancy of Al and Ge at the $4e$ and $4h$ *Wyckoff* positions, respectively, the isotropic atomic displacement parameters (ADP) appeared either unphysical (negative value) or too large beyond the Lindemann criterion⁷⁷.

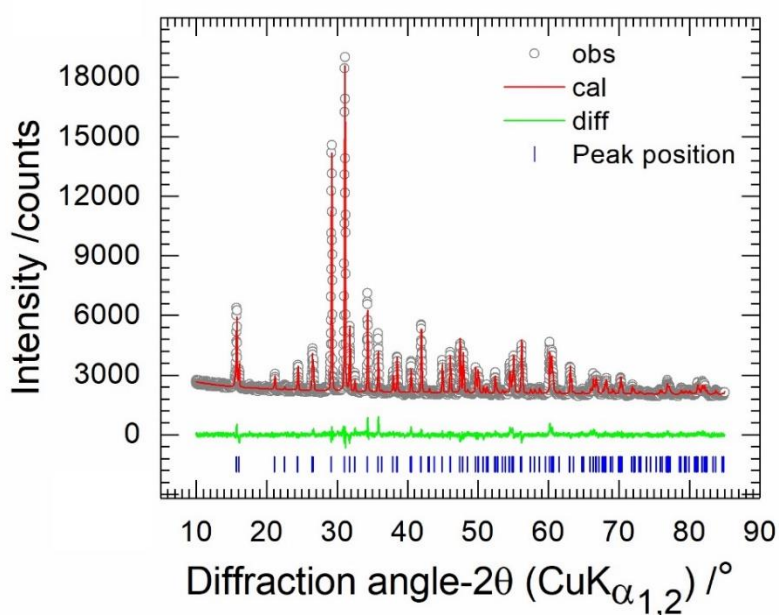
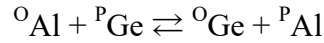


Figure 2: X-ray powder data Rietveld plot of $GdAlGeO_5$ compound.

However, considering a mixed occupancy (Al/Ge) between these two sites, the refinements converged to reliable ADPs (**Tab. 1** & **Tab. S1**), leading to reduce the Rwp from 10 – 12 to 2 – 3 %. Such exchanged occupation of cations on two different sites is well known for spinel phases^{62, 78, 79, 80, 81, 82, 83} as degree of inversion and depends on thermodynamic parameter at least from the synthesis temperature^{78, 79, 82}. As such, considering the degree of inversion to the alumogermanate mullite-type O10 phases, the cation distribution can be treated as a dynamic equilibrium according to the following interchange reaction, where octahedral and pyramidal sites are given as superscripted ‘O’ and ‘P’, respectively:



Deducing an inversion parameter (IP) from this relation would give the structural formula $R^{\circ}[\text{Al}_{1-x}\text{Ge}_x]^{\text{p}}[\text{Ge}_{1-x}\text{Al}_x]\text{O}_5$ with x being the IP value. The refined site occupancy factors of Al and Ge lead to the IP_R for different R-elements of $\text{IP}_Y = 0.28(1)$, $\text{IP}_{\text{Sm}} = 0.22(1)$, $\text{IP}_{\text{Eu}} = 0.25(1)$, $\text{IP}_{\text{Gd}} = 0.27(1)$, $\text{IP}_{\text{Tb}} = 0.26(1)$, $\text{IP}_{\text{Dy}} = 0.25(1)$, $\text{IP}_{\text{Ho}} = 0.27(1)$, $\text{IP}_{\text{Er}} = 0.29(1)$, $\text{IP}_{\text{Tm}} = 0.29(1)$, $\text{IP}_{\text{Yb}} = 0.30(1)$, and $\text{IP}_{\text{Lu}} = 0.30(1)$.

Table 2: Refined metric parameters of $R\text{AlGeO}_5$ phases.

Compound	a/pm	b/pm	c/pm	$V/\text{pm}^3 \times 10^6$
YAlGeO ₅	723.1(2)	834.1(2)	560.2(2)	337.8(1)
SmAlGeO ₅	734.7(1)	843.1(1)	564.7(1)	349.7(1)
EuAlGeO ₅	732.5(2)	841.4(2)	564.1(2)	347.6(2)
GdAlGeO ₅	730.0(2)	840.2(2)	563.3(2)	345.5(2)
TbAlGeO ₅	727.3(1)	837.7(1)	561.9(1)	342.4(1)
DyAlGeO ₅	725.2(2)	835.6(2)	561.2(1)	340.1(2)
HoAlGeO ₅	723.5(1)	834.2(2)	560.5(1)	338.3(1)
ErAlGeO ₅	721.1(2)	832.7(2)	559.8(2)	336.2(2)
TmAlGeO ₅	719.6(1)	830.9(1)	558.8(2)	334.1(1)
YbAlGeO ₅	718.1(1)	829.2(1)	558.4(1)	332.4(1)
LuAlGeO ₅	716.1(1)	828.2(1)	558.0(1)	330.9(1)

The $\text{IP}_{\text{Er}} = 0.27(1)$ remarkably lies close to the inversion parameter for erbium containing phases obtained by Durand *et al.*⁵³ who used a flux method at 1478 K to grow single crystals, which is indeed close to our synthesis condition (1473 K). Whether they represent the thermodynamic saturation⁷⁸ for this structure type requires to be further evaluated. The refined metric parameters are given in **table 2**. Each metric parameter shows almost a linear decrease with the successive decrease of the ionic radius of the rare-earth cation with

increasing atomic number, as shown in **figure 3**. A similar behavior of lanthanide contraction effect^{84, 85} was observed for RMn_2O_5 ⁸⁶ compounds.

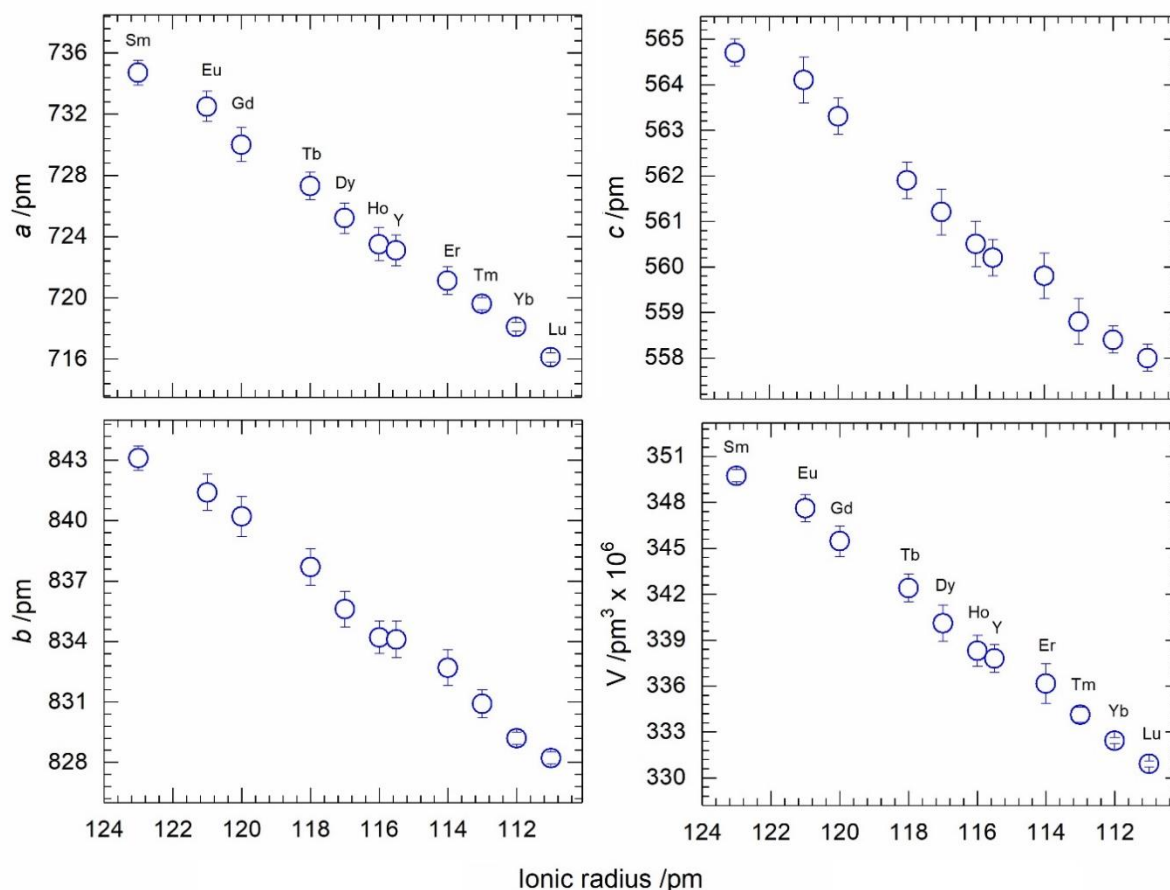


Figure 3: Change in metric parameters of $RAlGeO_5$ with respect to the ionic radius of R^{3+} ($R = Y$ and rare-earth element), represented corresponding to the lanthanide contraction.

The linear trend is persevered even in a solid solution of $(Bi_{1-x}R_x)_2Mn_4O_{10}$ for $R = Sm, Eu$ and Nd ⁴⁶. For a difference of 12 pm of the ionic radius between Sm^{3+} and Lu^{3+} ⁵⁴, the cell volume contracts about 5.4 % for $RAlGeO_5$. For comparison, the cell volume of $EuMn_2O_5$ is about 3 % smaller than that of $BiMn_2O_5$, however, with a comparable difference of about 10.4 pm between the Bi^{3+} and Eu^{3+} cation⁴⁶. The average $R-O$ distances decrease with decreasing R -cation radius in $RAlGeO_5$, in accordance with the lanthanide contraction effect, as shown in **figure 4**, which is comparable to the isotypic mullite-type O10 RMn_2O_5 ⁸⁷ phases. This

corresponds to the behavior of calculated bond-valence sum (BVS) values summarized in **table 3**.

Table 3: Bond valence sum (BVS)/ v.u. and global instability index (GII)/ v.u. of $RAlGeO_5$.

Compound	<i>R</i>	<Al>	<Ge>	GII
YAlGeO ₅	3.01(1)	2.86(1)	3.93(1)	0.08(1)
SmAlGeO ₅	2.96(1)	2.95(1)	4.17(1)	0.13(1)
EuAlGeO ₅	3.11(1)	2.77(1)	3.99(1)	0.10(1)
GdAlGeO ₅	3.09(1)	2.79(1)	4.02(1)	0.09(1)
TbAlGeO ₅	2.94(1)	2.81(1)	3.97(1)	0.09(1)
DyAlGeO ₅	2.81(1)	2.88(1)	4.08(1)	0.11(1)
HoAlGeO ₅	2.99(1)	2.86(1)	4.04(1)	0.07(1)
ErAlGeO ₅	2.81(1)	2.84(1)	4.01(1)	0.11(1)
TmAlGeO ₅	2.93(2)	2.90(1)	4.02(2)	0.06(1)
YbAlGeO ₅	2.83(1)	3.01(1)	4.15(1)	0.10(1)
LuAlGeO ₅	2.92(1)	2.92(1)	4.12(1)	0.09(1)

Al³⁺ is mainly found in octahedral and Ge⁴⁺ - in pyramidal coordination, and the disorder between aluminum and germanium over two different coordination sites leading to the inversion parameters is not a common feature. Disorder of Ge⁴⁺ on tetrahedral and octahedral sites is known in Fe₈Ge₃O₁₈⁸⁸ and Bi₂₆Mo₉GeO₆₈⁸⁹. Recently, Al/Ge ordering in octahedral site is reported in Li_{1+x}Al_xGe_{2-x}(PO₄)₃⁶¹ and mixed M³⁺ and M⁴⁺ occupation on tetrahedral sites was found in sodalites^{90, 91}. Our finding confirms the rarity of mixed occupation of Al³⁺/Ge⁴⁺ over pyramidal and octahedral sites. The average bond distances <Al/Ge-O> in octahedral site (187.2(2) pm, 190.9(2) pm, 191.7(2) pm for YAlGeO₅, GdAlGeO₅ and EuAlGeO₅, respectively) are slightly lower than the sum of ionic radii⁵⁴ with their fractional occupancy: $r(Al^{3+}_{1-x} + Ge^{4+}_x) + r(O^{2-}) = 191.4$ pm, 191.3 pm, and 191.4 pm for GdAlGeO₅, YAlGeO₅ and EuAlGeO₅, respectively.

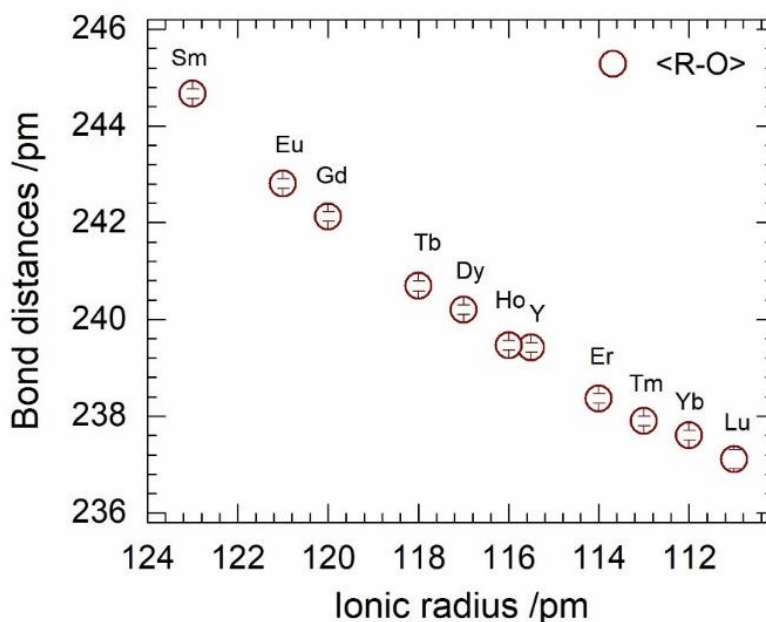


Figure 4: Change in interatomic average R -O bond distances of $RAlGeO_5$ compounds with respect to the ionic radius of R^{3+} ($R = Y$ and rare-earth element), represented corresponding to the lanthanide contraction.

In the similar way, the average bond distances $\langle Ge/Al-O \rangle$ in MO_5 site (184.6(2) pm, 182.8(2) pm and 182.9(2) pm for $YAlGeO_5$, $GdAlGeO_5$ and $EuAlGeO_5$, respectively) are also slightly higher than the sum of ionic radii⁵⁴ with their fractional occupancy: $r(Al^{3+}_{1-x} + Ge^{4+}_x) + r(O^{2-}) = 179.4$ pm for $GdAlGeO_5$ and 179.5 pm and 179.3 pm for $YAlGeO_5$ and $EuAlGeO_5$, respectively. This analogy satisfies the structural bond valence sum of Al (2.86(1), 2.77(1) and 2.79(1) v.u. for $YAlGeO_5$, $GdAlGeO_5$ and $EuAlGeO_5$, respectively) and Ge (3.93(1), 4.02(1) and 3.99(1) for $YAlGeO_5$, $GdAlGeO_5$ and $EuAlGeO_5$, respectively), as given in **table 3**. Clearly, the phases keep the formal valences of Al and Ge during the inversion on two sites. Moreover, the calculated lower global instability index (**Tab.3**)⁹² infers to the absence of intrinsic strains in these $RAlGeO_5$ compounds.

UV/Vis spectroscopy

From UV/Vis reflectance spectroscopic data, as shown in **figure 5** and **figure S11-S12**, calculation of electronic bandgap of a given semiconductor can be expressed as:

$$F(R) = B(h\nu - E_g)^n \quad (1)$$

where $F(R)$ is the Kubelka-Munk absorption calculated from the reflectivity R as $F(R) = (1-R)^2/(2R)$, B is the absorption parameter, h is the Planck's constant, ν is the frequency of light, and E_g is the bandgap energy [eV]. For plotting an expression as $(h\nu)^n$ versus E , n is the nature of transition with $n = 1/2, 2/3, 2$ or 3 for direct allowed, direct forbidden, indirect allowed and indirect forbidden transition, respectively. Nevertheless, it is necessary to know the nature of transition to calculate the electronic bandgap by this relationship. To overcome this difficulty, Souri *et al.*⁹³ came up with the idea for thin layer materials to get rid of the constant transition exponent n by calculating the derivative of the absorption spectrum. Following this procedure, Kirsch *et al.*⁹⁴ demonstrated that the type of bandgap can be estimated also for the powder samples. As such, we use the derivation of absorption spectra fitting method (DASF)⁹⁵:

$$A(\lambda) = D\lambda \left(\frac{1}{\lambda} - \frac{1}{\lambda_g} \right)^n \quad (2)$$

where $D = B(hc)^{n-1}z/2.303$, z is thickness of the reflecting layer, A is the layer absorbance, λ is the wavelength of light, λ_g is the wavelength for corresponding bandgap. Equation (2) can be also expressed as:

$$\frac{d[\ln(A(\lambda)/\lambda)]}{d(1/\lambda)} = \frac{n}{\left(\frac{1}{\lambda} - \frac{1}{\lambda_g} \right)} \quad (3)$$

which further leads to determine the absolute bandgap value $E_g = hc/\lambda_g = 1239.81/\lambda_g$ [eV]. Using the DASF method, the bandgaps E_g of 3.98(4), 4.43(4) and 5.39(4) eV were calculated for $YAlGeO_5$, $EuAlGeO_5$ and $GdAlGeO_5$, respectively. On the other hand, from the Tauc method^{96, 97} resulted in direct transition energies E_d of 4.12(3), 4.55(4), 5.56(6) eV and

indirect transition energies E_i of 3.64(3), 4.30(5) and 5.19(3) eV for YAlGeO_5 , EuAlGeO_5 and GdAlGeO_5 , respectively. The closeness between the E_g and E_d values suggests that the electronic bandgap arises from the respective direct transition. The experimental bandgap energy of YAlGeO_5 , calculated for an ordered structure (superscript O and I for the inverted structure), is in excellent agreement with ${}^{\text{O}}E_g^{\text{DFT}} = 4.0(1)$ eV calculated by DFT using the PBEsol functional. A separate DFT calculation using the hybrid HSE06 functional⁹⁸ provided a band gap of about 5.9 eV, which is, however, far away from our experimental value, and was not considered for comparison. From the DFT-PBEsol band structure, as shown in **figure 6**, it is also clear that direct transition occurs at the Brillouin zone center of $\text{Y}^{\text{O}}[\text{Al}]^{\text{I}}[\text{Ge}]\text{O}_5$.

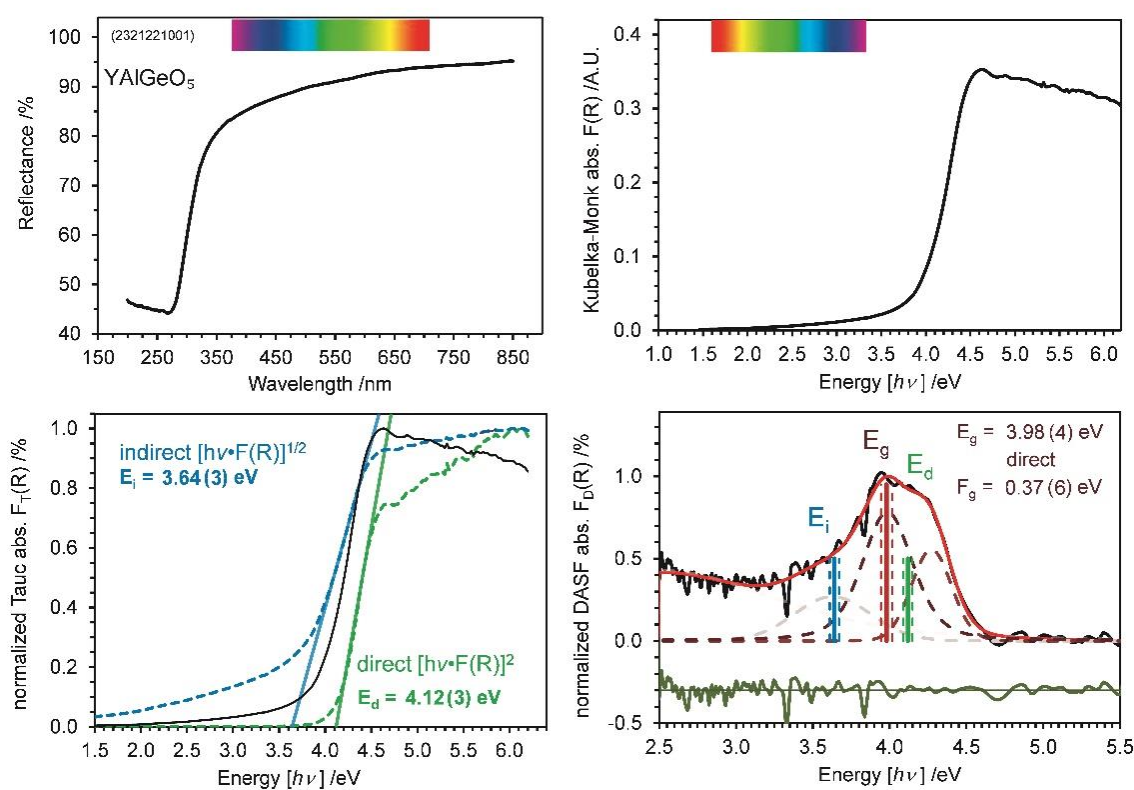


Figure 5: Measured reflectance (top left) and calculations absorbance spectrum (top right) of YAlGeO_5 , and bandgap energies (E_g) determined using the DASF methods (bottom right) and Tauc analysis for direct (E_d) and indirect (E_i) transition (bottom left).

The calculated bandgap energy of the counterpart inverted $Y^O[Ge]^P[Al]O_5$ phase shifted slightly to higher ${}^I E_g^{\text{DFT}}$ value of 4.1(1) eV. Of notes, in this case the bandgap is no longer direct (**Fig. 6**) as the valence band maximum shifts away from the zone-center. Since, the associated valence band is almost flat, the indirect nature of the transition requires to be resolved with high-resolution experimental data. Looking to the absorption spectrum of the measured sample (**Fig. 5**), a separation of two transitions could hardly be seen. The same is true while evaluating the bandgap energies for indirect and direct transitions using the Tauc method. Opposite, using the DASF method⁹⁴, a second transition peak could clearly be seen in the DASF plot (**Fig. 5**). The peak fitting analysis led to transition energies of ${}^O E_g = 3.98(4)$ eV and ${}^I E_g = 4.27(4)$ eV and full width at half maximum values of ${}^O F_g = 0.37(6)$ eV and ${}^I F_g = 0.29(6)$ eV for the ordered and inverted structure contributions, respectively. Fitting the area of the two different transition peaks results in ratio of 68(4) % to 32(4) % for the ordered and inverted structures, respectively, which lies close to the inversion parameter $IP_Y = 0.28(1)$ obtained from X-ray diffraction.

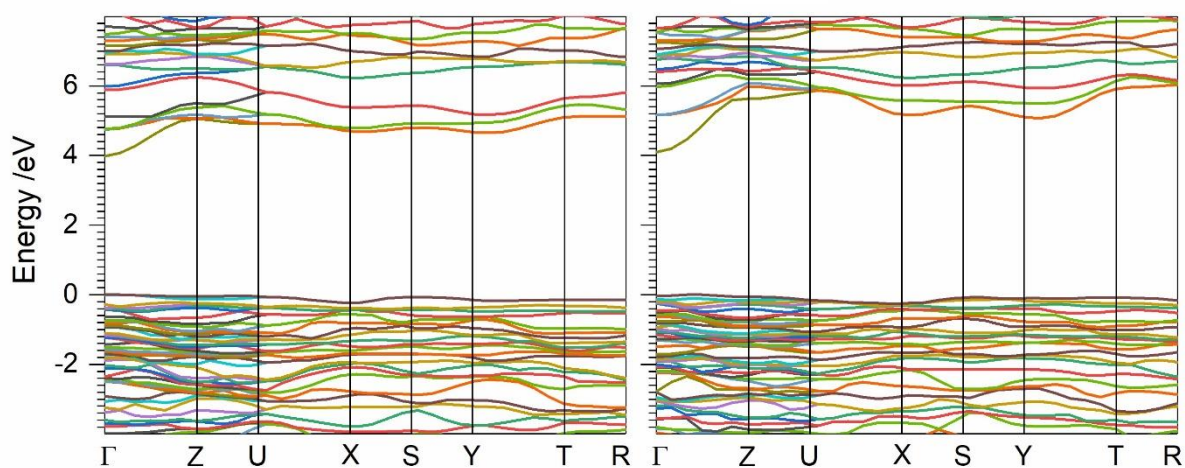


Figure 6: Electronic band structure at some high-symmetry directions of $YAIGeO_5$ compounds, where the Al and Ge atoms are placed in the $4e$ and $4h$ *Wyckoff* positions, respectively (left) and the respective dispersion for the inverted structure (right) with Ge and Al atoms are in the $4e$ and $4h$ *Wyckoff* positions, respectively.

While resolving two different transitions using the DASF method, which is rather impossible using the Tauc method, it is not surprising, that the obtained $E_d = 4.12(3)$ is slightly higher than that of the order phase of ${}^0E_g = 3.98(4)$ eV as the bandgap of the inverted structure of ${}^1E_g = 4.27(4)$ eV has to be concomitantly considered. Although DFT calculations show that for the latter case a flat-band indirect transition takes place, the experimental data tend more to have direct transitions of both contributing parts of the ordered and inverted structure contribution.

Vibrational spectroscopy

Since the fluorescence emissions is susceptible for 4f-4f transitions, Raman spectra were collected using three different lasers (532 nm, 633 nm, and 785 nm), as shown in **figure S13**, to distinguish between the electronic and phononic bands. The zone center IR and Raman wavenumbers calculated by the DFT are given in **table S3**. Moreover, the DFT calculated PDOS, as shown in **figure 7**, demonstrates that the highest possible first-order Raman frequency at 0 K is limited by about 900 cm^{-1} . Thus, Raman spectra collected by 633 nm laser for YAlGeO_5 , GdAlGeO_5 , and 785 nm laser for EuAlGeO_5 depict only the first-order vibrational features, as shown in **figure S14**. Factor group analysis predicts 96 modes ($13A_{1g} + 13B_{1g} + 11B_{2g} + 11B_{3g} + 9A_{1u} + 9B_{1u} + 15B_{2u} + 15B_{3u}$), where 48 modes are Raman active ($13A_{1g} + 13B_{1g} + 11B_{2g} + 11B_{3g}$), 36 are infrared active ($8B_{1u} + 14B_{2u} + 14B_{3u}$). $B_{1u} + B_{2u} + B_{3u}$ represent the acoustic modes and all nine A_{1u} modes are optically silent. Fitting the Raman spectra, neglecting different contributions from the ordered and inverted structural appearance, however, requires only 26 Pseudo-Voigt peaks for each compound. A comparison between the modes observed at 300 K and those calculated for 0 K calculated modes depict the same number of spectral intensity (peaks) assuming negligible quasi-harmonic effects in the spectral region of interest, as shown in **figure 7**. The partial PDOS (**Fig. 7**) assigns that the

vibrational contributions of the *R*-cations are limited over the low-frequency region ($< 300 \text{ cm}^{-1}$). Although Ge atoms contribute to the whole wavenumber range, the high intensity center lies at around 200 cm^{-1} . The Al- and light oxygen contribution can be seen elsewhere throughout the whole PDOS (**Fig. 7**). The experimental Raman shift mainly contributes with most intensive peaks in three regions: low-frequency region ($< 250 \text{ cm}^{-1}$), frequency region between $680\text{-}820 \text{ cm}^{-1}$ and high-frequency region ($> 820 \text{ cm}^{-1}$), as pointed out (**Fig. 7**). The low-frequency is contributed by *R*-cation, as seen in PDOS (dot line indicator) (**Fig. 7**) and the fitted peaks (**Fig. S15**) at lower region show red shift due to longer $\langle R\text{-O} \rangle$ bond lengths (**Fig. S15**). The peak near at 860 cm^{-1} , as seen in PDOS, is assigned to be contributed by Ge and O12 atoms (dash-dot line) that connects between octahedra and pyramid. Therefore, it is conceivable that the peak at the high-frequency region arises from the Ge-O12 vibrational feature as Ge-O12 is the smallest bond distance (**Tab. S2**) in the MO_5 pyramid. Two experimental Raman peaks at $680 - 800 \text{ cm}^{-1}$ (**Fig. 8**) can be explained by the contribution of Al (dash line), Ge (dash-dot line) and O2 (solely oxygen atom in octahedral site) as supported by the PDOS (**Fig. 7**).

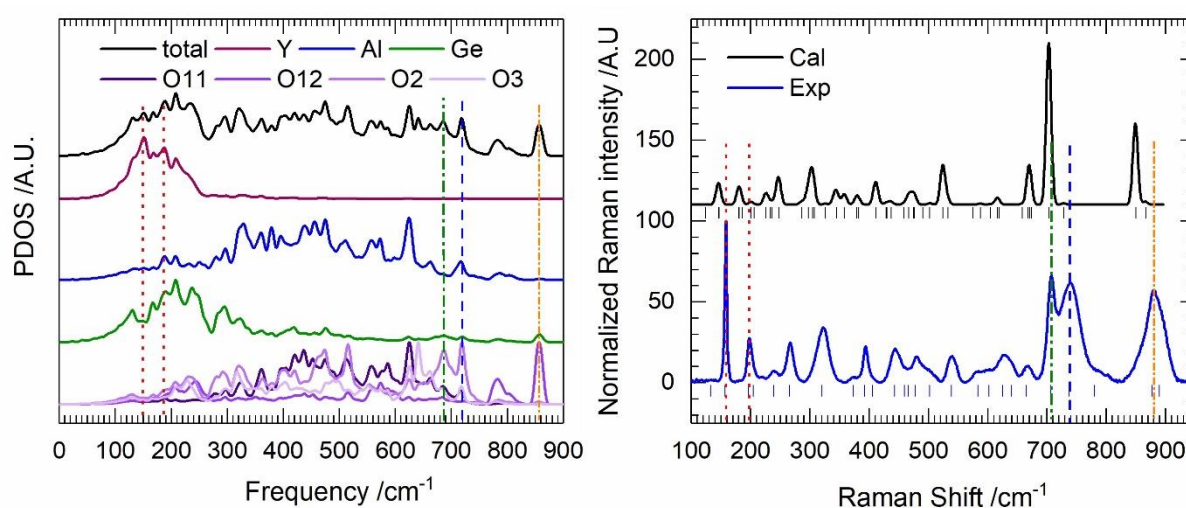


Figure 7: Calculated PDOS and its component contributions (left), and comparison between the calculated (0 K) and the experimental (300 K) Raman spectra (right) of YAlGeO_5

compound. The vertical dotted, dashed and dash-dotted lines indicate *R*-, Al- and Ge-atom, respectively.

Taking the bond distances and mass of the elements into account, peaks at 710 cm^{-1} and 740 cm^{-1} can be assigned to the stretching of Ge-O2 and Al-O2 (**Fig. 8**), respectively.

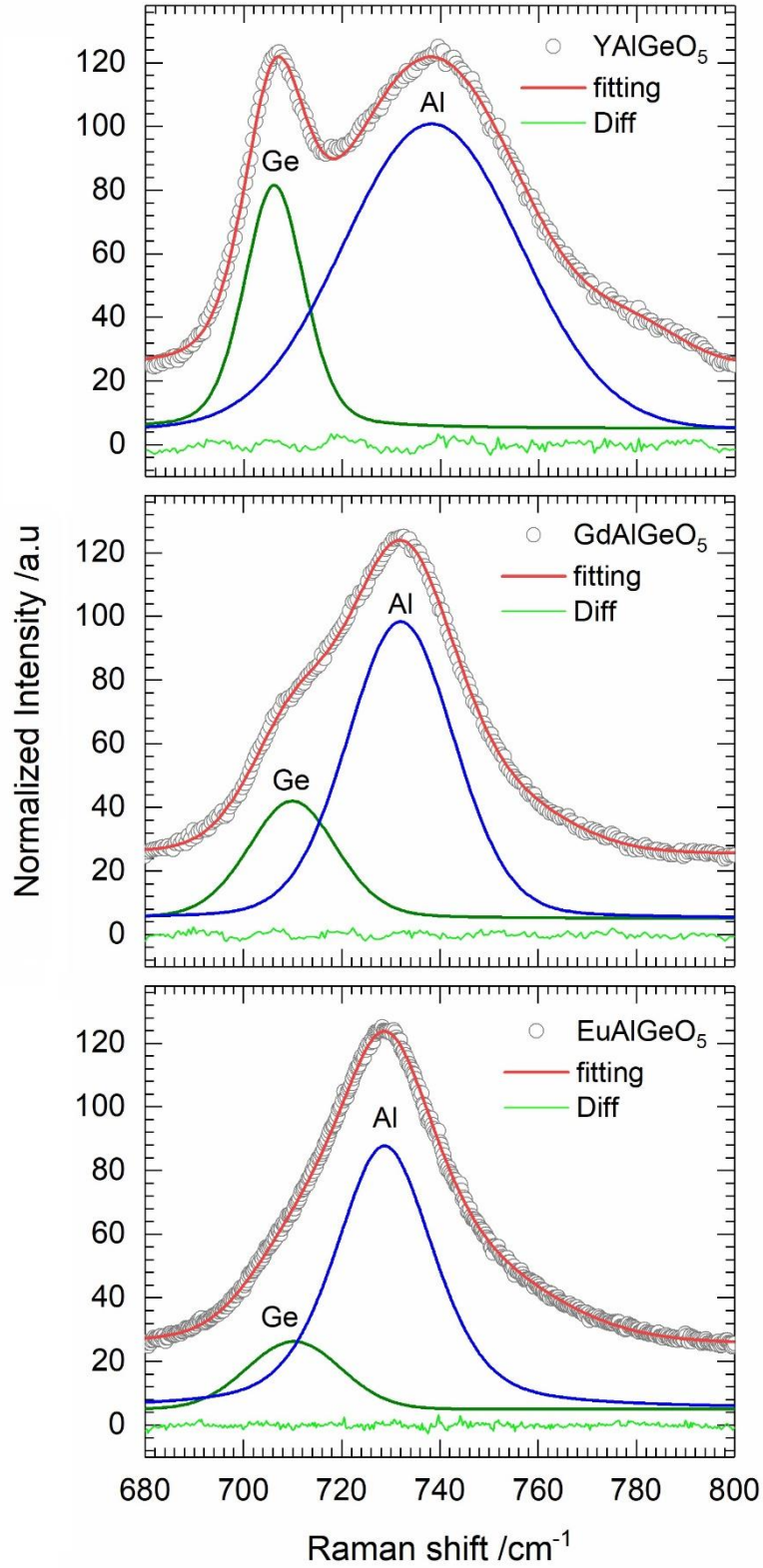


Figure 8: Raman peak fitting in the high-frequency region of $R\text{AlGeO}_5$ compounds.

Assuming that their differential Raman cross section be similar, the calculated ratio of area (0.32(1), 0.29(1) and 0.26(1) for GdAlGeO_5 , YAlGeO_5 and EuAlGeO_5 , respectively) under

the peaks are comparable with the Ge/Al occupancy ratio (0.37(1), 0.37(1) and 0.33(1) for GdAlGeO₅, YAlGeO₅ and EuAlGeO₅, respectively) in the octahedral sites. These findings further complement the XRD results for the inversion of Al and Ge on the octahedra and pyramidal sites. Since all our investigated phases comprise of centrosymmetric space group, the Raman active modes are IR inactive and vice versa. We therefore, also collected infrared spectra at ambient condition. **Figure S16** represents a comparative view between the IR spectra of RAlGeO₅, R = Y, Eu, Gd with DFT calculated peak positions (**Tab. S3**). A representative peak fitting model for R = Gd is shown in **figure S17**, and the fit parameters are given in **table S4**. Each spectrum requires seventeen bands, which is comparable with our previous report for RMn₂O₅ phases⁴⁶. As also observed in Raman spectra for the quasi-harmonic effect, a global red shift is seen in the infrared spectra due to the bigger ionic radii of the R-cations. The combined vibrational features of Raman and FTIR spectra of the centrosymmetric system certainly represents the Kieffer's PDOS^{99, 100} spectrum of the O10 phases.

Thermal analyses

Thermogravimetric analysis and respective DTA curves, as shown in **figure 9**, are the first thermal analysis of these alumogermanate RAlGeO₅ phases. Within the same structure type, BiMn₂O₅ compounds are known to decompose into Bi₂O₃ and Mn₃O₄ components whereas RMn₂O₅ - into RMnO₃ perovskite and Mn₃O₄⁴⁶. Unlike either BiMn₂O₅ or RMn₂O₅, the thermal decomposition of RAlGeO₅ compounds show higher weight loss of about 27.5(2), 13.0(2) and 21.0(2) % for YAlGeO₅, EuAlGeO₅ and GdAlGeO₅, respectively. In heating mode, the onset temperature for the first inflection was identified as the decomposition temperature of 1668(5), 1605(5) and 1662(5) K for YAlGeO₅, EuAlGeO₅ and GdAlGeO₅, respectively (**Fig. 9**). The decomposition temperatures are higher than those of BiMn₂O₅ and RMn₂O₅ phases⁴⁶, which can be explained in terms of higher bond strength value of Ge - O

(659.4 ± 12.6 kJ/mol) and Al - O (511 ± 3 kJ/mol) than that of Mn - O (402.9 ± 41.8 kJ/mol)¹⁰¹. As such, the similar decomposition temperature of YAlGeO₅ and GdAlGeO₅ can be explained in terms of their almost identical R - O bond strength¹⁰¹ of 719.6 ± 11.3 kJ/mol for R = Y and 719 ± 10 kJ/mol for R = Gd and the decomposition of EuAlGeO₅ at lower temperature due to the lower Eu - O bond strength of 479 ± 10 kJ/mol¹⁰¹.

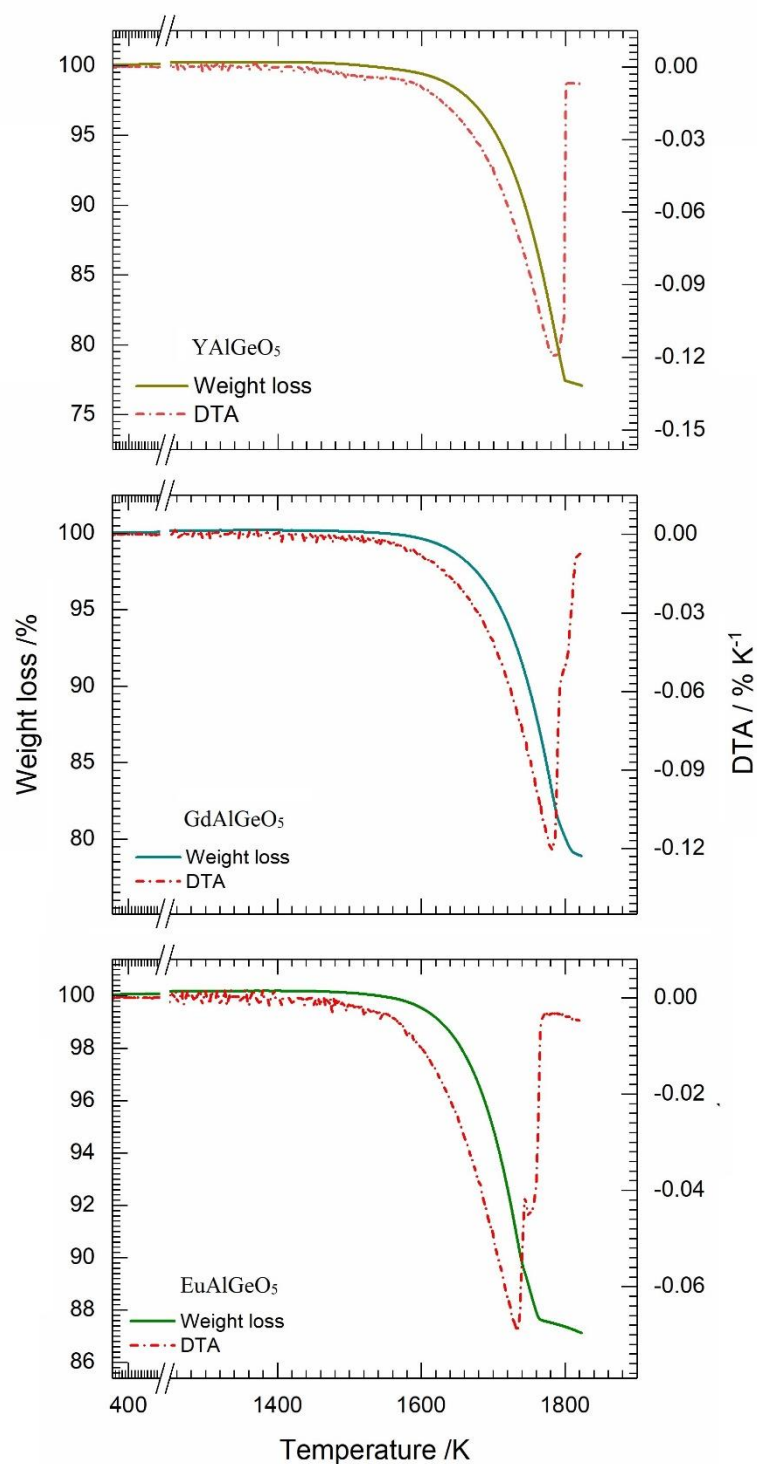


Figure 9: Thermogravimetric analysis of $RA\text{GeO}_5$ compounds.

Conclusion

The exchange of two differently charged cations on two different crystallographic positions was defined as inversion in 1947 by Verwey et al.¹⁰² for Fe_3O_4 and some iron spinel phases. Since then it is still a quite rare phenomenon, mainly reported for iron, cobalt or manganese spinels, where the cations are disordered between octahedrally and tetrahedrally coordinated cation sites in AB_2O_4 type $^{\text{T}}[\text{A}_{1-x}\text{B}_x]^{\text{O}}[\text{A}_x\text{B}_{2-x}]^{\text{O}_4}$ compounds. As the inversion has a direct influence on the physical properties of spinel phases¹⁰², a similar correlation could be assumed for the $RA\text{GeO}_5$ mullite-type O_{10} phases. Although the phase stability is mostly influenced by the bond strength of $R - \text{O}$ the global instability index demonstrates that the inversion of Al^{3+} with Ge^{4+} crystallizes the stable $R^{\text{O}}[\text{Al}_{1-x}\text{Ge}_x]^{\text{P}}[\text{Ge}_{1-x}\text{Al}_x]^{\text{O}_5}$ phases. UV/Vis spectral analysis demonstrated that the presence of inversion influences the bandgap energies. That is, placing Ge on the Al position widens the bandgap and the bandgap can be tuned with respect to the degree of inversion of these mullite-type phases.

References

1. S. C. Abrahams and J. L. Bernstein, "Crystal structure of paramagnetic DyMn_2O_5 at 298 K," *J Chem Phys*, 46[10] 3776 (1967).
2. J. A. Alonso, M. T. Casais, M. J. Martínez-Lope, J. L. Martínez, and M. T. Fernández-Díaz, "A structural study from neutron diffraction data and magnetic properties of RMn_2O_5 (R = La, rare earth)," *Journal of Physics: Condensed Matter*, 9[40] 8515-26 (1997).
3. R. X. Fischer, "The mullite-type family of crystal structure," *Wiley-VCH, Weinheim* 1-46 (2005).
4. L. M. Volkova and D. V. Marinin, "Crystal chemistry aspects of the magnetically induced ferroelectricity in TbMn_2O_5 and BiMn_2O_5 ," *Journal of Physics: Condensed Matter*, 21[1] 015903 (2009).
5. Z. H. Sun, B. L. Cheng, S. Dai, K. J. Jin, Y. L. Zhou, H. B. Lu, Z. H. Chen, and G. Z. Yang, "Effect of Ce substitution on magnetic and dielectric properties of BiMn_2O_5 ," *Journal of Applied Physics*, 99[8] 084105 (2006).
6. F. Ziegler, L. Köhler, H. GIBHARDT, T. M. Gesing, M. M. Murshed, O. Sobolev, A. Piovano, and G. Eckold, "Characterization of Multiferroic $\text{Bi}_2\text{Mn}_4\text{O}_{10}$ by Dielectric and Neutron Spectroscopy," *Physica Status Solidi B-Basic Solid State Physics*, 256[7] 7 (2019).
7. I. Kagomiya, K. Kohn, and T. Uchiyama, "Structure and Ferroelectricity of RMn_2O_5 ," *Ferroelectrics*, 280 131-43 (2011).

8. J. van den Brink and D. I. Khomskii, "Multiferroicity due to charge ordering," *Journal of Physics: Condensed Matter*, 20[43] 434217 (2008).
9. M. L. Ninh Nguyen, Annie Ducouret, Bernard Raveau, "Distribution of Mn³⁺ and Mn⁴⁺ species between octahedral and square pyramidal sites in Bi₂Mn₄O₁₀ -type structure," *Journal of Materials Chemistry*, 9 731-34 (1999).
10. F. Ziegler, M. M. Murshed, H. Gibhardt, O. Sobolev, T. M. Gesing, and G. Eckold, "Mechanical properties of multiferroic Bi₂Mn₄O₁₀: Full set of elastic constants determined by inelastic neutron scattering," *Physica Status Solidi B-Basic Solid State Physics*, 253[5] 976-82 (2016).
11. T. M. Gesing, C. B. Mendive, M. Curti, D. Hansmann, G. Nenert, P. E. Kalita, K. E. Lipinska, A. Huq, A. L. Cornelius, and M. M. Murshed, "Structural properties of mullite-type Pb(Al_{1-x}Mn_x)BO₄," *Zeitschrift Fur Kristallographie-Crystalline Materials*, 228[10] 532-43 (2013).
12. M. Gogolin, M. M. Murshed, M. Ende, R. Miletich, and T. M. Gesing, "Uniaxial negative thermal expansion in the mullite- and borax-type PbAlBO₄ polymorphs," *Journal of Materials Science*, 55[1] 177-90 (2020).
13. M. M. Murshed and T. M. Gesing, "Lattice thermal expansion of mullite-type PbMBO₄ for M = Al, Ga, Fe and Mn," *Acta Crystallographica a-Foundation and Advances*, A68 s195 (2012).
14. M. M. Murshed, C. B. Mendive, M. Curti, G. Nenert, P. E. Kalita, K. Lipinska, A. L. Cornelius, A. Huq, and T. M. Gesing, "Anisotropic lattice thermal expansion of PbFeBO₄: A study by X-ray and neutron diffraction, Raman spectroscopy and DFT calculations," *Materials Research Bulletin*, 59 170-78 (2014).
15. M. M. Murshed, G. Nenert, and T. M. Gesing, "Crystal structure of mullite-type PbMn_{0.5}Al_{0.5}BO₄ determined by combined X-ray and neutron diffraction data," *Zeitschrift Fur Kristallographie-New Crystal Structures*, 227[3] 285-86 (2012).
16. H. Park, J. Barbier, and R. P. Hammond, "Crystal structure and polymorphism of PbAlBO₄," *Solid State Sciences*, 5 565-71 (2003).
17. H. Park, R. Lam, J. E. Greedam, and J. Barbier, "Synthesis, crystal structure, crystal chemistry, and magnetic properties of PbMBO₄ (M = Cr, Mn, Fe): A new structure type exhibiting one-dimensional magnetism," *Chemistry of Materials*, 15 1703-12 (2003).
18. A. Byström and A. Westgren, "Crystal Structure of Pb₃O₄ and SnPb₂O₄," *Arkiv for Kemi Mineralogi Och Geologi*, B16 1-7 (1943).
19. R. Fischer and F. Pertlik, "Verfeinerung der Kristallstruktur des Schafarzikits, FeSb₂O₄," *Tschermaks Mineralogische Und Petrographische Mitteilungen*, 22 206 (1975).
20. J. A. Gonzalo, D. E. Cox, and G. Shirane, "The Magnetic Structure of FeSb₂O₄," *Physical Review*, 147[2] 415-18 (1966).
21. S. T. Gross, "The Crystal Structure of Pb₃O₄," *Journal of American Chemical Society*, 65 1107 (1943).
22. F. Pertlik, "Zur Synthese von Kristallen von CuAs₂O₄ (Trippkeit) und Cu₂As₃O₆CH₃COO," *Z. anorg. allg. Chem.*, 436 201-06 (1977).
23. L. Tokody, "Beiträge zur Kenntnis der kristallographischen und physikalischen eigenschaften des Schafarzikits," *Zeitschrift Fur Kristallographie*, 62 123 (1925).
24. H. T. Witteveen, "Magnetic susceptibility of NiAs₂O₄ and NiSb₂O₄," *Solid State Communications*, 9 1313-15 (1971).
25. J. Zemann, "Formel und Kristallstruktur des Schafarzikits," *Tschermaks mineralogische und petrographische Mitteilungen*, 2 166-75 (1951).
26. M. Burianek, M. Muhlberg, M. Woll, M. Schmucker, T. M. Gesing, and H. Schneider, "Single-crystal growth and characterization of mullite-type orthorhombic Bi₂M₄O₉ (M = Al³⁺, Ga³⁺, Fe³⁺)," *Crystal Research and Technology*, 44[10] 1156-62 (2009).

27. M. Curti, A. Kirsch, L. I. Granone, F. Tarasi, G. López-Robledo, D. W. Bahnemann, M. M. Murshed, T. M. Gesing, and C. B. Mendive, "Visible-light photocatalysis with mullite-type $\text{Bi}_2(\text{Al}_{1-x}\text{Fe}_x)_4\text{O}_9$: Striking the balance between bandgap narrowing and conduction band lowering," *ACS Catalysis*, 8[9] 8844-55 (2018).
28. R. X. Fischer, H. Schneider, and T. M. Gesing, "Temperature-dependent X-ray diffraction studies of mullite-type $(\text{Bi}_{1-x}\text{Sr}_x)_2\text{M}_4\text{O}_9$ phases," *Acta Crystallographica a-Foundation and Advances*, 65 232 (2009).
29. T. M. Gesing, R. X. Fischer, M. Burianek, M. Mühlberg, T. Debnath, C. H. Ruscher, J. Ottinger, J. C. Buhl, and H. Schneider, "Synthesis and properties of mullite-type $(\text{Bi}_{1-x}\text{Sr}_x)_2((\text{M}^1_{1-y}\text{M}^2_y)_4\text{O}_{9-x})$ ($\text{M} = \text{Al}, \text{Ga}, \text{Fe}$)," *Journal of the European Ceramic Society*, 31[16] 3055-62 (2011).
30. T. M. Gesing, M. Schowalter, C. Weidenthaler, M. M. Murshed, G. Nenert, C. B. Mendive, M. Curti, A. Rosenauer, J. C. Buhl, H. Schneider, and R. X. Fischer, "Strontium doping in mullite-type bismuth aluminate: a vacancy investigation using neutrons, photons and electrons," *Journal of Materials Chemistry*, 22[36] 18814-23 (2012).
31. T. F. Krenzel, J. Schreuer, T. M. Gesing, M. Burianek, M. Mühlberg, and H. Schneider, "Thermal expansion and elastic properties of mullite-type $\text{Bi}_2\text{Ga}_4\text{O}_9$ and $\text{Bi}_2\text{Fe}_4\text{O}_9$ single crystals," *International Journal of Materials Research*, 103[4] 438-48 (2012).
32. M. M. Murshed and T. M. Gesing, "Anisotropic thermal expansion and anharmonic phonon behavior of mullite-type $\text{Bi}_2\text{Ga}_4\text{O}_9$," *Materials Research Bulletin*, 48[9] 3284-91 (2013).
33. M. M. Murshed, C. B. Mendive, M. Curti, M. Sehovic, A. Friedrich, M. Fischer, and T. M. Gesing, "Thermal expansion of mullite-type $\text{Bi}_2\text{Al}_4\text{O}_9$: A study by X-ray diffraction, vibrational spectroscopy and density functional theory," *Journal of Solid State Chemistry*, 229 87-96 (2015).
34. M. M. Murshed, G. Nenert, M. Burianek, L. Robben, M. Mühlberg, H. Schneider, R. X. Fischer, and T. M. Gesing, "Temperature-dependent structural studies of mullite-type $\text{Bi}_2\text{Fe}_4\text{O}_9$," *Journal of Solid State Chemistry*, 197 370-78 (2013).
35. S. Ohmann, P. Fielitz, L. Dorrer, G. Borchardt, T. M. Gesing, R. X. Fischer, C. H. Ruscher, J. C. Buhl, K. D. Becker, and H. Schneider, "Electrical conductivity of mullite-type $\text{Bi}_2\text{Al}_4\text{O}_9$ ceramics in air," *Solid State Ionics*, 211 46-50 (2012).
36. H. Schneider, R. X. Fischer, T. M. Gesing, J. Schreuer, and M. Mühlberg, "Crystal chemistry and properties of mullite-type $\text{Bi}_2\text{M}_4\text{O}_9$: An overview," *International Journal of Materials Research*, 103[4] 422-29 (2012).
37. S. U. Weber, T. Gesing, J. Röder, F. J. Litterst, R. X. Fischer, and K. D. Becker, "Temperature-dependent Fe-57 Mossbauer spectroscopy and local structure of mullite-type $\text{Bi}_2(\text{Fe}_x\text{Al}_{1-x})_4\text{O}_9$ ($0.1 \leq x \leq 1$) solid solutions," *International Journal of Materials Research*, 103[4] 430-37 (2012).
38. S. U. Weber, T. M. Gesing, G. Eckold, R. X. Fischer, F. J. Litterst, and K. D. Becker, "Temperature-dependent Fe-57 Mossbauer spectroscopy and local structure of the mullite-type $\text{Bi}_2(\text{Fe}_x\text{Ga}_{1-x})_4\text{O}_9$ ($0.1 \leq x \leq 1$) solid solution," *Journal of Physics and Chemistry of Solids*, 75[3] 416-26 (2014).
39. R. X. Fischer, V. Kahlenberg, D. Voll, K. J. D. MacKenzie, M. E. Smith, B. Schnetger, H. J. Brumsack, and H. Schneider, "Crystal structure of synthetic $\text{Al}_4\text{B}_2\text{O}_9$: A member of the mullite family closely related to boralsilite," *American Mineralogist*, 93[5-6] 918-27 (2008).
40. K. Hoffmann, T. J. N. Hooper, M. M. Murshed, O. Dolotko, Z. Revay, A. Senyshyn, H. Schneider, J. V. Hanna, T. M. Gesing, and R. X. Fischer, "Formation, stability and crystal structure of mullite-type $\text{Al}_{6-x}\text{B}_x\text{O}_9$," *Journal of Solid State Chemistry*, 243 124-35 (2016).
41. K. Hoffmann, T. J. N. Hooper, H. Zhao, U. Kolb, M. M. Murshed, M. Fischer, H. Luhrs, G. Nenert, P. Kudejova, A. Senyshyn, H. Schneider, J. V. Hanna, T. M. Gesing, and R. X.

- Fischer, "Crystal chemical characterization of mullite-type aluminum borate compounds," *Journal of Solid State Chemistry*, 247 173-87 (2017).
42. K. Hoffmann, M. M. Murshed, R. X. Fischer, H. Schneider, and T. M. Gesing, "Synthesis and characterization of mullite-type $(Al_{1-x}Ga_x)_4B_2O_9$," *Zeitschrift Fur Kristallographie-Crystalline Materials*, 229[10] 699-708 (2014).
43. H. S. Zhao, K. Hoffmann, Y. Krysiak, B. Barton, H. Schneider, T. M. Gesing, R. X. Fischer, and U. Kolb, "Structural investigation of mullite-type $Al_4B_2O_9$ by electron diffraction," *Acta Crystallographica a-Foundation and Advances*, 72 S430-S30 (2016).
44. H. S. Zhao, Y. Krysiak, K. Hoffmann, B. Barton, L. Molina-Luna, R. B. Neder, H. J. Kleebe, T. M. Gesing, H. Schneider, R. X. Fischer, and U. Kolb, "Elucidating structural order and disorder phenomena in mullite-type $Al_4B_2O_9$ by automated electron diffraction tomography," *Journal of Solid State Chemistry*, 249 114-23 (2017).
45. M. Burianek, T. F. Krenzel, M. Schmittner, J. Schreuer, R. X. Fischer, M. Muhlberg, G. Nenert, H. Schneider, and T. M. Gesing, "Single crystal growth and characterization of mullite-type $Bi_2Mn_4O_{10}$," *International Journal of Materials Research*, 103[4] 449-55 (2012).
46. K. Ghosh, M. M. Murshed, and T. M. Gesing, "Synthesis and characterization of $(Bi_{1-x}R_x)_2Mn_4O_{10}$: structural, spectroscopic and thermogravimetric analyses for $R = Nd, Sm$ and Eu ," *Journal of Materials Science*, 54[21] 13651-59 (2019).
47. M. Curti, T. M. Gesing, M. M. Murshed, T. Bredow, and C. B. Mendive, "Liebau density vector: a new approach to characterize lone electron pairs in mullite-type materials," *Zeitschrift Fur Kristallographie-Crystalline Materials*, 228[12] 629-34 (2013).
48. A. Muñoz, J. A. Alonso, M. J. Martínez-Lope, and J. L. Martínez, "Synthesis, structural, and magnetic characterization of a new ferrimagnetic oxide: $YFeMnO_5$," *Chemistry of Materials*, 16[21] 4087-94 (2004).
49. A. Muñoz, J. A. Alonso, M. J. Martínez-Lope, and J. L. Martínez, "Synthesis and study of the crystallographic and magnetic structure of the ferrimagnetic oxide $ErFeMnO_5$," *Physical Review B*, 72[18] 184402 (2005).
50. A. Muñoz, J. A. Alonso, M. J. Martínez-Lope, and J. L. Martínez, "Synthesis and study of the crystallographic and magnetic structure of $HoFeMnO_5$," *European Journal of Inorganic Chemistry*, 2007[14] 1972-79 (2007).
51. R. V. Shpanchenko, A. A. Tsirlin, E. S. Kondakova, E. V. Antipov, C. Bougerol, J. Hadermann, G. van Tendeloo, H. Sakurai, and E. Takayama-Muromachi, "New germanates $RCrGeO_5$ ($R = Nd-Er, Y$): Synthesis, structure, and properties," *Journal of Solid State Chemistry*, 181[9] 2433-41 (2008).
52. O. Jarchow, K. H. Klaska, and M. Werk, "Erste Seltene Erden-Aluminium-Germanate vom Typ $REAlGeO_5$," *Naturwissenschaften*, 68[2] 92 (1981).
53. A. Durand, O. Mentre, F. Abraham, T. Fukuda, and B. Elouadi, "Crystal structure of $ErAlGeO_5$ and evidence of a peculiar double coordination sphere of Al(III) and Ge(IV) cations," *Solid State Sciences*, 8[2] 155-61 (2006).
54. R. D. Shannon, "Revised effective ionic radii and systematic studies of interatomic distances in halides and chalcogenides," *Acta Crystallogr A*, A32[5] 751-67 (1976).
55. J. Barbier and M. E. Fleet, "Investigation of phase-relations in the $(Na,K)AlGeO_4$ system," *Physics and Chemistry of Minerals*, 16[3] 276-85 (1988).
56. S. Kume and T. Matsumoto, "Dense form of germanate orthoclase ($KAlGe_3O_8$)," *Journal of Geophysical Research*, 71[20] 4999-5000 (1966).
57. T. Malcherek, M. A. Charoenter, H. Kroll, and E. K. H. Salje, "Cation ordering in $BaAl_2Ge_2O_8$ -feldspar : implications for the I1-C1 phase transition in anorthite," *Physics and Chemistry of Minerals*, 26[4] 354-66 (1999).
58. M. Wolfgang Friedrich, Y. Vojdan-Shemshadi, and H. Pentinghaus, "Transmission electron microscopic study of antiphase domains in $CaAl_2Ge_2O_8$ -feldspar," *Physics and Chemistry of Minerals*, 14[3] 235-37 (1987).

59. M. C. Gordillo and C. P. Herrero, "Al, Ge ordering in aluminogermanate sodalites - a Monte-Carlo study," *Journal of Physics and Chemistry of Solids*, 55[11] (1994).
60. T. Malcherek, H. Kroll, and E. K. H. Salje, "Al,Ge cation ordering in BaAl₂Ge₂O₈-feldspar: monodomain ordering kinetics," *Physics and Chemistry of Minerals*, 27[3] 203-12 (2000).
61. M. Weiss, D. A. Weber, A. Senyshyn, J. Janek, and W. G. Zeier, "Correlating transport and structural properties in Li_{1+x}Al_xGe_{2-x}(PO₄)₃ (LAGP) prepared from aqueous solution," *ACS Appl Mater Interfaces*, 10[13] 10935-44 (2018).
62. L. I. Granone, A. C. Ulpe, L. Robben, S. Klimke, M. Jahns, F. Renz, T. M. Gesing, T. Bredow, R. Dillert, and D. W. Bahnemann, "Effect of the degree of inversion on optical properties of spinel ZnFe₂O₄," *Physical Chemistry Chemical Physics*, 20[44] 28267-78 (2018).
63. E. C. O'Quinn, J. Shamblin, B. Perlov, R. C. Ewing, J. Neufeind, M. Feygenson, I. Gussev, and M. Lang, "Inversion in Mg_{1-x}Ni_xAl₂O₄ spinel: New insight into local structure," *Journal of American Chemical Society*, 139[30] 10395-402 (2017).
64. U. Schmocker and F. Waldner, "The inversion parameter with respect to the space group of MgAl₂O₄ spinels," *J. Phys. C: Solid State Phys.*, 9 L235 (1976).
65. E. F. Bertaut, G. Buisson, S. Quezel-Ambrunaz, and G. Quezel, "Structure magnetique et proprietes magnetiques de BiMn₂O₅," *Solid State Communications*, 5[1] 25-30 (1967).
66. D. Balzar, "Voigt-function model in diffraction line-broadening analysis," *Microstructure Analysis from Diffraction* 44 (1999).
67. D. Balzar, N. Audebrand, M. R. Daymond, A. Fitch, A. Hewat, J. I. Langford, A. Le Bail, D. Louer, O. Masson, C. N. McCowan, N. C. Popa, P. W. Stephens, and B. H. Toby, "Size-strain line-broadening analysis of the ceria round-robin sample," *Journal of Applied Crystallography*, 37[6] 911-24 (2004).
68. G. F. Clark, B. K. Tanner, and B. M. Wanlyn, "X-ray topographic assessment of fluxgrown crystals of rare earth germanates (R₂Ge₂O₇)," *Journal of Materials Science*, 15 1328 (1980).
69. Y. Kuwano, K. Suda, N. Ishizawa, and T. Yamada, "Crystal growth and properties of (Lu,Y)₃Al₅O₁₂," *Journal of Crystal Growth*, 260[1-2] 159-65 (2004).
70. S. J. Clark, M. D. Segall, C. J. Pickard, P. J. Hasnip, M. J. Probert, K. Refson, and M. C. Payne, "First principles methods using CASTEP," *Zeitschrift Fur Kristallographie*, 220[5-6] 567-70 (2005).
71. J. P. Perdew, A. Ruzsinszky, G. I. Csonka, O. A. Vydrov, G. E. Scuseria, L. A. Constantin, X. Zhou, and K. Burke, "Restoring the density-gradient expansion for exchange in solids and surfaces," *Physical Review Letters*, 100[13] 136406 (2008).
72. X. Gonze, "First-principles responses of solids to atomic displacements and homogeneous electric fields: Implementation of a conjugate-gradient algorithm," *Physical Review B*, 55[16] 10337-54 (1997).
73. X. Gonze and C. Lee, "Dynamical matrices, born effective charges, dielectric permittivity tensors, and interatomic force constants from density-functional perturbation theory," *Physical Review B*, 55[16] 10355-68 (1997).
74. D. Porezag and M. R. Pederson, "Infrared intensities and Raman-scattering activities within density-functional theory," *Physical Review B* 54[11] 7830-36 (1996).
75. K. Refson, P. R. Tulip, and S. J. Clark, "Variational density-functional perturbation theory for dielectrics and lattice dynamics," *Physical Review B*, 73[15] 155114 (2006).
76. A. Muñoz, J. A. Alonso, M. T. Casais, M. J. Martínez-Lope, J. L. Martínez, and M. T. Fernández-Díaz, "Magnetic structure and properties of BiMn₂O₅ oxide: A neutron diffraction study," *Physical Review B*, 65[14] 144423 (2002).
77. F. A. Lindemann, "The calculation of molecular vibration frequencies," *Phys. Zeitschrift*, 11 609-12 (1910).

78. A. Navrotsky and O. J. Kleppa, "The thermodynamics of cation distributions in simple spinels," *Journal of Inorganic and Nuclear Chemistry*, 29[11] 2701-04 (1967).
79. H. S. Oneill, "Temperature dependence of the cation distribution in zinc ferrite (ZnFe_2O_4) from powder XRD structural refinements," *Eur. J. Mineral.*, 4[3] 571-80 (1992).
80. K. Petrov, L. Markov, R. Ioncheva, and P. Rachev, "Zinc-cobalt oxide spinels with precursor-controlled degree of inversion," *Journal of Materials Science*, 23[1] 181-84 (1988).
81. V. Šepelák and K. D. Becker, "Comparison of the cation inversion parameter of the nanoscale milled spinel ferrites with that of the quenched bulk materials," *Materials Science and Engineering: A*, 375-377 861-64 (2004).
82. Z. J. Zhang, Z. L. Wang, B. C. Chakoumakos, and J. S. Yin, "Temperature dependence of cation distribution and oxidation state in magnetic Mn-Fe ferrite nanocrystals," *Journal of American Chemical Society*, 120[8] 1800-04 (1998).
83. J. Ziolkowski, "The morphological diagram of spinels," *Journal of Solid State Chemistry*, 121[2] 388-93 (1988).
84. T. Barth and G. lunde, "Der Einfluss der Lanthanidenkontraktion auf die Gitterdimensionen der kubischen Platinmetalle," *Zeitschrift für Physikalische Chemie*, 117U[1] 478-90 (1925).
85. S. Siekierski, "The shape of the lanthanide contraction as reflected in the changes of the unit cell volumes, lanthanide radius and the free energy of complex formation," *Journal of Inorganic and Nuclear Chemistry*, 33[2] 377-86 (1971).
86. J. A. Alonso, M. T. Casais, M. J. Martínez-Lope, and I. Rasines, "High oxygen pressure preparation, structural refinement, and thermal behavior of RMn_2O_5 (R = La, Pr, Nd, Sm, Eu)," *Journal of Solid State Chemistry*, 129[1] 105-12 (1997).
87. M. Tachibana, K. Akiyama, H. Kawaji, and T. Atake, "Lattice effects in multiferroic RMn_2O_5 (R = Sm–Dy,Y)," *Physical Review B*, 72[22] 224425-25 (2005).
88. V. Agafonov, A. Kahn, D. Michel, and M. P. Y. Jorba, "Structural Investigation of a New Iron Germanate $\text{Fe}_8\text{Ge}_3\text{O}_{18}$," *Journal of Solid State Chemistry*, 62[3] 397-401 (1986).
89. B. Bastide, S. Villain, R. Enjalbert, and J. Galy, "Oxygen diffusion pathway in the anionic conductor $\text{Bi}_{26}\text{Mo}_9\text{GeO}_{68}$," *Solid State Sciences*, 4[5] 599-608 (2002).
90. T. M. Gesing, "Structure and properties of tecto-gallosilicates. I. Hydrosodalites and their phase transitions," *Zeitschrift für Kristallographie*, 215[9] 510-17 (2000).
91. I. Poltz, L. Robben, J. C. Buhl, and T. M. Gesing, "Synthesis and crystal structure of body-centered gallogermanate chloride / hydrate sodalite," *Z. Kristallor.-Cryst. Mater. Supl.*, 33 75 (2013).
92. I. D. Brown, "Modeling the Structures of La_2NiO_4 ," *Zeitschrift Fur Kristallographie*, 199[3-4] 255-72 (1992).
93. D. Souri and Z. E. Tahan, "A new method for the determination of optical band gap and the nature of optical transitions in semiconductors," *Applied Physics B*, 119[2] 273-79 (2015).
94. A. Kirsch, M. M. Murshed, M. Schowalter, A. Rosenauer, and T. M. Gesing, "Nanoparticle precursor into polycrystalline $\text{Bi}_2\text{Fe}_4\text{O}_9$: An evolutionary investigation of structural, morphological, optical, and vibrational properties," *Journal of Physical Chemistry C*, 120[33] 18831-40 (2016).
95. M. Teck, M. M. Murshed, M. Schowalter, N. Lefeld, H. K. Grossmann, T. Grieb, T. Hartmann, L. Robben, A. Rosenauer, L. Madler, and T. M. Gesing, "Structural and spectroscopic comparison between polycrystalline, nanocrystalline and quantum dot visible light photo-catalyst Bi_2WO_6 ," *Journal of Solid State Chemistry*, 254 82-89 (2017).
96. J. Tauc, R. Grigorovici, and A. Vancu, "Optical properties and electronic structure of amorphous germanium," *Physica status solidi B*, 15[2] 627-37 (1966).
97. J. Tauc and A. Menth, "States in the gap," *Journal of Non-Crystalline Solids*, 8-10[C] 569-85 (1972).

98. A. V. Krukau, O. A. Vydrov, A. F. Izmaylov, and G. E. Scuseria, "Influence of the exchange screening parameter on the performance of screened hybrid functionals," *The Journal of Chemical Physics*, 125[22] 224106 (2006).
99. S. W. Kieffer, "Thermodynamics and lattice vibrations of minerals: 1. Mineral heat capacities and their relationships to simple lattice vibrational models," *Reviews of Geophysics and Space Physics*, 17[1] 1-19 (1979).
100. S. W. Kieffer, "Thermodynamics and lattice vibrations of minerals: 4. Application to chain and sheet silicates and orthosilicates," *Reviews of Geophysics and Space Physics*, 18[4] 862-86 (1980).
101. D. R. Lide, "CRC handbook of chemistry and physics," *CRC Press. Boca Raton, FL* (2005).
102. E. J. Verwey, P. W. Haayman, and F. C. Romeijn, "Physical properties and cation arrangement of oxides with spinel structures II. Electronic conductivity," *The Journal of Chemical Physics*, 15[4] 181-87 (1947).

Acknowledgement

KG gratefully thanks the University of Bremen for the financial supports. MF is indebted to Andreas Lüttge and Rolf Arvidson for generous access to the Asgard cluster for CASTEP calculations.

Supporting Information

X-ray powder data Rietveld plot of $RAI\text{GeO}_5$ compound for $R = \text{Eu, Sm, Tb, Dy, Ho, Er, Tm, Yb}$ and Lu .

UV/Vis diffuse reflectance spectra of $RAI\text{GeO}_5$ compounds together with Tauc and DASF analyses for bandgap calculations.

Raman and FTIR spectra of $RAI\text{GeO}_5$ compounds and representative peak fittings and fit parameters

Structural parameter and interatomic bond distances of $RAI\text{GeO}_5$ compounds.

Notes

The authors declare no competing financial interest.

Supplementary Information

Aluminum to germanium inversion in mullite-type $RAlGeO_5$: characterization of a rare phenomenon for $R = Y, Sm - Lu$

Kowsik Ghosh^{1#}, M. Mangir Murshed^{1,2*#}, Michael Fischer^{2,3#}, Thorsten M. Gesing^{1,2#}

¹Institute of Inorganic Chemistry and Crystallography, University of Bremen, Faculty of Biology and Chemistry, Leobener Straße 7, D-28359 Bremen, Germany

²MAPEX Center for Materials and Processes, University of Bremen, Bibliothekstraße 1, D-28359 Bremen, Germany

³Crystallography, Faculty of Geosciences, University of Bremen, Klagenfurter Straße 2-4, D-28359 Bremen, Germany

*Corresponding author: e-mail address: murshed@uni-bremen.de, phone: +49 (0)421 218 63144, fax: +49 421 218 63145.

#ORCID:

KG: 0000-0003-2622-7046

MMM: 0000-0002-9063-372X

MF: 0000-0001-5133-1537

TMG: 0000-0002-4119-2219

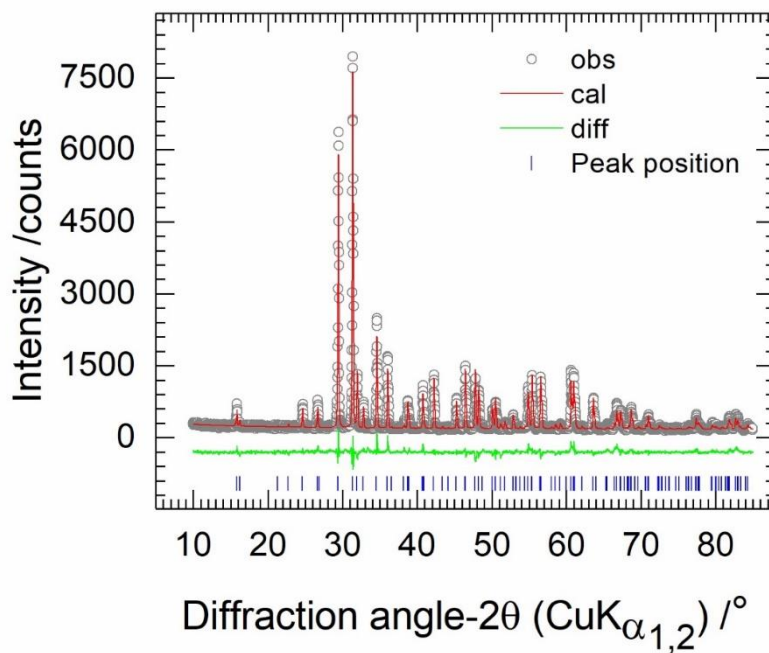


Figure S1: X-ray powder data Rietveld plot of YAAlGeO₅ compound.

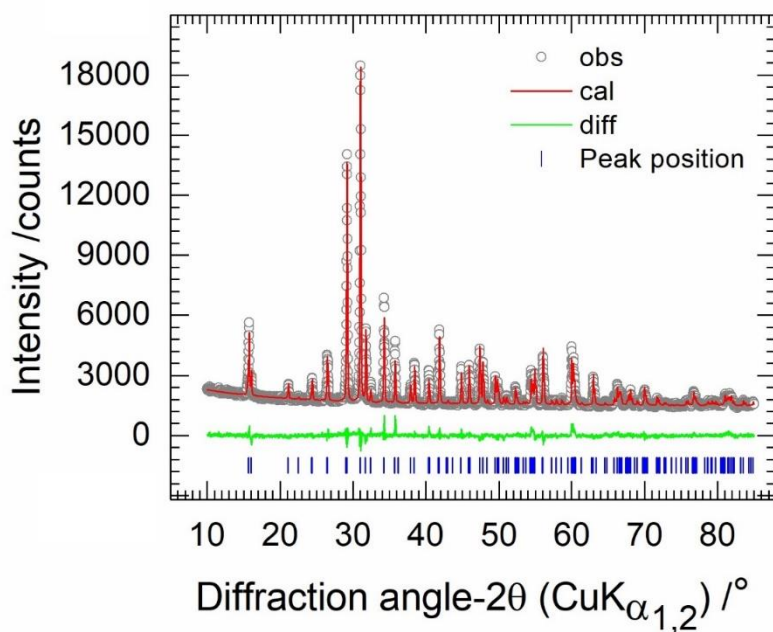


Figure S2: X-ray powder data Rietveld plot of EuAlGeO₅ compound.

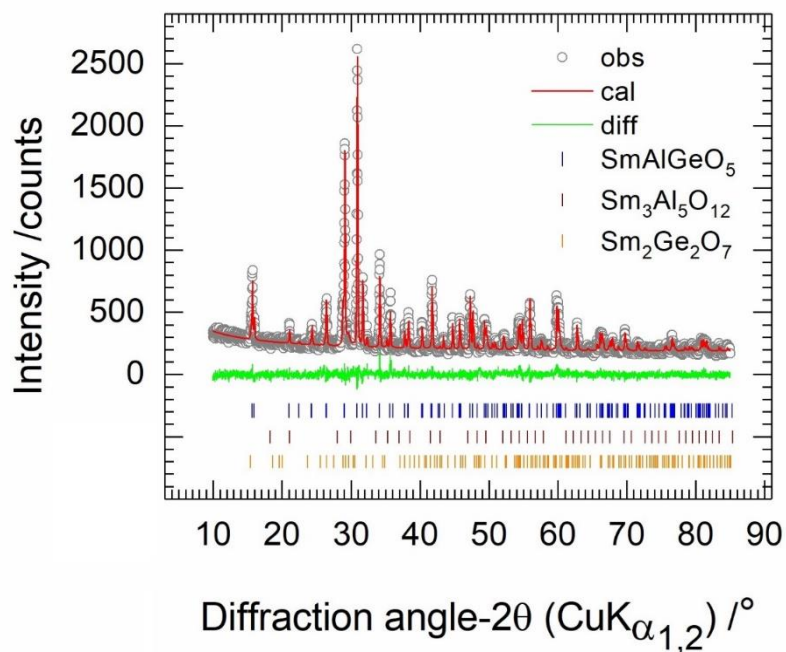


Figure S3: X-ray powder data Rietveld plot of SmAlGeO₅ compound.

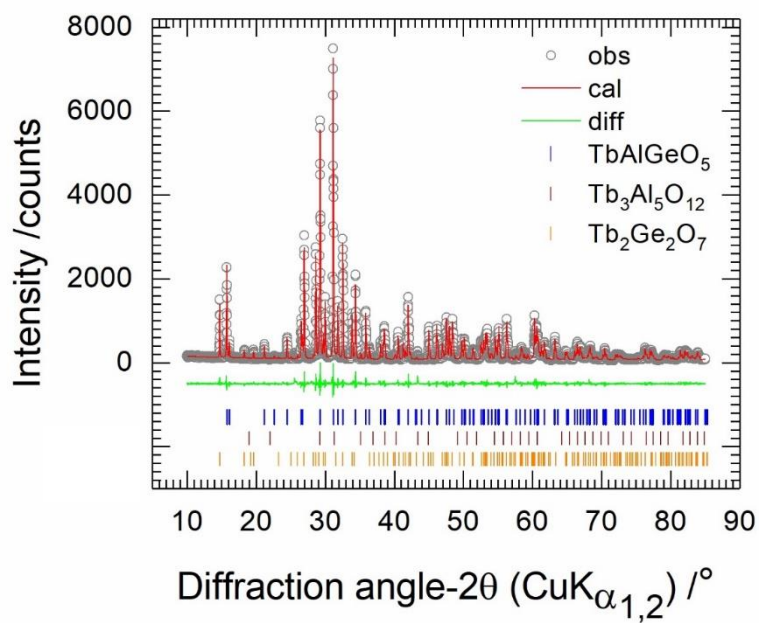


Figure S4: X-ray powder data Rietveld plot of TbAlGeO₅ compound.

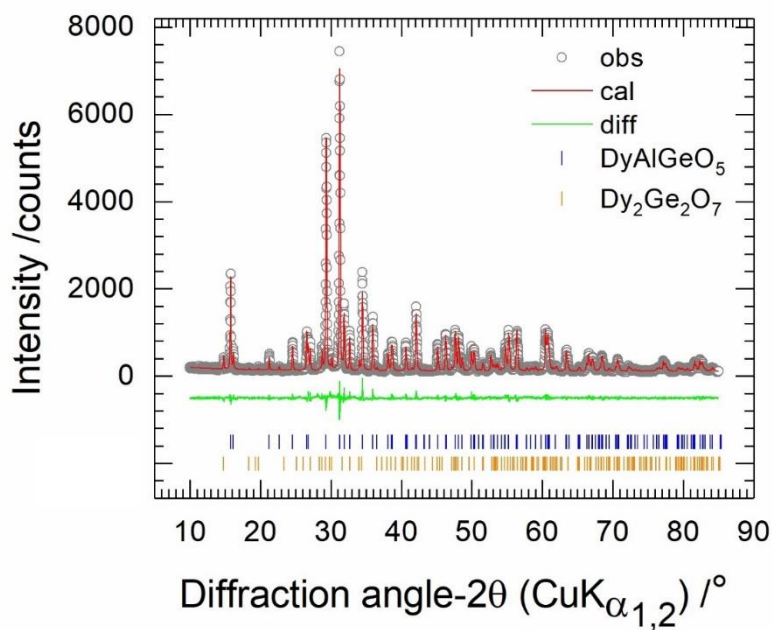


Figure S5: X-ray powder data Rietveld plot of DyAlGeO₅ compound.

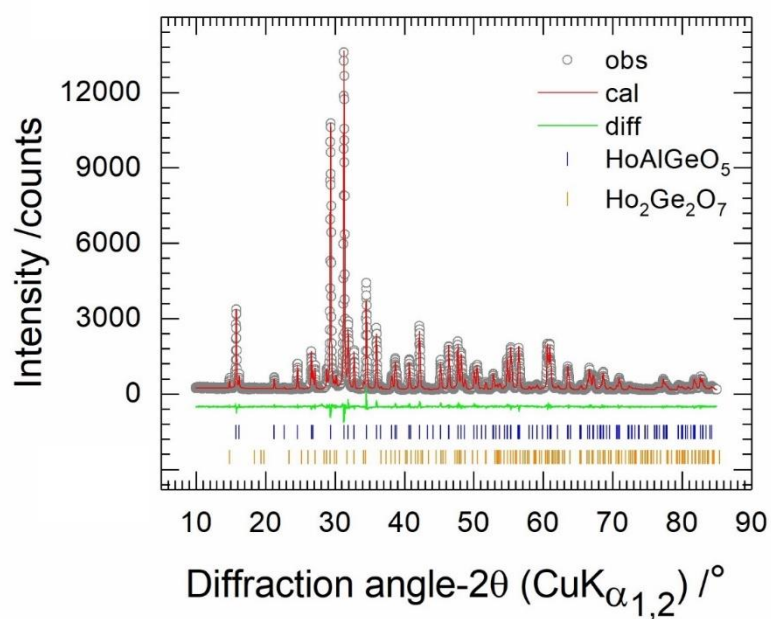


Figure S6: X-ray powder data Rietveld plot of HoAlGeO₅ compound.

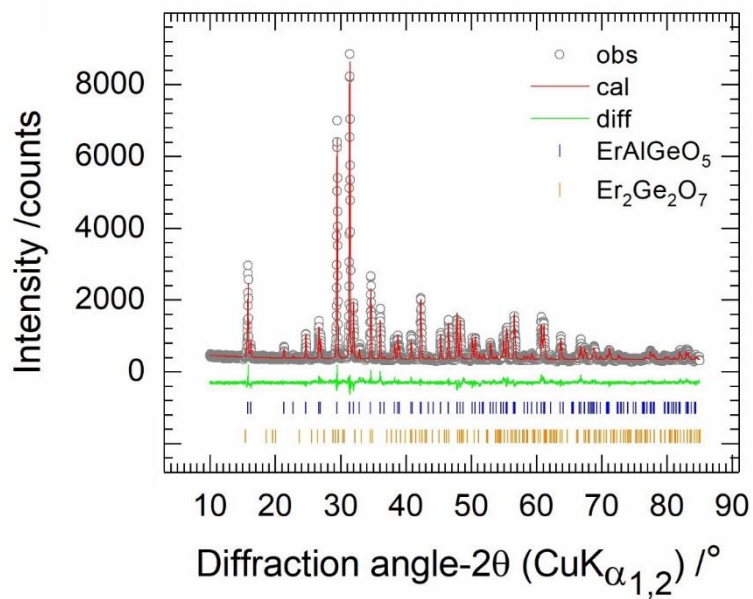


Figure S7: X-ray powder data Rietveld plot of ErAlGeO_5 compound.

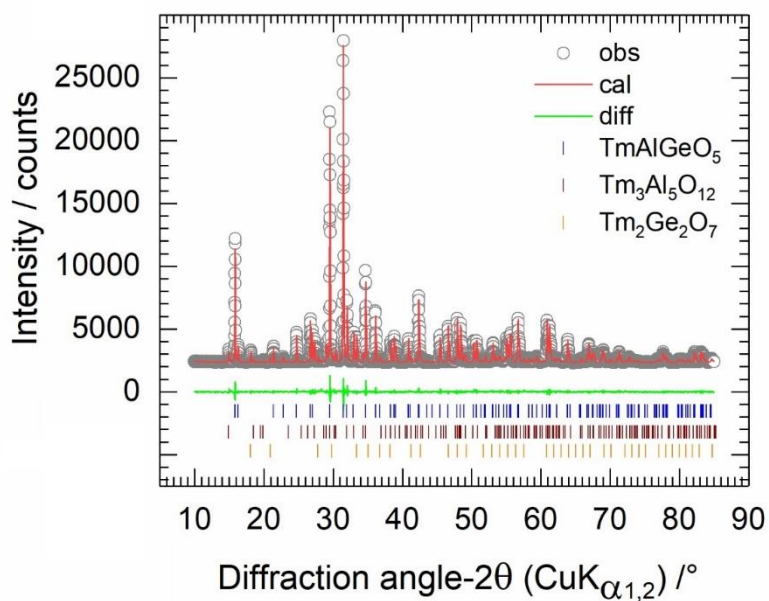


Figure S8: X-ray powder data Rietveld plot of TmAlGeO_5 compound.

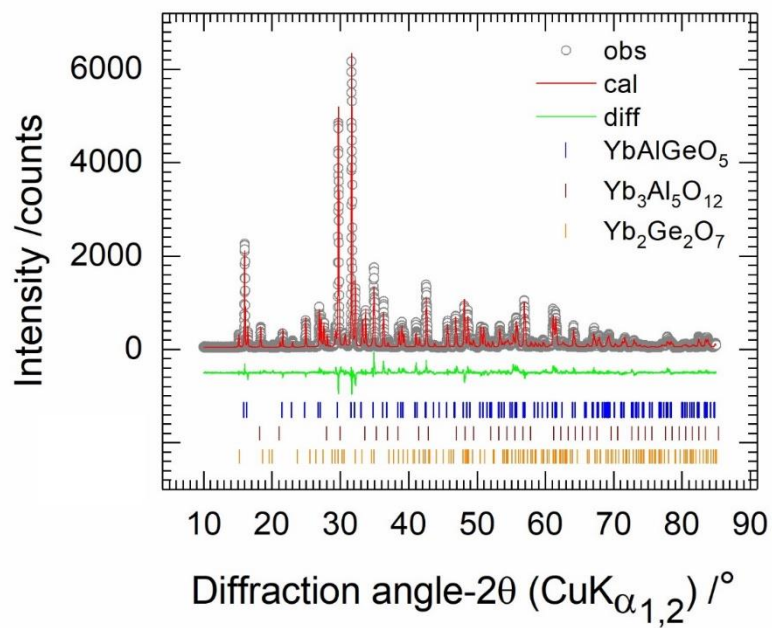


Figure S9: X-ray powder data Rietveld plot of YbAlGeO₅ compound.

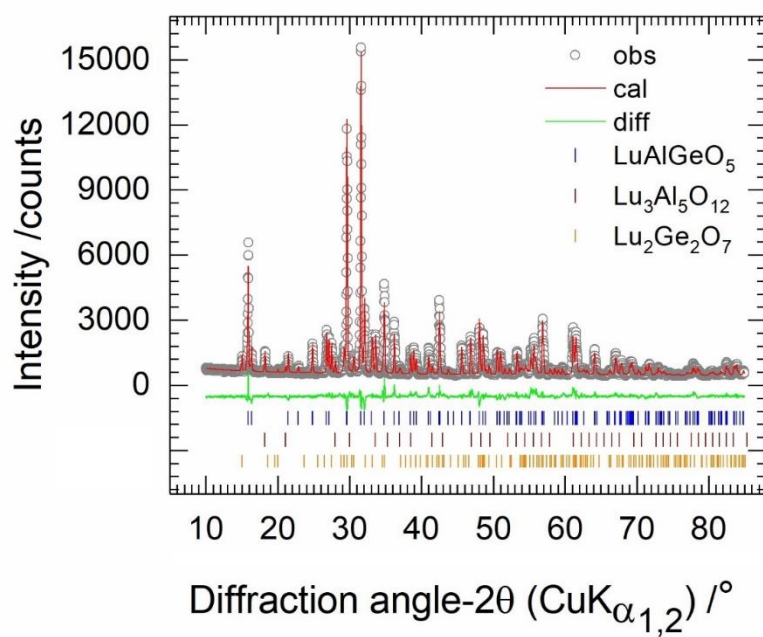


Figure S10: X-ray powder data Rietveld plot of LuAlGeO₅ compound.

Table S1: Refined structural parameter of $RAlGeO_5$ compounds with the space group of $Pbam$.

SmAlGeO ₅						
Atom	Site	Occupancy	x	y	z	$U_{iso}/10^{-4} \text{ pm}^2$
Sm	4g	1	0.1436(1)	0.3276(1)	0	0.31(1)
Al/Ge(1)	4e	0.78(1)/0.22(1)	0	0	0.2560(1)	0.25(1)
Ge/Al(2)	4h	0.22(1)/0.78(1)	0.3861(1)	0.1442(1)	½	0.25(1)
O11	4g	1	0.1639(1)	0589(1)	0	0.25(1)
O12	4h	1	0.1452(1)	0514(1)	½	0.25(1)
O2	8i	1	0.1019(1)	0.7848(1)	0.2641(1)	0.25(1)
O3	4f	1	0	½	0.3136(1)	0.79(1)
TbAlGeO ₅						
Tb	4g	1	0.1413(1)	0.3260(1)	0	0.51(1)
Al/Ge(1)	4e	0.74(1)/0.26(1)	0	0	0.2510(1)	0.25(1)
Ge/Al(2)	4h	0.26(1)/0.74(1)	0.3867(1)	0.1414(1)	½	0.25(1)
O11	4g	1	0.1639(1)	0491(1)	0	0.75(1)
O12	4h	1	0.1542(1)	0672(1)	½	0.25(1)
O2	8i	1	0.1008(1)	0.7866(1)	0.2630(1)	0.26(1)
O3	4f	1	0	½	0.2839(1)	0.97(1)
DyAlGeO ₅						
Dy	4g	1	0.1406(1)	0.3279(1)	0	0.63(1)
Al/Ge(1)	4e	0.75(1)/0.25(1)	0	0	0.2542(1)	0.25(1)
Ge/Al(2)	4h	0.25(1)/0.75(1)	0.3845(1)	0.1428(1)	½	0.56(1)
O11	4g	1	0.1589(1)	0517(1)	0	0.25(1)
O12	4h	1	0.1475(1)	0656(1)	½	0.25(1)
O2	8i	1	0.1001(1)	0.7856(1)	0.2605(1)	0.25(1)
O3	4f	1	0	½	0.2913(1)	1.52(1)
HoAlGeO ₅						
Ho	4g	1	0.1397(1)	0.3282(1)	0	0.47(1)
Al/Ge(1)	4e	0.73(1)/0.27(1)	0	0	0.2537(1)	0.25(1)
Ge/Al(2)	4h	0.27(1)/0.73(1)	0.3842(1)	0.1433(1)	½	0.73(1)
O11	4g	1	0.1607(1)	0686(1)	0	0.25(1)
O12	4h	1	0.1503(1)	0687(1)	½	0.25(1)
O2	8i	1	0.0999(1)	0.7877(1)	0.2581(1)	0.25(1)
O3	4f	1	0	½	0.2870(1)	1.58(1)
ErAlGeO ₅						
Er	4g	1	0.1399(1)	0.3276(1)	0	0.55(1)
Al/Ge(1)	4e	0.71(1)/0.29(1)	0	0	0.2498(1)	0.26(1)
Ge/Al(2)	4h	0.29(1)/0.71(1)	0.3837(1)	0.1433(1)	½	0.26(1)
O11	4g	1	0.1623(1)	0525(1)	0	0.25(1)
O12	4h	1	0.1501(1)	0699(1)	½	0.55(1)
O2	8i	1	0.1082(1)	0.7883(1)	0.2587(1)	0.30(1)
O3	4f	1	0	½	0.2873(1)	0.54(1)

TmAlGeO ₅						
Tm	4g	1	0.1398(1)	0.3280(1)	0	0.56(1)
Al/Ge(1)	4e	0.71(1)/0.29(1)	0	0	0.2523(1)	0.36(1)
Ge/Al(2)	4h	0.29(1)/0.71(1)	0.3840(1)	0.1437(1)	½	0.40(1)
O11	4g	1	0.1611(1)	0.535(1)	0	0.27(1)
O12	4h	1	0.1535(1)	0.689(1)	½	0.53(1)
O2	8i	1	0.1062(1)	0.7886(1)	0.2547(1)	0.35(1)
O3	4f	1	0	½	0.2877(1)	0.87(1)
YbAlGeO ₅						
Yb	4g	1	0.1432(1)	0.3324(1)	0	0.50(1)
Al/Ge(1)	4e	0.70(1)/0.30(1)	0	0	0.2551(1)	0.25(1)
Ge/Al(2)	4h	0.30(1)/0.70(1)	0.3805(1)	0.1413(1)	½	0.25(1)
O11	4g	1	0.1623(1)	0.564(1)	0	1.14(1)
O12	4h	1	0.1455(1)	0.766(1)	½	0.25(1)
O2	8i	1	0.1060(1)	0.7803(1)	0.2599(1)	0.84(1)
O3	4f	1	0	½	0.2944(1)	0.25(1)
LuAlGeO ₅						
Lu	4g	1	0.1395(1)	0.3286(1)	0	0.68(1)
Al/Ge(1)	4e	0.70(1)/0.30(1)	0	0	0.2474(1)	0.25(1)
Ge/Al(2)	4h	0.30(1)/0.70(1)	0.3839(1)	0.1539(1)	½	0.48(1)
O11	4g	1	0.1610(1)	0.576(1)	0	0.25(1)
O12	4h	1	0.1528(1)	0.674(1)	½	0.27(1)
O2	8i	1	0.1078(1)	0.7884(1)	0.2551(1)	0.97(1)
O3	4f	1	0	½	0.2854(1)	0.91(1)

Table S2: The interatomic bond distances in pm unit of $RAlGeO_5$ compounds.

	R	Y	Sm	Eu	Gd	Tb	Dy	Ho	Er	Tm	Yb	Lu
Al-O2(2x)	Al-O11(2x)	R-O3(2x)	R-O2(2x)	R-O2(2x)	R-O2(2x)	R-O11(1x)	R-O11(1x)	R-O11(1x)	R-O11(1x)	R-O11(1x)	R-O11(1x)	R-O11(1x)
192.65(1)	184.43(1)	240.37(1)	249.40(1)	234.92(1)	234.92(1)	229.08(1)	236.87(1)	236.87(1)	236.87(1)	229.08(1)	236.87(1)	229.08(1)
195.64(1)	178.83(1)	250.51(1)	251.78(1)	243.11(1)	243.11(1)	231.39(1)	235.23(1)	235.23(1)	235.23(1)	231.39(1)	235.23(1)	231.39(1)
196.36(1)	189.46(1)	244.33(1)	251.23(1)	239.68(1)	239.68(1)	231.78(1)	240.18(1)	240.18(1)	240.18(1)	231.78(1)	240.18(1)	231.78(1)
195.23(1)	188.91(1)	241.81(1)	252.42(1)	238.41(1)	238.41(1)	233.06(1)	238.68(1)	238.68(1)	238.68(1)	233.06(1)	238.68(1)	233.06(1)
193.42(1)	187.87(1)	239.35(1)	248.86(1)	240.88(1)	240.88(1)	232.51(1)	234.83(1)	234.83(1)	234.83(1)	232.51(1)	234.83(1)	232.51(1)
193.38(1)	183.15(1)	239.37(1)	246.70(1)	240.74(1)	240.74(1)	231.15(1)	236.86(1)	236.86(1)	236.86(1)	231.15(1)	236.86(1)	231.15(1)
191.45(1)	184.30(1)	238.05(1)	246.74(1)	239.31(1)	239.31(1)	230.49(1)	236.97(1)	236.97(1)	236.97(1)	230.49(1)	236.97(1)	230.49(1)
193.83(1)	182.09(1)	237.61(1)	251.05(1)	231.78(1)	231.78(1)	229.93(1)	236.07(1)	236.07(1)	236.07(1)	229.93(1)	236.07(1)	229.93(1)
191.61(1)	185.12(1)	237.45(1)	248.03(1)	233.89(1)	233.89(1)	228.60(1)	235.87(1)	235.87(1)	235.87(1)	228.60(1)	235.87(1)	228.60(1)
201.49(1)	180.72(1)	232.25(1)	261.97(1)	221.43(1)	221.43(1)	233.65(1)	235.86(1)	235.86(1)	235.86(1)	233.65(1)	235.86(1)	233.65(1)
205.02(1)	182.82(1)	231.21(1)	261.93(1)	221.34(1)	221.34(1)	231.93(1)	235.99(1)	235.99(1)	235.99(1)	231.93(1)	235.99(1)	231.93(1)

Ge-O3(2x)	Ge-O2(2x)	Ge-O12(1x)
189.57(1)	182.22(1)	179.24(1)
178.29(1)	177.76(1)	197.80(1)
187.12(1)	181.39(1)	177.64(1)
188.23(1)	180.58(1)	176.16(1)
188.51(1)	180.47(1)	180.39(1)
187.12(1)	183.23(1)	180.07(1)
188.37(1)	181.88(1)	180.76(1)
188.59(1)	181.94(1)	176.63(1)
187.89(1)	182.54(1)	177.11(1)
189.82(1)	174.25(1)	184.87(1)
191.17(1)	176.67(1)	185.37(1)

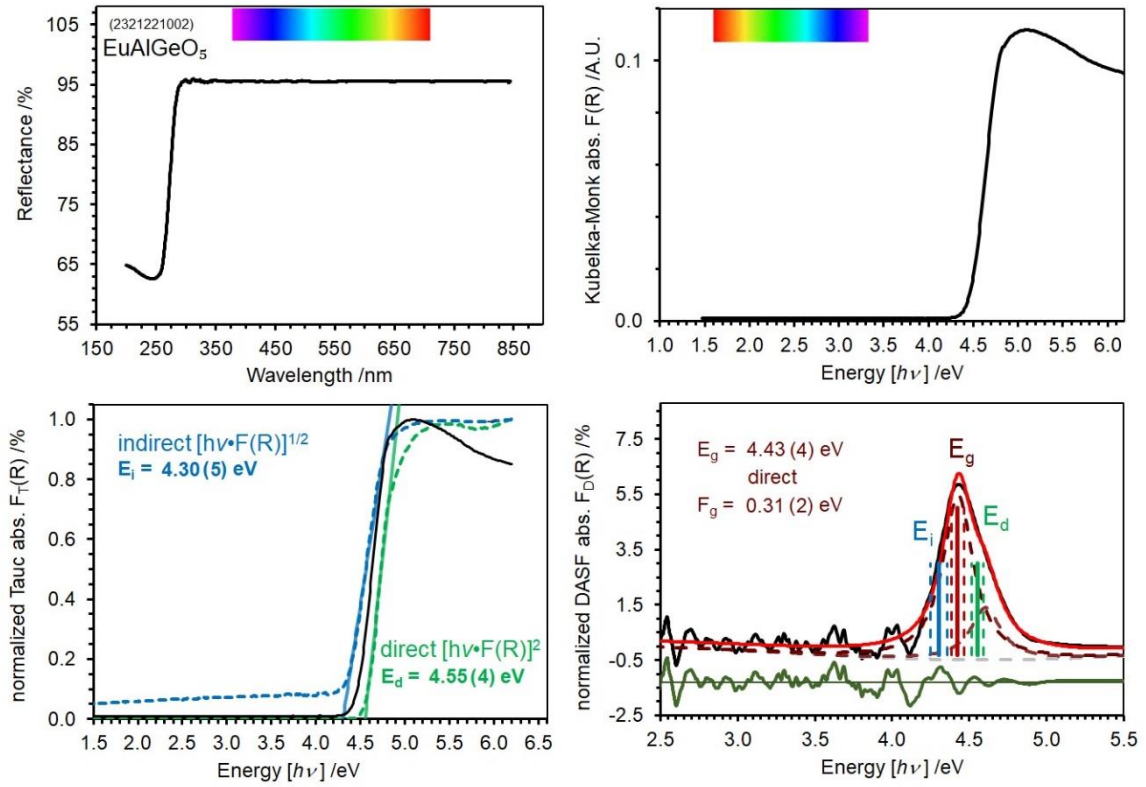


Figure S11: Measured reflectance (top left) and calculations absorbance spectrum (top right) of EuAlGeO_5 , and bandgap energies (E_g) determined using the DASFA methods (bottom right) and Tauc analysis for direct (E_d) and indirect (E_i) transition (bottom left).

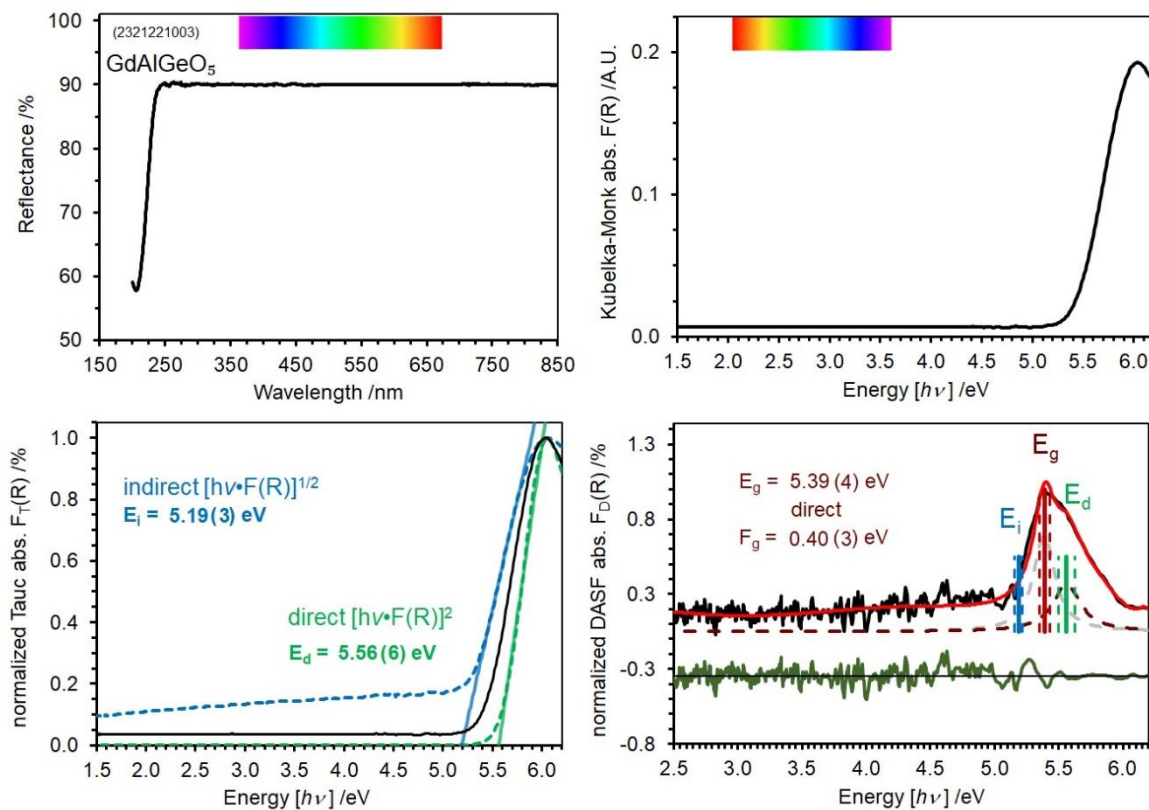


Figure S12: Measured reflectance (top left) and calculations absorbance spectrum (top right) of GdAlGeO₅, and bandgap energies (E_g) determined using the DASF methods (bottom right) and Tauc analysis for direct (E_d) and indirect (E_i) transition (bottom left).

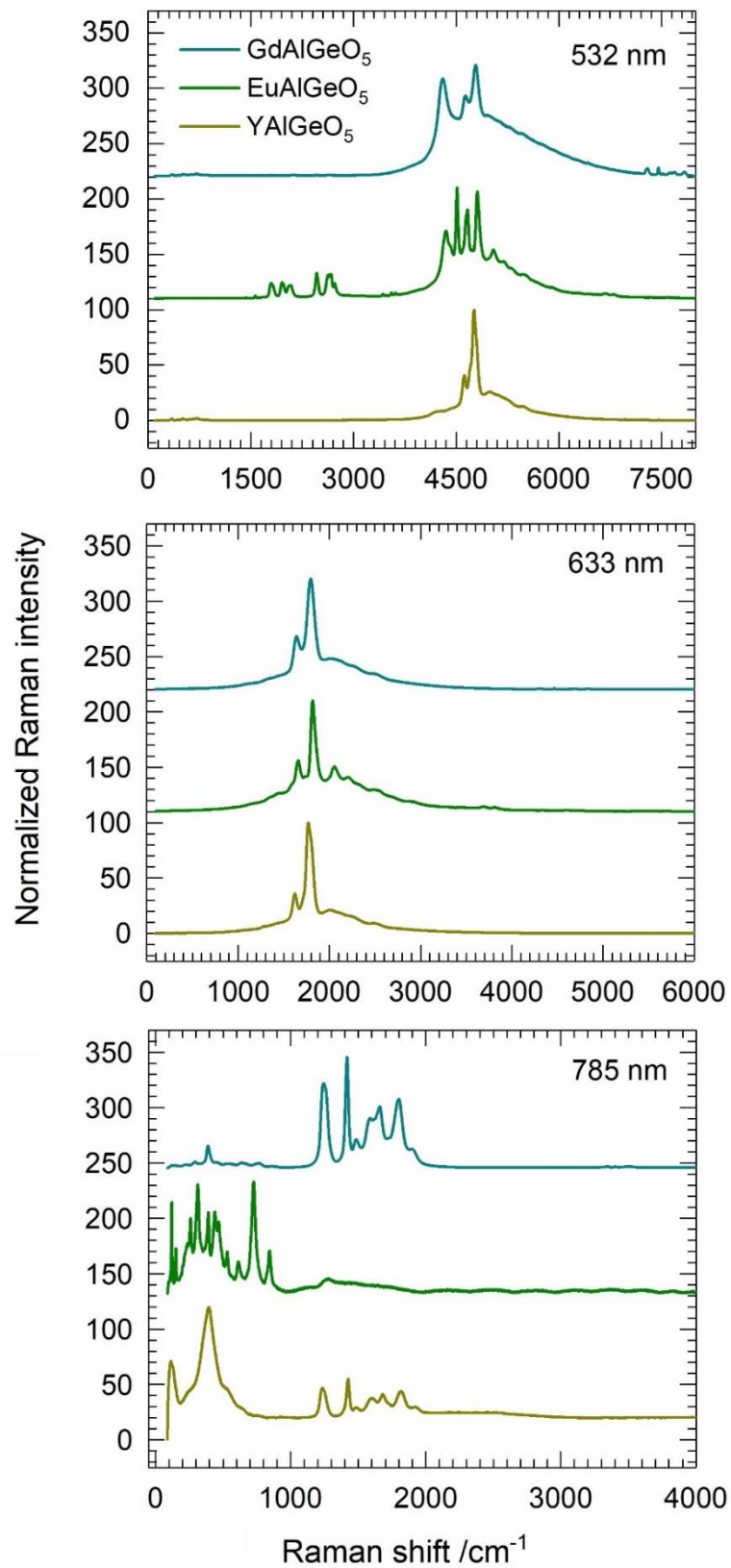


Figure S13: Raman spectra of RAlGeO_5 compounds collected using different lasers.

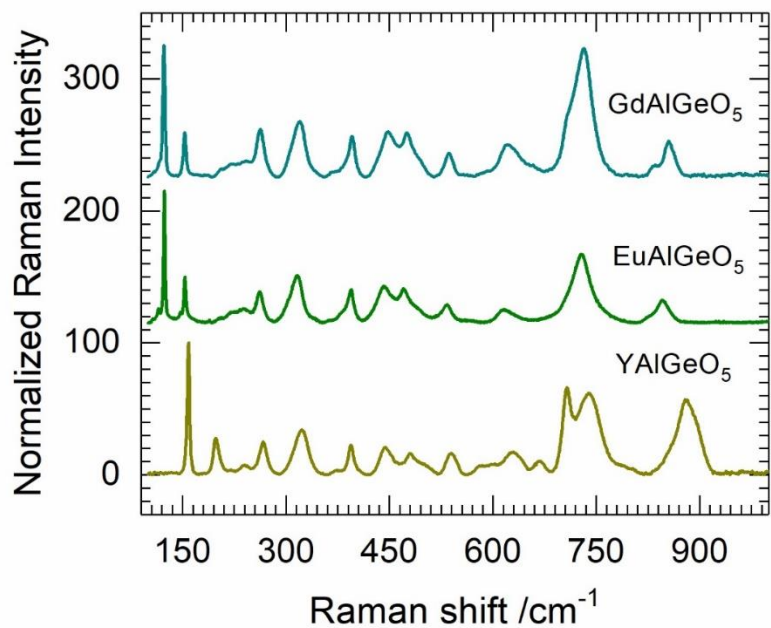


Figure S14: Stack plots of Raman spectra of *RA*lGeO₅ compounds.

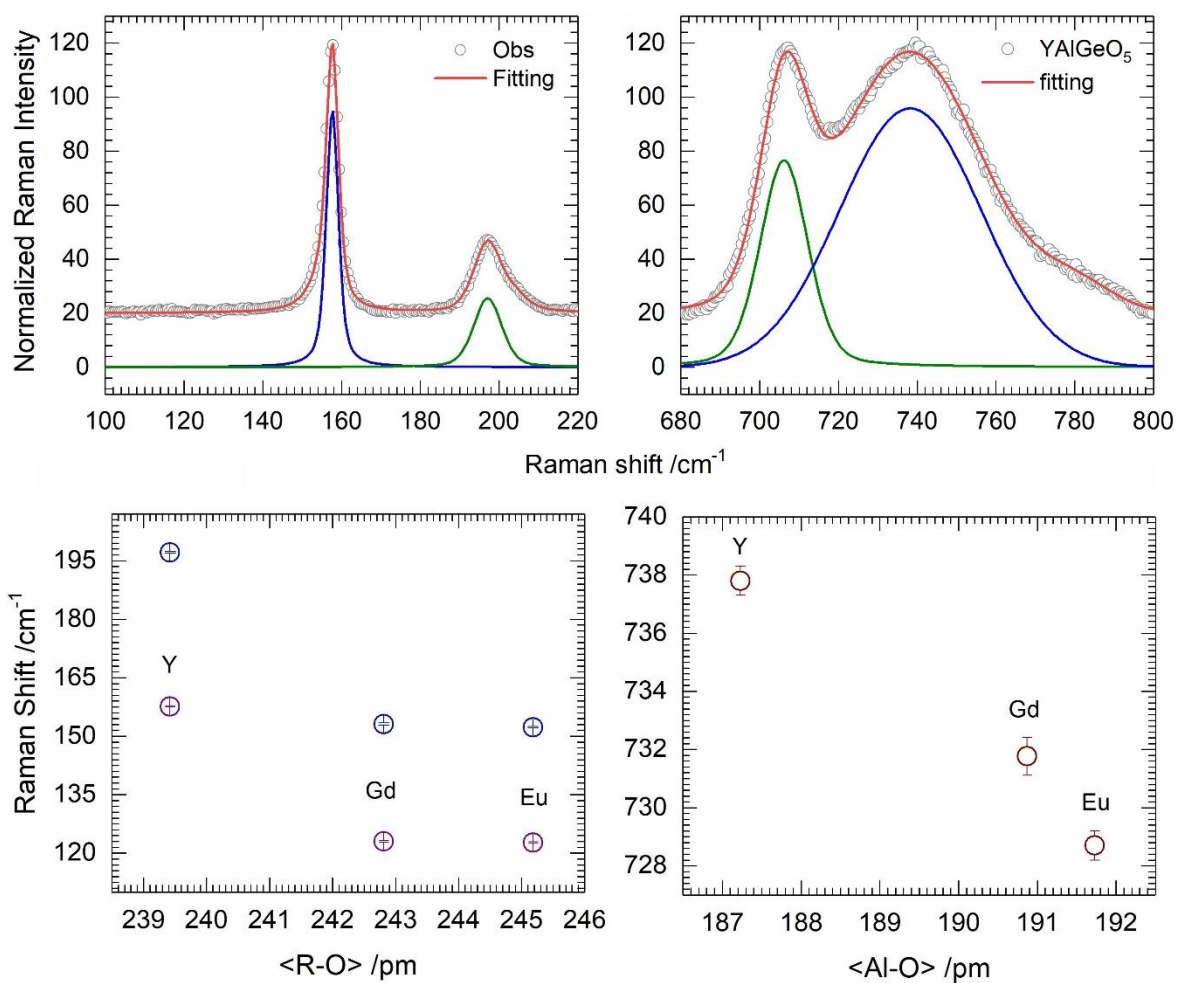


Figure S15: Representative Raman peak fittings at low- and high-frequency regions (right) for YAlGeO_5 compound. The observed Raman frequencies are plotted against the average R-O and Al-O bond distances of RAlGeO_5 compounds (bottom).

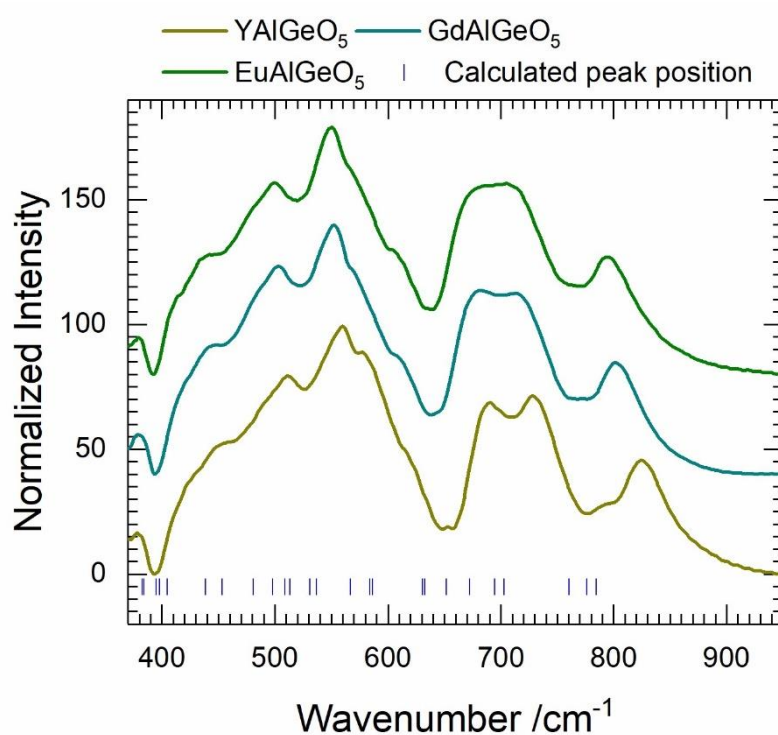


Figure S16: Stack plots of FTIR spectra of RAlGeO_5 compounds along with DFT calculated band frequencies.

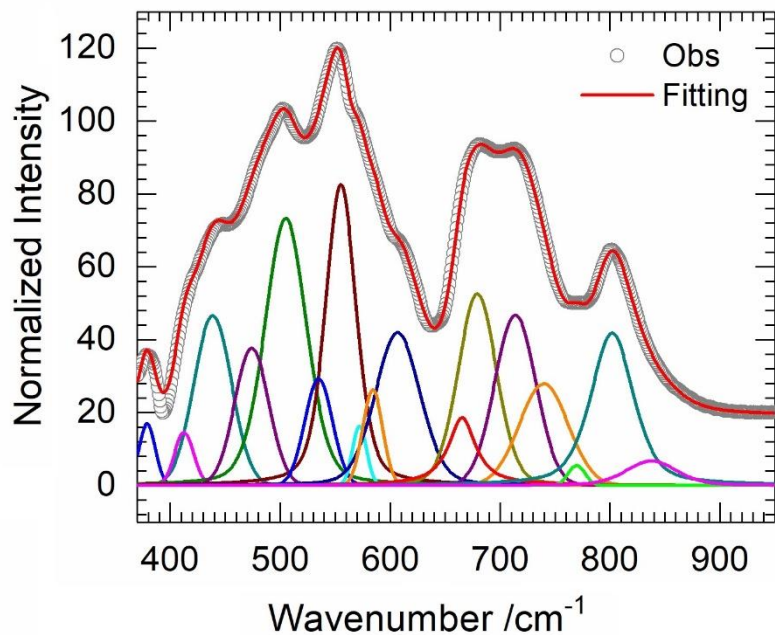


Figure S17: Representative model fitting of FTIR spectrum of GdAlGeO₅ in the mid-infrared region.

Table S3: DFT calculated zone center IR and Raman active mode positions (ω/ cm^{-1}) of YAlGeO₅ compound.

No.	Raman	IR
1	124.29	135.83
2	146.67	148.51
3	147.06	164.66
4	180.26	181.76
5	181.48	194.41
6	185.97	197.10
7	200.79	215.76
8	201.09	226.32
9	206.13	227.76
10	226.62	280.73
11	233.42	295.38
12	236.49	302.89
13	247.82	307.68
14	287.17	343.25
15	297.83	364.78

16	304.77	384.19
17	308.14	395.15
18	326.49	398.10
19	342.51	404.68
20	345.14	438.61
21	358.24	480.78
22	379.36	497.95
23	382.50	508.73
24	411.40	513.18
25	428.47	530.88
26	430.00	566.87
27	437.31	584.12
28	459.31	586.41
29	467.18	630.77
30	475.14	632.49
31	476.19	651.59
32	490.58	694.45
33	502.05	702.74
34	524.17	760.40
35	532.76	776.39
36	574.81	784.55
37	587.77	-
38	604.70	-
39	616.40	-
40	619.37	-
41	658.37	-
42	668.10	-
43	670.65	-
44	674.12	-
45	703.64	-
46	728.28	-
47	849.84	-
48	866.47	-

Table S4: FTIR fit parameters of peak position (ω/ cm^{-1}) and the full-width at half-maximum (FWHM / cm^{-1}) of RAlGeO_5 compounds.

No.	GdAlGeO_5		EuAlGeO_5		YAlGeO_5	
	ω	$FWHM$	ω	$FWHM$	ω	$FWHM$
1	378.7(1)	15.8(1)	377.4(1)	14.9(1)	377.1(1)	16.4(1)
2	414.4(1)	19.8(1)	406.8(1)	12.9(1)	408.1(1)	12.0(1)
3	439.8(1)	38.7(1)	417.9(1)	20.2(1)	421.1(1)	21.7(1)
4	473.0(1)	34.6(1)	438.4(1)	33.9(1)	448.9(1)	42.5(1)
5	504.9(1)	44.6(1)	466.5(1)	30.1(1)	478.6(1)	30.1(1)
6	533.3(1)	26.5(1)	497.7(1)	51.2(1)	507.7(1)	47.8(1)
7	554.1(1)	32.2(1)	550.4(1)	45.3(1)	559.1(1)	50.4(1)
8	572.9(1)	15.0(1)	573.3(1)	16.8(1)	581.0(1)	12.7(1)
9	584.8(1)	18.9(1)	586.0(1)	16.1(1)	592.2(1)	19.8(1)
10	604.0(1)	54.6(1)	605.7(1)	45.9(1)	612.6(1)	51.8(1)
11	665.7(1)	30.8(1)	636.4(1)	5.5(1)	652.1(1)	10.3(1)
12	679.5(1)	41.4(1)	661.6(1)	22.3(1)	685.8(1)	35.5(1)
13	713.8(1)	43.7(1)	677.0(1)	49.0(1)	729.5(1)	51.7(1)
14	739.5(1)	52.4(1)	718.1(1)	50.2(1)	766.3(1)	24.2(1)
15	769.1(1)	18.2(1)	761.8(1)	39.5(1)	788.3(1)	24.5(1)
16	802.5(1)	46.2(1)	794.9(1)	34.8(1)	823.3(1)	40.1(1)
17	844.5(1)	50.0(1)	817.8(1)	71.1(1)	844.1(1)	82.6(1)

Chapter 5

Structural, vibrational, thermal and magnetic properties of mullite-type NdMnTiO₅ ceramic

A published paper “Reproduced with permission from The American Ceramic Society”.
<https://ceramics.onlinelibrary.wiley.com/doi/10.1111/jace.18261>. Copy right permission site:
<https://www.wiley.com/network/researchers/latest-content/how-to-clear-permissions-for-a-thesis-or-dissertation>

Kowsik Ghosh^{1#}, M. Mangir Murshed^{1,2#}, Thomas Frederichs^{3#}, Naveen K. C. Muniraju^{4,5#}, Thorsten M. Gesing^{1,2}

¹University of Bremen, Institute of Inorganic Chemistry and Crystallography, Leobener Straße 7, D-28359 Bremen, Germany

²MAPEX Center for Materials and Processes, Bibliothekstraße 1, D-28359 Bremen, Germany

³University of Bremen, Faculty of Geosciences, Klagenfurter Straße 2-4, D-28359 Bremen, Germany

⁴Institute of Physics, Bijenička 46, 10000 Zagreb, Croatia

⁵AGH University of Science and Technology, Faculty of Physics and Applied Computer Science, 30-059 Krakow, Poland

*Corresponding author: e-mail address: murshed@uni-bremen.de, phone: +49 (0)421 218 63144, fax: +49 421 218 63145.

#ORCID:

KG: 0000-0003-2622-7046

MMM: 0000-0002-9063-372X

TF: [0000-0003-0976-0332](https://orcid.org/0000-0003-0976-0332)

NK: [0000-0002-8867-8291](https://orcid.org/0000-0002-8867-8291)

TMG: 0000-0002-4119-2219

Abstract

Mullite-type RMn_2O_5 ($R = Y$, rare-earth element) ceramics are of ongoing research attentions because of their interesting crystal-chemical and magnetic properties. We report nuclear and magnetic structures of $NdMnTiO_5$ together with its spectroscopic, thermogravimetric and magnetic properties. The polycrystalline sample is prepared by solid-state synthesis and characterized from neutron and X-ray powder diffraction data Rietveld refinements. $NdMnTiO_5$ crystallizes in the orthorhombic space group $Pbam$ with metric parameter $a = 755.20(1)$ pm, $b = 869.91(1)$ pm, $c = 582.42(1)$ pm and $V = 382.62(1) 10^6$ pm³. The Mn^{3+} and Ti^{4+} cations are observed to be located in the octahedral and pyramidal sites, respectively. The vibrational features in these polyhedral sites are characterized by Raman and Fourier transform infrared spectroscopies. The higher decomposition temperature of $NdMnTiO_5$, compared to other RMn_2O_5 phases, is explained in terms of higher bond strength of Ti-O bonds than those of Mn-O bonds. Temperature-dependent DC magnetic susceptibility suggests a paramagnetic to antiferromagnetic phase transition at 43(1) K. Inverse susceptibility in the paramagnetic region above 120 K follows the Curie-Weiss law, resulting in a magnetic moment of 6.33(1) μ_B per formula unit. Neutron diffraction data collected at 7.5 K reveal that the magnetic moments of Nd^{3+} and Mn^{3+} in $NdMnTiO_5$ are incommensurately ordered with a propagation vector $\mathbf{k} = (0, 0.238, 0.117)$.

Introduction

Mullite-type RMn_2O_5 ($R = Y$, and rare-earth element) ceramics crystallize in the $DyMn_2O_5$ structure type ¹, are isostructural to $BiMn_2O_5$ ² and are well-studied systems regarding their crystal chemistry ^{3, 4, 5}, magnetic ^{3, 6} and ferroelectric ^{7, 8, 9} properties. The crystal structure of $NdMn_2O_5$, as shown in **figure 1**, was described in the orthorhombic space group $Pbam$ ¹⁰, where the edge-sharing MnO_6 octahedra form one dimensional infinite chains running parallel to the crystallographic **c**-axis. These chains are interconnected by double pyramids formed by edge-sharing MnO_5 . It is well established that Mn^{4+} cations in $BiMn_2O_5$ as well as in all RMn_2O_5 phases are located in the MnO_6 octahedra and Mn^{3+} in the MnO_5 pyramids ^{9, 11, 12}. The R^{3+} cations are sitting in the 5-ring channels build by the octahedral and pyramidal chains, forming distorted RO_8 polyhedra. The dipoles of the constituent $Mn^{4+}O_6$ (along **c**-axis) and $Mn^{3+}O_5$ (along **b**-axis) polyhedra of the paramagnetic and paraelectric RMn_2O_5 phases at ambient condition are oriented in different directions [16]. The factor that may lead to ferroelectricity in RMn_2O_5 ceramics is the charge-ordering between the Mn^{3+} and Mn^{4+} cations [16]. The polyhedral geometric tilting can also be regarded as possible sources of the ferroelectric behavior for the paramagnetic phases. It is also argued that a complex interplay between magnetic induction [17] and any one or more of these factors may play roles for the ferroelectric behavior. Indeed, due to poor electrical polarization ⁹ the associated ferroelectric displacement is likely to be too small to be detected within the experimental uncertainty. To understand their multiferroic behavior ^{7, 13} is still intriguing. As such, one of the fascinating properties of RMn_2O_5 is the magnetoelectric effect ^{14, 15, 16}, that is, the application of external magnetic field leads to electric polarization ^{17, 18}.

Following Chattopadhyay et al. ¹⁰, **figure 1** also depicts a five-membered loop in the *ab* plane, showing three non-equivalent nearest-neighbor antiferromagnetic (AFM) superexchange interactions between the Mn-cations; J_3 , J_4 and J_5 , respectively, refer to spin coupling contributions between $Mn^{3+} \leftrightarrow Mn^{4+}$, $Mn^{4+} \leftrightarrow Mn^{3+}$ and $Mn^{3+} \leftrightarrow Mn^{3+}$ magnetic sublattices.

The AFM nature of these J_3 , J_4 and J_5 couplings are known to induce magnetic frustration in the system¹⁹, leading to slightly displacement of the Mn^{3+} cations from their centrosymmetric sites to release the magnetic frustration via *exchange striction* mechanism. That is, the inversion symmetry is broken, which is claimed to induce the ferroelectricity along the **b**-direction^{19, 20, 21}. The layers of the Mn^{3+} and R^{3+} cations are alternatively located between two adjacent layers of the Mn^{4+} cations (**Fig. 1**), giving rise to two types of Mn^{4+} – Mn^{4+} exchange interactions, namely, J_2 (through the Mn^{3+} layers) and J_1 (through the R^{3+} layers). Using neutron powder diffraction Munoz et al.⁵ demonstrated the commensurability of BiMn_2O_5 in terms of ferromagnetic (FM) indirect (J_2 via Mn^{4+} – O – Mn^{3+} – O – Mn^{4+}) and AFM direct (J_1 via Mn^{4+} – O – Mn^{4+}) couplings. The competition between J_1 and J_2 interactions govern the alignment of magnetic moments of the Mn^{4+} cation in the MnO_6 octahedral chain and the commensurability of the magnetic structure. The successive lanthanide contraction in RMn_2O_5 ceramics are reported to shorten the $\langle \text{Mn}^{4+}$ – $\text{O} \rangle$ bond lengths²². As a consequence, the J_2 coupling is enhanced, resulting in the incommensurability of the magnetic structures along the **c**-direction. As such, the incommensurate component k_z of $\mathbf{k} = (\frac{1}{2}, 0, k_z)$ was shown to be the function of the size of the R -cation^{23, 24}. For instance, whereas the magnetic ordering of LaMn_2O_5 ²⁵ showed commensurate character with propagation vector $\mathbf{k} = (0, 0, \frac{1}{2})$, R^{3+} cations with relatively smaller ionic radii in RMn_2O_5 showed different incommensurate k_z components^{20, 23, 24, 26, 27, 28}. Most of RMn_2O_5 ceramics are known to show AFM ordering with T_N of about 40 K^{3, 5, 23, 24, 25}. To tune the magnetic phase-transition temperature in RMn_2O_5 , Mn^{3+} in the pyramidal site was replaced by Fe^{3+} ^{29, 30, 31} and Cr^{3+} ^{32, 33}. The ferrimagnetic ordering was also reported with T_c of 153 – 165 K for RFeMnO_5 ($R = \text{Y, Ho, Er}$)^{29, 30, 31} and 85 K for YCrMnO_5 ³². Clearly, replacing Mn^{3+} with other transition-cations such as Cr^{3+} or Fe^{3+} changes the type and magnitude of the associated J -couplings, leading to a wide field of magnetic properties.

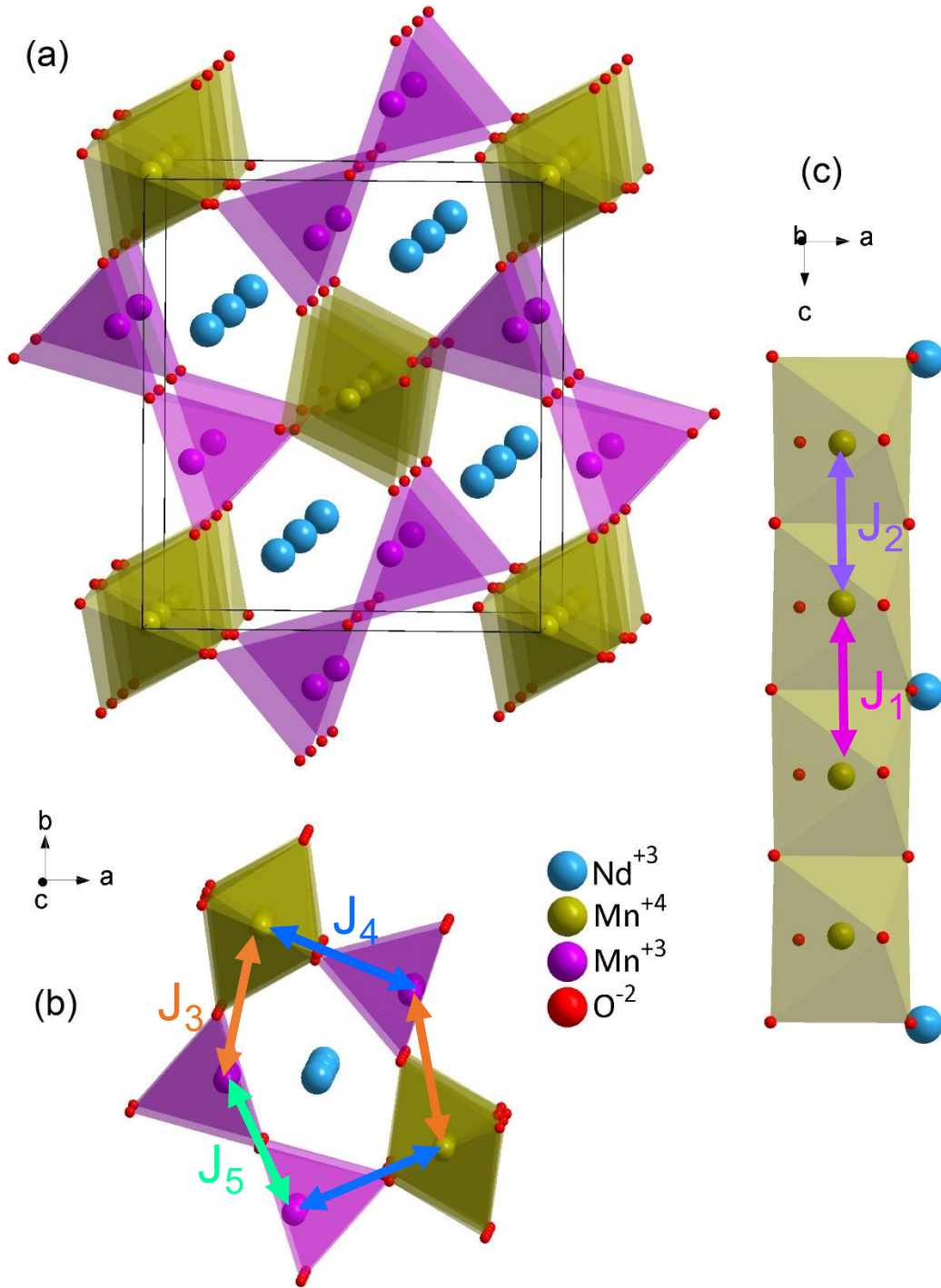


Figure 1. Representative (a) crystal structure of NdMn_2O_5 showing (b) 5-ring chain of MnO_6 octahedra and MnO_5 pyramid with BiO_8 coordination and (c) MnO_6 octahedral chain in the c -direction with representative magnetic ordering.

The relatively lower T_N of 2.5 K, 18.5 K and 20.5 K, respectively, for $R\text{CrGeO}_5$ ³⁴, NdFeTiO_5 ^{35, 36}, and NdCrTiO_5 ³⁷ ceramics can be understood as the $4h$ site is found to be occupied by

the non-magnetic Ti^{4+} cation and the J_3 -, J_4 - and J_5 -couplings are completely absent. Thus, only the J_1 and J_2 exchanges play the pivotal roles of the spin-orderings assuming that the R^{3+} cations remain paramagnetic much below the spin-ordering temperature^{37, 38}. The present study addresses both the nuclear and magnetic structures of NdMnTiO_5 along with some details of the physico-chemical properties. The investigation includes *in-situ* neutron powder diffraction (NPD), X-ray powder diffraction (XRPD), Raman and Fourier transform infrared (FTIR) spectroscopy, thermogravimetry and temperature-dependent magnetic susceptibility measurements.

2. Experimental

2.1. Synthesis

Dark brown colored polycrystalline NdMnTiO_5 was prepared by standard solid state sol-gel synthesis method. Stoichiometric amount of Nd_2O_3 , TiO_2 and $\text{Mn}(\text{NO}_3)_2 \cdot 4\text{H}_2\text{O}$ were mixed with 30 wt% glycerin (1,2,3-propantriol) into a glass beaker and heated at 353 K under magnetic stirring for about half an hour to get a gel solution. This solution was then heated at 473 K for about 2 h. Afterward, the resulting foam-like solid was homogenously crushed into powder and put into a corundum crucible followed by heating at 1323 K for 48 h. The applied glycerin method is useful when there is no issue of subtle changes of oxidation states due to redox potentials of the starting cations²² in air.

2.2. Neutron powder diffraction

Time-of-flight (TOF) NPD was performed on 5 g of a NdMnTiO_5 sample loaded in 8 mm diameter vanadium can. Temperature-dependent NPD data were collected at the Spallation Neutron Source (SNS) at Oak Ridge National Laboratory on the high-resolution neutron powder diffractometer POWGEN. Longer measured datasets (1 h) collected between 7.5 K and 300 K covered a d -spacing from 30 pm to 620 pm. The Rietveld refinements were performed using GSAS-II³⁹. The magnetic structure refinements were carried out using

*FullProf*⁴⁰. It is worth noting that POWGEN uses a TOF profile function that varies from the standard lineshape originally derived for GSAS⁴¹. The variation in peak shape and peak position with the POWGEN diffractometer is calculated using a function related to thermal and epithermal components of the neutron spectrum and implemented in GSAS-II to accurately determine the metric parameters. The starting atomic coordinates were taken from the isostructural crystal data of NdFeTiO₅⁴². During the Rietveld refinement the scale factor, absorption coefficient, two profile shape parameters, lattice parameters, fractional coordinates of the atoms and their displacement parameters were optimized.

2.3. X-ray powder diffraction

X-ray powder diffraction data were collected on an X'Pert MPD PRO diffractometer (PANalytical GmbH, Almelo, The Netherlands) equipped with an X'Celerator multi-strip (128) detector system. The X-ray patterns were collected using Ni-filtered CuK _{α 1,2} radiation ($\lambda_{K\alpha 1} = 154.05929(5)$ pm, $\lambda_{K\alpha 2} = 154.4414(2)$ pm) in Bragg-Brentano geometry. Data were collected at ambient condition from 5° to 135° 2θ with a step width of 0.0167° 2θ and a measurement time of 75 s per step. The obtained data were refined using the Rietveld method (TOPAS V6, Bruker AXS) and the fundamental parameter approach was used for profile fitting, where the fundamental parameters were fitted against a standard material (LaB₆). The starting atomic coordinates of NdFeTiO₅ are available elsewhere⁴². During Rietveld refinements the background, sample displacement, metric parameters, profile parameters and atomic parameters were optimized.

2.4. Vibrational spectroscopy

Raman spectra were recorded on a LabRam ARAMIS (Horiba Jobin Yvon) Micro-Raman spectrometer equipped with laser working at 633 nm and less than 20 mW. A 50× objective (Olympus) with a numerical aperture of 0.75 provides a maximum focus spot of about 1.03 μm diameter when closing the confocal hole to 200 μm . Each spectrum ranges between 90 cm^{-1} and 1000 cm^{-1} with a spectral resolution of approximately 1.2 cm^{-1} using a grating of

1800 grooves/mm and a thermoelectrically cooled CCD detector (Synapse, 1024×256 pixels). Fourier transform infrared (FTIR) spectra were collected in the mid-infrared range from 370 cm⁻¹ to 4000 cm⁻¹ on a Bruker IFS66v/S spectrometer. The spectra were collected using the standard KBr method (2 mg of each sample mixed with 200 mg KBr), obtained from 128 scans with a spectral resolution of 2 cm⁻¹.

2.5. Thermogravimetric analysis

TGA/DSC measurements were taken on TGA/DSC 3⁺ STARe System of Mettler Toledo. The samples were measured with a heating rate of 10 K/min and a continuous N₂ flow of 20 mL/min from 298 K to 1623 K. An amount of 21.0(1) mg of NdMnTiO₅ powder sample was measured relative to an empty corundum crucible reference. Evaluation of the DTA curve was done by “Mettler Toledo STARe Evaluation Software” to get the decomposition temperature, where intercept of two fitting lines of before and after the decomposition treated as the decomposition temperature. A drift correction to the data was applied using an empty corundum sample crucible measurement.

2.6. Magnetic susceptibility

Temperature-dependent DC magnetic susceptibility measurements were carried out with a Magnetic Property Measurement System MPMS-XL7 (Quantum Design, San Diego, USA) using the field-cooling process at a magnetic field of 0.01 T. The polycrystalline NdMnTiO₅ (91.3 mg) sample was sealed in a gel capsule and attached to a nonmagnetic sample holder. Data were collected between 300 K and 2 K with an incremental cooling rate of 2 K/min. The magnetic signal was well above the standard deviations, where the order of the instrumental noise was estimated to be $\sim 10^{-11}$ Am².

3. Results and discussion

Nuclear structure

Both NPD and XRPD confirm that the polycrystalline sample of NdMnTiO₅ crystallizes in the orthorhombic symmetry (*Pbam*); the respective Rietveld refinement plots are shown in **figure 2**. The refined metric parameters obtained from NPD and XRPD are given in **table 1**. A comparative view of metric parameters between some Nd-containing phases is shown in **table 2**.

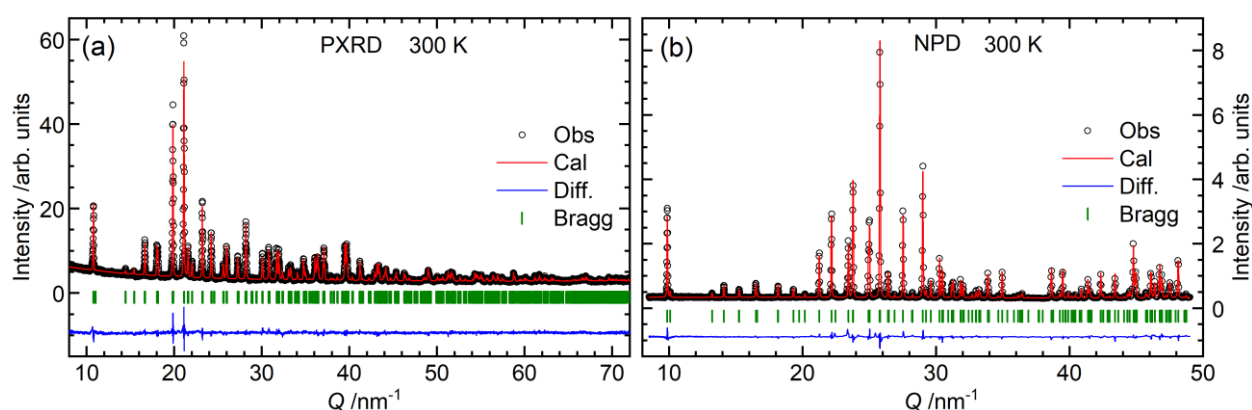


Figure 2. (a) Rietveld refinement results of (a) X-ray powder diffraction and (b) time-of-flight neutron powder diffraction patterns of NdMnTiO₅ at 300 K. Open circles and solid lines represent the observed and the calculated patterns, respectively. The difference between the observed and the calculated intensity is shown at the bottom. The vertical bars are for the calculated Bragg reflection positions.

Whereas in BiMn₂O₅ and RMn₂O₅ the Mn⁴⁺ cations are located at the MnO₆ octahedral site XRPD data Rietveld refinement of NdMnTiO₅ suggest that Mn³⁺ is located on the octahedral site and that of Ti⁴⁺ at the pyramidal site. As such, the expansion of the *c*-lattice parameter can be explained in terms of higher Mn-Mn bond distances in NdMnTiO₅ (296.9(1) pm) than that of in NdMn₂O₅ (273.4(9) pm)³ in the octahedral site due to larger cationic size of Mn³⁺ in the Mn³⁺O₆ octahedra connected through O11 and O12 along the *c*-axis, as shown in **figure 3**.

Table 1. Time-of-flight neutron powder data and XRPD (*italic*) Rietveld refined structural parameters of NdMnTiO₅ in the space group *Pbam*.

$R_{wp} = 3.71(1) / 4.87(1), GOF = 0.48(1) / 1.36(1)$						
Atom	Site	<i>x</i>	<i>y</i>	<i>z</i>	Occupancy	$U_{iso} / 10^{-4} \text{ pm}^2$
Nd	4g	0.1388(1)	0.3280(1)	0	1	0.46(1)
		<i>0.1397(1)</i>	<i>0.3287(1)</i>			<i>0.53(1)</i>
Mn	4e	0	0	0.2545(7)	1	0.90(1)
				<i>0.2608(1)</i>		<i>1.07(1)</i>
Ti	4h	0.4022(6)	0.1472(5)	½	1	0.40(1)
		<i>0.4009(1)</i>	<i>0.1486(1)</i>			<i>0.25(1)</i>
O11	4g	0.1634(1)	0.0535(1)	0	1	0.25(1)
		<i>0.1572(1)</i>	<i>0.0521(1)</i>			<i>0.25(1)</i>
O12	4h	0.1569(3)	0.0739(1)	½	1	0.60(1)
		<i>0.1596(1)</i>	<i>0.0695(1)</i>			<i>0.25(1)</i>
O2	8i	0.1033(1)	0.7904(1)	0.7478(3)	1	0.51(1)
		<i>0.1075(1)</i>	<i>0.7887(1)</i>	<i>0.7263(1)</i>		<i>1.36(1)</i>
O3	4f	0	½	0.2831(4)	1	0.44(1)
				<i>0.2954(1)</i>		<i>0.25(1)</i>

Whereas O11 is solely connected by the octahedral chain, O12 serves for bridging oxygen between the octahedra and pyramid. The Mn-O2 (198(1) pm), Mn-O11 (199(1) pm) and Mn-O12 (197(1) pm) bond distances lie close to each other (**Tab. 2**), and the <O2-Mn-O2 (179.2(1)°) and <O11-Mn-O12 (175(1)°) bond angles remain close to 180°. The bond length distortion of $4.1(1) \cdot 10^{-3}$, Halasyamani distortion⁴³ of 0.03(1) pm and octahedral mean quadratic elongation of 1.004(1) indicates to almost regular MnO₆ octahedra in the structure. The difference between the basal (Ti-O2 and Ti-O3) and axial (Ti-O12) bond distances of about 5(1) pm (**Tab. 2**) leads to a bond distortion of $1.05(1) \cdot 10^{-4}$ in the TiO₅ pyramid.

Table 2. Selective bond distances, bond valence (BV) and bond valence sum (BVS) of the coordination cations in NdMnTiO₅.

Bond	Distance /pm	BV /v.u.
Nd–O11 (1x)	239.3(1)	0.47(1)
Nd–O11 (1x)	247.0(1)	0.39(1)
Nd–O2 (2x)	246.5(1)	0.39(1)
Nd–O2 (2x)	256.6(1)	0.30(1)
Nd–O3 (2x)	246.2(1)	0.39(1)
<Nd–O>	248.1(1)	BVS = 3.02(1)
Ti–O3 (2x)	194.7(1)	0.70(1)
Ti–O2 (2x)	190.9(1)	0.77(1)
Ti–O12 (1x)	195.6(1)	0.68(1)
<Ti–O>	193.4(1)	BVS = 3.63(1)
Mn–O2 (2x)	198.4(1)	0.55(1)
Mn–O11 (2x)	198.9(1)	0.54(1)
Mn–O12 (2x)	196.6(1)	0.57(1)
<Mn–O>	198.0(1)	BVS = 3.31(1)

The NdO₈ polyhedra share edge and corner to a layer in the *ab*-plane, connecting two layers with different bond distances. For instance, the connecting Nd-O11 bond distance (239(1) pm) (**Fig. 3**) differs about 8(1) pm from another Nd-O11 (247(1) pm), resulting in a slight bond distortion of $16.7(1) \cdot 10^{-3}$ in NdO₈. The <Mn-O> bond distance of (198(1) pm) in MnO₆ octahedra and <Nd-O> of 248(1) pm in NdO₈ polyhedra in NdMnTiO₅ are larger than those (<Mn-O> = 191.4(2) pm) and <Nd-O> = 245.1(1) pm) in NdMn₂O₅³ support the enlargement of the *a*- and *b*-cell parameters.

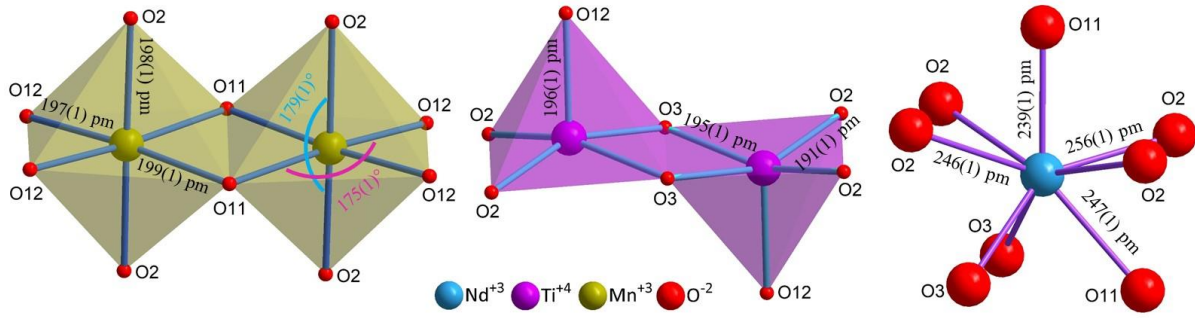


Figure 3. Selective structural components of NdMnTiO₅ at 300 K, showing respective M-O bond lengths in Mn³⁺O₆ (left-panel), Ti⁴⁺O₅ (middle-panel) and NdO₈ polyhedra (right-panel).

Whereas the structural bond valence sum (BVS)⁴⁴ of Nd-atom lies close to 3 v.u, the BVS of Mn- and Ti-atom differs from the respective integer values (**Tab. 2**). Nearly 10 % deviation of BVS values for both cations indicate the inversion of Mn/Ti between the octahedral and pyramidal sites. Of notes, as much as 5 % inversion was reported for NdCrTiO₅ and NdFeTiO₅⁴² and more than 20 % inversion was found in RAlGeO₅ (R = Y, Sm-Lu)⁴⁵ ceramics.

Table 3. Metric parameters of NdMn₂O₅ and NdMTiO₅ (M = Cr, Mn, Fe).

Mullite-type	<i>a</i> /pm	<i>b</i> /pm	<i>c</i> /pm	V /pm ³ x 10 ⁶	Ref.
NdMn ₂ O ₅	750.51(2)	762.09(1)	570.22(1)	368.93(3)	[2]
NdCrTiO ₅	756	867	580	380.16	[22]
NdMnTiO ₅	755.20(1)	869.91(1)	582.42(1)	382.62(1)	this work (NPD*)
NdFeTiO ₅	754	871	585	384.19	[22]

*NPD = Neutron powder diffraction

Vibrational property

The room-temperature Raman and FTIR spectra of NdMnTiO₅ are shown in **figure 4**. Factor group analysis predicts 96 modes (13A_{1g} + 13B_{1g} + 11B_{2g} + 11B_{3g} + 9A_{1u} + 9B_{1u} + 15B_{2u} + 15B_{3u}), where 48 modes are Raman active (13A_{1g} + 13B_{1g} + 11B_{2g} + 11B_{3g}), 36 are infrared active (8B_{1u} + 14B_{2u} + 14B_{3u}). B_{1u} + B_{2u} + B_{3u} represents the acoustic modes and nine A_{1u}

modes are optically silent ⁴⁶. A representative fitting shows the compound and component spectra leading to respective peak position and full-width half-maximum (*FWHM*), which are given in **table 4**.

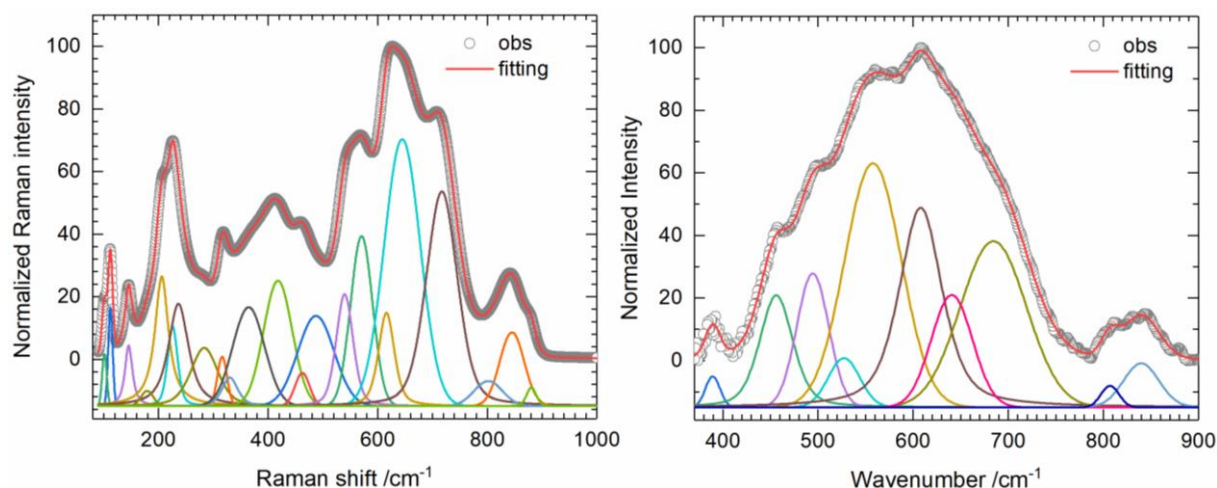


Figure 4. Raman (left-panel) and fourier transform infrared (right-panel) spectra fitting of NdMnTiO₅.

Fitting the Raman spectra (**Fig. 4**) requires 22 Pseudo-Voigt peaks for NdMnTiO₅, which is comparable with a previous report for other *RMn₂O₅* phases ²². To better describe the vibrational features, each Raman spectrum can be categorized into three spectral regions at low- (< 250 cm⁻¹), mid- (250 - 550 cm⁻¹) and high frequency (> 550 cm⁻¹). The low-frequency region is mainly dominated by the vibrational features of the NdO₈. The peak maxima at 206(1) cm⁻¹ and 226(1) cm⁻¹ (**Tab. 4**) can be assigned to the Nd-O stretching vibration similar to those of *R*-O stretching in *RMn₂O₅* (*R* = Bi, Nd, Sm, Eu) ²² and *RA*lGeO₅ (*R* = Y, Eu, Gd) ceramics ⁴⁵. Lattice dynamics calculation suggests the B_{1g} mode associated with the Nd-O stretching could be observed rather at much lower frequencies of 112(1) cm⁻¹ and 145(1) cm⁻¹ ⁴⁷. The mid-range region is mainly contributed by the M-O stretching and O-M-O bending modes of TiO₅ and MnO₆. For instance, the band at 364(1) cm⁻¹ can be assigned to O-Ti-O bending with the analogy of the rutile-type Nd₂TiO₅ ceramic ⁴⁸ where the pyramidal site is

occupied by Ti^{4+} -cation. The high-frequency region is dominated by the M-O stretching vibrations ⁴⁷.

Table 4. Raman and fourier transform infrared (FTIR) spectra fit parameters of peak-maximum (ω/cm^{-1}) and full-width at half-maximum (FWHM/ cm^{-1}) of NdMnTiO_5 .

Peak	Raman		FTIR	
	ω	FWHM	ω	FWHM
1	101.3(1)	9.7(1)	389.2(1)	18.1(1)
2	112.1(1)	9.6(1)	456.1(1)	41.2(1)
3	145.6(1)	16.3(1)	494.5(1)	39.7(1)
4	179.2(1)	27.0(1)	527.3(1)	39.3(1)
5	205.9(1)	29.7(1)	557.8(1)	70.0(1)
6	225.8(1)	21.7(1)	608.0(1)	53.2(1)
7	236.4(1)	43.4(1)	640.7(1)	50.9(1)
8	283.5(1)	58.6(1)	684.4(1)	81.9(1)
9	316.2(1)	20.9(1)	807.0(1)	22.3(1)
10	330.2(1)	34.2(1)	839.9(1)	44.0(1)
11	364.5(1)	68.3(1)		
12	418.0(1)	61.4(1)		
13	462.4(1)	31.5(1)		
14	487.4(1)	78.3(1)		
15	539.7(1)	36.1(1)		
16	570.6(1)	47.2(1)		
17	616.0(1)	34.2(1)		
18	644.8(1)	77.5(1)		
19	717.1(1)	67.1(1)		
20	801.8(1)	61.2(1)		
21	845.1(1)	52.5(1)		
22	880.5(1)	20.6(1)		

Both theoretical and experimental findings ^{22, 47} suggest that the broad peak maxima at $616(1) \text{ cm}^{-1}$ and $645(1) \text{ cm}^{-1}$ are contributed by the different Mn-O stretching modes (A_g and B_{1g}) of the MnO_6 octahedra as their bond distances lie close to each other (**Tab. 4**). Due to higher strength of Ti-O bonds ($672.4 \pm 9.2 \text{ kJ/mol}$) than those of Mn-O bond ($402.9 \pm 41.8 \text{ kJ/mol}$) ⁴⁹, the peak maxima observed between 775 cm^{-1} and 875 cm^{-1} can be assigned to the Ti-O stretching modes ⁴⁸. The intense band at 845 cm^{-1} along with a shoulder at 880 cm^{-1} corresponds to Ti-O asymmetric stretchings in the TiO_5 pyramid. To better

understand the vibrational spectra of the centrosymmetric system, we also collected FTIR spectra at ambient condition. The MIR spectrum (**Fig. 4**), however, requires only ten Pseudo-Voigt peaks (**Tab. 4**). As complimentary to the Raman, the observed peaks can be explained in similar manner (see above). For instance, the IR band at $389(1) \text{ cm}^{-1}$ can be explained in terms of the TiO_5 vibrational features⁴⁸. Comparing the infrared absorption of BiMn_2O_5 ⁴⁷ the band maxima at 608 cm^{-1} and 641 cm^{-1} may belong to the B_{1u} and B_{3u} modes of the MnO_6 octahedra, respectively. Alike the Raman frequency, the IR spectral intensities at higher frequencies above 750 cm^{-1} are correlated to the Ti-O vibrations⁴⁸. The MIR mode at $807(1) \text{ cm}^{-1}$ with a shoulder at $840(2) \text{ cm}^{-1}$ is contributed from the Ti-O asymmetric stretchings of the TiO_5 pyramid.

Thermal property

Thermogravimetric analysis shows both, weight loss (TG) and the difference thermal analysis (DTA), as shown in **figure 5**. It was earlier reported that BiMn_2O_5 decomposed into Bi_2O_3 and Mn_3O_4 , whereas RMn_2O_5 ($R = \text{Nd, Sm and Eu}$) into RMnO_3 and Mn_3O_4 ²².

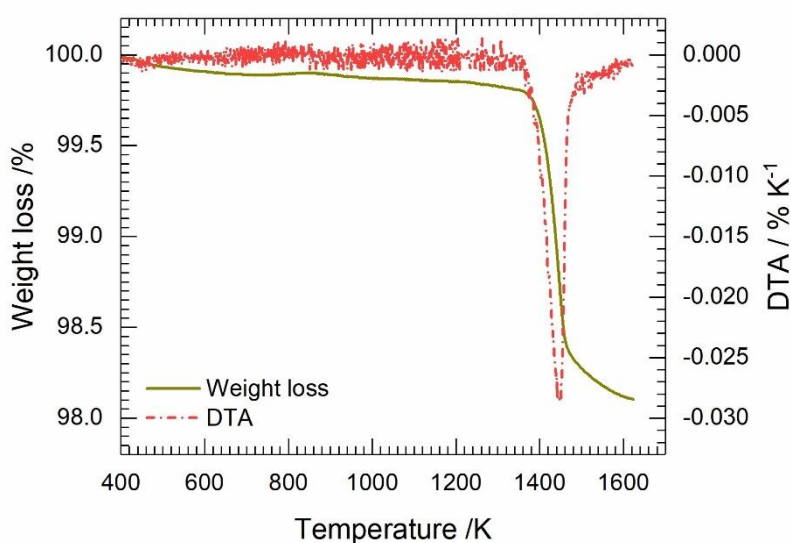


Figure 5. Thermogravimetric analysis of NdMnTiO_5 .

The weight loss of 1.65(1) wt% for NdMnTiO₅ amounts half of the weight loss observed in the RMn₂O₅ system²². That is, NdMnTiO₅ decomposes into NdMnO₃ and TiO₂ along with some other unidentified phases. From the DTA curve, the decomposition temperature is found to be 1385(5) K. Indeed, the decomposition temperature of NdMnTiO₅ is observed to be higher than those of BiMn₂O₅ and RMn₂O₅ system ($R = \text{Nd, Sm and Eu}$)²², which can be explained in terms of the higher bond strength value of Ti-O compared to Mn-O⁴⁹.

Magnetic property

Temperature-dependent field-cooled (FC) and zero-field-cooled (ZFC) DC magnetic susceptibility curves of NdMnTiO₅ are shown in **figure 6**. A significant enhancement of susceptibility was observed at temperatures lower than 50 K for both ZFC and FC magnetizations. This ZFC magnetic behavior is a common feature in rare-earth manganates. The powder ZFC magnetic susceptibility (**Fig. 6**) undergoes a maximum at 42(1) K (T_{max}) followed by a steep decrease, which is typical for an antiferromagnetic ordering. To better identify the magnetic transition from the low-temperature upturn, the Fisher's curve⁵⁰ ($-\text{d}\chi/\text{d}T$ vs T) (**Fig. 6**) manifests the onset of long-range ordering at 43(1) K, which lies close to the T_{max} within the estimated uncertainty. Indeed, Fisher's curve gives a good approximation for the magnetic contributions to heat capacity of a given system. A large deviation between ZFC and FC susceptibility below ~ 50 K indicates the presence of competing interactions and/or possible magnetic anisotropy in the orthorhombic system. Beside the Mn \leftrightarrow Mn couplings, NdMnTiO₅ comprises of possible Nd³⁺ \leftrightarrow Nd³⁺ and Nd³⁺ \leftrightarrow Mn³⁺ exchange interactions within our investigated temperature range, which in some cases, however, was not reported for spin-ordering⁵¹. The magnetic susceptibility monotonically increases throughout the paramagnetic region followed by a point of inflection at low temperature, showing typical paramagnetic to long-range spin ordering.

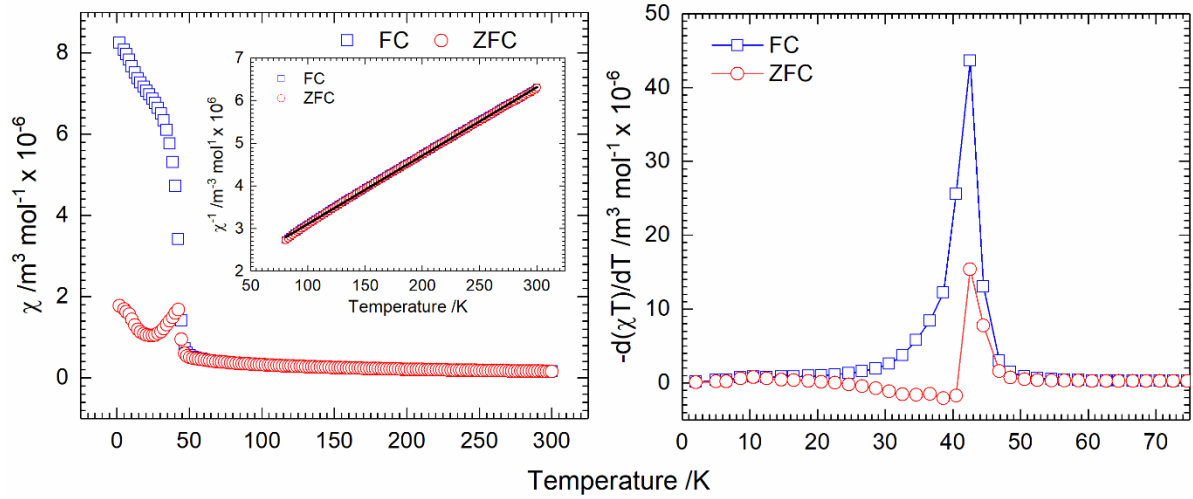


Figure 6. Temperature-dependent field-cooled DC magnetic susceptibility and inverse susceptibility (inset) (left-panel), and Fisher's curve (right-panel) of NdMnTiO₅.

The inverse susceptibility (χ^{-1}) curve (inset of **Fig. 6**) asymptotically approaches toward a Curie-Weiss behavior ($1/\chi = T/C - \Theta/C$) with increasing temperature. Fitting the paramagnetic regions above 120 K, the Curie-Weiss temperature (Θ), Curie constant and calculated effective magnetic moment (μ_{eff}) are obtained as -97(1) K, $6.29(6) \times 10^{-5} \text{ mol m}^{-3} \text{ K}^{-1}$ and $6.33(1) \mu_{\text{B}}$, respectively. The negative Θ -value indicates that the dominant magnetic interactions are of AFM type. The spin-only paramagnetic moment can be calculated considering the moment value $\mu_{\text{Mn}} = 4.9 \mu_{\text{B}}$ for Mn^{3+} (for the spin only $S = 4$) and $\mu_{\text{Nd}} = 3.62 \mu_{\text{B}}$ for Nd^{3+} ($J = 9/2$) and assuming that the total magnetic moment $\mu_{\text{cal}} = [\mu_{\text{Mn}}^2 + \mu_{\text{Nd}}^2]^{1/2} = 6.1 \mu_{\text{B}}$. That is, μ_{eff} calculated from the Curie-Weiss fit is in good agreement with the theoretical spin-only magnetic moment value contributed by both Mn^{3+} and Nd^{3+} magnetic sublattices. The magnetic frustration parameter⁵² ($|\Theta|/T_{\text{N}} = 97/43$) indicates that the system is moderately frustrated, and each magnetic cation is associated with significant exchange interactions with more than its nearest neighbors³⁷. The observed frustration value of 2.25 lies close to $47/20.5 = 2.3$ of NdCrTiO₅³⁷, however, almost half ($85.5/18 = 4.75$) observed by Saha et al.³⁸.

Magnetic structure

To better understand the microscopic nature of magnetic ordering of Mn^{3+} and Nd^{3+} sublattices in NdMnTiO_5 , TOF-NPD data were collected for both paramagnetic and spin-ordered phases. Rietveld plots of evaluated NPD data collected at 7.5 K and 50 K are presented in **figure 7**. The k -search included in the FullProf suite is used to determine the magnetic propagation vector (\mathbf{k}) which is found to be $\mathbf{k} = (0, 0.238, 0.117)$. The representational analysis allows for the determination of symmetry-allowed magnetic structures resulting from a second-order magnetic phase transition. These calculations were carried out using the program BasIreps (also included in the FullProf suite) assuming simultaneous ordering of both Nd and Mn sublattices. While the magnetic propagation vector determines the modulation going from one unit cell to another, magnetic symmetry analysis is needed to determine the coupling between the symmetry-related magnetic sites within one crystallographic unit cell. BasIreps is used to compute all the allowed symmetry couplings in form of irreducible representations and their respective basis vectors. From the irreducible representation analysis for the current \mathbf{k} -vector, there are two possible irreducible representations. The goodness of fit of magnetic structure refinements using either representation was identical. By comparing the NPD data at 50 K and 7.5 K, there are only two discernible magnetic Bragg peaks $(0 \ 2-k_y \ 0)$ and $(1 \ -k_y \ 1-k_z)$, where k_y and k_z are incommensurate magnetic propagation vector components along crystallographic b and c -directions, respectively.

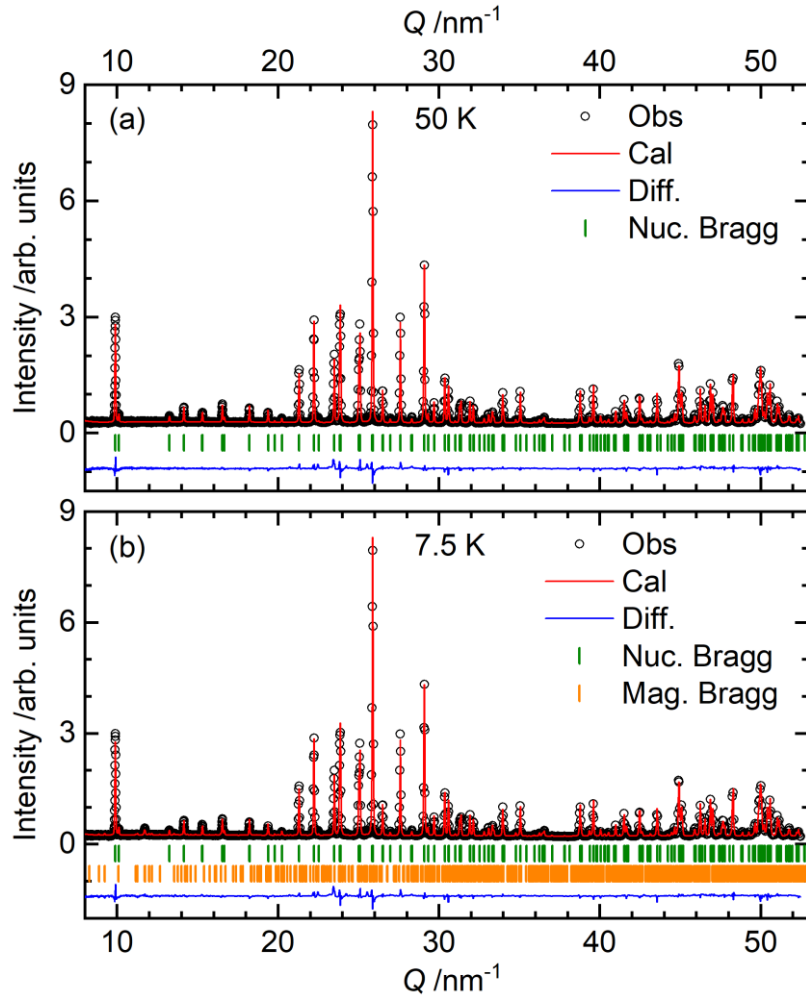


Figure 7. Neutron powder diffraction data Rietveld patterns of NdMnTiO_5 at (a) 50 K and (b) 7.5 K. Open circles and solid lines represent the observed and the calculated patterns, respectively. The difference between the observed and the calculated intensity is shown at the bottom. The vertical bars are for the calculated Bragg reflection positions.

These two peaks lie close to each other around $Q=12.75 \text{ nm}^{-1}$. The temperature-dependent relative intensity of these magnetic reflections and a second-order Landau-type phase-transition fitting are shown in **figure 8**, resulting in a T_N value of 40(1) K which is an excellent agreement with the Fischer's heat capacity curve (**Fig. 6**). Although magnetic structure determination from a low-intense magnetic reflection, where only $(0 \ 2-k_y \ 0)$ and $(1 - k_y \ 1-k_z)$ is significantly intense, of the NPD data seems to be difficult.

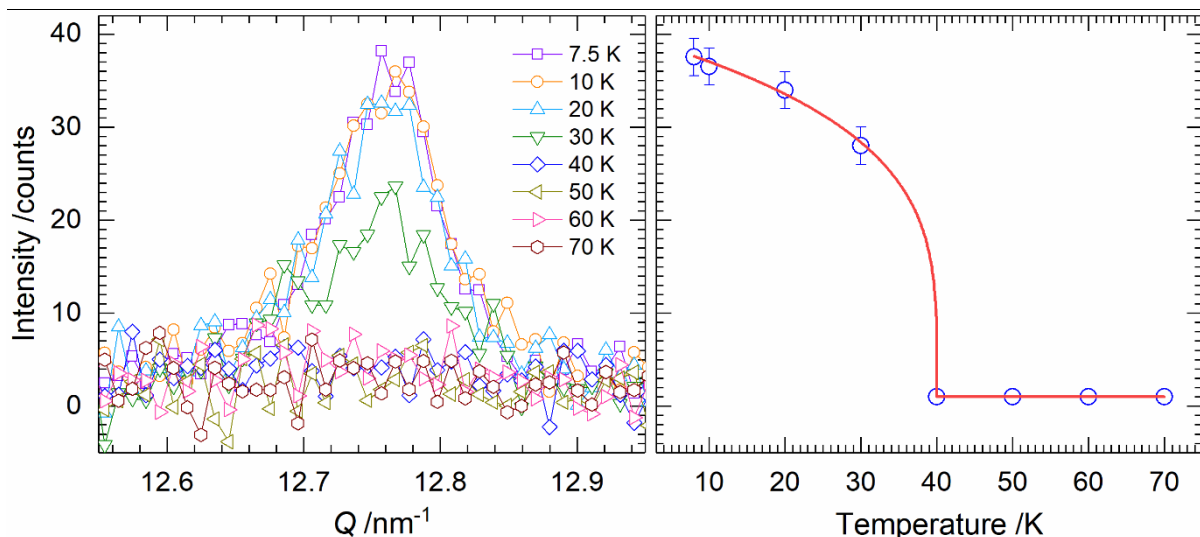


Figure 8. Temperature-dependent relative intensity of the $(0 \ 2-k_y \ 0)+(1 \ -k_y \ 1-k_z)$ magnetic reflections of the neutron powder diffraction data (left-panel) and a Landau-type fitting (right-panel), showing $T_N = 40 \text{ K}$.

Our careful analyses suggest for the incommensurate magnetic wave-vector along with an excellent Rietveld refinement fit for the observed magnetic intensity (**Fig. 7**). The refined magnetic structure is presented in **figure 9**, showing incommensurate magnetic moments within $1 \times 4 \times 4$ nuclear unit cells. The maximum amplitudes of ordered magnetic moments of Nd^{3+} and Mn^{3+} are found to be $2.00(5) \mu_B$ and $1.89(5) \mu_B$, respectively. The smaller moment values for both cations may due to lack of saturation at the given low-temperature. It is also well possible that Nd and Mn may not simultaneously order at T_N as seen for NdCrTiO_5 ⁵³. Since Nd^{3+} locates at the low-symmetry site, the ground state $^4 1_{9/2}$ can be split into five Kramers' doublets by the crystal field, and only at sufficiently low-temperatures the magnetic moment of the lowest lying Kramer's doublet is populated, which may lie beyond the investigated lowest temperature. Further high-resolution NPD measurements would provide more magnetic structural details of such polycrystalline sample.

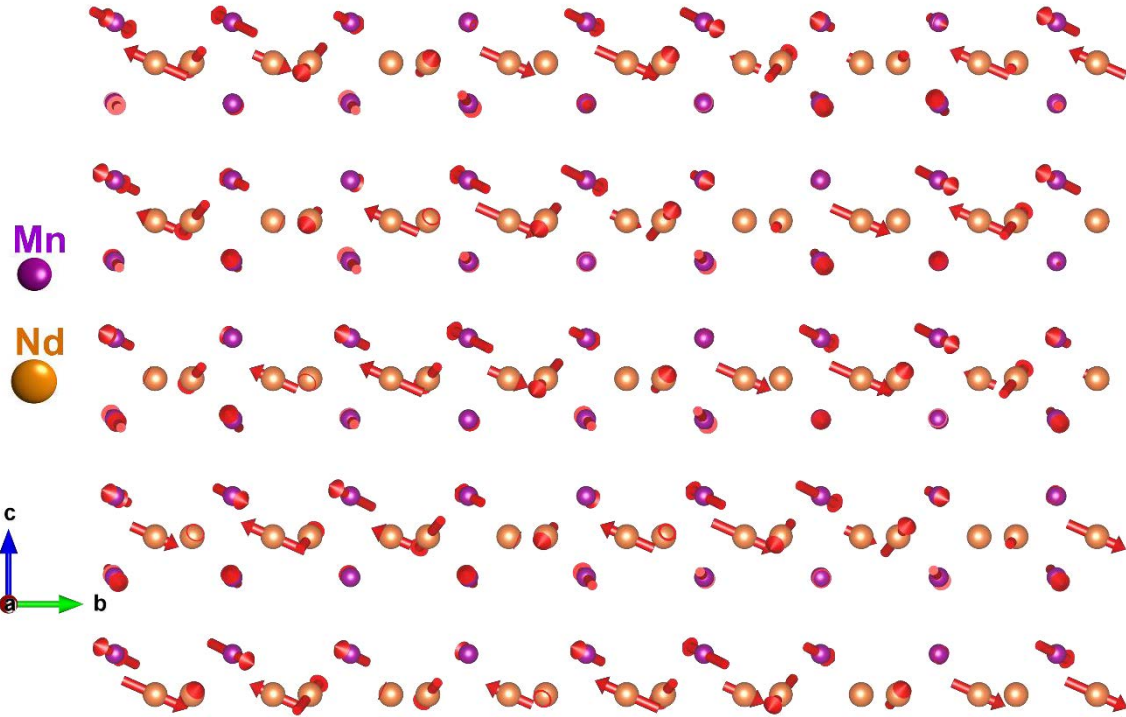


Figure 9: Incommensurate magnetic structure of NdMnTiO₅ is shown within 1, 4, and 4 nuclear unit cells along the **a**-, **b**- and **c**-directions, respectively.

4. Conclusion

While the isotopic NdCrTiO₅ and NdFeTiO₅⁴² show spin-ordering with $\mathbf{k} = (0, 0, 0)$ ⁵³ and $\mathbf{k} = (0, 0, \frac{1}{2})$, respectively, the present NPD data analyses suggests an incommensurate magnetic structure for NdMnTiO₅ ceramic with $\mathbf{k} = (0, 0.238, 0.117)$. Both the XRPD and NPD data analysis do not suggest an apparent issue of Ti/Mn mixed occupancy in the 4*f* and 4*h* sites. Moreover, Raman bands at higher frequencies do not suggest for Ti-O stretching in the octahedral sites⁴⁵. The bond valence sum, however, indicates for about 10 % inversion between Mn and Ti in the octahedral and pyramidal sites, which is comparable to 5 % inversion of Ti/Cr and Ti/Fe⁴² for the corresponding phases. Within the scope of the present NPD data quality it still remains open whether the system even possesses a non-centrosymmetric (*Pba2*) space group sufficiently below the observed Néel temperature⁵³. As

such, low-temperature single crystal neutron diffraction and multiferroic investigations of NdMnTiO₅ ceramic would be of prospective interests.

References

1. S. C. Abrahams and J. L. Bernstein, "Crystal structure of paramagnetic DyMn₂O₅ at 298 K," *J Chem Phys*, 46[10] 3776 (1967).
2. E. F. Bertaut, G. Buisson, S. Quezel-Ambrunaz, and G. Quezel, "Structure magnetique et proprietes magnetiques de BiMn₂O₅," *Solid State Communications*, 5[1] 25-30 (1967).
3. J. A. Alonso, M. T. Casais, M. J. Martínez-Lope, J. L. Martínez, and M. T. Fernández-Díaz, "A structural study from neutron diffraction data and magnetic properties of RMn₂O₅ (R = La, rare earth)," *Journal of Physics: Condensed Matter*, 9[40] 8515-26 (1997).
4. R. X. Fischer, "The mullite-type family of crystal structure," *Wiley-VCH, Weinheim* 1-46 (2005).
5. A. Muñoz, J. A. Alonso, M. T. Casais, M. J. Martínez-Lope, J. L. Martínez, and M. T. Fernández-Díaz, "Magnetic structure and properties of BiMn₂O₅ oxide: A neutron diffraction study," *Physical Review B*, 65[14] 144423 (2002).
6. L. M. Volkova and D. V. Marinin, "Crystal chemistry aspects of the magnetically induced ferroelectricity in TbMn₂O₅ and BiMn₂O₅," *Journal of Physics: Condensed Matter*, 21[1] 015903 (2009).
7. I. Kagomiya, K. Kohn, and T. Uchiyama, "Structure and Ferroelectricity of RMn₂O₅," *Ferroelectrics*, 280 131-43 (2011).
8. Z. H. Sun, B. L. Cheng, S. Dai, K. J. Jin, Y. L. Zhou, H. B. Lu, Z. H. Chen, and G. Z. Yang, "Effect of Ce substitution on magnetic and dielectric properties of BiMn₂O₅," *Journal of Applied Physics*, 99[8] 084105 (2006).
9. F. Ziegler, L. Köhler, H. Gibhardt, T. M. Gesing, M. M. Murshed, O. Sobolev, A. Piovano, and G. Eckold, "Characterization of Multiferroic Bi₂Mn₄O₁₀ by Dielectric and Neutron Spectroscopy," *Physica Status Solidi B-Basic Solid State Physics*, 256[7] 7 (2019).
10. S. Chattopadhyay, V. Balédent, F. Damay, A. Gukasov, E. Moshopoulou, P. Auban-Senzier, C. Pasquier, G. André, F. Porcher, E. Elkaim, C. Doubrovsky, M. Greenblatt, and P. Foury-Leylejian, "Evidence of multiferroicity in NdMn₂O₅," *Physical Review B*, 93[10] 104406 (2016).
11. M. L. Ninh Nguyen, Annie Ducouret, Bernard Raveau, "Distribution of Mn³⁺ and Mn⁴⁺ species between octahedral and square pyramidal sites in Bi₂Mn₄O₁₀ -type structure," *Journal of Materials Chemistry*, 9 731-34 (1999).
12. F. Ziegler, M. M. Murshed, H. Gibhardt, O. Sobolev, T. M. Gesing, and G. Eckold, "Mechanical properties of multiferroic Bi₂Mn₄O₁₀: Full set of elastic constants determined by inelastic neutron scattering," *Physica Status Solidi B-Basic Solid State Physics*, 253[5] 976-82 (2016).
13. J. Brink van den and D. I. Khomskii, "Multiferroicity due to charge ordering," *Journal of Physics: Condensed Matter*, 20[43] 434217 (2008).
14. A. Inomata and K. Kohn, "Pyroelectric effect and possible ferroelectric transition of helimagnetic GdMn₂O₅, YMn₂O₅ and YMn₂O₅," *Journal of Physics: Condensed Matter*, 8 2673-78 (1996).
15. A. M. Kadomtseva, Y. F. Popov, G. P. Vorob'ev, K. I. Kamilov, P. N. Makhov, M. M. Tehranchi, and A. Phirouznia, "Induced by magnetic field spin reorientation in YMn₂O₅," *Physica B*, 329 856-57 (2003).

16. Y. F. Popov, A. M. Kadomtseva, S. S. Krotov, G. P. Vorob'ev, and M. M. Lukina, "Magnetoelectric Effect in YMn_2O_5 in strong pulsed magnetic fields," *Ferroelectrics*, 279[1] 147-56 (2002).
17. Y. Noda, H. Kimura, M. Fukunaga, S. Kobayashi, I. Kagomiya, and K. Kohn, "Magnetic and ferroelectric properties of multiferroic RMn_2O_5 ," *Journal of Physics: Condensed Matter*, 20[43] (2008).
18. Y. F. Popov, A. M. Kadomtseva, S. S. Krotov, G. P. Vorob'ev, K. I. Kamilov, M. M. Lukina, and M. M. Tegranchi, "Magnetic and structural phase transitions in YMn_2O_5 ferromagnetoelectric crystals induced by a strong magnetic field," *Journal of Experimental and Theoretical Physics*, 96 961-65 (2003).
19. S. W. Cheong and M. Mostovoy, "Multiferroics: a magnetic twist for ferroelectricity," *Nature Materials*, 6 13-20 (2007).
20. L. C. Chapon, G. R. Blake, M. J. Gutmann, S. Park, N. Hur, P. G. Radaelli, and S. W. Cheong, "Structural anomalies and multiferroic behavior in magnetically frustrated TbMn_2O_5 ," *Physical Review Letters*, 93[17] 177402 (2004).
21. P. G. Radaelli and L. C. Chapon, "A neutron diffraction study of RMn_2O_5 multiferroics," *Journal of Physics: Condensed Matter*, 20[43] (2008).
22. K. Ghosh, M. M. Murshed, and T. M. Gesing, "Synthesis and characterization of $(\text{Bi}_{1-x}\text{R}_x)_2\text{Mn}_4\text{O}_{10}$: structural, spectroscopic and thermogravimetric analyses for $\text{R} = \text{Nd}, \text{Sm}$ and Eu ," *Journal of Materials Science*, 54[21] 13651-59 (2019).
23. G. Buisson, "Structures magnetiques sinusoidales et helicoidales de la terre rare dans TMn_2O_5 ," *Physica status solidi A*, 17 191 (1973).
24. G. Buisson, "Ordre helimagnetique du manganese dans la serie TMn_2O_5 ," *Physica status solidi A*, 16 533 (1973).
25. A. Muñoz, J. A. Alonso, M. T. Casais, M. J. Martínez-Lope, J. L. Martínez, and M. T. Fernández-Díaz, "A study of the magnetic structure of LaMn_2O_5 from neutron powder diffraction data," *European Journal of Inorganic Chemistry*, 2005[4] 685-91 (2005).
26. P. P. Gardner, C. Wilkinson, J. B. Forsyth, and B. M. Wanklyn, "The magnetic structures of the rare-earth manganates ErMn_2O_5 and TbMn_2O_5 ," *Journal of Physics C: Solid State Physics*, 21 5653-61 (1988).
27. V. Polyakov, V. Plakhty, M. Bonnet, P. Burlet, L. P. Regnault, S. Gavrilov, I. Zobkalo, and O. Smirnov, "Coupled magnetic and structural transitions in EuMn_2O_5 as studied by neutron diffraction and three-dimensional polarization analysis," *Physica B Condensed Matter*, 297[1-4] 208-12 (2001).
28. C. Wilkinson, F. Sinclair, P. Gardner, J. B. Forsyth, and B. M. R. Wanklyn, "The antiferromagnetic structure of DyMn_2O_5 at 4.2 K," *Journal of Physics C: Solid State Physics*, 14 1671-83 (1981).
29. A. Muñoz, J. A. Alonso, M. J. Martínez-Lope, and J. L. Martínez, "Synthesis, structural, and magnetic characterization of a new ferrimagnetic oxide: YFeMnO_5 ," *Chemistry of Materials*, 16[21] 4087-94 (2004).
30. A. Muñoz, J. A. Alonso, M. J. Martínez-Lope, and J. L. Martínez, "Synthesis and study of the crystallographic and magnetic structure of the ferrimagnetic oxide ErFeMnO_5 ," *Physical Review B*, 72[18] 184402 (2005).
31. A. Muñoz, J. A. Alonso, M. J. Martínez-Lope, and J. L. Martínez, "Synthesis and study of the crystallographic and magnetic structure of HoFeMnO_5 ," *European Journal of Inorganic Chemistry*, 2007[14] 1972-79 (2007).
32. J. A. Alonso, M. J. Martínez-Lope, M. T. Casais, J. L. Martínez, and V. Pomjakushin, "Synthesis, structural, and magnetic characterization of YCrMnO_5 ," *European Journal of Inorganic Chemistry*[13] 2600-06 (2005).
33. F. Pomiro, J. Lohr, E. V. P. Miner, V. Nassif, R. D. Sánchez, and R. E. Carbonio, "Crystal structure, magnetic and electrical properties of compounds in the RCrMnO_5 family ($\text{R} = \text{Sm}$,

- Eu, Gd, Tb, Ho and Er) synthesized under high oxygen pressure," *European Journal of Inorganic Chemistry*, 2015[28] 4737-49 (2015).
34. R. V. Shpanchenko, A. A. Tsirlin, E. S. Kondakova, E. V. Antipov, C. Bougerol, J. Hadermann, G. van Tendeloo, H. Sakurai, and E. Takayama-Muromachi, "New germanates RCrGeO_5 (R = Nd–Er, Y): Synthesis, structure, and properties," *Journal of Solid State Chemistry*, 181[9] 2433-41 (2008).
35. I. Yaeger, "Magnetic susceptibility studies of NdFeTiO_5 single crystals," *Journal of Applied Physics*, 49[3] 1513-15 (1978).
36. I. Yaeger, "Crystal growth and magnetic properties of NdFeTiO_5 ," *Materials Research Bulletin*, 13[8] 819-25 (1978).
37. M. Greenblatt, R. M. Hornreich, and B. Sharon, "Magnetoelectric compounds with two sets of magnetic sublattices: UCrO_4 and NdCrTiO_5 ," *Journal of Solid State Chemistry*, 10[4] 371-76 (1974).
38. J. Saha, G. Sharma, and S. Patnaik, "Evidence for multiferroic characteristics in NdCrTiO_5 ," *Journal of Magnetism and Magnetic Materials*, 360 34-37 (2014).
39. B. H. Toby, "EXPGUI, a graphical user interface for GSAS," *Journal of Applied Crystallography*, 34 201-13 (2001).
40. J. Rodríguez-Carvajal, "Recent advances in magnetic structure determination by neutron powder diffraction," *Physica B: Condensed Matter*, 192 55-69 (1993).
41. R. B. V. Dreele, J. D. Jorgensen, and C. G. Windsor, "Rietveld refinement with spallation neutron powder diffraction data," *Journal of Applied Crystallography*, 15 581-89 (1982).
42. G. Buisson, "Etude par rayons X et neutrons de la serie isomorphe ATiO_5 (A = Cr, Mn, Fe, T = Terres rares)," *J. Phys. Chem. Solids*, 31 1171-83 (1970).
43. P. S. Halasyamani, "Asymmetric cation coordination in oxide materials: Influence of lone-pair cations on the intra-octahedral distortion in d^0 transition metals," *Chemistry of Materials*, 16 3586-92 (2004).
44. I. D. Brown and D. A. Termatt, "Bond-valence parameters obtained from a systematic analysis of the inorganic crystal structure database," *Acta Crystallographica*, B41 244-47 (1985).
45. K. Ghosh, M. M. Murshed, M. Fischer, and T. M. Gesing, "Aluminum to germanium inversion in mullite-type RAlGeO_5 : characterization of a rare phenomenon for R = Y, Sm – Lu," *Journal of the American Ceramic Society*, 00 1-14 (2021).
46. E. Kroumova, M. I. Aroyo, J. M. Perez-Mato, A. Kirov, C. Capillas, S. Ivantchev, and H. Wondratschek, "Bilbao Crystallographic Server : Useful databases and tools for phase-transition studies," *Phase Transitions*, 76[1-2] 155-70 (2003).
47. F. M. Silva Júnior, C. W. A. Paschoal, R. M. Almeida, R. L. Moreira, W. Paraguassu, M. C. Castro Junior, A. P. Ayala, Z. R. Kann, and M. W. Lufaso, "Room-temperature vibrational properties of the BiMn_2O_5 mullite," *Vibrational Spectroscopy*, 66 43-49 (2013).
48. M. T. Paques-ledent, "Infrared and raman studies of M_2TiO_5 compounds (M = rare earths and Y): isotopic effect and group theoretical analysis," *Spectrochimica Acta Part A: Molecular Spectroscopy*, 32[6] 1139-44 (1976).
49. D. R. Lide, "CRC handbook of chemistry and physics," *CRC Press. Boca Raton, FL* (2005).
50. M. E. Fisher, "Relation between the specific heat and susceptibility of an antiferromagnet," *Philosophical Magazine*, 7[82] 1731-43 (1962).
51. L. Sorace and D. Gatteschi, "Lanthanides and actinides in molecular magnetism, First Edition. 1. Electronic structure and magnetic properties of lanthanide molecular complexes," *Wiley-VCH Verlag GmbH & Co. KGaA* 1-25 (2015).
52. A. P. Ramirez, "Chapter 4 Geometrical frustration," *Handbook of Magnetic Materials*, 13 423-520 (2001).

53. K. Gautam, A. Ahad, K. Dey, S. S. Majid, S. Francoual, V. G. Sathe, I. da Silva, and D. K. Shukla, "Symmetry breaking and spin lattice coupling in NdCrTiO₅," *Physical Review B*, 100[10] 104106 (2019).

Acknowledgement

KG gratefully thanks the University of Bremen for the financial supports. The research at Spallation Neutron Source, Oak Ridge was sponsored by the Scientific User Facilities Division, Office of Basic Energy Sciences, U.S. Department of Energy. Our sincere thanks to Dr. Qiang Zhang for collecting the Neutron data. CMNK acknowledges support from the Polish National Agency for Academic Exchange under the 'Polish Returns 2019' programme, grant PPN/PPO/2019/1/00014, and the subsidy of the Ministry of Science and Higher Education of Poland.

Notes

The authors declare no competing financial interest.

Chapter 6

Synthesis of relevant O10-phases and characterizations

In order to get new mullite-type phases in O10-structure type, several synthetizations were carried with different chemical compositions. Further details are as followed:

1. Polycrystalline sample of $RCrGeO_5$ ($R = \text{Eu, Gd}$) were synthesized by standard sol-gel method. Stoichiometric amounts of respective nitrates were mixed with 20 wt% glycerine into a glass beaker and heated at 353 K under magnetic stirring for about half an hour to make gel solution. This gel was further dried at 473 K for about 2 h. A foam-like solid was formed was homogenously crushed into powder and put into platinum crucible followed by heating at 1473 K for 48 h to get polycrystalline powder samples.

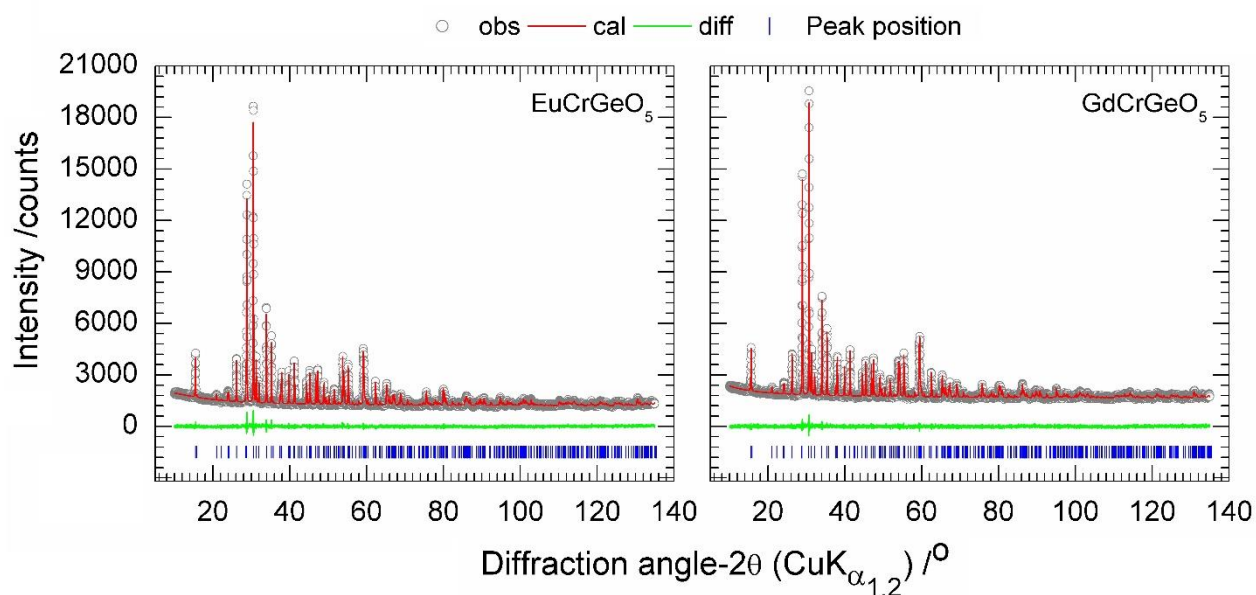


Figure 8.1: Rietveld refinement plots of XRPD data for $RCrGeO_5$ ($R = \text{Eu, Gd}$) crystallize in orthorhombic space group $Pbam$.

The Rietveld refinements of X-ray powder diffraction (XRPD) data (**Fig. 8.1**) confirmed that the polycrystalline samples crystalline in the space group of $Pbam$ with metric parameter

$a = 743.90(1) / 741.21(1)$ pm, $b = 847.87(1) / 846.82(1)$ pm, $c = 571.71(1) / 571.11(1)$ pm and $V = 360.59(1) 10^6 / 358.47(1) 10^6$ pm³ for EuCrGeO₅ and GdCrGeO₅ (in italic). Lattice parameter of these phases can be compared with previous report by Shanpanchenko et. al. [1]. Though the crystal structure and magnetic properties of this phases [1] were reported, detail investigations of vibrational and UV/Vis spectroscopic and thermal properties of these phases would be future aspects to be carried out. Moreover, temperature dependent studies of these samples would be desired works in future.

2. Polycrystalline sample of NdMGeO₅ ($M = \text{Cr and Fe}$) were synthesized by sol-gel method. Stoichiometric amounts of respective nitrates were mixed with 20 wt% glycerine into a glass beaker and heated at 353 K under magnetic stirring for about half an hour to make gel solution. This gel was further dried at 473 K for about 2 h. A foam-like solid was formed was homogenously crushed into powder and put into platinum crucible followed by heating at 1323 K for 48 h. Rietveld refinement plots of XRPD data of these phases are shown in **figure 8.2**, confirmed the sample crystallization in orthorhombic O10-mullite structure. The found metric parameter is a good agreement with previous reports [2-5] where crystal structure and magnetic properties of these phases are well known.

These samples are mostly reported as single crystals. We successfully synthesized single phase powder polycrystalline samples of these structure type. And their vibrational, UV/Vis spectroscopic properties and thermal properties are still missing at ambient condition. Moreover, temperature dependent studies of these phases would be prospective work in future.

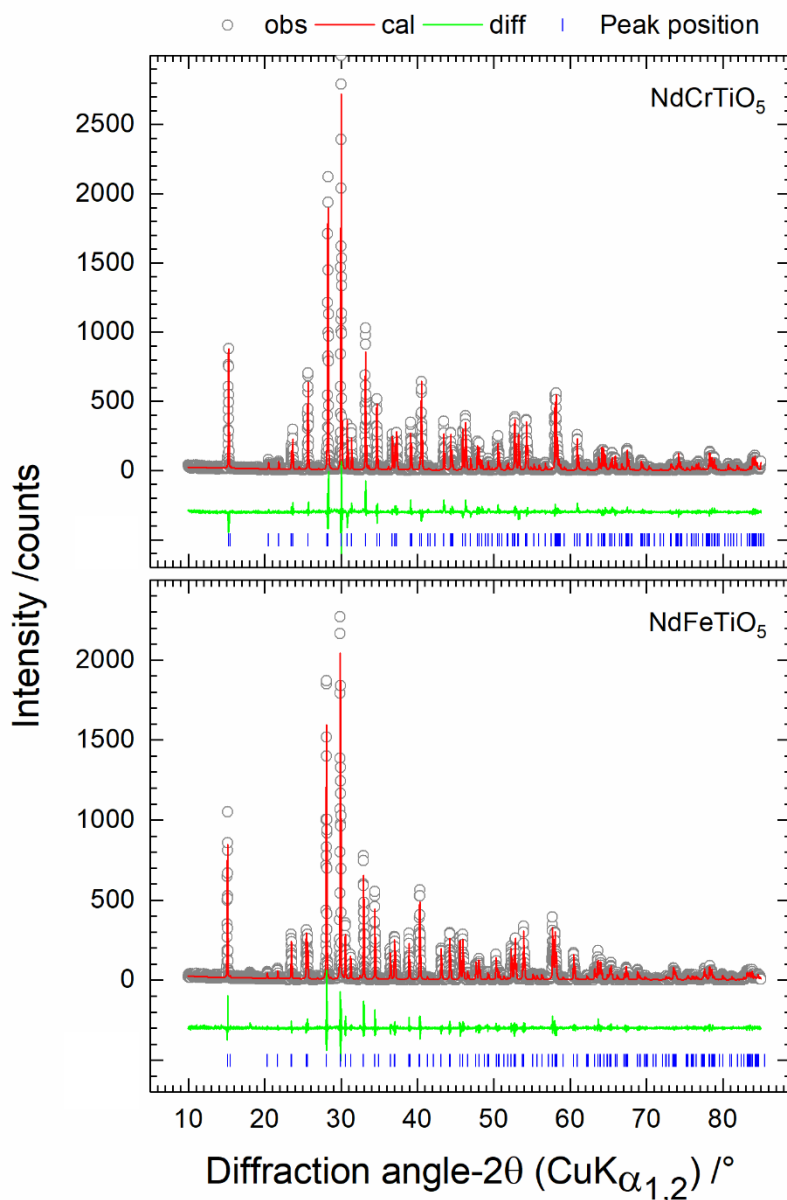


Figure 8.2: Rietveld refinement plots of XRPD data for NdMGeO_5 ($M = \text{Cr}$ and Fe).

Reference

- [1] R.V. Shpanchenko, A.A. Tsirlin, E.S. Kondakova, E.V. Antipov, C. Bougerol, J. Hadermann, G. van Tendeloo, H. Sakurai, E. Takayama-Muromachi, New germanates RCrGeO_5 ($R = \text{Nd-Er, Y}$): Synthesis, structure, and properties, *Journal of Solid State Chemistry* 181(9) (2008) 2433-2441. Doi:10.1016/j.jssc.2008.05.043
- [2] G. Buisson, Etude par rayons X et neutrons de la serie isomorphe ATiTO_5 ($A = \text{Cr, Mn, Fe, T} = \text{Terres rares}$), *J. Phys. Chem. Solids* 31 (1970) 1171-1183. Doi:10.1016/0022-3697(70)90326-4
- [3] M. Greenblatt, R.M. Hornreich, B. Sharon, Magnetolectric compounds with two sets of magnetic sublattices: UCrO_4 and NdCrTiO_5 , *Journal of Solid State Chemistry* 10(4) (1974) 371-376. Doi:10.1016/0022-4596(74)90046-2

- [4] I. Yaeger, Magnetic susceptibility studies of NdFeTiO₅ single crystals, *Journal of Applied Physics* 49(3) (1978) 1513-1515. Doi:10.1063/1.324940
- [5] I. Yaeger, Crystal growth and magnetic properties of NdFeTiO₅, *Materials Research Bulletin* 13(8) (1978) 819-825. Doi:10.1016/0025-5408(78)90045-4
- [6] J.-R. Gavarri, D. Weigel, Oxydes de Plomb. I. Structure cristalline du minium Pb₃O₄, à température ambiante (293 K), *Journal of Solid State Chemistry* 13(3) (1975) 252-257. Doi:10.1016/0022-4596(75)90127-9
- [7] J. Zemmann, Formel und Kristallstruktur des Schafarzikits, *Tschermaks Mineral. Petro. Mitt.* 2 (1951) 166-175.

Outlook

Within the scope of this cumulative dissertation, several mullite-type O10-phases were reported and investigated. From the refined crystal data, the strength of the stereochemical activity of the LEP-Bi³⁺ cation was calculated in terms of WLE value for (Bi_{1-x}R_x)₂Mn₄O₁₀ (*R* = Nd, Sm, Eu) solid solution. The larger ionic radii of *R*-cation in the RO₈ polyhedra played roles in decreasing the thermal stability of the O10-phases, which was explained in terms of the respective *R*-O bond strength values. Whether the geometric distortions of the MnO₆ and MnO₅ directly associated with the stereochemical activity of the Bi³⁺ LEPs (WLE parameter value) and thereby change the magnetic properties of the O10-phases remains open. Thus, neutron diffraction on each member of the (Bi_{1-x}R_x)₂Mn₄O₁₀ series would shed lights on the magnetic properties (commensurate /incommensurate magnetic structure) and multiferroic properties.

Looking for new phases with different chemical composition, some RAlGeO₅ (*R* = Y, Sm-Lu) phases extend the O10-mullite family. Whereas cationic inversion between the tetrahedral and octahedral sites in spinals are common, a rare Al/Ge inversion was found in these O10-phases, which influences their physical properties. Again, the sizes of the *R*-cations and the *R*-O bond strengths are identified for the respective thermal stability. Synthesis of single crystal of these phases and their characterization would provide better understanding of the Al/Ge inversion. For their wide bandgap values, these phases would be potential materials for white light LED applications.

Incorporating of Ti⁴⁺ cation in the square pyramidal site in the NdMnTiO₅ mullite-type structure exhibits an incommensurate magnetic structure. The magnetic frustration value (Curie-Weiss temperature /Néel temperature) of 2.25 indicates that the nearest-neighbor superexchange interactions in the penta-Cairo 5-ring channel breaks down possible magnetic frustration at temperatures below the *T_N* due to presence of non-magnetic Ti⁴⁺ cation in the MO₅ pyramidal site. Whether this moderate frustration is associated with the powder sample

(surface over volume factor) growth of single crystals and relevant investigations would clarify the issue. The single crystal neutron data also clarify if the manganese cations are even displaced from their centrosymmetric positions to release the magnetic frustration. That is, the possible multiferroic nature of the compound would be of interesting future studies.

Appendix

Figure A1: Abstract figure for the published manuscript titled as “Aluminum to germanium inversion in mullite-type $RAI\text{GeO}_5$: characterization of a rare phenomenon for $R = \text{Y, Sm} - \text{Lu}$ ”, *Journal of the American Ceramic Society* 105 (2022) 728-741. Doi:10.1111/jace.18085.

Figure A2: Abstract figure for the published manuscript titled as “Structural; vibrational, thermal and magnetic properties of NdMnTiO_5 ceramic”, *Journal of the American Ceramic Society* (Accepted 2021). DOI: 10.1111/jace.18261.

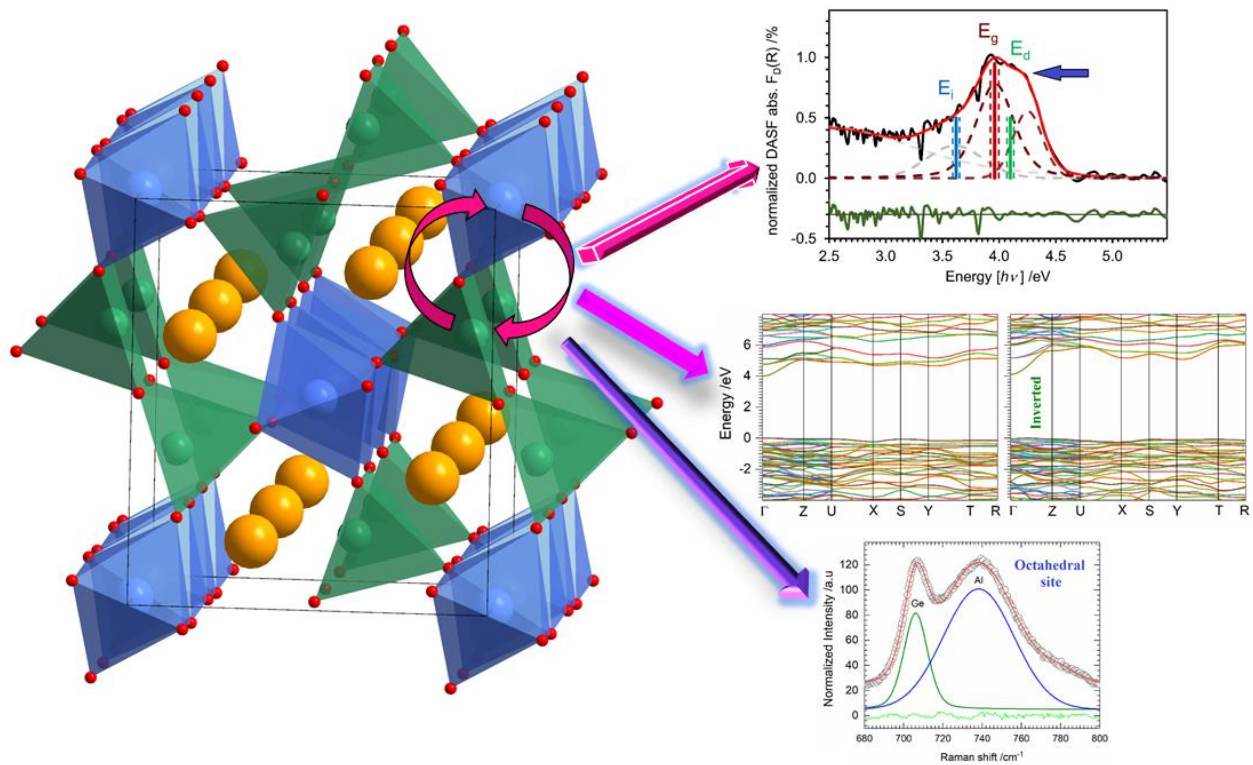


Figure A1: Rare inversion of Al/Ge between octahedral and pyramidal sites are observed in mullite-type $RAI\text{GeO}_5$ ($R = \text{Y, Eu-Lu}$) ceramics. The $\langle \text{Al/Ge-O} \rangle$ bond distances and their bond valence sums, and selective vibrational bands support the inversions. UV/Vis absorption spectra analyzed by both DASF and Tauc's methods demonstrate the direct transition and complemented by DFT calculations.

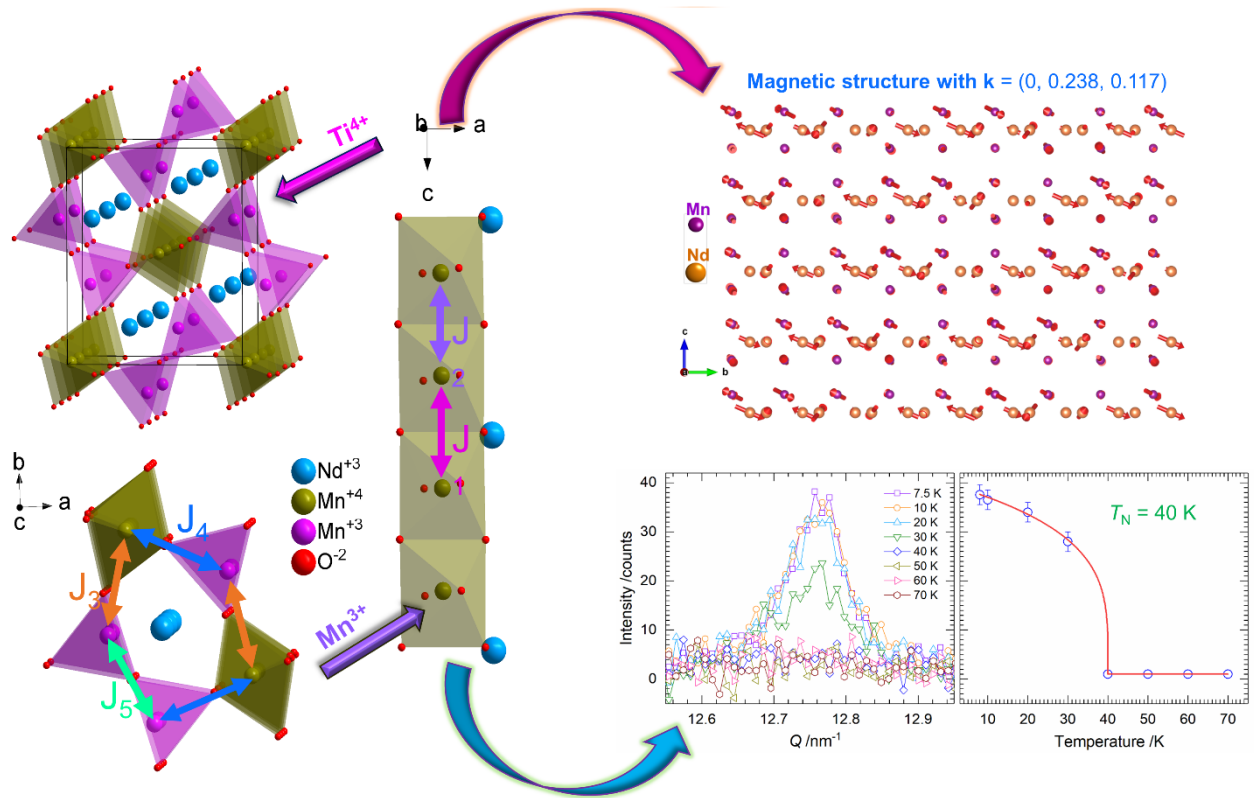


Figure A2: Crystal structure of mullite-type NdMn₂O₅ ceramic, where Mn³⁺ is replaced by Ti⁴⁺ in the MO₅ pyramidal site, leading to an incommensurate magnetic structure of NdMnTiO₅. Temperature-dependent relative intensity of the magnetic reflections of the neutron powder diffraction data support the Landau-type phase transition.

Curriculum Vitae

KOWSIK GHOSH

+49-15210360608

kowsikckt@gmail.com / ghosh@uni-bremen.de

Education

PhD Research associate (October, 2018 –February, 2022)
Institute of Inorganic Chemistry and Crystallography.
University of Bremen, Bremen, Germany.

Integrated Master of Science (M.Sc)
Applied Chemistry (2013 - 2018)
National Institute of Technology (NIT), Surat, India.
CGPA: 9.54 (out of 10)

Experience

University of Bremen, Bremen, Germany.
BISIP Scholar (July 2018 - September 2018).
Project Title: "Sealed tube synthesis and Characterization of SnMBO₄ (M = Al, Ga, Cr, Mn, Fe)".

University of Bremen, Bremen, Germany.
DAAD WISE Research Scholar (May 2017 - July 2017).
Project Title: "Vacuum sealed tube synthesis and Characterization of mixed valence Schafarikite (ML₂O₄; M = Fe, Mn, Cr and L = (PbSb), (PbBi))".

University of Bremen, Bremen, Germany.
Summer Research Intern (May 2016 - July 2016).
Project Title: "Synthesis and Characterization of Mullite-type (Bi_{1-x}Eu_x)₂Mn₄O₁₀".

Indian Institute of Science Education and Research (IISER), Mohali, India.
Summer Research Fellow (May 2015 - July 2015)
Project Title: "Synthesis and Characterization of Triazine based Ligands and Metal Complexes".

Oil and Natural Gas Corporation (ONGC), Govt. of India
Summer Trainee (May 2014 - June 2014)
Project Title: Quality and Process Control

Awards

DAAD Scholar for Congress 2021 program (August 2021)
Silver medalist at Department of Applied Chemistry, NIT, Surat, India (2018).
Bremen International Student Research Program (**BISIP**) Scholar (July 2018)
DAAD WISE Research Scholar (Funding ID: 57340829) (May 2017)
Summer Research Fellow at IISER, Mohali, India. (May 2015)

Publications

1. **K. Ghosh**, M. M. Murshed, T. Frederichs, C. M. N. Kumar, Th. M. Gesing; Structural, spectroscopic, thermal and magnetic properties analyses of NdMnTiO₅ ceramic. *Journal of the American Ceramic Society* (Accepted 2021). DOI: 10.1111/jace.18261.

2. **K. Ghosh**, M. M. Murshed, M. Fischer, Th. M. Gesing; Aluminum to germanium inversion in mullite-type RAlGeO₅: characterization of a rare phenomenon for R = Y, Sm-Lu., *Journal of the American Ceramic Society* 105 (2022) 728-741. <https://doi.org/10.1111/jace.18085>.

3. **K. Ghosh**, M. M. Murshed, Th. M. Gesing; Synthesis and characterization of (Bi_{1-x}R_x)₂Mn₄O₁₀: structural, spectroscopic and thermogravimetric analyses for R = Nd, Sm and Eu, *Journal of Materials Science* 54 (2019) 13651-13659. <https://doi.org/10.1007/s10853-019-03852-7>.

4. **K. Ghosh**, S. S. Satapathy, S. Ghosh, S. Jauhari, C. Nath Kundu, S. Si; Green chemistry approach for gold nanoparticles synthesis using plant extracts: a potential material towards catalysis and biology. *Adv. Nat. Sci.: Nanosci. Nanotechnol.* 11 (2020) 035012. DOI: <https://doi.org/10.1088/2043-6254/ab9f2b>.

5. S. Ghosh, S. S. Satapathy, **K. Ghosh**, S. Jauhari, S. K. Panda, S. Si; Carbon Dots Assisted Synthesis of Gold Nanoparticles and Their Catalytic Activity in 4-Nitrophenol Reduction. *ChemistrySelect* 4 (2019) 3416–3422. DOI: <https://doi.org/10.1002/slct.20180404>

Conferences

25th Congress of International Union of Crystallography (**IUCr**) 2021, Prague, Czech Republic. (**August, 2021**)
27th Annual Meeting of the German Crystallographic Society (**DGK**), Leipzig, Germany. (**March, 2019**)
NDDK, Technical University, Braunschweig, Germany. (**September, 2018**)

Skills

XRD and NPD Rietveld Refinement, Solid state synthesis, Solid state spectroscopic methods, Magnetic properties analysis, Structure property relationship.

Software known: Topas, GSAS, FullProf, Labspec, Vesta, Diamond, Lamp, Matlab, Struplo, Origin, ChemDraw.

Instruments known: Powder X-Ray Diffractometer, Single X-Ray Diffractometer, Raman Spectroscopy, FTIR and Solid UV/Vis spectroscopy, TGA-DSC, EDX and SEM.
